

**CHARACTERISTICS OF ULTRA HIGH PERFORMANCE
CONCRETE SUBJECTED TO DYNAMIC LOADING**

by

Sukhoon Pyo

A dissertation submitted in partial fulfillment
of the requirements for the degree of
Doctor of Philosophy
(Civil Engineering)
in the University of Michigan
2014

Doctoral Committee:

Professor Sherif El-Tawil, Chair
Assistant Professor Samantha H. Daly
Assistant Professor Jason P. McCormick
Emeritus Professor Antoine E. Naaman

© Sukhoon Pyo 2014

DEDICATION

To my parents, MyoungChul Pyo and GiSoon Baek

To my beloved wife, Seongkum,

To my son JiYul

ACKNOWLEDGEMENTS

This dissertation is the culmination of a journey marked by the hard work, sacrifices, support and guidance of a number of individuals who, over the years, have influenced me in numerous ways and helped me become the person I am today. I would like to take this opportunity to express my gratitude toward all these individuals.

Foremost I would like to express my most profound gratitude to my academic advisors, Professor Sherif El-Tawil for his extraordinary enthusiasm, optimism, ideas, insight, encouragement, support, and guidance during the course of this research. Professor El-Tawil introduced me to the rich world of ultra high performance concrete (UHPC) and gave me the opportunity to work on projects regarding UHPC and dynamic testing. Professor El-Tawil is a great mentor and a strong role-model as a scholar.

I would also like to thank my dissertation committee members: Professor Antoine E. Naaman, Professor Jason P. McCormick and Professor Samantha H. Daly. In particular, I am very grateful to Professor Naaman for his invaluable lessons on experiments, theoretical backgrounds and infinite ideas coming out of his long-term experience on research of strain-hardening cement-based materials.

The next group of people to whom I owe a debt of gratitude are my fellow graduate students and scholars at the University of Michigan with whom I have grown as a researcher and as a person. In particular: Dr. Junhee Kim, Dr. Bang Yeon Lee and Dr. Jongho Kim. An extra special thanks go to Dr. Philip Park for his support, encouragement and inspiring. I also thank the brilliant members in research team of the Computational Structural Simulation Laboratory (CSSL), Dr. Honghao Li, Ms. Julie Fogarty, Mr. Jieshi Fang, Mr. Mo Alkaysi and Dr. Yuh Shiou Tai. Furthermore, I would like to acknowledge Mr. Robert Fischer, Mr. Robert Spence and Mr. Jan Pantolin for all their help in preparing my experiments.

Outside of the academic realm, I must also thank those individuals at the University of Michigan who made my social life during my graduate studies one I will look upon fondly: Seung Yup Lee, Seungjun Ahn, Enjin Jang, Youngbum Kwon, Seongjoon Park, Sean O'Connor, Mike Kane, Courtney Peckens, Kyubum Kim, Eunsoo Kim, Taehoon Kang, HyonSohk Ohm, Paul A. Beata and all my soccer team members (FC Blue Tigers).

Above all, I must acknowledge the love and support of my incredible family: my beautiful wife, Seongkum, who has always provided me with a reminder of what is truly important in life, and has been a constant source of strength, inspiration, and love; my adorable son JiYul who has been a constant source of motivation; and my parents, MyoungChul Pyo and GiSoon Baek, who have always told me that I could accomplish anything I put my mind to, and have lovingly supported every step of my academic journey since my first day at kindergarten. I owe them everything.

TABLE OF CONTENTS

DEDICATION	ii
ACKNOWLEDGMENTS	iii
LIST OF TABLES	ix
LIST OF FIGURES	x
ABSTRACT	xvii
CHAPTER 1. INTRODUCTION	1
1.1 GENERAL BACKGROUND	1
1.2 ULTRA HIGH PERFORMANCE CONCRETE	2
1.3 OBJECTIVES AND TASKS	4
1.4 STRUCTURE OF THE DISSERTATION	6
CHAPTER 2. LITERATURE REVIEW	9
2.1 ULTRA HIGH PERFORMANCE CONCRETE	9
2.2 STRAIN RATE EFFECT ON CONCRETE	11
2.2.1 Strain Rate Properties of Concrete in Compression	11
2.2.2 Strain Rate Properties of Concrete in Tension	11
2.2.2.1 Strain Rate Properties of Regular Concrete and Cementitious Composites in Tension under Low Strain Rates	12
2.2.2.2 Strain Rate Properties of Regular Concrete and Cementitious Composites in Tension under High Strain Rates	13
2.2.3 Strain Rate Response of UHPC	14
2.3 TESTING METHODS FOR CONCRETE UNDER VARIABLE STRAIN RATE	15
2.3.1 Testing Methods for Concrete in Tension under Quasi-Static Loading	15

2.3.2 Testing Methods for High Strain Rate Loading	16
2.3.2.1 Split Hopkinson Pressure Bar (SHPB)	17
2.3.2.2 Tension Testing using SHPB	18
2.3.2.3 Strain Energy Impact Test System (SEITS) and Strain Energy Frame Impact Machine (SEFIM)	19
2.4 THEORETICAL APPROACHES FOR MODELING THE DYNAMIC RESPONSE OF CONCRETE	21
2.4.1 Crack Speed in Solids	23
2.4.2 Simulation of Crack Propagation in Solids	24
2.5 SUMMARY	25

CHAPTER 3. PROPERTIES OF ULTRA HIGH PERFORMANCE FIBER REINFORCED CONCRETE (UHP-FRC) UNDER LOW STRAIN RATE TENSION	26
3.1 EXPERIMENTAL PROGRAM	26
3.1.1 Materials and Fabrication	30
3.1.2 Test Setup and Procedure	31
3.1.3 Test Results	32
3.2 EVALUATION OF EXPERIMENTAL RESULTS	39
3.2.1 Separate Effects of Fiber Volume Fraction, Aspect Ratio, Length, and Type	39
3.2.2 Equivalent Bond	46
3.2.3 Effect of Reinforcing Index $V_f(l_f/d_f)$	46
3.2.4 Energy Absorption Capacity	46
3.2.5 Cracking	49
3.2.6 Fiber Tensile Stress	51
3.2.7 DIF	51
3.2.8 General Trends in the Test Data	55
3.3 CONCLUSIONS	55

CHAPTER 4. IMPACT TESTING OF STRAIN HARDENING CEMENTITIOUS COMPOSITES IN DIRECT TENSION USING RELEASED STRAIN ENERGY	57
4.1 BACKGROUND	57
4.2 MODIFIED SEFIM TO CAPTURE HARDENING AND POST PEAK RESPONSE ...	58
4.3 FE MODELING OF M-SEFIM	60
4.4 PARAMETRIC SIMULATIONS	64
4.5 SPECIMEN PREPARATION FOR IMPACT TESTING	66
4.6 STRAIN MEASUREMENT UNDER IMPACT LOADING	69
4.7 EXERCISING THE M-SEFIM SETUP	73
4.8 LIMITATIONS AND POTENTIAL OF M-SEFIM	79
4.9 CONCLUSIONS	82
CHAPTER 5. DIRECT TENSILE BEHAVIOR OF UHP-FRC AT HIGH STRAIN RATES	84
5.1 EXPERIMENTAL PROGRAM	84
5.2 SELECTION OF SPECIMEN LENGTH	85
5.3 EVALUATION OF EXPERIMENTAL RESULTS	94
5.3.1 Effect of Fiber Type and Aspect Ratio	95
5.3.2 DIF	105
5.3.3 Comparison with Theoretical Predictions	108
5.3.4 Discussion	112
5.4 CONCLUSIONS	112
CHAPTER 6. CRACK PROPAGATION SPEED IN ULTRA HIGH PERFORMANCE CONCRETE (UHPC)	115
6.1 EXPERIMENTAL PROGRAM	115
6.2 REVIEW OF EDGE DETECTION AND CRACK SPEED ANALYSIS	122
6.3 EVALUATION OF EXPERIMENTAL RESULTS	123
6.3.1 Critical Stress Intensity Factor	123
6.3.2 Crack Speed in UHPC	124

6.3.3 Discussion	141
6.4 CONCLUSIONS	146
CHAPTER 7. CRACK VELOCITY-DEPENDENT DYNAMIC TENSILE BEHAVIOR OF CONCRETE	148
7.1 EXPRESSION FOR CRACK VELOCITY IN CONCRETE	148
7.2 CRACK VELOCITY-DEPENDENT MODEL FOR CONCRETE UNDER TENSILE LOADING	154
7.2.1 Broberg (1960)'s Approach	154
7.2.2 Freund (1972)'s Approach	155
7.2.3 Application of the DIF Model to UHPC	158
7.3 CONSTITUTIVE MODELING	159
7.4 CONCLUSIONS	163
CHAPTER 8. RESEARCH SUMMARY AND DIRECTIONS OF FUTURE RESEARCH	166
8.1 SUMMARY OF RESEARCH	166
8.1.1 Characterization of UHP-FRC under Direct Tension at Low Strain Rates	166
8.1.2 Development of New Impact Testing System for UHP-FRC	168
8.1.3 Characterization of UHP-FRC under Direct Tension at High Strain Rates	169
8.1.4 Characterization of Crack Propagation in UHPC	170
8.1.5 Development of a Theoretical Modeling Scheme for Concrete under Dynamic Tension	171
8.2 FUTURE RESEARCH	173
REFERENCES	175

LIST OF TABLES

Table 2.1: Direct tension test setups – Dogbone / Dumbbell shape (Wille et al. 2014)	16
Table 3.1: Mixtures proportions by weight (based on Wille et al. (2011b))	27
Table 3.2: Grain Size Distribution (GSD) of sand (Wille et al. 2011b)	28
Table 3.3: Properties of steel fibers used in this study	28
Table 3.4: UHP-FRC test series investigated in this study	29
Table 3.5: Rate effect on the average tensile properties of UHP-FRC	35
Table 3.6: Equivalent bond strength for UHP-FRC with 2% fiber content	39
Table 3.7: Least square fit approximations of results in Figures 3.13 and 3.14	48
Table 4.1: Transmitter bar material characteristics	60
Table 5.1: Summary of impact test results	87
Table 5.2: Fiber tensile stress and equivalent bond strength of UHP-FRC under impact loading	112
Table 6.1: Mixtures proportions by weight (based on Wille et al. (2011b))	116
Table 6.2: Properties of steel fibers used in this study	116
Table 6.3: Number of UHPC specimens investigated in this study	117
Table 6.4: Mechanical and fracture properties of UHPC	117
Table 6.5: Summary of crack speed results	126

LIST OF FIGURES

Figure 1.1: Regimes of strain rates (Hentz et al. 2004)	1
Figure 1.2: Example of dense particle packing (http://quizlet.com)	3
Figure 1.3: Effect of scratching of the brass coating in steel fibers embedded in UHPC: (a) non scratched fiber; (b) partly scratched fiber; (c) fiber end (Wille and Naaman 2010) ..	4
Figure 1.4: Research roadmap including future work	6
Figure 1.5: Structure of the dissertation	8
Figure 2.1: A typical SHPB setup (Song et al. 2009)	17
Figure 2.2: 100-mm-diameter SHPB system for concrete under compression (Li and Xu 2009)	18
Figure 2.3: Schematic of tension setup proposed by Harding and Welsh (1983)	19
Figure 2.4: Prototype of the SEITS setup developed by Kim et al. (2011)	20
Figure 2.5: Schematic of the strain energy frame impact machine (SEFIM)	21
Figure 2.6: Strain rate dependency for concrete under tensile loading: (a) Strain rate effect on DIF (Leppanen 2006); (b) stress-strain behavior (Zielinski et al. 1981)	22
Figure 3.1: Steel fiber tensile test setup using a Test Resources load frame (Model# 830L)	29
Figure 3.2: Mixing procedure of UHP-FRC: (a) fluid state without fibers; (b) adding fibers ...	30
Figure 3.3: Direct tensile test setup	31
Figure 3.4: Typical interpretation and measurement of test results: (a, b) typical variables; (c) typical averaging of stress-strain curve (T-0.3-18-2% & $\dot{\epsilon} = 0.01$ /sec) (Note: strain valid up to peak stress only.)	32
Figure 3.5: Rate effect on the tensile behavior of T-0.3-25 UHP-FRC with increasing fiber volume content (Note: strain valid up to peak stress only.)	36
Figure 3.6: Rate effect on the tensile behavior of S-0.2-25 UHP-FRC with increasing fiber volume content (Note: strain valid up to peak stress only.)	37
Figure 3.7: Rate effect on the tensile behavior of UHP-FRC using fibers with about same aspect ratio (Note: strain valid up to peak stress only.)	38

Figure 3.8: Rate effect on the first cracking strength of UHP-FRC: (a) specimens with different fiber volume fractions; (b) specimens with 2 % fiber volume fraction	41
Figure 3.9: Rate effect on the post cracking strength of UHP-FRC: (a) specimens with different fiber volume fractions; (b) specimens with 2 % fiber volume fraction	42
Figure 3.10: Rate effect on the energy absorption capacity of UHP-FRC: (a) specimens with different fiber volume fractions; (b) specimen with 2 % fiber volume fraction ...	43
Figure 3.11: Rate effect on the strain capacity of UHP-FRC: (a) specimens with different fiber volume fractions; (b) specimens with 2 % fiber volume fraction	44
Figure 3.12: Rate effect on the elastic modulus of UHP-FRC: (a) specimens with different fiber volume fractions; (b) specimens with 2 % fiber volume fraction	45
Figure 3.13: Effects of the fiber reinforcing index on mechanical properties of UHP-FRC: (a) Post cracking strength; (b) First cracking strength	47
Figure 3.14: Effects of $V_f(l_f^2/d_f)$ on energy absorption capacity of UHP-FRC	48
Figure 3.15: Representative multiple cracking patterns in UHP-FRC specimens	49
Figure 3.16: Rate effect on number of cracks of UHP-FRC: (a) specimens with different fiber volume fractions; (b) specimens with 2 % fiber volume fraction	50
Figure 3.17: Rate effect on the fiber tensile stress of UHP-FRC: (a) specimens with different fiber volume fractions; (b) specimens with 2 % fiber volume fraction	52
Figure 3.18: Dynamic increase factor (DIF) of UHP-FRC: (a) First cracking strength; (b) Post cracking strength; (c) Energy absorption capacity; (d) Strain capacity	53
Figure 4.1: Stress signal travel: (a) approaching the strain gage; (b) reaching the end of the transmitter bar; (c) reflecting back to the strain gage	59
Figure 4.2: Prototype of the proposed impact testing system	61
Figure 4.3: Finite element model of the proposed test setup	62
Figure 4.4: Stress-strain responses obtained from simulations: (a) material with small failure strain; (b) material with larger failure strain	63
Figure 4.5: M-SEFIM with 0.95 m long steel transmitter bar: (a) finite element model; (b) installation of the proposed testing setup	65
Figure 4.6: Computed material behavior from simulation results: (a) Strain data; (b) Stress data; (c) Stress-strain relationship in comparison with assigned constitutive model	66

Figure 4.7: (a) UHP-FRC mold for tension testing; (b) A UHP-FRC specimen for low strain rates testing used in Chapter 3; (c) A UHP-FRC specimen cut to desired length	67
Figure 4.8: Example of speckle patterns in this study: (a) specimen sprayed with white paint; (b) random speckle patterns with black paint	68
Figure 4.9: Connection between the transmitter bar and aluminum housing	68
Figure 4.10: Example of strain field computed using the DIC technique: (a) before major crack development; (b) after crack localization	71
Figure 4.11: Example of DIC results: (a) comparison of strain calculations methods; (b) stress data; (c) comparison of stress-strain relationships obtained by various methods ..	72
Figure 4.12: (a) Stress, strain rate and strain during an impact test; (b) Corresponding stress-strain relationship obtained from the data	74
Figure 4.13: Experimentally obtained stress-strain relationship contaminated by signal interference	75
Figure 4.14: Experimentally obtained stress-strain responses under different strain rates for direct tension tests	75
Figure 4.15: Failed specimen after testing	76
Figure 4.16: Examples of failed specimens: (a) S-0.2-25-1%; (b) S-0.2-25-2%; (c) S-0.4-25-2%; (d) S-0.4-25-3%; (e) T-0.3-25-1%; (f) T-0.3-25-2%; (g) T-0.3-25-3%	77
Figure 4.17: Detail demensions of couplers: (a) Type 1; (b) Type 2; (c) Type 3	80
Figure 4.18: Three types of couplers: (a) couplers before test; (b) fractured couplers	81
Figure 4.19: Effect of coupler characteristics on strain rate (computational and experiment data)	82
Figure 5.1: Example of data reading (T-0.3-25-1%): (a) Stress reading; (b) Strain reading; (c) Stress-strain relation (Note: strain valid up to peak stress only.)	86
Figure 5.2: Examples of the averaging process for obtaining the stress-strain response: (a) S-0.2-25-1%; (b) S-0.4-25-3% (Note: strain valid up to peak stress only.)	88
Figure 5.3: Specimen length of UHP-FRC specimens	89
Figure 5.4: Stress-strain responses from the parametric study using simulations	89
Figure 5.5: Examples of failure of UHP-FRC specimens in simulations: (a) $l = 55\text{mm}$; (b) $l = 60\text{mm}$; (c) $l = 65\text{mm}$	90

Figure 5.6: Examples of failure of UHP-FRC specimens in experiments: (a) $l = 55\text{mm}$; (b) $l = 60\text{mm}$; (c) $l = 65\text{mm}$ (note that the darker lower part of the photos is part of the gripping fixture of the machine)	90
Figure 5.7: Stress-strain responses from the parametric study using experiments	91
Figure 5.8: Experimentally obtained dynamic increase factor (DIF) of UHP-FRC specimens with different lengths: (a) First cracking strength; (b) Post cracking strength; (c) Energy absorption capacity; (d) Strain capacity	92
Figure 5.9: Strain rate versus specimen length	94
Figure 5.10: Rate effect on stress-strain response under tension of UHP-FRC using different fibers (Note: strain valid up to peak stress only.)	96
Figure 5.11: Rate effect of UHP-FRC using different fibers: (a) First cracking strength; (b) Post cracking strength; (c) Energy absorption capacity; (d) Strain capacity	100
Figure 5.12: Examples of failed specimens: (a) S-0.2-25-1%; (b) S-0.2-25-2%; (c) S-0.4-25-2%; (d) S-0.4-25-3%; (e) T-0.3-25-1%; (f) T-0.3-25-2%; (g) T-0.3-25-3%	102
Figure 5.13: Dynamic increase factor (DIF) for post cracking strength (excluding lower strain rate data)	106
Figure 5.14: Dynamic increase factor (DIF) of UHP-FRC: (a) First cracking strength of smooth fiber; (b) First cracking strength of twisted fiber; (c) Post cracking strength of smooth fiber; (d) Post cracking strength of twisted fiber; (e) Energy absorption capacity of smooth fiber; (f) Energy absorption capacity of twisted fiber; (g) Strain capacity of smooth fiber; (h) Strain capacity of twisted fiber	107
Figure 5.15: Effects of the fiber reinforcing index on post cracking strength: (a) Smooth fibers; (b) Twisted fibers	110
Figure 5.16: Effects of $V_f(l_f^2/d_f)$ on energy absorption capacity of UHP-FRC: (a) Smooth fibers; (b) Twisted fibers	111
Figure 6.1: Specimen failure after compression test: (a) CS-0 %; (b) CS-0.5 %	118
Figure 6.2: Schematic of the specimen employed in the crack speed study (unit: mm)	118
Figure 6.3: Actual UHPC specimen	119
Figure 6.4: Test setup for three-point bending testing using a MTS	120
Figure 6.5: Impact testing system for crack propagation: (a) finite element model of the system; (b) as-built setup	121

Figure 6.6: Examples of load curves for the slow loading cases: (a) CS-0% tested at 0.0076 mm/sec; (b) CS-0% tested at 7.6 mm/sec; (c) CS-0.5% tested at 7.6 mm/sec; (d) CS-1% tested at 7.6 mm/sec	125
Figure 6.7: Examples of crack propagation in CS-0% specimens under various loading speed: (a) 0.0076 mm/sec (using MTS machine); (b) 7.6 mm/sec (using MTS machine); (c) Type 1 coupler (M-SEFIM); (d) Type 2 coupler (M-SEFIM)	128
Figure 6.8: Examples of crack propagation in CS-0.5% specimens under various loading speed: (a) 7.6 mm/sec using MTS; (b) Type 1 coupler using the impact testing system; (c) Type 2 coupler using the impact testing system	130
Figure 6.9: Examples of crack propagation in CS-1.0% specimens under various loading speed: (a) 7.6 mm/sec (using the MTS machine); (b) Type 1 coupler (using M-SEFIM); (c) Type 2 coupler (using M-SEFIM)	132
Figure 6.10: Examples of strain rate calculations: (a) CS-0% tested at 0.0076 mm/sec (0.0589 /sec); (b) CS-0.5% tested at 7.6 mm/sec (0.203 /sec)	134
Figure 6.11: Example of crack edge detection in a CS-1.0% specimen for 7.6 mm/sec loading speed (using the MTS machine)	135
Figure 6.12: Examples of the final crack stage in captured and calculated images for CS-0% specimens under various loading speed: (a) 0.0076 mm/sec (using the MTS machine); (b) 7.6 mm/sec (using the MTS machine); (c) Type 1 coupler (using M-SEFIM); (d) Type 2 coupler using (M-SEFIM)	136
Figure 6.13: Examples of the final crack stage in captured and calculated images for CS-0.5% specimens under various loading speed: (a) 7.6 mm/sec (using the MTS machine); (b) Type 1 coupler (using M-SEFIM); (c) Type 2 coupler (using M-SEFIM) ...	137
Figure 6.14: Examples of the final crack stage in captured and calculated images for CS-1.0% specimens under various loading speed: (a) 7.6 mm/sec (using the MTS machine); (b) Type 1 coupler (using M-SEFIM); (c) Type 2 coupler (using M-SEFIM) ...	138
Figure 6.15: Examples of calculated crack speeds: (a) CS-0% tested at 0.0076 mm/sec; (b) CS-1.0% tested at 7.6 mm/sec; (c) CS-0% tested using Type 2 coupler in M-SEFIM; (d) CS-0.5% tested using Type 1 coupler in M-SEFIM	139
Figure 6.16: Calculated crack speed as a function of notch tip strain rate: (a) with high strain rate results; (b) without high strain rate results	140

Figure 6.17: Examples of CS-0% specimens after testing: (a) 0.0076 mm/sec (using the MTS machine); (b) 7.6 mm/sec (using the MTS machine); (c) Type 1 coupler (using M-SEFIM); (d) Type 2 coupler (using M-SEFIM)	141
Figure 6.18: Examples of CS-0.5% specimens after testing: (a) 7.6 mm/sec (using the MTS machine); (b) Type 1 coupler (using M-SEFIM); (c) Type 2 coupler (using M-SEFIM)	143
Figure 6.19: Examples of CS-1.0% specimens after testing: (a) 7.6 mm/sec (using the MTS machine); (b) Type 1 coupler (using M-SEFIM); (c) Type 2 coupler (using M-SEFIM)	144
Figure 6.20: Examples of CS-0.5% specimens with crushing failure tested in M-SEFIM with Type 3 coupler	145
Figure 6.21: Examples of specimens with crushing failure tested in M-SEFIM with Type 3 couplers: (a) CS-0.5%; (b) CS-1.0%	146
Figure 7.1: Bilinear cohesive traction-displacement curve	149
Figure 7.2: Medium mesh used in the simulation near the crack tip when crack length is 6 mm	150
Figure 7.3: Crack velocity of concrete as a function of strain rate	152
Figure 7.4: Stress profile within cohesive elements when crack length is 6 mm (a) $\dot{\epsilon}=7.70$ /sec; (b) $\dot{\epsilon}=14.6$ /sec; (c) $\dot{\epsilon}=20.9$ /sec	153
Figure 7.5: Normalized dynamic stress intensity factor versus normalized crack speed using Broberg (1960)'s and Freund (1972)'s approaches	156
Figure 7.6: Dynamic intensity factor (DIF) versus normalized crack velocity using Broberg (1960)'s and Freund (1972)'s approaches	157
Figure 7.7: Comparison between the proposed models and experimental data in Leppanen (2006)	158
Figure 7.8: Comparison between experimental data obtained in Chapters 3 and 5 and the Freund approach incorporated with crack speed data obtained in Chapter 6	159
Figure 7.9: (a) Schematic of concrete with randomly distributed circular aggregates; (b) Schematic of interfacial crack between aggregate and matrix	160

Figure 7.10: Stress-strain response under uniaxial tensile loading using Broberg (1960)'s and Freund (1972)'s approaches with various strain rate values: (a) $V_f = 0.3$; (b) $V_f = 0.5$ 162

Figure 7.11: Comparison between the predicted and experimental data (Zielinski et al. 1981) for overall uniaxial tensile response of concrete under static and dynamic loading 163

ABSTRACT

Characteristics of Ultra High Performance Concrete subjected to Dynamic Loading

by

Sukhoon Pyo

Chair: Professor Sherif El-Tawil

Ultra High Performance Concrete (UHPC) is among the most promising cementitious materials developed to date. It has the potential to be a viable solution for improving the resilience and sustainability of the built infrastructure because of its high strength, durability and energy absorption capacity. Pilot studies have shown that its impact resistance is particularly impressive, yet there is hardly any information about its dynamic behavior.

The experimental effort of this work focuses on investigating the strain rate sensitivity of UHPC as a function of fiber type (straight or twisted), characteristics and volume fraction. Low strain rate tests are conducted using a hydraulic actuator, whereas high strain rate tests are conducted using a new device that employs suddenly released elastic strain energy to apply an impact pulse. Developed and optimized through computational modeling, the new device permits accurate and practical testing of UHPC specimens in direct tension, under high strain rate, and can capture both hardening and post peak responses. It is compact compared to existing test

methods and permits the use of specimens that are similar in size and geometry to the specimens tested with the hydraulic actuator.

A key experimental observation is that UHPC becomes significantly more energy dissipative in tension under increasing strain rates, which highlights the material's potential for use in impact- and blast-resistant applications. Although specimens with twisted steel fibers show somewhat better mechanical properties than specimens with straight fibers due to the untwisting mechanism, comparable benefits could be obtained by using straight fibers with higher aspect ratios. Crack propagation studies show that crack speed increases asymptotically as notch tip strain rate increases.

The analytical portion of the study focuses on the source of strength enhancement for concrete materials under high rate tensile loadings, a topic of current controversy in the literature. Dynamic fracture models considering crack velocity dependency prove that strain rate sensitivity is strongly associated with the characteristics of dynamic crack growth, especially the asymptotic nature of crack speed versus strain rate and inertial effects at the crack boundaries. The theoretical observations are corroborated with experimental data in the literature and new data produced by this work.

CHAPTER 1

INTRODUCTION

1.1 GENERAL BACKGROUND

Civil engineers designing specialized facilities, such as nuclear power plants and high rise buildings, have to take into account the possibility of extreme loading events, such as aircraft impact, missile attack by terrorists, or earthquake loading, because failure of these facilities can result in catastrophic consequences. Extreme events typically generate rapid loading conditions that apply large stresses coupled with high strain rates on the materials used for construction. Therefore, understanding the behavior of construction materials under a wide range of external loading speeds is essential (see Figure 1.1). Since concrete is widely used as a primary construction material, investigation of its behavior under dynamic loading is an important research topic.

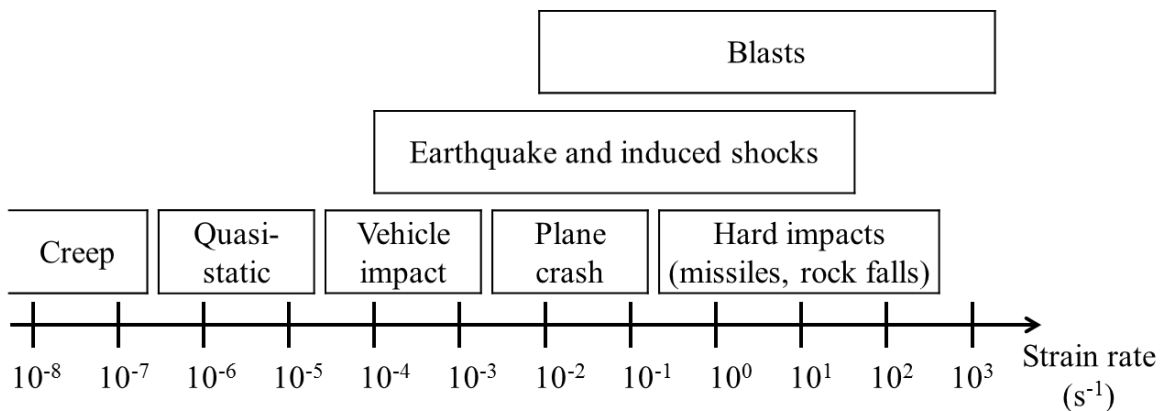


Figure 1.1. Regimes of strain rates (Hentz et al. 2004)

A significant amount of experimental research has been conducted to characterize the dynamic behavior of regular concrete. Research efforts that have focused on understanding concrete behavior under dynamic loads include Ross et al. (1989), Tedesco and Ross (1993), Ross et al. (1995) and (1996), Malvar and Crawford (1998), Klepaczko (2003), Li and Xu (2009). However, most of the research conducted so far has mostly focused on compressive loading for two main reasons: 1) the tensile capacity of concrete was felt to be negligible because the tensile capacity of conventional concrete is low; and 2) conducting tensile testing, especially at high strain rates, is substantially more complex than compression testing.

Concrete encounters not only compression but also tension under impact loading. This is because a compressive stress wave can be reflected in structural elements as a tensile stress wave, which can jeopardize the integrity of concrete structures (Zielinski et al. 1981). This phenomenon is well understood and has been experimentally demonstrated and even exploited to explore materials' properties. For example, concrete tension experiments have been conducted using the reflected compressive stress wave, such as the spall experiments done using a modified split Hopkinson pressure bar (Schuler et al. 2006). Moreover, it can be argued that the compressive strength of concrete is actually dependent upon its tensile strength, since microcrack propagation from pre-existing defects can influence its compressive response, as studies have shown (Dyskin et al. 1999; Lim et al. 2000). Therefore, a full understanding of concrete behavior under impact loading necessitates understanding its tensile response, particularly under high strain rates.

1.2 ULTRA HIGH PERFORMANCE CONCRETE

Ultra High Performance Concrete (UHPC) is among the most advanced and promising cementitious materials developed to date. It has the potential to be a viable solution for improving the resilience and sustainability of buildings and other infrastructure components because of its high strength, durability and energy absorption capacity compared with conventional concrete. It is generally characterized by its superior compressive strength (higher than 150 MPa, or 21.7 ksi) and contains fiber reinforcement to decrease brittleness and enhance tensile capacity.

The key behind UHPC's excellent characteristics is high particle packing density. This is achieved by carefully tailoring the particle sizes and gradations of all of its components and using a low water to cement ratio (lower than 0.25). As such, UHPC has an extremely dense microstructure with low material porosity. Figure 1.2 shows an example of dense particle packing. UHPC's are typically made using cement (substantially more than conventional concrete), superplasticizer and silica fume (Habel et al. 2006), and fine sands (maximum grain size of 0.8 mm). Typical sand-to-cement ratio is around 1.4.

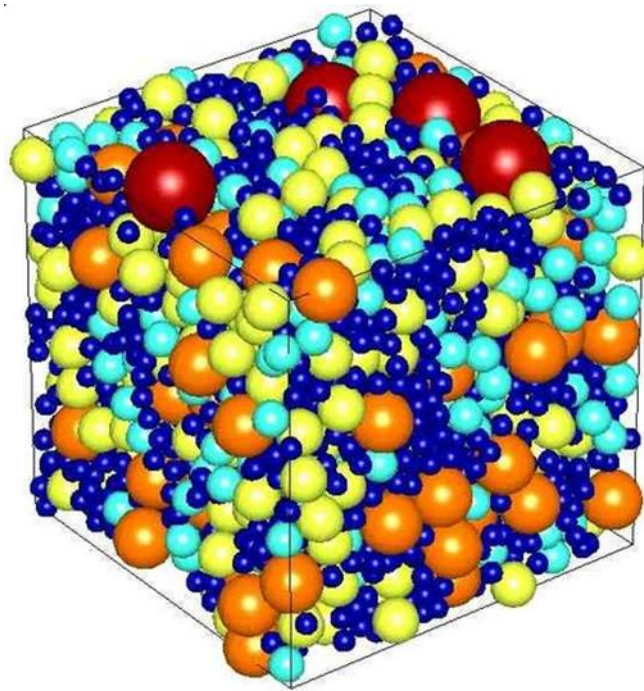


Figure 1.2. Example of dense particle packing (<http://quizlet.com>)

Tensile strain-hardening behavior can be achieved in UHPC by incorporating a sufficient amount of high strength steel fibers (Wille et al. 2011a). It is necessary to have good bond between the fibers and the surrounding matrix in order to fully mobilize the fibers, promote multiple cracking under tensile loading and ensure strain hardening response prior to crack localization. The high particle packing density of UHPC is one of key characteristics that ensures strong physical/chemical bonding between fibers and matrix, as noted by Lowke et al. (2012). Figure 1.3 shows examples of brass coated fiber under a microscope, where it is clear that fibers are severely scratched as they are pulled out from a UHPC matrix.

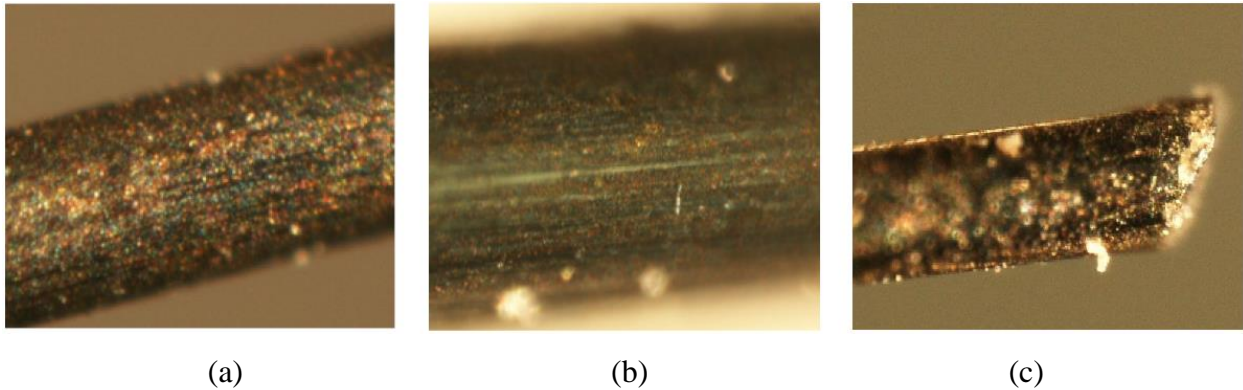


Figure 1.3. Effect of scratching of the brass coating in steel fibers embedded in UHPC: (a) non scratched fiber; (b) partly scratched fiber; (c) fiber end (Wille and Naaman 2010)

Many studies have shown that UHPCs are highly durable against chemical attack, freeze-thaw cycles, abrasion, and chloride penetration (Graybeal 2006; Pfeifer et al. 2009; Graybeal 2011). Although UHPC is just starting to be used in real construction applications (Graybeal 2011), its characteristics, especially under tensile loading, have not yet been fully investigated and are the key focus of this work. In spite of preliminary studies (Habel and Gauvreau 2008, Nöldgen et al. 2009, Millard et al. 2010) that suggests that UHPC may be highly damage tolerant, especially under impact, data about its high strain rate tensile response is especially lacking providing further motivation for this effort. A detailed literature review of UHPC and its applications can be found in Sections 2.1 and 2.2.3.

1.3 OBJECTIVES AND TASKS

The overarching goals of this research are to: a) investigate the strain rate sensitivity of UHP-FRC under a wide range of loading rates, especially in tension, b) develop rigorous theoretical models for concrete under dynamic tension loading, and c) tailor fiber characteristics and volume fraction for optimal impact resistance. Specific research objectives are as follows. Figure 1.4 illustrates the roadmap of the research including the path toward future research efforts that stem naturally from this work.

1. **Characterize the Low Strain Rate Tensile Response of UHP-FRC:** The objective of this thrust is to investigate the behavior of composites incorporating steel fibers with different features (e.g., shape and aspect ratio) and volume fractions under low strain rates ranging from 0.0001 /sec to 0.1 /sec. Specimen performance is characterized in terms of first cracking strength, post-cracking strength, energy absorption capacity, strain capacity, elastic modulus, fiber tensile stress and number of cracks.
2. **Develop a New Impact Testing System for Direct Tension Testing of UHP-FRC:** Current impact test methods, e.g. Split Hopkinson Pressure Bar, are expensive and also require large open space, which has limited their widespread applicability. A key objective of this work is to develop a new compact impact testing system for UHP-FRC that overcomes the limitations of traditional test techniques and that can capture the unique strain hardening response of UHP-FRC in tension.
3. **Characterize the Response of UHP-FRC under High Strain Rates:** To the knowledge of the author, there is no data on the high strain rate response of UHP-FRC under direct tension loading. Therefore, a key objective of this work is to obtain unique test data for strain rates on the order of 10^2 /sec. A related objective is to evaluate the effects of fiber characteristics on the high strain rate response of UHP-FRC.
4. **Characterize Crack Propagation in UHP-FRC:** The objective of this thrust is to establish a relationship between crack speed and strain rate in UHPC. To achieve this, the developed impact testing system is modified to accommodate crack-propagation test specimens and exercised to enable the study.
5. **Develop a Theoretical Model of Concrete under Dynamic Tension:** As discussed in Chapter 2, controversy still surrounds the reasons for the dynamic increase factor (DIF) for concrete under tension. A specific objective is therefore to develop a better understanding of the sources of dynamic strength enhancement in concrete under tension through theoretical modeling based upon crack-velocity dependent dynamic fracture mechanics.

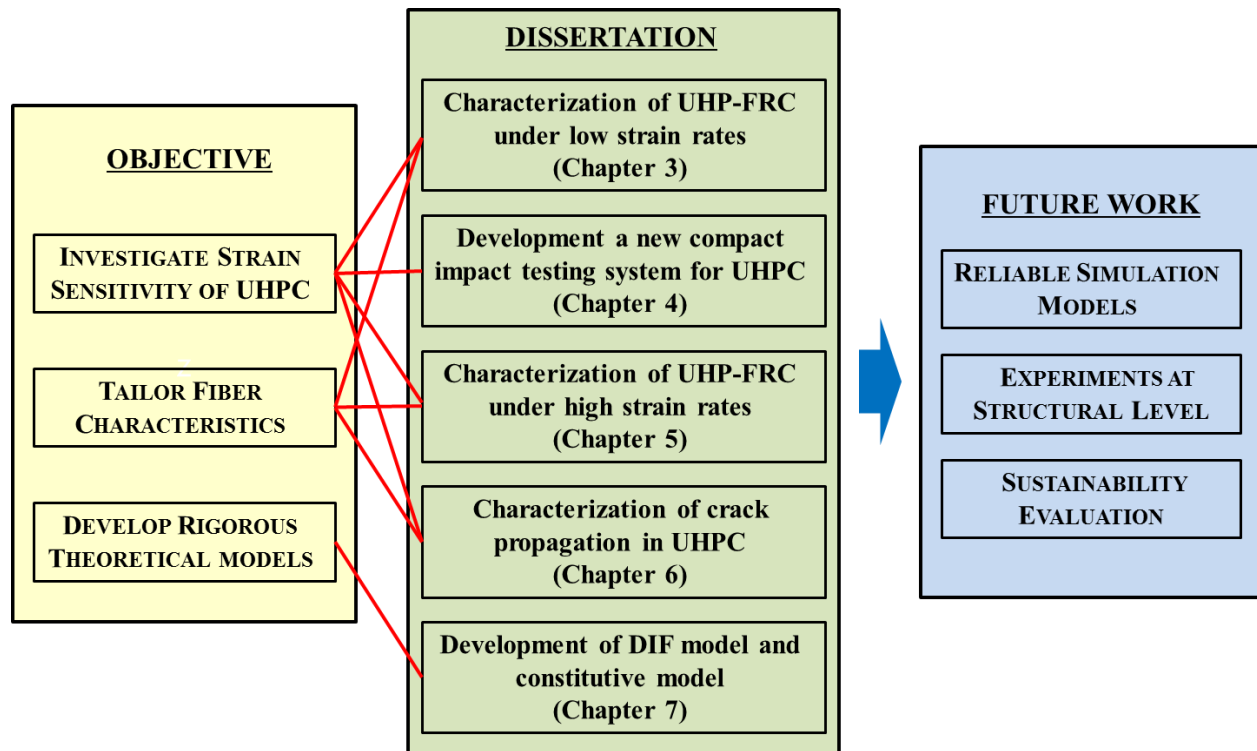


Figure 1.4. Research roadmap including future work

1.4 STRUCTURE OF THE DISSERTATION

This dissertation is composed of eight chapters covering five subjects: characterization of UHP-FRC (Chapters 3), development of a new impact testing system (Chapter 4), characterization of UHP-FRC using the new system (Chapters 5), measuring crack speed in UHPC (Chapter 6), and proposing a theoretical modeling scheme (Chapter 7). Figure 1.5 shows the structure of the dissertation. The details of each chapter are as follows:

Chapter 1: Introduction. This chapter covers the background, research significance and objectives. A research roadmap including future work is presented.

Chapter 2: Literature Review. A literature survey of the main topics studied in this dissertation is presented. Previous research on advanced cement based composites, testing methods of concrete under tension, theoretical modeling of concrete under tension and crack propagation in solids are discussed.

Chapter 3: Characterization of UHP-FRC under Low Strain Rates. This chapter characterizes the tensile response of UHP-FRC under low strain rates with different types of steel fibers. Identified material properties are compared with theoretical models developed for conventional fiber reinforced cement-based composites to investigate whether UHP-FRC behaves similarly to conventional cement-based composites. In Chapter 5, the results of this chapter are compared to high strain data to show the effect of strain rate over a broad range of rates.

Chapter 4: Development of New Impact Testing System for UHP-FRC. This chapter proposes a new compact impact testing system that can accommodate various concretes with brittle or strain hardening response in tension. The capabilities of the new system are investigated by comparing between experimental results and simulation data. The detailed design procedure and optimization process of the developed impact testing system are described. The developed testing system is used to characterize UHP-FRC tensile response under high strain rate in Chapter 5. A modified version of the impact testing system is used to carry out crack propagation studies under impact loading in Chapter 6.

Chapter 5: Characterization of UHP-FRC under High Strain Rates. This chapter characterizes the tensile response of UHP-FRC under high strain rates. A proper specimen size of UHP-FRC is suggested for the impact testing system developed in Chapter 4. Lower strain rate results reported in Chapter 3 are used to compare rate sensitivity of UHP-FRC under various rates of loading.

Chapter 6: Characterization of Crack Propagation in UHPC. This chapter characterizes crack propagation in UHPC under various rates of loading to establish the relationship between crack speed and strain rate. The relationship between these properties is used as input for the theoretical models proposed in Chapter 7 to explain the rate sensitivity of UHPC demonstrated in Chapters 3 and 5.

Chapter 7: Theoretical Modeling of Concrete under Dynamic Tension. This chapter proposes two dynamic increase factor (DIF) models that are based on crack-velocity dependent dynamic fracture mechanics and a constitutive model that is based on meso-mechanics for concrete under dynamic tension. This chapter is intended to provide theoretical background to

generally explain the observed rate sensitivity in concrete (Chapters 3 and 5) and employs the experimental research results obtained in Chapter 6.

Chapter 8: Conclusions and Future Research. This chapter provides a summary of the major conclusions that can be drawn from the research. Several recommendations for future work that stem from this work are also provided.

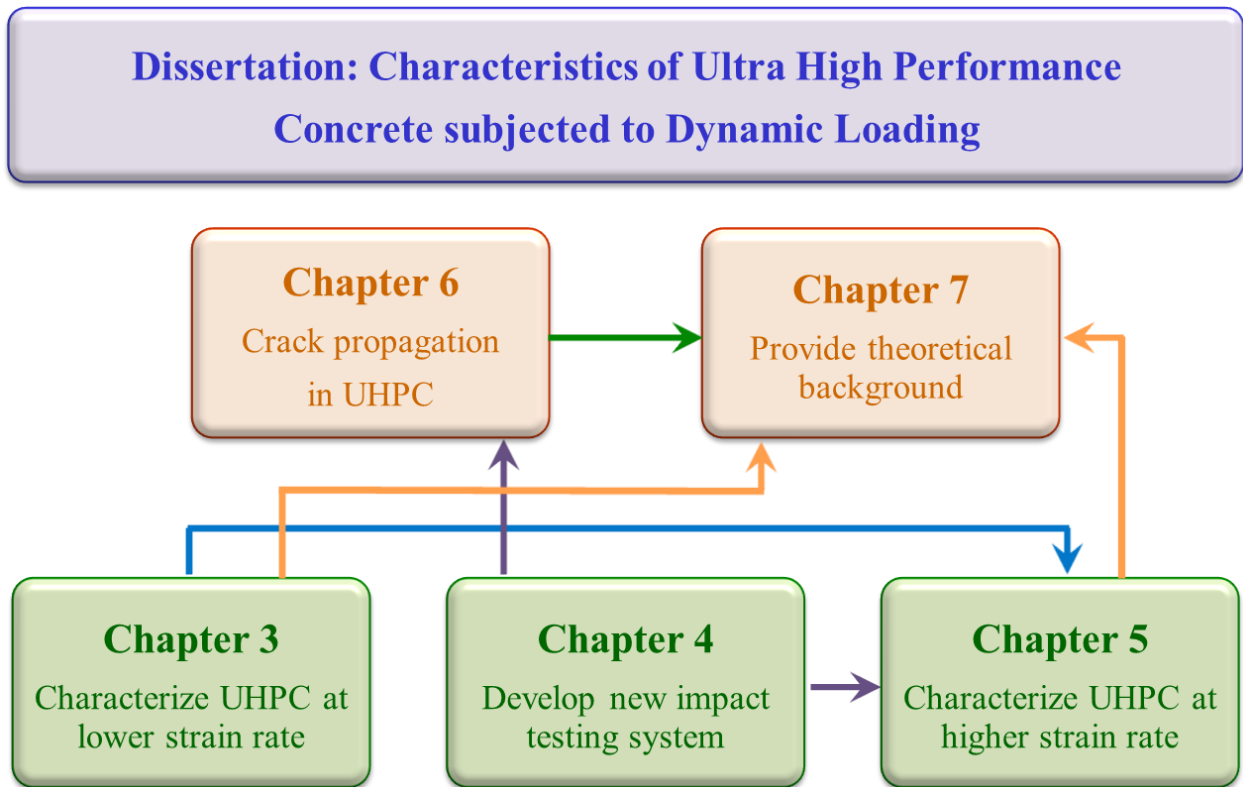


Figure 1.5. Structure of the dissertation

CHAPTER 2

LITERATURE REVIEW

This chapter presents a literature survey of the main topics studied in the dissertation. The first section discusses Ultra High Performance Concrete (UHPC), which is the target material characterized throughout this work. The second section summarizes the literature on strain rate effects on concrete, mainly focusing on the tensile behavior of concrete. The third section introduces testing methods for concrete under both quasi-static and high strain rate loading. The fourth section reviews theoretical approaches and studies of crack speed in solids.

2.1 ULTRA HIGH PERFORMANCE CONCRETE

As understanding of the properties and behavior of concrete has accumulated, civil engineers have developed high performance concrete materials displaying significant strength and enhanced ductility, even in tension. Examples of concretes with enhanced tensile properties include: Fiber Reinforced Concretes (FRC) (Brandt 2008), Slurry Infiltrated Fiber Concrete (SIFCON) (Naaman and Homrich 1989), Multi-Scale Cement Composite (MSCC) (Rossi 1997), Hybrid Fiber Concretes (HFC) (Markovic 2006), High Performance Fiber Reinforced Cement Composites (HPFRCC) (Naaman and Reinhardt 2006), Engineered Cementitious Composite (ECC) (Li et al. 2001, Li 2003) and Ultra High Performance Fiber Reinforced Concrete (UHP-FRC) (Wille et al. 2011b).

As is clear from several of the names, these concretes listed above are reinforced with fibers (polymeric or/and steel); i.e., they derive some of their enhanced performance through the addition of fibers. Fiber reinforced concretes resist tensile stress through composite action

between the cement matrix and the embedded fibers. The transmission of forces between these two components occurs through interfacial bonding. After cracking of the cement matrix, fibers bridge the cracks, providing resistance to crack opening and enhancing structural behavior and durability. Many researchers have recently contributed to the characterization of the tension behavior of these concrete materials. Examples of such research efforts can be found in Dugat et al. (1996), Li et al. (2001), Fischer et al. (2002), Naaman (2002), Parant (2003), Wille et al. (2011b), Wille and Parra-Montesinos (2012).

Among the most promising of the new cementitious materials is UHP-FRC. Although different researchers have defined UHPC and UHP-FRC using several criteria (Rossi 2008, Graybeal 2011, Naaman and Wille 2012), American Concrete Institute (ACI) Committee 239 suggests the following definition: “*Concrete, ultra-high performance - concrete that has a minimum specified compressive strength of 150 MPa (22,000 psi) with specified durability, tensile ductility and toughness requirements; fibers are generally included to achieve specified requirements.*” There appears to be consensus in the research literature that well designed UHP-FRC can be highly durable against chemical attack, freeze-thaw cycles, abrasion, and chloride penetration (Graybeal 2006; Pfeifer et al. 2009; Graybeal 2011), and therefore there is strong interest in exploring its material properties. Recent work suggests that the mechanical and durability properties of UHP-FRC make it an ideal candidate for use in developing new solutions to pressing concerns about infrastructure deterioration, repair, and replacement (Graybeal 2009). Since 2000, when UHP-FRC became commercially available in the United States, a series of projects have demonstrated the very high capabilities of the material (Bierwagen and Abu-Hawash 2005, Keierleber et al. 2008, Wipf et al. 2009, Rouse et al. 2011).

Although UHP-FRC has exceptional material properties, its cost is significantly higher than that of normal strength concretes. High material cost (about 35 times the cost of regular concrete) coupled with complicated and costly construction procedures have hindered the widespread adoption of UHPC in the US (Graybeal 2013). An alternative UHPC that was developed by Wille et al. (2011b) has the potential to remove all practical obstacles preventing widespread adoption of UHPC in the US, and is estimated to cost about one-fifth of similar commercial UHPC products. Although some tests have been conducted to characterize this

material's static response (Wille et al. 2011a, Wille and Naaman 2012, Wille and Parra-Montesinos 2012, Wille et al. 2014), its dynamic response has yet to be explored.

2.2 STRAIN RATE EFFECT ON CONCRETE

This section introduces strain rate effect on concrete under both compression and tension. This section starts with brief reviews of compression cases and primarily reviews rate effects of various concrete materials under tension loading, since this dissertation mainly focuses on tensile behavior of UHPC.

2.2.1 Strain Rate Properties of Concrete in Compression

Experimental studies focusing on the dynamic compressive behavior of concrete have been conducted by numerous researchers. These studies have generally shown that the measured dynamic compressive strength is a function of strain rate and have commonly held that strength increase in compression is primarily a material property (Ross et al. 1989, Tang et al. 1992, Tedesco and Ross 1993, Ross et al. 1995 and 1996, Malvar and Crawford 1998, Zhao 1998, Klepaczko 2003, Li and Xu 2009). Recently, many researchers have conducted theoretical and numerical studies to explain the experimental findings (Donzé et al. 1999, Li and Meng 2003, Georgin and Reynouard 2003, Cotsovos and Pavlovic 2005, Cullis et al. 2008, Kim et al. 2010, Elmer et al. 2012). For example, Li and Meng (2003) attributed the strength increase with increasing strain rate to the well-known pressure sensitivity of concrete. Kim et al. (2010) suggested that while pressure sensitivity may play a key role, it does not fully explain the experimentally observed strength increases. Elmer et al. (2012) indicated that pressure sensitivity is a necessary but not sufficient condition for dynamic strength increase and that shear dilation is another key factor in the dynamic strength increase of concrete materials loaded in compression.

2.2.2 Strain Rate Properties of Concrete in Tension

In contrast to the abundant studies reporting test results for concrete subjected to dynamic compression, studies focusing on the dynamic tensile behavior of concrete are limited. This is

mainly because it is much harder to test and measure the dynamic response of concrete in tension than in compression. The existing database of test results has consistently shown that, as in compression, the tensile strength of concrete becomes higher as the strain rate increases (Malvar and Crawford 1998, Leppanen 2006, Cadoni et al. 2009). The effect of strain rate on strength of concrete is typically reported as a dynamic increase factor (DIF) – i.e. the ratio of dynamic to static strength – versus strain rate ($\dot{\epsilon}$) relationship. The CEB model (CEB 1998) suggests that the $\log(\text{DIF})$ versus $\log(\dot{\epsilon})$ relation is bilinear with a change in slope around 30 /sec, whereas Leppanen (2006) claimed that the turning point is at 1 /sec. Although the reasons for existence of a turning point are not clear at present, some researchers have pointed out that it may be due to inertial effects, e.g. Brace and Jones (1971) and Walley (2010).

2.2.2.1 Strain Rate Properties of Regular Concrete and Cementitious Composites in Tension under Low Strain Rates

A number of tests have been carried out to investigate the response of concrete and fiber reinforced concrete under tension loading applied at relatively low strain rates. Yan and Lin (2006) carried out a series of experiments to characterize strain-rate-dependent tensile behavior of concrete at strain rates ranging from 10^{-5} to $10^{-0.3}$ /sec. They used dumbbell-shaped concrete specimens and employed a servo-hydraulic testing machine, and observed that the fracture surfaces of the specimens became more flattened with increasing strain rate. They also found that as strain rate increased, the number of broken coarse aggregates along the fracture surface increased. They concluded from the observations that a higher stress level is needed to lead specimens to failure as strain rate increased because rapid loading cracks are forced to propagate through regions of greater resistance. They also established log linear relationships between DIF of tensile strength and strain rates.

Maalej et al. (2005) investigated the tensile behavior of ECC containing a combination of high-modulus steel fibers and relatively low-modulus polyethylene fibers at strain rates ranging from 2×10^{-6} to 0.2 /sec. They concluded that the tensile strength doubled but that there was no obvious change in strain capacity with increasing strain rate. Yang and Li (2005) investigated the tensile strength of ECC reinforced with polyvinyl alcohol (PVA) fibers at strain rates ranging from 10^{-5} to 10^{-1} /sec. They found that the tensile strength of ECC doubled whereas the strain

capacity decreased from 3 % to 0.5 %. They attributed these observations to the sensitivity of fiber interfacial chemical bond strength to loading speed.

Kim et al. (2009) investigated the tensile behavior of HPFRCC using two types of deformed, high-strength steel fibers, namely twisted and hooked fibers, at strain rates of 10^{-4} to 10^{-1} /sec. They observed that the DIF increased up to 2.0 and 1.7 for the first-cracking strength and post-cracking strength, respectively, depending on fiber type, fiber volume fraction, and matrix strength. In contrast to the findings of Yang and Li (2005) for ECC, strain capacity remained largely unaffected by strain rate. Douglas and Billington (2011) investigated the strain rate sensitivity of two HPFRCC materials (PVA fiber reinforced ECC and twisted high strength steel fiber reinforced HPFRCC) in cylindrical specimens under monotonic tension at strain rates ranging from 2×10^{-5} to 0.2 /sec. Both HPFRCC materials showed enhancements in strengths (25-120 % for ECC and 77-165 % for steel fiber reinforced HPFRCC) as strain rate increased. Both types of materials experienced a 50-55 % decrease in strain capacity as the strain rate increased. They noted that unlike thin coupon specimens that tend to align fibers along the loading direction, cylindrical specimens permit random, three-dimensional fiber alignment, which leads to less efficient fiber bridging.

2.2.2.2 Strain Rate Properties of Regular Concrete and Cementitious Composites in Tension under High Strain Rates

Zhu et al. (2011) conducted a series of dynamic tensile tests (loading speed: 1000 mm/s) for three types of fabric (polyethylene (PE), alkali resistant (AR) glass , and carbon) reinforced cement composites using a high speed servo-hydraulic testing machine, and compared their mechanical properties with the properties obtained from cases under quasi-static loading. The researchers reported that 1) strength of the PE composite is similar under high speed loading and quasi-static loading; 2) strength of the AR glass composite is about 35 % higher at high speed loading; and 3) strength of the carbon composite significantly decreases with increased loading rate. They concluded that the strength decrease for the carbon composite case under high speed loading is due mainly to sliding friction of filaments against neighboring filaments. Xu et al. (2012) performed drop-weight splitting tension tests on FRCs with different steel fibers to study their dynamic material properties. They found that FRC specimens show better performance than

plain concrete material under both quasi-static and dynamic splitting tests in terms of tensile strength, fracture energy, post-peak energy, DIF, maximum measurable strain capacity and crack growth velocity.

Many dynamic tensile tests have been carried out using the split Hopkinson pressure bar (SHPB). Mechtcherine et al. (2011) conducted high strain rate testing on strain hardening cement-based composites (SHCC) under tension. They used the spall configuration of the modified SHPB and compared results with quasi-static responses of SHCC. They noted that even though spall experiments can measure a materials' dynamic Young's modulus, dynamic tensile strength and dynamic fracture energy, there are key limitations, e.g., inability to produce stress-strain relationship. Brara et al. (2001) conducted a series of strain rate tests up to 100 /sec of concrete under tension loading using the spalling phenomenon. They found that the tensile strength increases from 4 up to about 12 times the quasi-static strength. Cadoni et al. (2001) carried out dynamic tension tests on concrete by means of a Hopkinson Bar Bundle, which is more than 100 m long. Although they got good results using the long testing configuration, very few laboratories in the world can duplicate this experiment. Cadoni et al. (2009) carried out high strain rate testing on two types of concrete reinforced with steel and PVA fibers under tension using a modified SHPB apparatus. They found that despite the fact that the ratio between the dynamic and static strength of FRCs increases remarkably with strain rate, the FRCs become more brittle as strain rate increases. Chen et al. (2011) used Brazilian disc samples and applied dynamic load with a modified SHPB system to examine the dynamic tensile properties of plain concrete and FRC with steel fibers. They found that there is a significant enhancement in tensile strength as loading rate increases.

2.2.3 Strain Rate Response of UHPC

Fujikake et al. (2006) investigated the tensile behavior of UHP-FRC (comprised of the commercial mix, Ductal Premix) under various strain rates ranging from 10^{-6} to 0.5 /sec. Based on the obtained stress-elongation relationships in uniaxial tension, they proposed a rate-dependent bridging law expressing the relation between tensile stress and crack opening. Wille et al. (2012) reported on the strain rate dependent tensile behavior of a non-proprietary UHP-FRC with three different fiber volume fractions at strain rates ranging from 10^{-4} to 10^{-1} /sec. They

observed that strength and energy absorption capacity both increased with an increase in fiber volume fraction for a given strain rate.

Very limited experimental studies of the high strain rate behavior of UHPC have been carried out to date. Among the few examples are Habel and Gauvreau (2008), who conducted drop weight tests on UHPC bending specimens and then converted their results to equivalent dynamic tensile properties. Nöldgen et al. (2009) carried out high strain rate loading tests in tension on UHPC using the spall version of the SHPB to evaluate its dynamical material properties such as the tensile strength, Young's modulus and fracture energy. Millard et al. (2010) conducted flexural and shear high-speed loading tests of UHP-FRC using a drop-hammer testing apparatus. They found that the DIF of the flexural tensile strength rises at the strain rate of 1 /sec on a slope of 1/3 on a log(strain rate) versus log(DIF) plot. To the best knowledge of this author, there have been no high strain rate tests under direct (pure) tension for UHPC, especially to evaluate its stress-strain behavior under high strain rate loading. The absence of this experimental study further motivated the work in this dissertation.

2.3 TESTING METHODS FOR CONCRETE UNDER VARIABLE STRAIN RATE

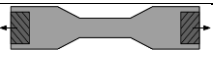











As previously alluded to, various setups for testing of concrete under quasi-static and high strain rate loading have been used in the past. Following is a survey of the most commonly used techniques.

2.3.1 Testing Methods for Concrete in Tension under Quasi-Static Loading

In contrast to bending or compression, there is no standard for direct tensile tests of concrete, even under quasi-static loading. Li et al. (1993b) argued that this is mainly because controlling the application of stress is difficult in the direct uniaxial tension test. To tackle the difficulty, different research groups have used different test setups for concrete under tension with different specimen shapes (e.g., dogbone / dumbbell shape, unnotched and notched prism or cylinder) and different types of gripping systems (e.g., fixed or rotating boundary condition) (see Table 2.1). These setups all have some advantages but each also has disadvantages. Given the

lack of one consistent approach, direct comparisons between results are difficult. Therefore, a standard concrete specimen and test setup are needed in order to properly compare the tensile responses, under both static and dynamic loadings at varying strain rates.

Table 2.1. Direct tension test setups – Dogbone / Dumbbell shape (Wille et al. 2014)

Shape	Material	Level	Constant Area (Total Specimen)			Diff. Area	Grip	DOF top- bottom
			L	W	D			
dogbone / dumbbell	-	-	L	W	D			
	UHP-FRC	4	80 (330)	30 (60)	13 (13)	50%	fixed	0-0
	HPFRCC	4	152 (457)	38 (76)	76 (76)	50%	self-clamping friction grip	1-1
	HPFRCC	3	150 (200)	25 (40)	25 (25)	63%	anchored/ pinned	1-1
	HPFRCC	3	200 (525)	50 (125)	13 (13)	40%	anchored/ pinned	1-1
	UHP-FRC	3-4	178 (525)	51 (125)	25 (25)	41%	anchored/ pinned	1-1
	UHP-FRC	3-4	200 (750)	100 (300)	50 (50)	33%	top glued/ anchored	0-0
	UHP-FRC	3	250 (740)	100 (200)	35 (35)	50%	side glued/ pinned	1-1
	UHP-FRC	3	200 (700)	160 (200)	45 (45)	80%	side glued + anchored (greased)	0-0
	HPFRCC	3-4	80 (330)	30 (60)	13/30 (13/30)	50%	clamped/ fixed/pinned	0/2-0/2
	Plain Concrete	0	200 (400)	60 (100)	100 (100)	60%	top glued	0-0
	Plain Concrete	0	0 ^b (150) ^b	60 (100)	100 (100)	60%	top glued / pinned	2-2
	Plain Lightweight Concrete	0	0 (270)	80 (100)	-	64%	top glued	0-0

2.3.2 Testing Methods for High Strain Rate Loading

The SHPB is regarded as the gold standard for testing materials, including concretes and ceramics, under dynamic loading. New alternatives based on sudden release of strain energy have been recently proposed. These methods are discussed next.

2.3.2.1 Split Hopkinson Pressure Bar (SHPB)

The SHPB configuration has been widely used in the material science field to explore materials' dynamic behavior in both compression and tension (Kolsky 1949, Hauser et al. 1961, Lindholm and Yeakley 1968, Nicholas 1981, Harding and Welsh 1983, Staab and Gilat 1991, Li et al. 1993a, Li and Xu 2009, Owens and Tippur 2009, Song et al. 2009). The basic configuration of the SHPB system for compression testing is shown in Figure 2.1. The conventional SHPB configuration poses two key hindrances to simply adopting it to test concrete materials, unlike other composite materials, e.g., fiber reinforced polymers and metal alloys. First, the device generally requires specimens that are of a completely different geometry from those used in pseudo static testing, which raises concerns about whether specimen geometry and size affect direct comparisons between static and dynamic results. This complicates the drawing of strong conclusions about the effects of high strain rate on concrete response. Second, to successfully test concrete under high strain rate in a SHPB, the specimens must have a certain minimum size dictated by the characteristic size of the constituents of the concrete. For regular concrete, the limiting constituent is the aggregate, while for fiber reinforced concrete and cementitious composites, fiber length must also be considered. The specimen must be several times the characteristic size of the aggregate or fiber so that the results are not adversely influenced by the

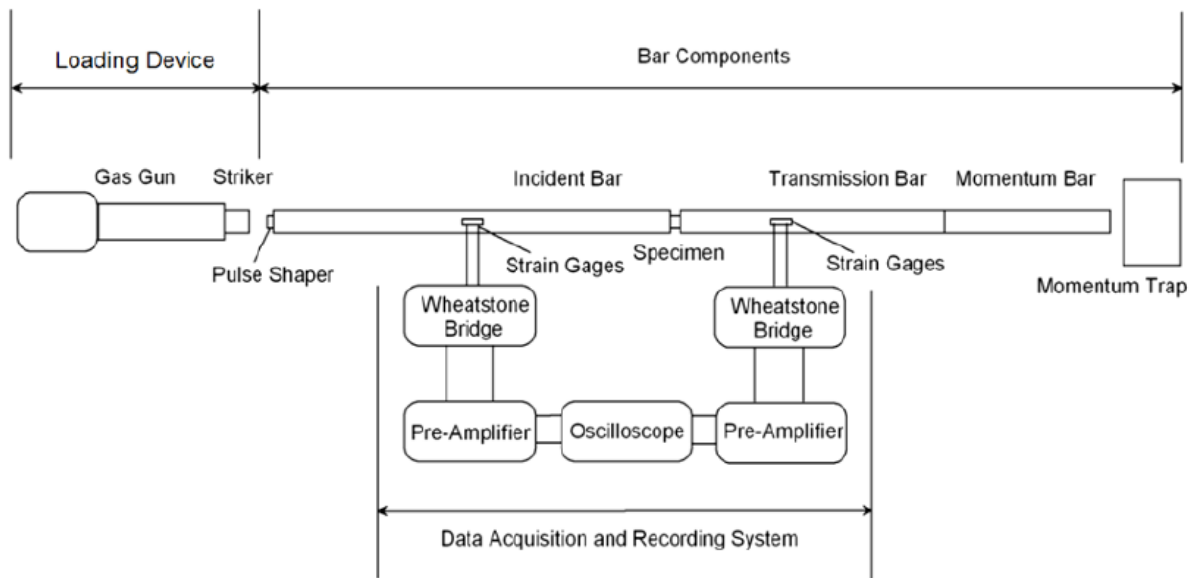


Figure 2.1. A typical SHPB setup (Song et al. 2009)

size effect. In addition, both of the bars (incident and transmitter) of the SHPB must be at least 20 times longer than the length of the specimen to avoid signal interference within the bars. Therefore, concrete testing using SHPB typically requires the use of relatively large specimens and, therefore, that the SHPB be commensurately long, e.g. a 75 mm thick SHPB can be 10 – 12 m. Of course, the bigger the SHPB, the more expensive it becomes. Figure 2.2 shows a 100-mm-diameter SHPB for concrete under compression test.

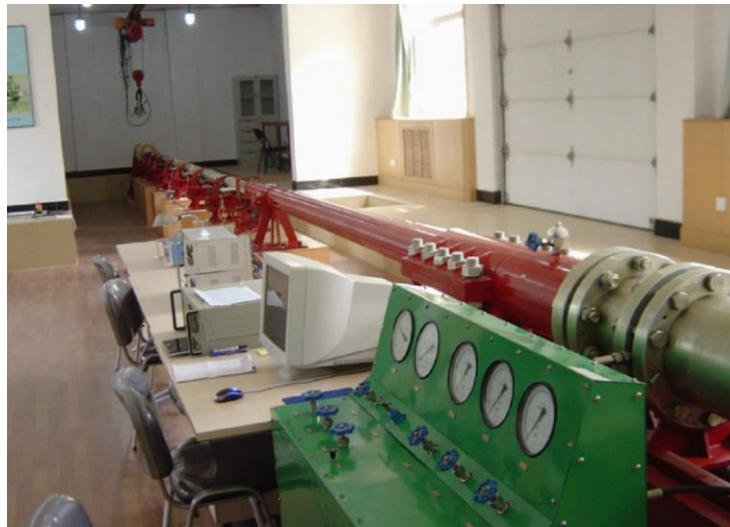


Figure 2.2. 100-mm-diameter SHPB system for concrete under compression (Li and Xu 2009)

2.3.2.2 Tension Testing using SHPB

In order to characterize tensile behavior of various materials under high strain rate loading, many researchers have attempted to modify SHPB setups. For example, Harding and Welsh (1983) used a mechanism that employed a weighbar tube striking a yoke connected to the end of the input bar (see Figure 2.3). Staab and Gilat (1991) used a clamp to release a stored tensile load. Owens and Tippur (2009) used a gas gun chamber attached to the side of the incident bar to launch a striker toward the anvil, generating a tensile wave. Other investigators who used the SHPB for tensile testing include Lindholm and Yeakley (1968), Nicholas (1981), Li et al. (1993a), Li and Xu (2009), and Song et al. (2009).

Modified SHPB setups have also been used to characterize concrete under tension. Ross (1989) used a modified SHPB to accommodate direct tension testing of concrete at high strain rate by using a hollow cylindrical striker bar sliding on the incident bar of the SHPB. Ross et al. (1989) conducted dynamic splitting tension testing (dynamic Brazilian testing) for determining failure strength of concrete using the SHPB by inserting a cylindrical specimen between the bars with its axis perpendicular to the bars. Brara et al. (2001) developed a spalling version of the SHPB for concrete to determine the tensile strength at high strain rates up to 120 /sec. Cadoni et al. (2001) used the Hopkinson Bar Bundle with 100 m-long strain energy storing steel cables for a large concrete specimen with a square cross section of $200 \times 200 \text{ mm}^2$. The setup was devised to diminish the non-uniform distribution of axial stress across the large sized bars and achieved a strain rate of 10 /sec.

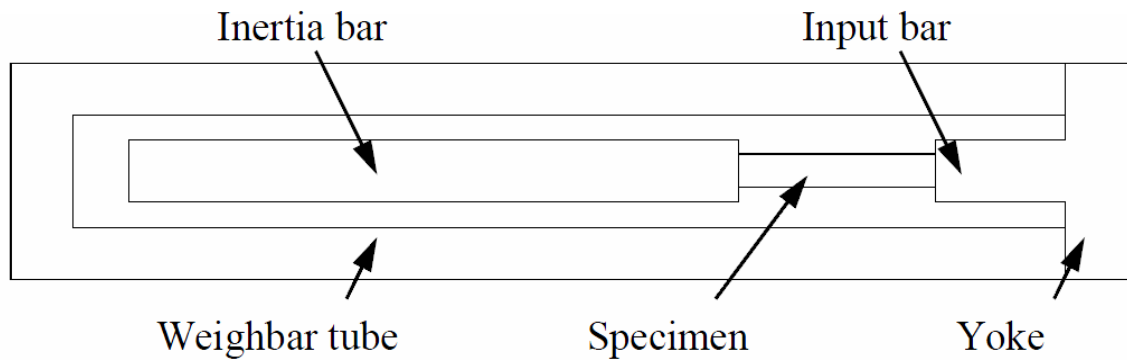


Figure 2.3. Schematic of tension setup proposed by Harding and Welsh (1983)

2.3.2.3 Strain Energy Impact Test System (SEITS) and Strain Energy Frame Impact Machine (SEFIM)

In order to decrease the need for space, Kim et al. (2011) proposed SEITS, which, unlike conventional impact test methods for generating high rate impact pulses, uses a coupler and energy bars to store elastic energy, as shown in Figure 2.4. The way by which SEITS works can be described as follows: a load is first applied to a short pull bar, and then the tensile force is transmitted through a coupler to an energy bar where elastic strain energy is stored. After sudden fracture of the coupler under the load, the stored elastic energy is transferred to two concrete

specimens, eventually propagating through the two transmitter bars. The stress in the specimen is captured by reading the transmitted stress wave using a strain gage and oscilloscope, just as in the SHPB system. Details of the system can be found in Kim et al. (2011).

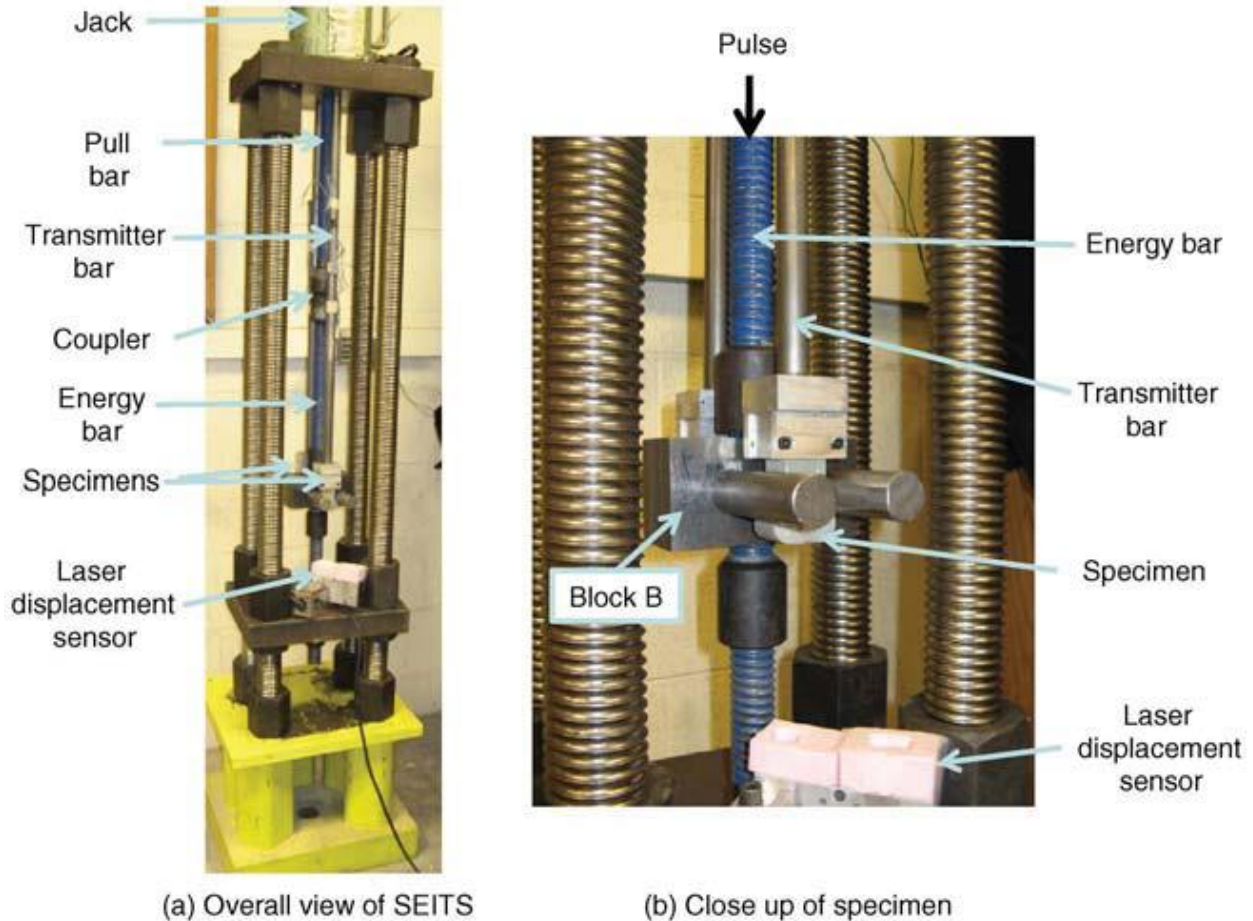


Figure 2.4. Prototype of the SEITS setup developed by Kim et al. (2011)

SEITS has a key disadvantage, i.e. the need to simultaneously load two identical specimens. This is problematic because: 1) specimens are costly and time consuming to make, reducing the practicality of the device, and 2) specimens can never be exactly alike, leading to lack of symmetry in loading. To alleviate this problem, Tran and Kim (2012, 2013) subsequently modified SEITS into the strain energy frame impact machine, SEFIM. The modification entailed replacing the single energy bar with a load frame, which transmits load to a single specimen

instead of a pair of specimens as in SEITS. Figure 2.5 shows a schematic of SEFIM. The way SEFIM works is similar to SEITS. Applying displacement to the pull bar induces the load frame to store elastic energy. After sudden failure of the coupler, the stored elastic energy in the load frame is transmitted to the specimen in the form of a load pulse. The stress in the specimen is measured using strain gages attached to a transmitter bar, and strain is calculated by post-processing images of the specimen using a high speed camera. However, the short transmitter bar in the original version of SEFIM is problematic when the system is applied to strain hardening cementitious composites. The reasons for this observation and its remedy are discussed in detail in Chapter 4.2.

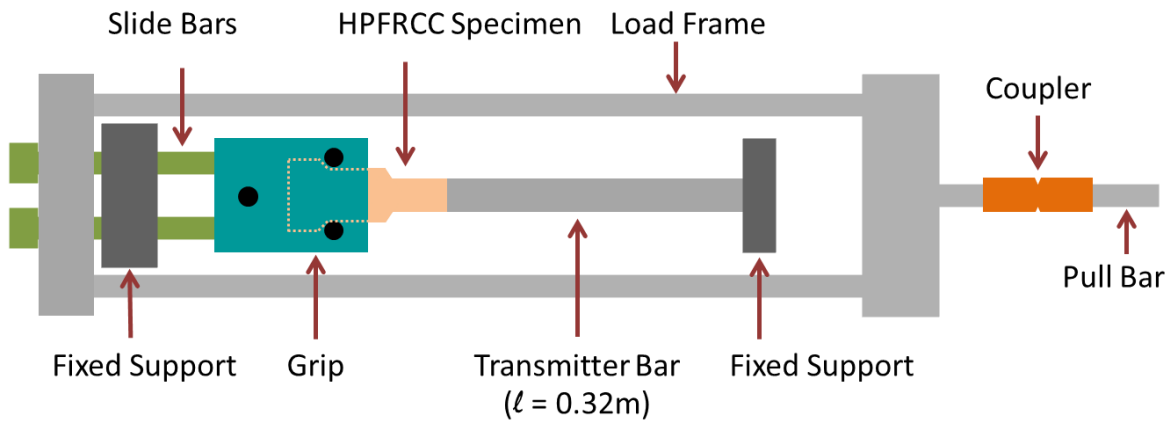


Figure 2.5. Schematic of the strain energy frame impact machine (SEFIM)

2.4 THEORETICAL APPROACHES FOR MODELING THE DYNAMIC RESPONSE OF CONCRETE

Experiments have consistently shown that the tensile strength of concrete increases with increasing strain rate (see Figure 2.6). The DIF, defined as the ratio of the dynamic strength to the quasi-static strength, is widely used to measure this effect. A few hypotheses have been proposed to explain the phenomena expressed by DIF. Barpi (2004) deemed viscosity to be a key reason for the existence of DIF. He proposed a viscoplasticity-based model that incorporated a viscosity parameter as a function of strain rate. Despite describing strain rate influence well, this approach leads to a regularization problem in the softening range of the material behavior. Lu

and Li (2011) conducted a qualitative study based on a micro-mechanism model. They concluded that, at the macroscopic level, the dynamic tensile strength enhancement observed in dynamic tensile tests is associated with intrinsic material properties, rather than with structural effects. Furthermore, they state that the inertial effect associated with microcracks is one of the mechanisms responsible for the existence of DIF. Several other researchers have theoretically investigated concrete dynamic behavior under tension, including Bićanić and Zienkiewicz (1983) and Sercombe et al. (1998). Nevertheless, widespread controversy still exists about the origins of DIF, and a rigorous theoretical model is still needed to fully explain it.

Due to the brittle nature and failure pattern of concrete, fracture mechanics is generally regarded as a suitable means of describing the behavior of concrete under tensile loading. However, situations involving inertial forces or high strain rates are better addressed using dynamic fracture mechanics. Nevertheless, finding closed form solutions to dynamic crack problems is in general extremely difficult, and only some special problems have been solved analytically to date (Gao 1993). The dynamic fracture problem becomes tractable if the crack speed in concrete is known or can be estimated, which is the approach adopted in this dissertation. The following subsections review crack speed in solids and simulation of crack propagation in solids.

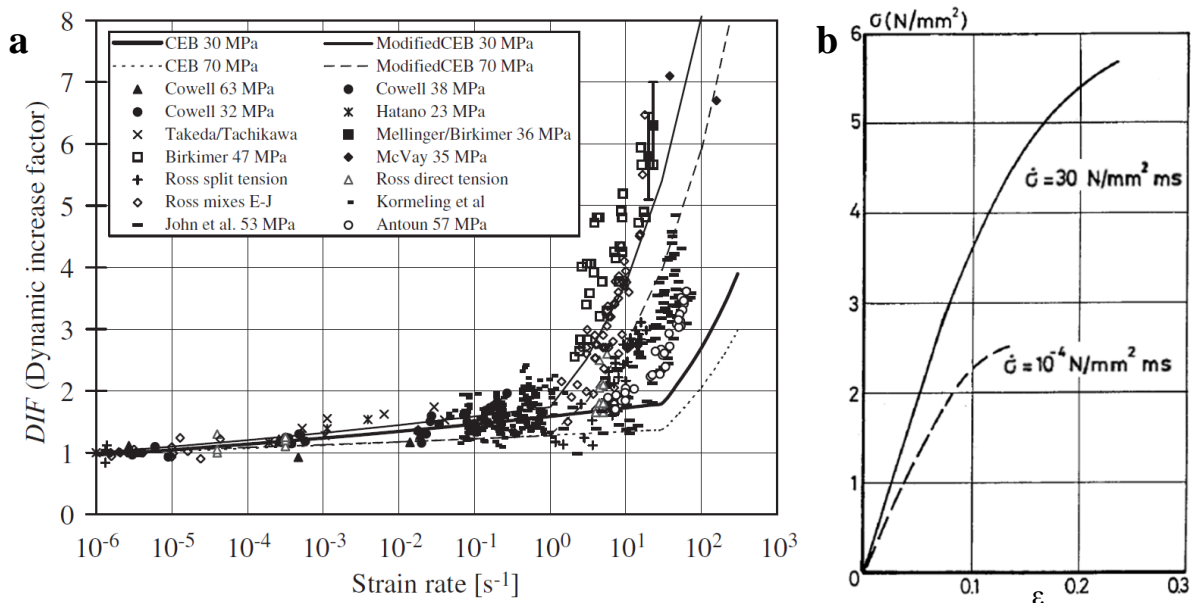


Figure 2.6. Strain rate dependency for concrete under tensile loading: (a) Strain rate effect on DIF (Leppanen 2006); (b) stress-strain behavior (Zielinski et al. 1981)

2.4.1 Crack Speed in Solids

Crack propagation in brittle materials is a major mechanism in material failure and is a complex process to analyze, especially under dynamic loading. To understand the phenomenon of dynamic fracture in brittle material, different approaches have been carried out by many researchers, e.g. experiments (Shukla and Nigam 1986, Dally et al. 1990, Sharon and Fineberg 1999, Arakawa et al. 2000, Évora et al. 2005), analytical approaches (Gao 1993, Lee et al. 1996, Landis et al. 2000), and numerical simulations (Camacho and Ortiz 1996, Belytschko et al. 2000, Duarte et al. 2001, Remmers et al. 2008). A comprehensive review of research on crack propagation has been presented by Freund (1990).

There are disagreements about fundamental aspects of the dynamic fracture process. For example, the observed maximum crack velocities in most materials are lower than the theoretically predicted crack speed (i.e. the Rayleigh wave speed). Gao (1993) proposed a wavy-crack model to explain the phenomenon of reduced apparent crack velocity by incorporating small deviations of the crack tip from its original crack path. Xie and Sanderson (1995) suggested that measured crack velocity cannot reach the Rayleigh wave speed because the dynamic stress intensity factor approaches zero when crack velocity is about half of the Rayleigh wave speed. Sharon and Fineberg (1999) insisted that intrinsic instabilities such as multiple-crack and micro-branching might explain the phenomenon that apparent maximum crack velocities in amorphous materials are far slower than their predicted values. However, they concluded that measured peak crack velocities approach the theoretical predictions by using instantaneous velocity rather than averaged velocity.

With some assumptions, the stress field near the moving crack tip can be expressed as a single parameter, the stress intensity factor, in linear elastic brittle solids under small-scale yielding (Évora et al. 2005). This suggests that a relationship between crack velocity and the stress intensity factor can be established (Krafft and Irwin 1965, Dally et al. 1985, Évora et al. 2005). Shukla and Nigam (1986) carried out a series of dynamic experiments on Homalite 100 to investigate the relationship between the stress intensity factor and crack velocity. Arakawa et al. (2000) experimentally evaluated the relationship among dynamic stress intensity factor, crack velocity and acceleration in poly(methyl methacrylate) (PMMA). Évora et al. (2005) also

experimentally established a relationship between the dynamic stress intensity factor and the crack tip velocity of polyester/TiO₂ nanocomposites.

A number of analytical and numerical approaches have been proposed with the assumption of constant crack velocity at a given strain rate. Lee et al. (1996) derived relationships between dynamic stress intensity factor and dynamic stress/displacement fields of orthotropic materials by assuming that a crack propagates at constant speed. Landis et al. (2000) used an elastic-viscoplastic constitutive law incorporating a rate dependent fracture process zone to explain Mode I steady-state crack growth in strain rate dependent materials. They computed the macroscopic work of fracture as a function of crack velocity.

2.4.2 Simulation of Crack Propagation in Solids

Fast crack propagation in solids is a complex process that mobilizes both mechanical and material mechanisms (Zhou et al. 2005). This is because in addition to the energy required to fracture a material, other sources of energy dissipation may operate simultaneously, including plastic work, viscosity, and heat conduction (Ruiz et al. 2001). Classical fracture mechanics is not well suited to model such complex phenomena, primarily because of the need to assume a pre-existing dominant crack and/or small fracture process zone relative to the geometrical dimensions of the problem. An alternative and practical approach for modeling rapid fracturing is based on the use of cohesive models (Xu and Needleman 1994, Ruiz et al. 2001, Shet and Chandra 2002, Zhai et al. 2004, Zhou et al. 2005, Cusatis and Schaufert 2009). In general, cohesive zone methods can take into account all inelastic energy dissipation while fracture progresses, e.g. energy required for grain-bridging, cavitation, internal sliding, surface energy (Shet and Chandra 2002).

Application of the cohesive zone method in simulation studies requires the use of cohesive elements, which explicitly simulate the crack process zone. Many researchers have employed cohesive zone models within the finite element framework and have proved its effectiveness in the simulation of complex fracture processes, e.g. fragmentation of brittle materials (Camacho and Ortiz 1996; Repetto et al. 2000), and fracture of three-point-bend concrete beam subjected to dynamic loading (Ruiz et al. 2001). Cusatis and Schaufert (2009) conducted an analysis of the

size effect in concrete using a cohesive crack model. Zhou et al. (2005) also demonstrated successful use of the cohesive zone model in simulating high-speed crack propagation in brittle materials. Arias et al. (2007) presented a systematic integrated numerical–experimental approach to the verification and validation of finite element dynamic fracture simulations of dynamic fracture along weak planes using cohesive elements. Therefore, it can be concluded that the cohesive zone method is a suitable method to simulate high-speed crack propagation in concrete, and is adopted in this dissertation.

2.5 SUMMARY

This chapter surveyed previous research related to the topics of this dissertation. The literature search suggests that there are significant gaps in knowledge about the strain rate dependent response of UHP-FRC, in particular. Moreover, the controversy surrounding why DIF occurs in the first place requires further investigation to better understand the origins and effects of strain rate sensitivity in cementitious composites. As is clear from the limited references listed, in contrast to the many investigations that have been carried out to understand the rate dependent properties of conventional concrete, very limited information is available on the rate-dependent response of fiber-reinforced concretes and almost no information exists about UHPC and UHP-FRC. Furthermore, the disadvantages of existing impact testing systems imply that there is a need for a more suitable test system to characterize UHP-FRC under high strain rate.

CHAPTER 3

PROPERTIES OF ULTRA HIGH PERFORMANCE FIBER REINFORCED CONCRETE (UHP-FRC) UNDER LOW STRAIN RATE TENSION

The results of an experimental investigation of UHP-FRC tensile response under a range of low strain rates are presented. The strain rate-dependent tests are conducted on dogbone-shaped specimens using a hydraulic servo-controlled testing machine. The experimental variables are strain rate, which ranges from 0.0001 /sec to 0.1 /sec, fiber type, and fiber volume fraction. Five different types of fibers are considered including straight and twisted fibers with different geometric properties. The rate sensitivity of the composite material in tension is evaluated in terms of its first cracking strength, post-cracking strength, energy absorption capacity, strain capacity, elastic modulus, fiber tensile stress and number of cracks. The test results show pronounced rate effects on post-cracking strength and energy absorption capacity. Further, post cracking strength varies linearly with the fiber reinforcing index and energy absorption capacity varies linearly with the product of the fiber length and the reinforcing index, as predicted from theory.

3.1 EXPERIMENTAL PROGRAM

An experimental program was carried out to investigate the rate sensitivity of UHP-FRC under uniaxial tension. The mix proportions of UHP-FRC with three different volume fractions of fiber are given in Table 3.1. Following Wille et al. (2011b), the mix constituents were selected from commercially available materials. The cement used has a low amount of C_3A , so as to have high amount of $C_3S + C_2S$. The hydration process of C_3A is fast and accommodates the associated increase in the surface area of the particles and the demand for water to surround the

particles during the mixing process, which leads to a higher viscosity (Wille et al. 2011b). Silica Fume with a median particle size of approximately 0.5 μm was added to the mix since Silica Fume improves the packing density of the matrix. Glass powder with a median particle size of 1.7 μm was also used to enhance the packing density of the paste. Two types of fine silica sand were used, with the gradations shown in Table 3.2. Five different fibers were used with the properties described in Table 3.3. The twisted fibers were made in the lab out of round wire stock. They have a square cross section with a pitch of 5 mm, where the fiber pitch is the length of one full (360-degree) twist around the fiber axis (Wille and Naaman 2012).

Table 3.1. Mixtures proportions by weight (based on Wille et al. (2011b))

Fiber Volume Fraction	1%	2%	3%
Cement	1.00	1.00	1.00
Silica Fume	0.25	0.25	0.25
Glass Powder	0.25	0.25	0.25
Water	0.22	0.22	0.22
Superplasticizer	0.005	0.005	0.005
Sand A [†]	0.27	0.26	0.26
Sand B [§]	1.07	1.05	1.02

[†] Maximum grain size = 0.2 mm (1/128 in.).

[§] Maximum grain size = 0.8 mm (1/32 in.).

The different fibers are designated by their type, diameter and length as shown in Table 3.2, e.g. S-0.2-25 is a straight smooth fiber with 0.2 mm diameter and 25 mm length. Tensile strength of fibers was evaluated using a Test Resources load frame (see Figure 3.1) and listed in Table 3.3. Each UHP-FRC test series is designated by the fiber used to make it, appended with a number that reflects the volume fraction of fiber, e.g. S-0.2-25-2% represents a mix with 2% fiber volume fraction. Nine series of UHP-FRC tensile test specimens were prepared and tested as shown in Table 3.4.

Dogbone-shaped specimens were selected for the tensile testing program following earlier research reported in Wille et al. (2014). Such specimens fulfill AASHTO T 132-87 (2009) requirements. UHP-FRC specimens are evaluated in terms of their first cracking strength, post-cracking strength, energy absorption capacity, strain capacity, elastic modulus, fiber tensile stress and number of cracks within the gage length.

Table 3.2. Grain Size Distribution (GSD) of sand (Wille et al. 2011b)

Sieve Size in μm	Amount in %, that went through the sieve	
	Sand A	Sand B
841	100	100
595	78	100
420	7	100
297	1	99.3
210	0	95.3
149	0	77.3
105	0	33.3
74	0	8.3
53	0	0.3
44	0	0

Table 3.3. Properties of steel fibers used in this study

Notation	Form	d_f (mm)	l_f (mm)	l_f / d_f	Tensile strength MPa (ksi)
T-0.3-25	Twisted*	0.3	25	83	2670 (387) [†]
S-0.2-25	Straight	0.2	25	125	2860 (415)
S-0.4-25	Straight	0.4	25	62.5	1850 (268)
S-0.3-18	Straight	0.3	18	60	2330 (338)
T-0.3-18	Twisted*	0.3	18	60	2670 (387) [†]

* Manufactured out of round wire with $d_f = 0.30$ mm at the University of Michigan Structural Laboratories

[†] Tensile strength of fiber after twisting

The strain rates considered range from 0.0001 /sec, which represents pseudo static loading, to 0.1 /sec, which is commonly considered as representative of seismic loading rates (Scott et al. 1982, Douglas and Billington 2011). All tests were conducted using a hydraulic servo-controlled testing machine (MTS-810). Three specimens for each loading rate in each test series were tested, resulting in 108 specimens in total (9 series \times 4 loading rates \times 3 specimens) as summarized in Table 3.4.

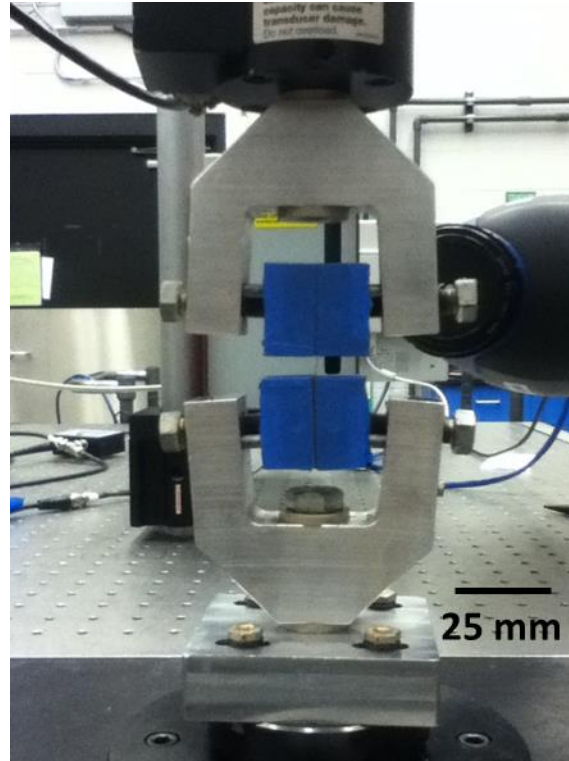


Figure 3.1. Steel fiber tensile test setup using a Test Resources load frame (Model# 830L)

Table 3.4. UHP-FRC test series investigated in this study

Test series	Fiber volume fraction (V_f)			$V_f(l_f/d_f)$	Strain Rate
	1%	2%	3%		
T-0.3-25-1%	X			0.83	0.1
T-0.3-25-2%		X		1.67	0.01
T-0.3-25-3%			X	2.50	0.001
T-0.3-25-3%			X	2.50	0.0001
S-0.2-25-1%	X			1.25	0.1
S-0.2-25-1%	X			1.25	0.01
S-0.2-25-2%		X		2.50	0.001
S-0.2-25-2%		X		2.50	0.0001
S-0.4-25-2%		X		1.25	0.1
S-0.4-25-2%		X		1.25	0.01
S-0.4-25-3%			X	1.88	0.001
S-0.4-25-3%			X	1.88	0.0001
S-0.3-18-2%		X		1.20	0.1
S-0.3-18-2%		X		1.20	0.01
S-0.3-18-2%		X		1.20	0.001
S-0.3-18-2%		X		1.20	0.0001
T-0.3-18-2%		X		1.20	0.1
T-0.3-18-2%		X		1.20	0.01
T-0.3-18-2%		X		1.20	0.001
T-0.3-18-2%		X		1.20	0.0001

3.1.1 Materials and Fabrication

A Hobart type laboratory mixer was used to prepare the UHP-FRC mixture. The mixing procedure followed Wille et al. (2011b). First, silica fume was mixed with all the sand for approximately 5 minutes. Then, cement and glass powder were added and mixed together for at least another 5 minutes before the water and superplasticizer were added. The cementitious mixture became fluid after approximately 5 minutes of adding the liquid ingredients (see Figure 3.2a). When the cementitious mixture started to show adequate flowability and viscosity, fibers were dispersed by hand in the mix (see Figure 3.2b). The cementitious mixture with uniformly distributed fibers was poured into dogbone shaped molds without any vibration. After casting, the specimens were covered with plastic sheets and stored at room temperature for 24 hours prior to demolding. The specimens were then placed in a water tank for an additional 26 days without any special curing such as heat or pressure treatment. All specimens were tested in a dry condition at the age of 28 days, after 24 hours of drying in the laboratory environment.

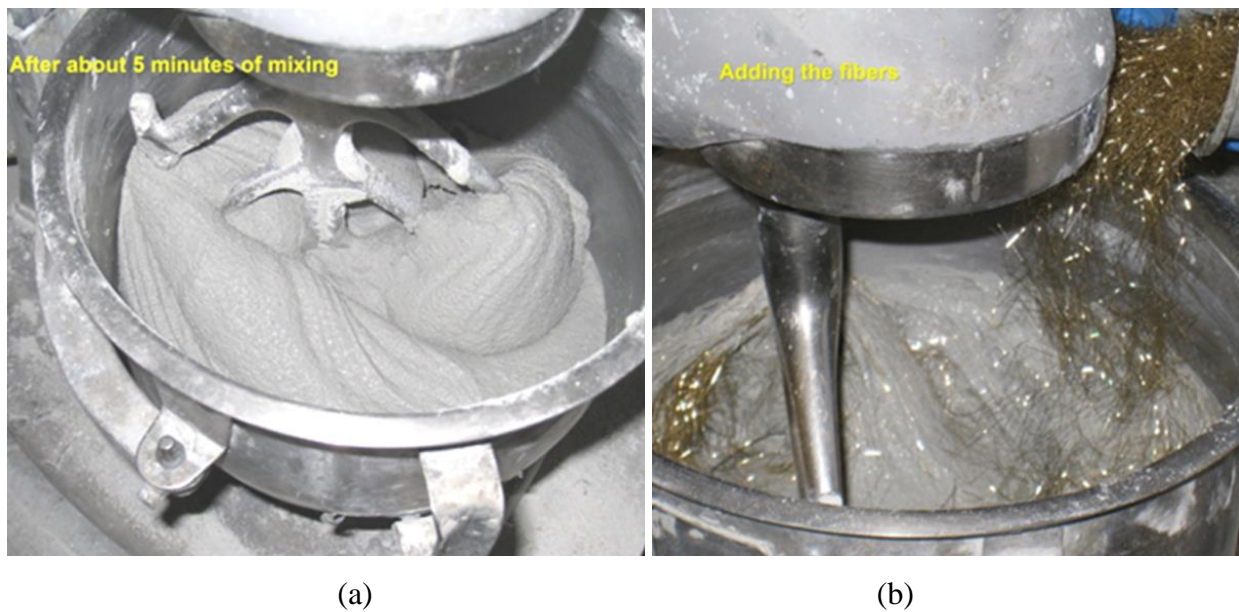


Figure 3.2. Mixing procedure of UHP-FRC: (a) fluid state without fibers; (b) adding fibers

3.1.2 Test Setup and Procedure

Wille et al. (2014) surveyed the various techniques used for tensile testing of cementitious composites and selected a specific method with the best ability to capture strain hardening behavior. Figure 3.3 shows the geometry of the specimen and test set up that were also adopted in this research. The gage length of the dogbone type tensile test specimen is 76 mm (= 3 inch). Tests were conducted using displacement control, where the displacement of the actuator in the hydraulic servo-controlled testing machine was used as the control variable. Two OPTOTRAK markers (for noncontact displacement measurement) were attached to the surface of the specimen. Three cameras were used to measure the movement of markers and the OPTOTRAK system calculated the deformation of the specimen. The applicability of the OPTOTRAK system for this type of measurement was confirmed in a similar study done by Kim et al. (2009) for HPFRCC. The tensile load history was recorded via the load cell attached to the testing machine and synchronized to the deformation history recorded by the OPTOTRAK system.

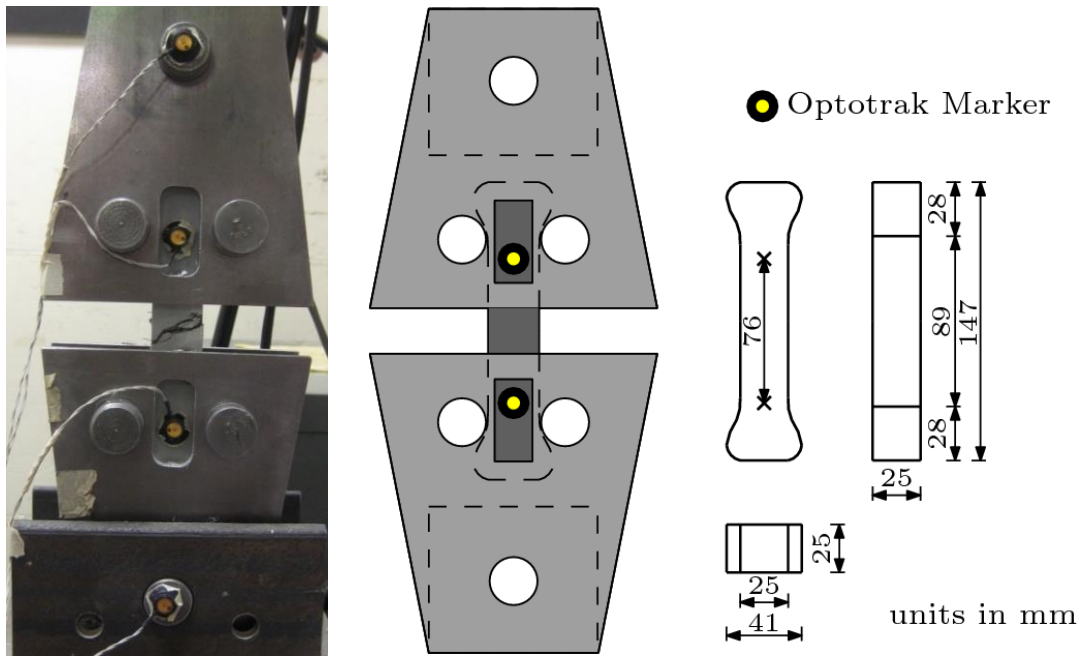


Figure 3.3. Direct tensile test setup

3.1.3 Test Results

Referring to Figures 3.4a and 3.4b, the parameters considered in this investigation are: 1) the first cracking strength (σ_{cc}), 2) the post cracking strength (σ_{pc}), 3) the energy absorption capacity (g), 4) the strain capacity, which is the strain value at post cracking strength (ϵ_{pc}), 5) the elastic modulus (E_{cc}) up to the first cracking strength, 6) the fiber tensile stress (σ_{fpc}), and 7) number of cracks within the gage length. It is important to note that σ_{cc} is the turning point between elastic and strain hardening parts and does not necessarily represent the stress when the

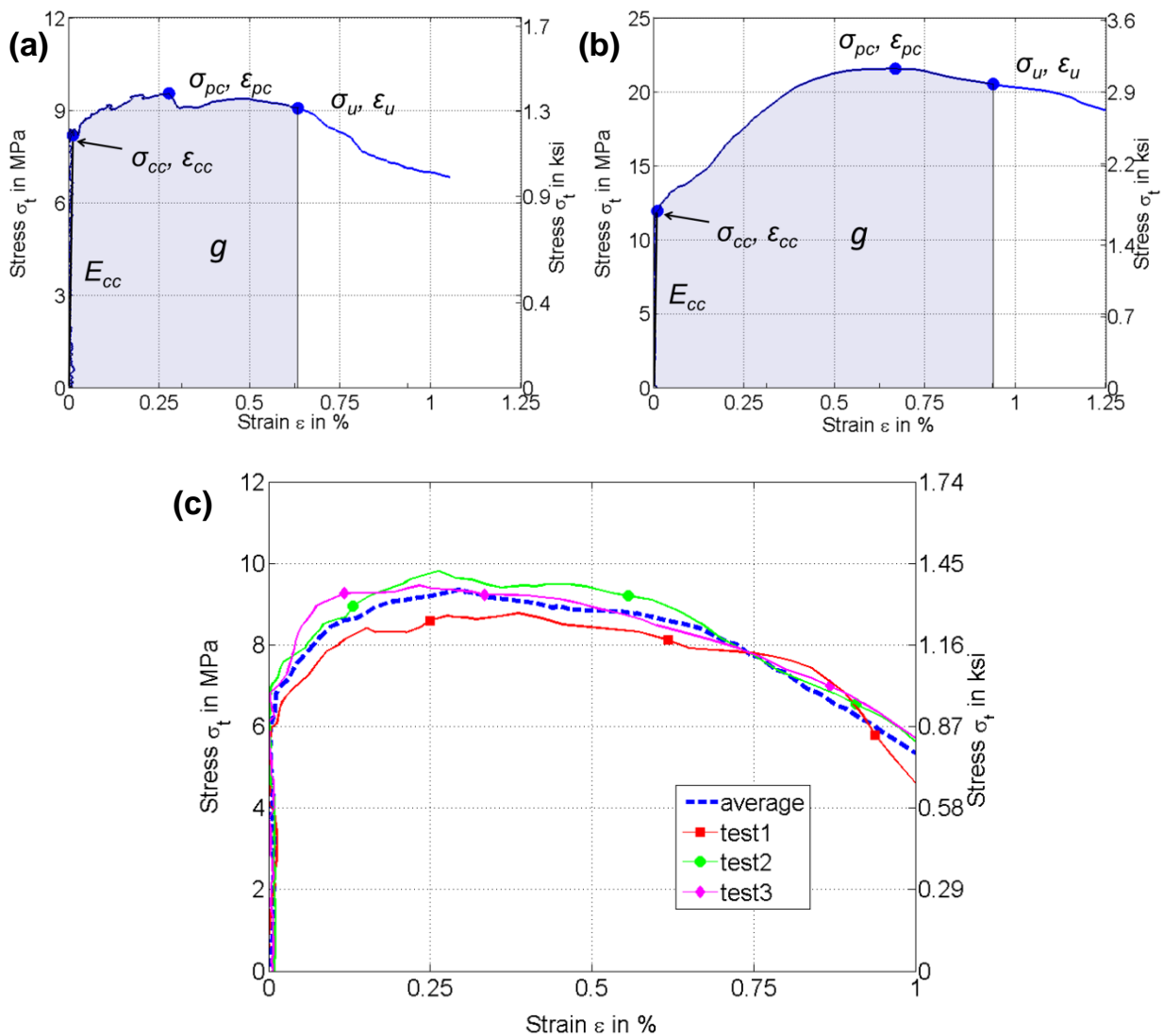


Figure 3.4. Typical interpretation and measurement of test results: (a, b) typical variables; (c) typical averaging of stress-strain curve (T-0.3-18-2% & $\dot{\epsilon} = 0.01$ /sec) (Note: strain valid up to peak stress only.)

first crack developed. It also should be noted that g is the area under stress-strain curve up to an arbitrarily selected value: $\sigma_u = 0.95\sigma_{pc}$.

The variable σ_{fpc} represents the average tensile stress in the fiber at maximum stress in the composite. It is calculated by Equation (3.1) as follows (Wille et al. 2014):

$$\sigma_{fpc} = \frac{\sigma_{pc}}{\phi \cdot V_f} \quad (3.1)$$

where, ϕ is a fiber orientation factor, taken 0.9 for all series following Wille et al. (2014). Table 3.5 summarizes all the test results. All the values given in Table 3.5 are averaged values from at least three specimens. A Dynamic Increase Factor (DIF), which is the ratio between dynamic response and static response, is computed for four parameters (σ_{cc} , σ_{pc} , g , ε_{pc}) to effectively illustrate the effect of strain rate on strength and other material parameters. In this study the values measured at the lowest strain rate of 0.0001 /sec were considered to be the reference, i.e. pseudostatic loading rate. The DIF values are also listed in Table 3.5.

Figure 3.4c shows an example averaged stress-strain curve, plotted along with raw data to give a sense of the spread in the test data. In order to get an averaged curve, the raw data set is divided into two parts, one before and one after the peak load. The two parts are then assigned fractions of peak load strain, and then raw data sets are averaged for the two different parts. It is clear from Figure 3.4c, and this was generally observed throughout the test program, that specimen-to-specimen variability within each strain rate was relatively low for all parameters. The average tensile stress-strain curves for each series under four different strain rates are plotted in Figures 3.5 to 3.7. All test series maintained performance Level 3 as classified in Naaman and Reinhardt (2003) for all loading rates, i.e., strain hardening was observed for all loading rates. Furthermore, T-0.3-25-2%, T-0.3-25-3%, and S-0.2-25-2% series maintained performance Level 4 as classified by Naaman and Reinhardt (2003), which is defined as high energy absorbing with $g \geq 50 \text{ kJ/m}^3$ as suggested by Wille et al. (2014) for all loading rates.

According to Naaman (2003), the post cracking strength of composites reinforced with short discontinuous fibers is proportional to fiber aspect ratio and their volume fraction as follows:

$$\sigma_{pc} = \lambda \tau_{eq} V_f (l_f / d_f) \quad (3.2)$$

where λ is a factor equal to the product of several coefficients that account for average pullout length, group reduction effect, and fiber orientation effect. τ_{eq} is the equivalent bond strength. The product $V_f (l_f / d_f)$ is termed the fiber reinforcing index. Table 3.6 shows the effect of the fiber aspect ratio on post cracking strength based on the results of Equation (3.2) for the pseudostatic and seismic loading rates and 2 % fiber content. Moreover, the surface energy of pull-out, which gives a good estimate of the fracture energy in the type of tensile tests carried out here can be put in the following form (Naaman 2002):

$$\gamma_g = \zeta \tau_{eq} V_f (l_f^2 / d_f) \quad (3.3)$$

where ζ is the product of λ in Equation (3.2) and the ratio of average bridging stress to the maximum post-cracking stress over the expected maximum pull-out length. It can be thus observed that the expected fracture energy varies with the square of the fiber length or with the product of the fiber length by the reinforcing index.

Table 3.5. Rate effect on the average tensile properties of UHP-FRC

Test series	Strain rate	First cracking strength (σ_{cc})		Post cracking strength (σ_{pc})		Energy absorption capacity (g)		Strain capacity (ϵ_{pc})		Elastic modulus (E_{cc})	Fiber tensile stress (σ_{fpc})	Average Number of cracks
		MPa	DIF	MPa	DIF	kJ/m^3	DIF	%	DIF	GPa	MPa	EA
T-0.3-25-1%	0.0001	6.890	1.000	8.305	1.000	33.49	1.000	0.190	1.000	54.48	922.8	7
	0.001	7.541	1.094	8.911	1.073	37.86	1.131	0.228	1.200	54.60	990.1	7
	0.01	7.038	1.021	9.422	1.134	47.64	1.423	0.263	1.384	57.13	1047	8
	0.1	8.129	1.180	10.84	1.305	60.65	1.811	0.342	1.801	58.93	1204	9
T-0.3-25-2%	0.0001	9.031	1.000	11.60	1.000	63.54	1.000	0.421	1.000	60.06	644.1	13
	0.001	9.135	1.011	12.56	1.083	83.40	1.312	0.504	1.196	60.41	697.8	14
	0.01	8.726	0.966	13.75	1.186	84.07	1.323	0.548	1.301	54.32	763.8	11
	0.1	8.865	0.982	14.01	1.209	102.5	1.613	0.701	1.664	60.83	778.6	11
T-0.3-25-3%	0.0001	11.82	1.000	20.93	1.000	108.1	1.000	0.481	1.000	71.31	775.1	13
	0.001	11.49	0.972	21.74	1.039	142.9	1.322	0.616	1.280	70.03	805.2	13
	0.01	12.02	1.017	23.46	1.121	177.3	1.641	0.679	1.412	70.31	868.8	12
	0.1	12.11	1.025	24.08	1.151	186.3	1.724	0.787	1.636	76.14	891.9	12
S-0.2-25-1%	0.0001	6.215	1.000	8.110	1.000	34.53	1.000	0.331	1.000	47.72	901.1	9
	0.001	7.855	1.264	9.485	1.170	51.90	1.503	0.485	1.468	56.07	1054	13
	0.01	6.915	1.113	8.289	1.022	48.09	1.393	0.386	1.168	51.14	920.9	10
	0.1	6.699	1.078	9.012	1.111	47.61	1.379	0.430	1.301	54.04	1001	13
S-0.2-25-2%	0.0001	9.732	1.000	14.92	1.000	84.35	1.000	0.546	1.000	66.62	828.7	13
	0.001	9.189	0.944	14.64	0.981	83.13	0.985	0.593	1.087	63.22	813.2	12
	0.01	11.22	1.153	15.45	1.036	87.22	1.034	0.605	1.108	64.75	858.4	14
	0.1	9.646	0.991	15.51	1.040	89.27	1.058	0.554	1.015	67.82	861.5	17
S-0.4-25-2%	0.0001	6.864	1.000	8.315	1.000	35.92	1.000	0.270	1.000	54.50	462.0	8
	0.001	6.783	0.988	8.650	1.040	36.78	1.024	0.297	1.103	51.23	480.5	10
	0.01	8.125	1.184	9.956	1.197	48.29	1.344	0.345	1.279	57.74	553.1	9
	0.1	8.304	1.210	9.723	1.169	56.09	1.561	0.417	1.548	54.97	540.1	9
S-0.4-25-3%	0.0001	7.671	1.000	9.413	1.000	41.34	1.000	0.241	1.000	61.42	348.6	10
	0.001	8.197	1.068	9.628	1.023	48.45	1.172	0.277	1.151	60.98	356.6	9
	0.01	8.693	1.133	12.49	1.327	74.76	1.808	0.471	1.957	62.79	462.6	9
	0.1	8.713	1.136	12.81	1.361	78.78	1.906	0.467	1.938	59.94	474.3	7
S-0.3-18-2%	0.0001	7.047	1.000	8.443	1.000	20.04	1.000	0.173	1.000	56.53	469.1	7
	0.001	8.452	1.199	9.799	1.161	28.07	1.401	0.211	1.221	61.08	544.4	7
	0.01	7.046	1.000	9.319	1.104	34.15	1.704	0.232	1.345	53.14	517.7	6
	0.1	7.660	1.087	9.699	1.149	38.30	1.911	0.311	1.801	53.36	538.8	6
T-0.3-18-2%	0.0001	7.734	1.000	9.040	1.000	27.79	1.000	0.256	1.000	56.13	502.2	7
	0.001	8.529	1.103	10.41	1.151	34.63	1.246	0.220	0.860	55.00	578.1	8
	0.01	7.319	0.946	9.628	1.065	47.31	1.703	0.294	1.150	50.42	534.9	7
	0.1	7.373	0.953	10.80	1.195	54.46	1.960	0.435	1.701	56.91	600.2	7

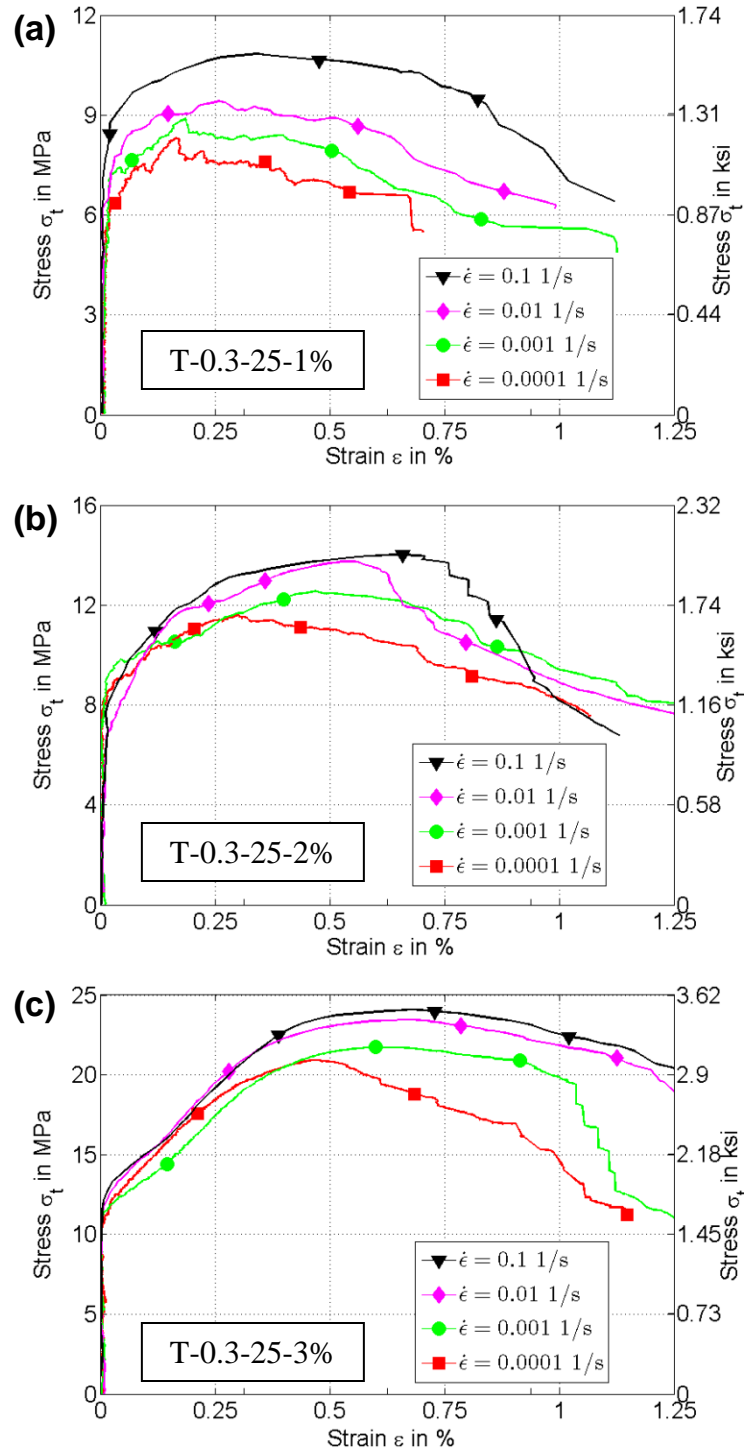


Figure 3.5. Rate effect on the tensile behavior of T-0.3-25 UHP-FRC with increasing fiber volume content (Note: strain valid up to peak stress only.)

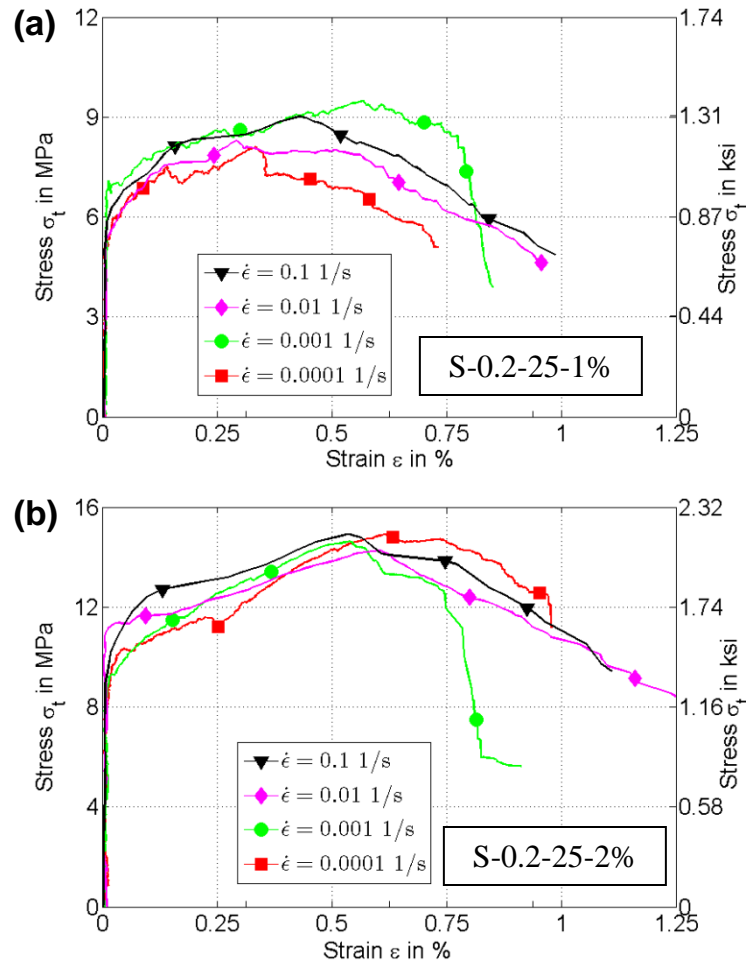


Figure 3.6. Rate effect on the tensile behavior of S-0.2-25 UHP-FRC with increasing fiber volume content (Note: strain valid up to peak stress only.)

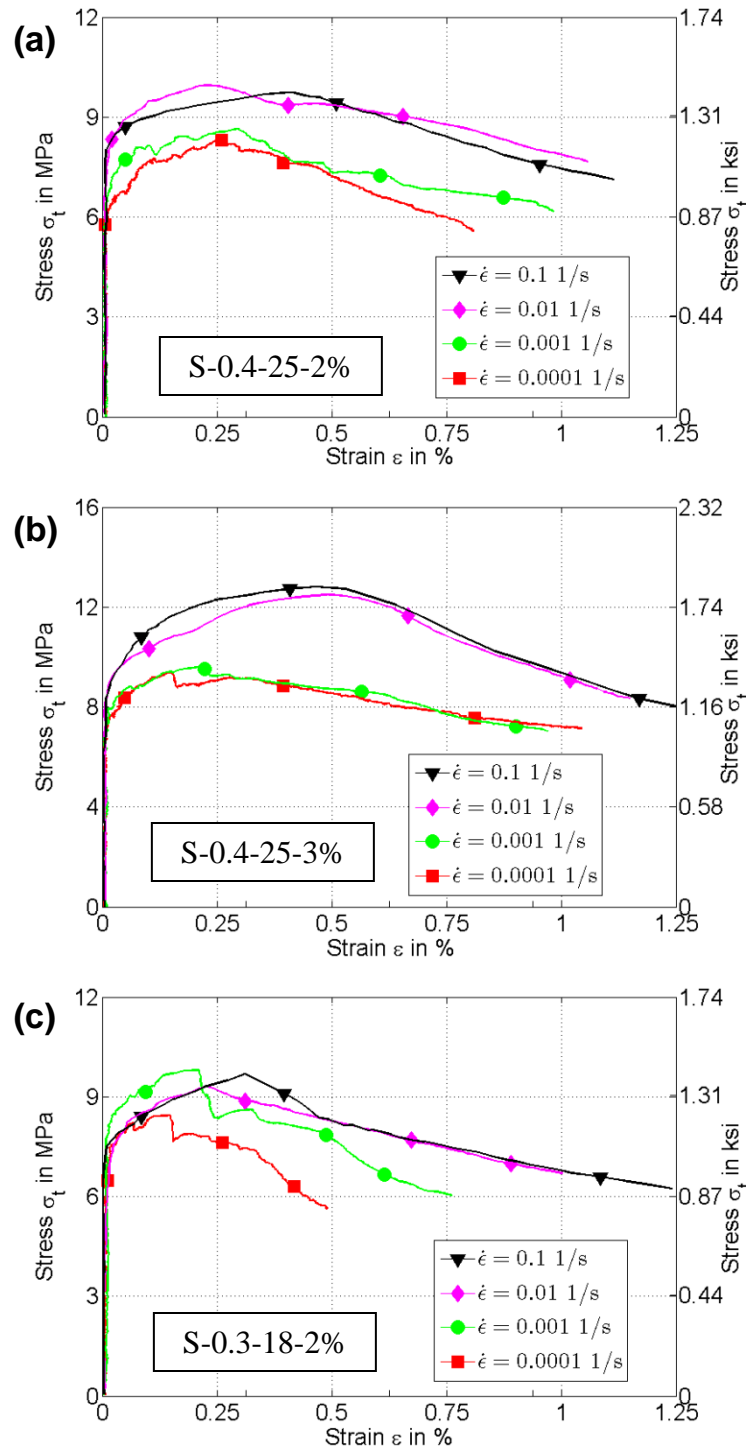


Figure 3.7. Rate effect on the tensile behavior of UHP-FRC using fibers with about same aspect ratio (Note: strain valid up to peak stress only.)

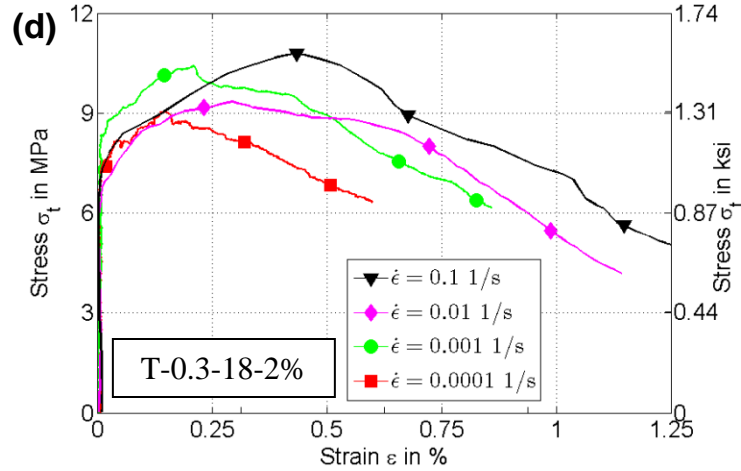


Figure 3.7. continued

Table 3.6. Equivalent bond strength for UHP-FRC with 2% fiber content

Test series	l_f / d_f	$\dot{\epsilon} = 0.0001 / \text{sec}$		$\dot{\epsilon} = 0.1 / \text{sec}$	
		σ_{pc} (MPa)	$\lambda\tau_{eq}$ (MPa)	σ_{pc} (MPa)	$\lambda\tau_{eq}$ (MPa)
T-0.3-25-2%	83	11.60	6.984	14.01	8.440
S-0.2-25-2%	125	14.92	5.967	15.51	6.204
S-0.4-25-2%	62.5	8.315	6.653	9.723	7.778
S-0.3-18-2%	60	8.443	7.037	9.699	8.083
T-0.3-18-2%	60	9.040	7.533	10.80	9.000

3.2 EVALUATION OF EXPERIMENTAL RESULTS

The average numerical results are summarized in Table 3.5. Figures 3.5 to 3.17 illustrate the effects of various parameters on the response of the composite at various strain rates.

3.2.1 Separate Effects of Fiber Volume Fraction, Aspect Ratio, Length, and Type

Figure 3.5 illustrates the effects of volume fraction of fibers and strain rate on the tensile response of composites reinforced with twisted steel fibers. It can be observed that the post-cracking strength and the corresponding strain generally increase with an increase in both volume fraction of fibers and strain rate. Typically, the post-cracking strength more than doubles

when the volume fraction of fiber goes from 1 % to 3 %. Figure 3.6 illustrates similar trends when for S-0.2-25 fibers with 1 % and 2 % fiber volume content. Figure 3.7 shows the response of four series of tests having about the same fiber aspect ratio. Clearly, the trend continues, that is, the post-cracking strength and strain typically increases with an increase in strain rate.

The effect of fiber aspect ratio by itself, l_f / d_f , can be evaluated by comparing series with 2 % volume fraction from the three figures (Figures 3.5 to 3.7 and Table 3.6). Not only does the post cracking strength generally increase with fiber aspect ratio, but the first cracking strength also increases. For example, S-0.2-25-2% shows better performance than S-0.4-25-2%, exceeding by 33 % its first cracking strength, 66 % its post cracking strength, 78 % its strain capacity and 100 % its energy absorption capacity, averaged across all strain rates, respectively.

From a qualitative perspective, increasing fiber volume fraction leads to an increase in tensile strength (see Figure 3.8 and Figure 3.9), energy absorption capacity (see Figure 3.10), and strain capacity (see Figure 3.11). Although the elastic modulus was measured for all specimens tested, the large scatter in the data makes it difficult to draw a firm conclusion regarding the effect of aspect ratio or fiber volume fraction or strain rate on elastic modulus (see Figure 3.12).

Overall, the twisted fiber series shows better performance than straight fiber series because of the additional anchorage effect associated with the untwisting action that occurs during pullout. Kim et al. (2008) discussed the untwisting mechanism. However, it was noticed that for a given volume fraction, T-0.3-25 and S-0.2-25 fibers show similar mechanical performances. The T-0.3-18-2% series shows marginally better mechanical properties than S-0.3-18-2%. The increase is most prominent in energy absorption capacity, where it is 36 % higher on average across all strain rates. This is attributed to the fact that the number of S-0.2-25 fibers, which are thinner than the T-0.3-25 fibers, is 225 % more in a unit volume than T-0.3-25 fibers, making up for the additional anchorage mechanism of the twisted fibers. The good performance of S-0.2-25 fibers, however, comes at a price because the larger number of the fibers makes it more difficult to mix. In general, it was not possible to make mixes with more than 2 % volume fraction of S-0.2-25 fibers. In contrast, mixes with up to 3 % volume fraction of T-0.3-25 fibers were feasible. The opposite argument can be made for the T-0.3-25 fibers versus the S-0.4-25 fibers.

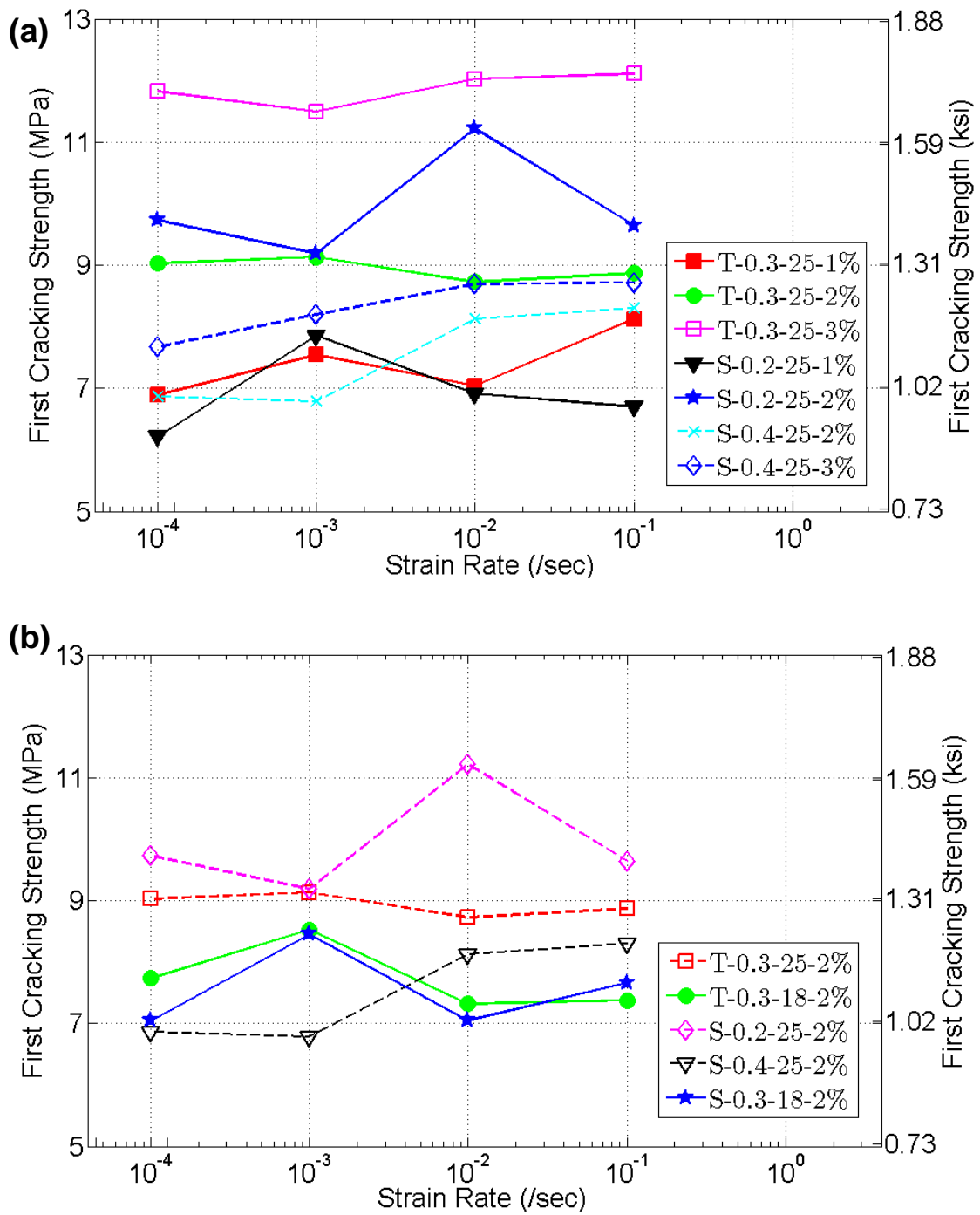


Figure 3.8. Rate effect on the first cracking strength of UHP-FRC: (a) specimens with different fiber volume fractions; (b) specimens with 2 % fiber volume fraction

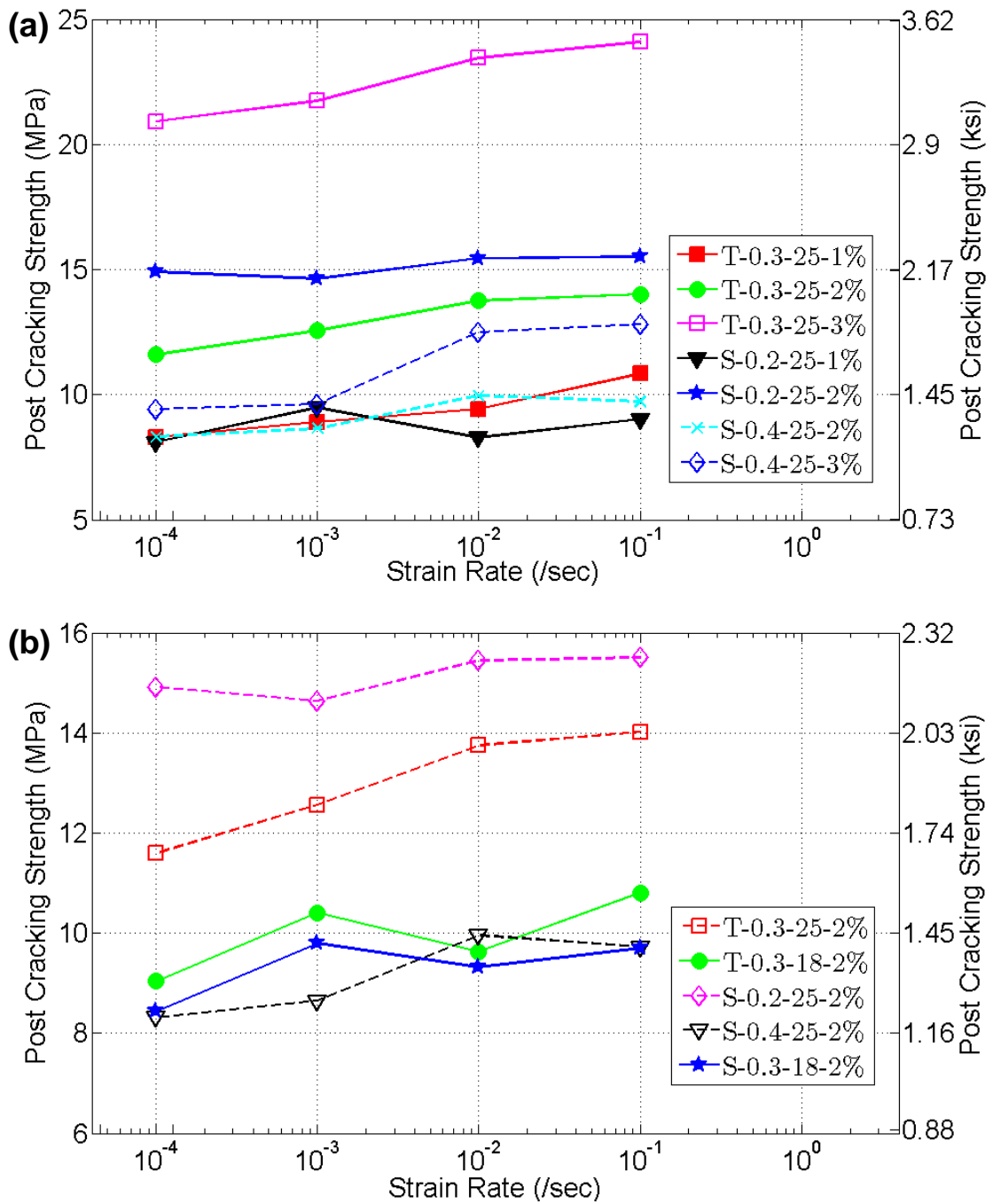


Figure 3.9. Rate effect on the post cracking strength of UHP-FRC: (a) specimens with different fiber volume fractions; (b) specimens with 2 % fiber volume fraction

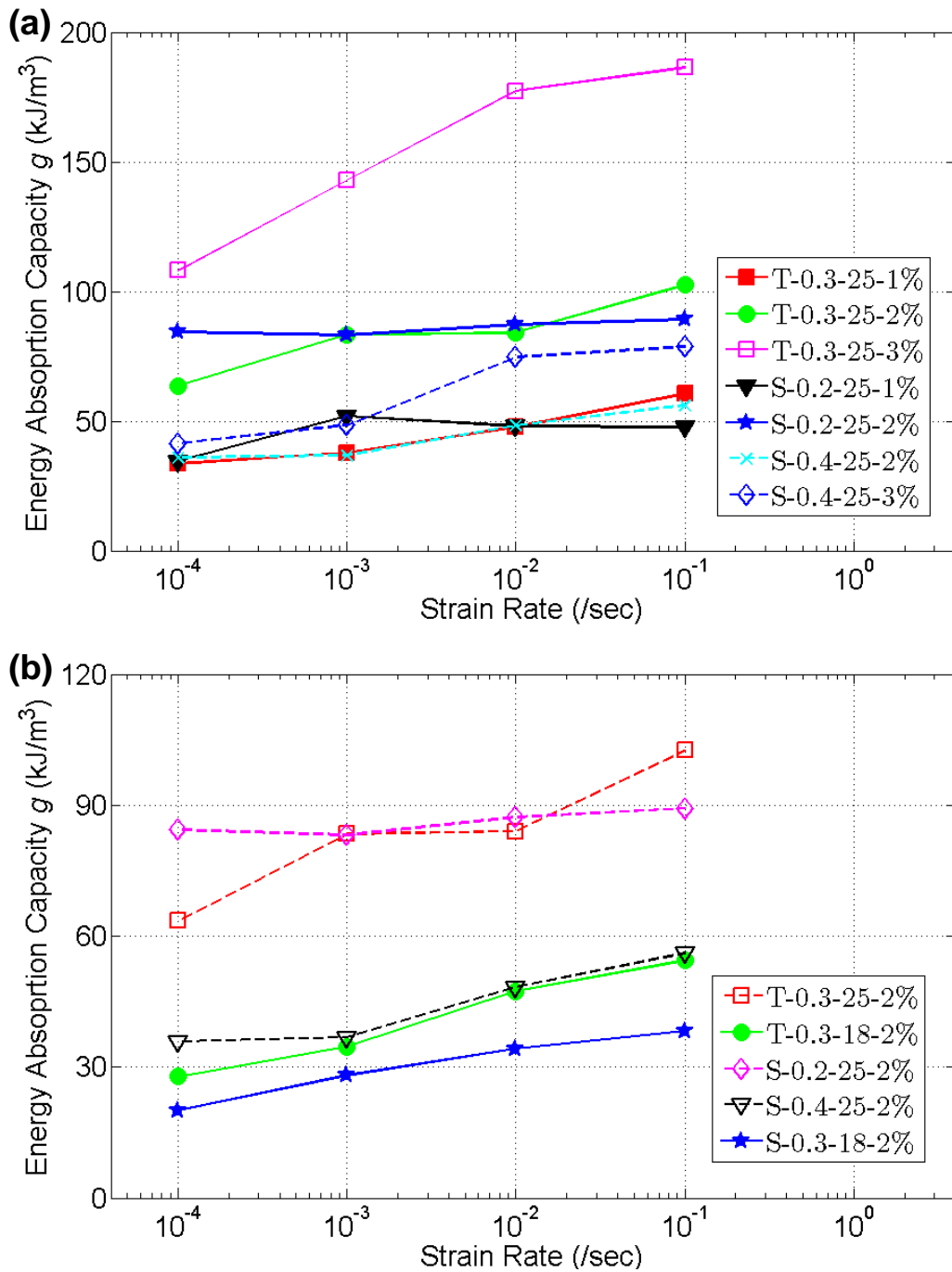


Figure 3.10. Rate effect on the energy absorption capacity of UHP-FRC: (a) specimens with different fiber volume fractions; (b) specimen with 2 % fiber volume fraction

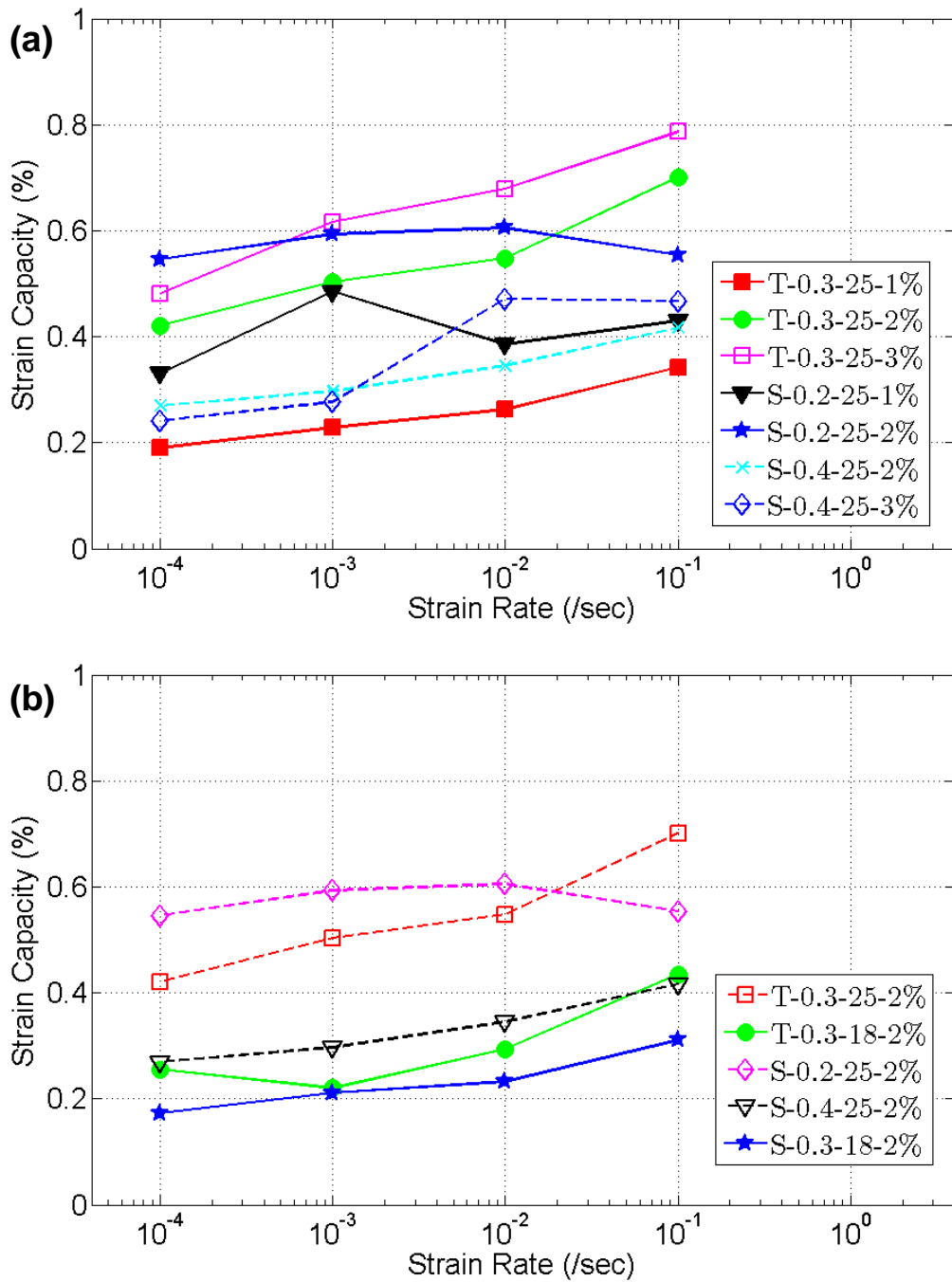


Figure 3.11. Rate effect on the strain capacity of UHP-FRC: (a) specimens with different fiber volume fractions; (b) specimens with 2 % fiber volume fraction

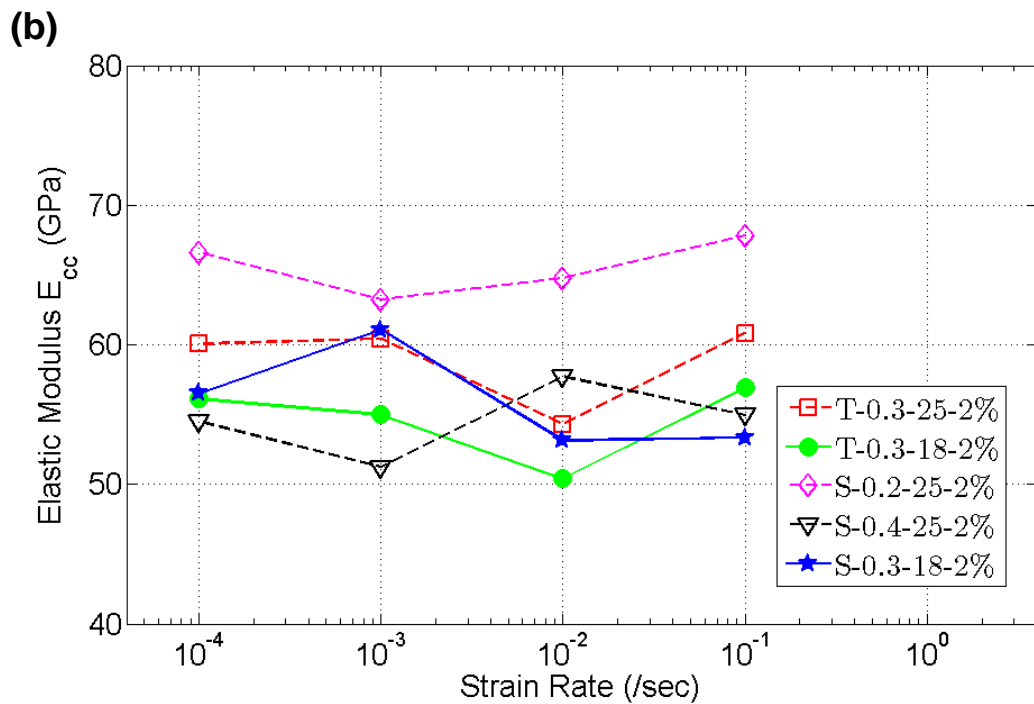
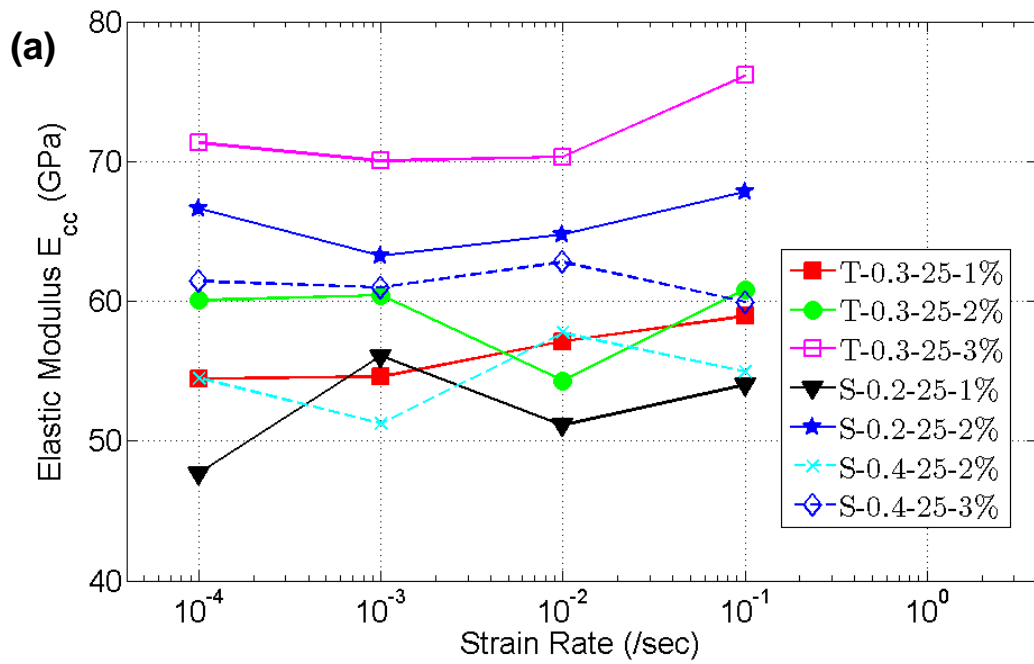


Figure 3.12. Rate effect on the elastic modulus of UHP-FRC: (a) specimens with different fiber volume fractions; (b) specimens with 2 % fiber volume fraction

3.2.2 Equivalent Bond

The results of all test series with 2 % volume fraction of fibers are summarized in Table 3.6. Looking across all entries in the 4th and 6th columns suggests that $\lambda\tau_{eq}$ is almost independent of fiber type, diameter and length. This unexpected result may be attributed to the use of a UHPC matrix where the bond for smooth straight fiber is reported to be excellent due to surface abrasion (see recent paper by Wille et al. (2012)), and is likely due to the very high packing density of the cementitious matrix around the fiber. It is also noted that the equivalent bond is an average value estimated over a small crack opening (related to ε_{pc}) and is different from a similar value obtained from a complete fiber pull-out curve.

3.2.3 Effect of Reinforcing Index $V_f(l_f/d_f)$

Equation (3.2) suggests that, for the same $\lambda\tau_{eq}$, the post-cracking strength of the composite is directly proportional to the fiber reinforcing index, that is, the product of the volume fraction times the aspect ratio of fiber. Figure 3.13a provides a summary of the data observed for the post-cracking strength versus the reinforcing index at different strain rates. The trend predicted by Equation (3.2) is clearly confirmed by the data, that is, the post-cracking strength increases with the fiber reinforcing index. To best quantify the data, the least square fit lines for the four loading rates ranging from quasi-static (0.0001 /sec) to seismic (0.1 /sec) are listed in Table 3.7 and the extreme ones shown in Figure 3.13. It can be further observed that the post-cracking strength increases with strain rate.

Figure 3.13b illustrates the variation of the first cracking strength of the composite versus the fiber reinforcing index at different strain rates. Here also the least square fit lines of the data are plotted and suggest that the first cracking strength increases with both the reinforcing index and the strain rate.

3.2.4 Energy Absorption Capacity

Following the format of Equation (3.3), the observed energy absorption capacity (see Figure 3.4) is plotted in Figure 3.14 versus the quantity $V_f(l_f^2/d_f)$ for different strain rates. The

trend observed confirms theoretical predictions; that is, the energy increases with both $V_f(l_f^2/d_f)$ and the strain rate. The least square fit lines provided in the figures and Table 3.7 offer a good means for quantifying the data.

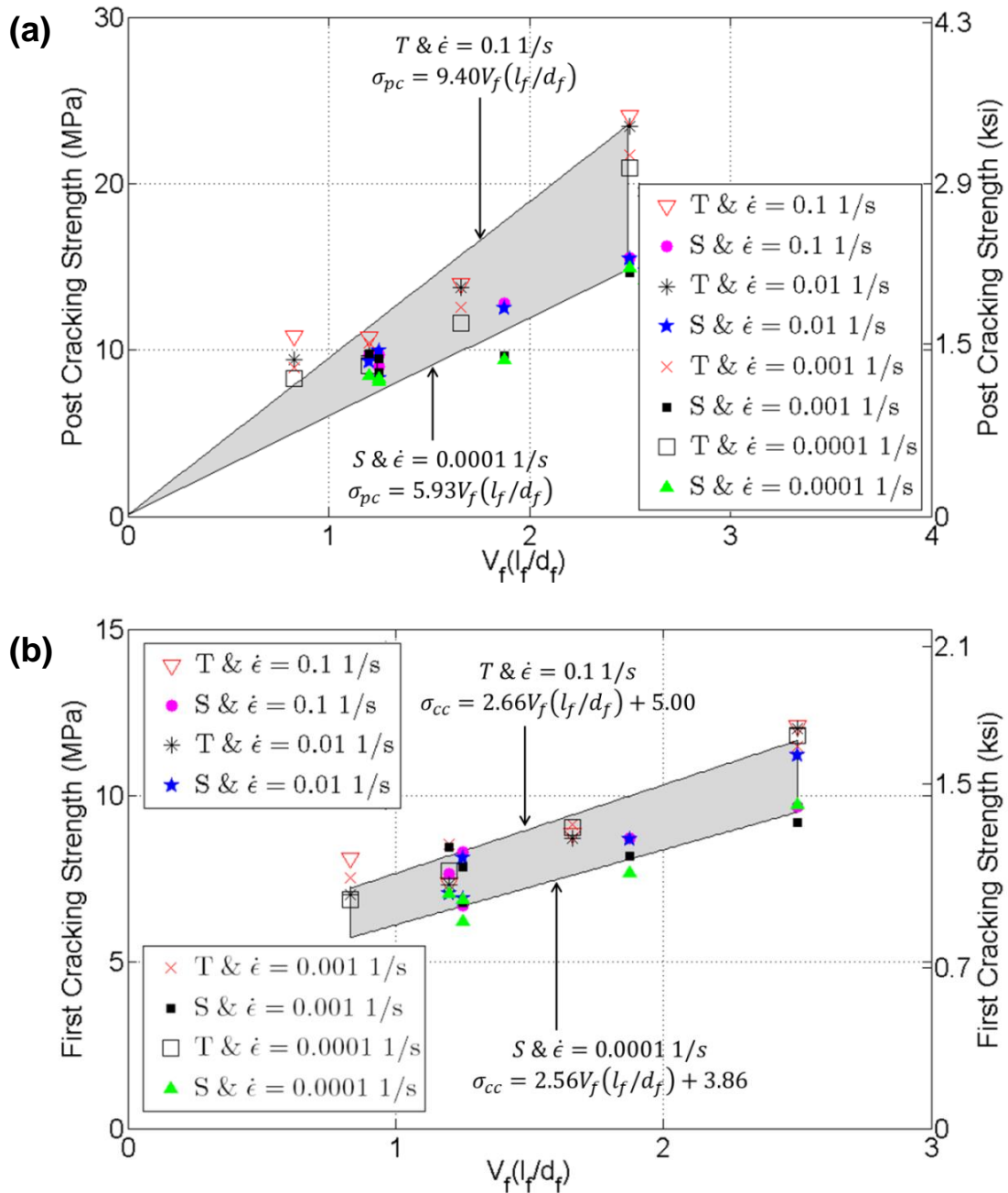


Figure 3.13. Effects of the fiber reinforcing index on mechanical properties of UHP-FRC: (a) Post cracking strength; (b) First cracking strength

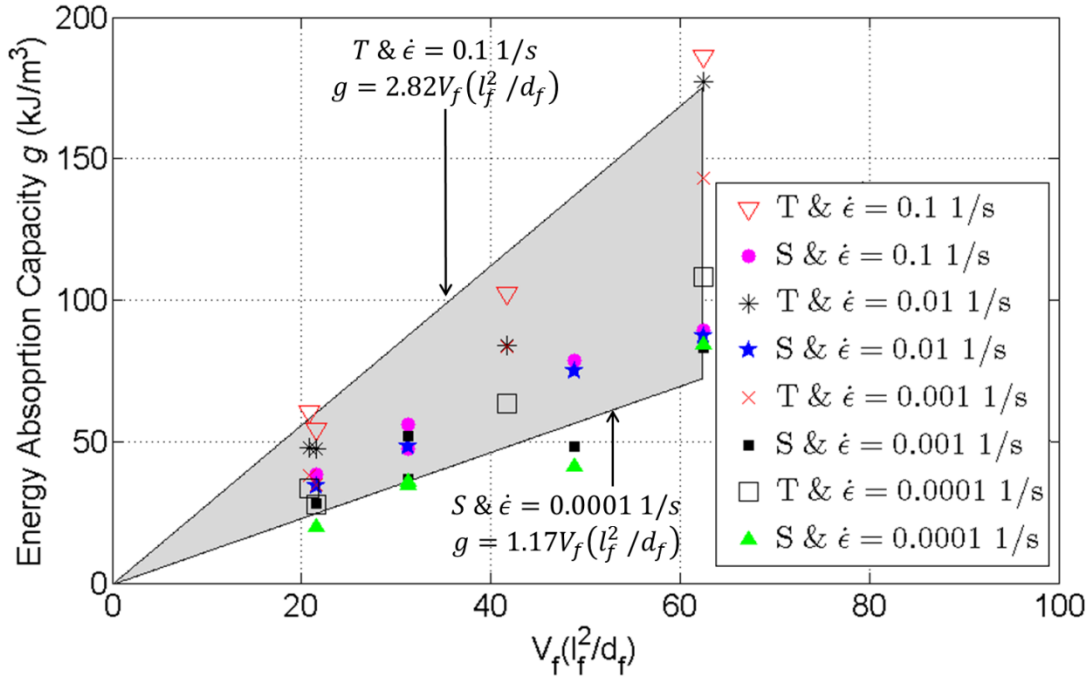


Figure 3.14. Effects of $V_f(l_f^2/d_f)$ on energy absorption capacity of UHP-FRC

Table 3.7. Least square fit approximations of results in Figures 3.13 and 3.14

Index	Strain Rate (1/sec)	T-Fiber	S-Fiber
First Cracking Strength	$\dot{\epsilon} = 0.0001$	$\sigma_{cc} = 2.98V_f(l_f/d_f) + 4.25$	$\sigma_{cc} = 2.56V_f(l_f/d_f) + 3.86$
	$\dot{\epsilon} = 0.001$	$\sigma_{cc} = 2.31V_f(l_f/d_f) + 5.59$	$\sigma_{cc} = 1.10V_f(l_f/d_f) + 6.33$
	$\dot{\epsilon} = 0.01$	$\sigma_{cc} = 3.11V_f(l_f/d_f) + 3.96$	$\sigma_{cc} = 2.93V_f(l_f/d_f) + 3.67$
	$\dot{\epsilon} = 0.1$	$\sigma_{cc} = 2.66V_f(l_f/d_f) + 5.00$	$\sigma_{cc} = 1.67V_f(l_f/d_f) + 5.52$
Post Cracking Strength	$\dot{\epsilon} = 0.0001$	$\sigma_{pc} = 7.98V_f(l_f/d_f)$	$\sigma_{pc} = 5.93V_f(l_f/d_f)$
	$\dot{\epsilon} = 0.001$	$\sigma_{pc} = 8.41V_f(l_f/d_f)$	$\sigma_{pc} = 6.12V_f(l_f/d_f)$
	$\dot{\epsilon} = 0.01$	$\sigma_{pc} = 9.04V_f(l_f/d_f)$	$\sigma_{pc} = 6.65V_f(l_f/d_f)$
	$\dot{\epsilon} = 0.1$	$\sigma_{pc} = 9.40V_f(l_f/d_f)$	$\sigma_{pc} = 6.76V_f(l_f/d_f)$
Energy Absorption Capacity	$\dot{\epsilon} = 0.0001$	$g = 1.66V_f(l_f^2/d_f)$	$g = 1.17V_f(l_f^2/d_f)$
	$\dot{\epsilon} = 0.001$	$g = 2.16V_f(l_f^2/d_f)$	$g = 1.27V_f(l_f^2/d_f)$
	$\dot{\epsilon} = 0.01$	$g = 2.56V_f(l_f^2/d_f)$	$g = 1.48V_f(l_f^2/d_f)$
	$\dot{\epsilon} = 0.1$	$g = 2.82V_f(l_f^2/d_f)$	$g = 1.55V_f(l_f^2/d_f)$

3.2.5 Cracking

Figure 3.15 shows the observed cracking patterns in a UHP-FRC specimen, which indicates that UHP-FRC materials exhibit multiple cracking after first cracking along with hardening behavior. The number of cracks within the gage length is also an important indicator of energy absorption capacity and strain at peak load. It appears from the results (see Figure 3.16) that both the number of cracks and the energy capacity increase as fiber volume fraction increases. However, it is difficult to draw a clear conclusion about the effect of strain rate on the number of cracks, due to the variability in the test data. It should be noted that the crack counting process itself is somewhat subjective because of the difficulty of ascertaining the presence of a crack after unloading.



Figure 3.15. Representative multiple cracking patterns in UHP-FRC specimens

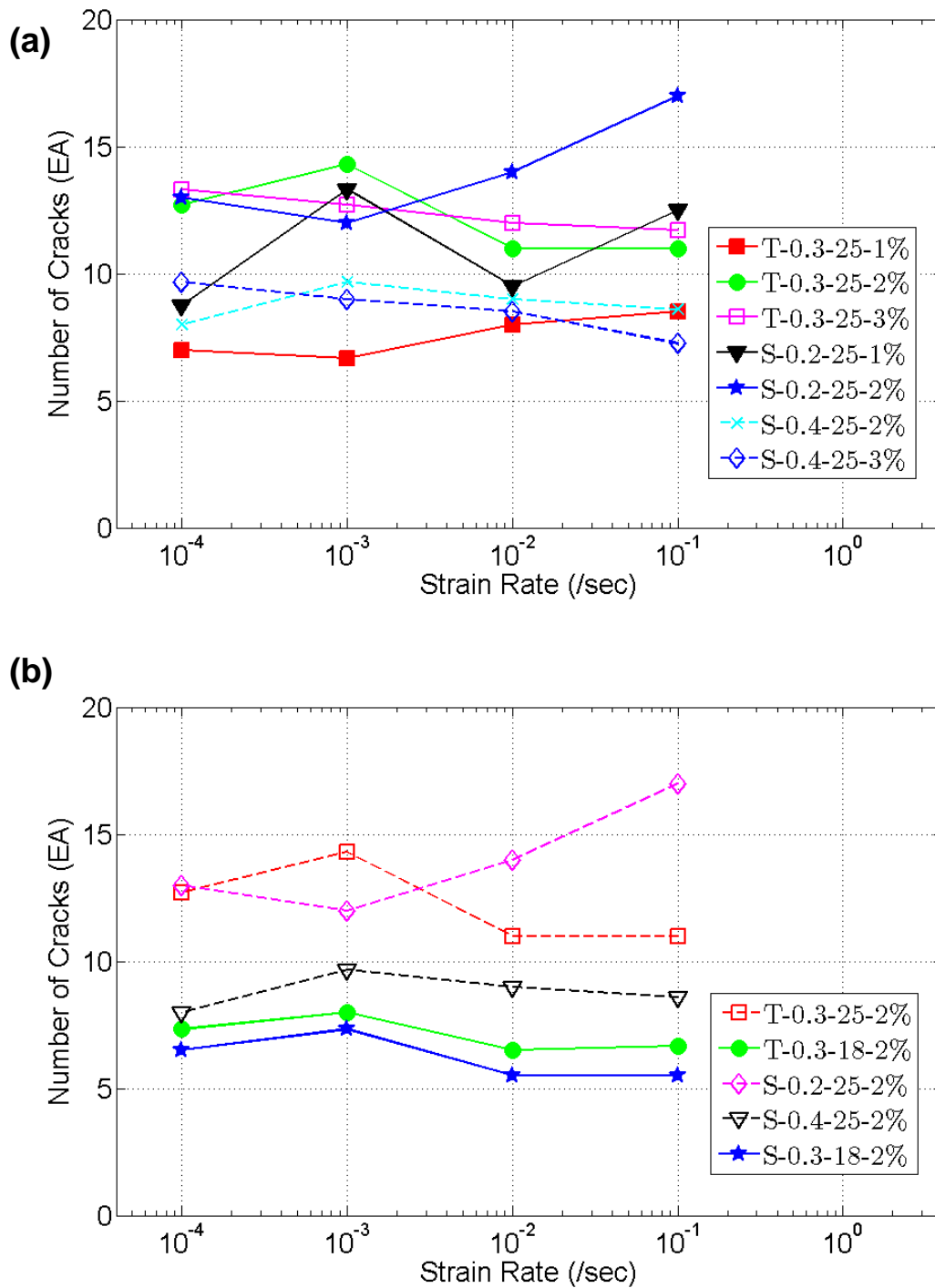


Figure 3.16. Rate effect on number of cracks of UHP-FRC: (a) specimens with different fiber volume fractions; (b) specimens with 2% fiber volume fraction

3.2.6 Fiber Tensile Stress

Figure 3.17 shows rate effects on the fiber tensile stress of UHP-FRC. The fiber tensile stress (Equation (3.1)), which represents the effectiveness of fiber usage, increases as strain rate increases. Even though higher fiber volume fraction led to better mechanical properties of UHP-FRC, it generally decreases, from a qualitative perspective, as fiber volume fraction increases, in contrast to other mechanical parameters (see Figure 3.17), likely due to the fiber-group effect. Increases in performance attributed to volume fraction are also limited by another practical limitation, i.e. difficulty of mixing with a large quantity of fibers.

3.2.7 DIF

DIF was evaluated for four key parameters, first cracking strength, post cracking strength, energy absorption capacity and strain capacity. Plots of DIF versus strain rate for first cracking strength, post cracking strength, energy absorption capacity and strain capacity are compared in Figure 3.18. The increases in DIF for the four parameters can be reasonably simulated by a log-linear trend with the increase in strain rate. Figure 3.18a shows that the highest rate sensitivity of first cracking strength occurs in series with S-0.4-25 fibers, while the lowest occurs in series with T-0.3-18 fibers. Similarly, S-0.4-25 series shows the highest rate sensitivity in post cracking strength, energy absorption capacity and strain capacity, but S-0.2-25 series shows less rate sensitivity in those parameters as shown in Figures 3.18b, 3.18c and 3.18d, respectively.

Fitted log-linear relationships for first cracking strength, post cracking strength, energy absorption capacity and strain capacity with strain rate are shown in Figure 3.18. The figure indicates that the increase in DIF is moderate and nearly linear in log-linear space at strain rates up to 0.1/sec. This general tendency has been observed in other cement-based materials such as ordinary concrete, high-performance concrete or UHPC (Kim et al. 2009, Wille et al. 2012, Pyo and El-Tawil, 2013).

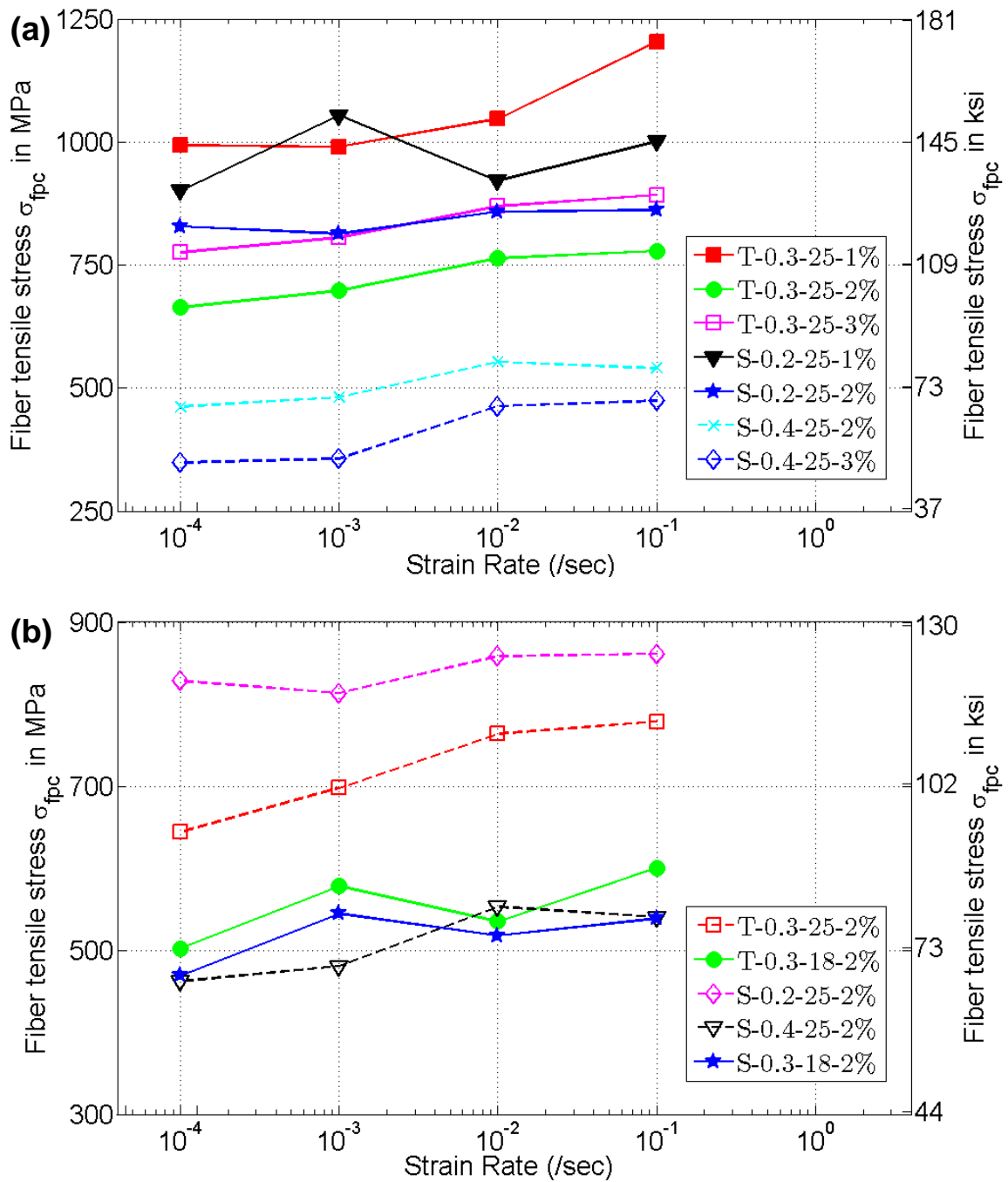


Figure 3.17. Rate effect on the fiber tensile stress of UHP-FRC: (a) specimens with different fiber volume fractions; (b) specimens with 2 % fiber volume fraction

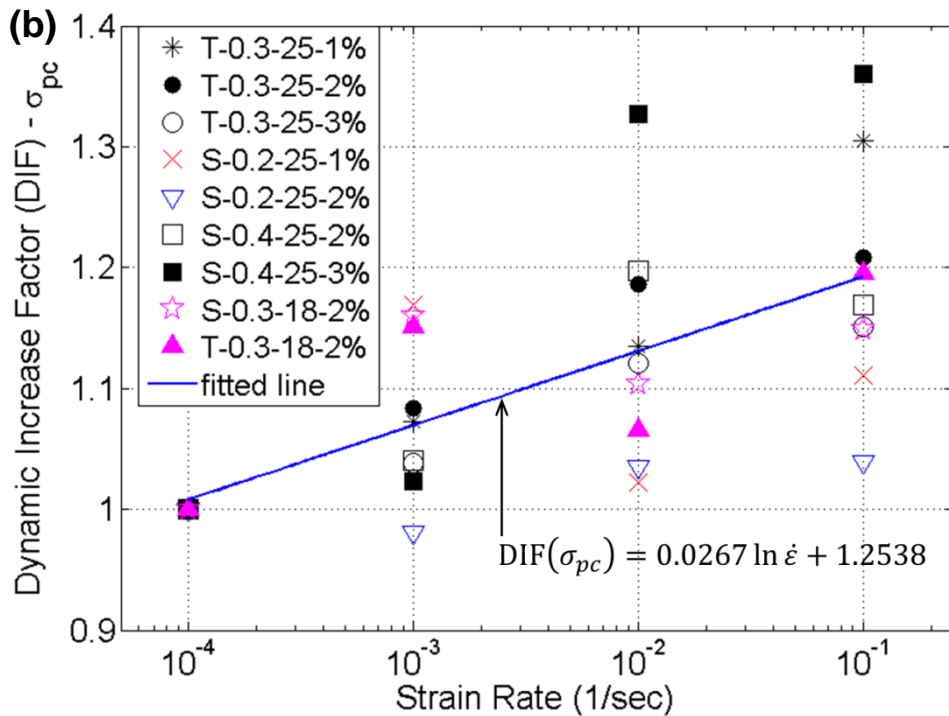
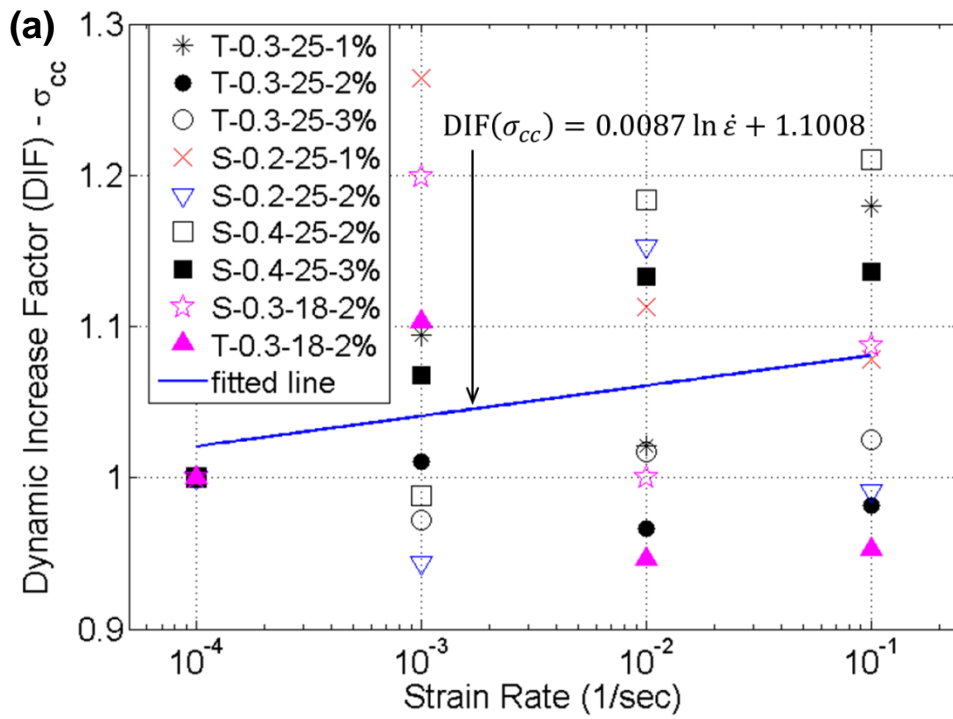


Figure 3.18. Dynamic increase factor (DIF) of UHP-FRC: (a) First cracking strength; (b) Post cracking strength; (c) Energy absorption capacity; (d) Strain capacity

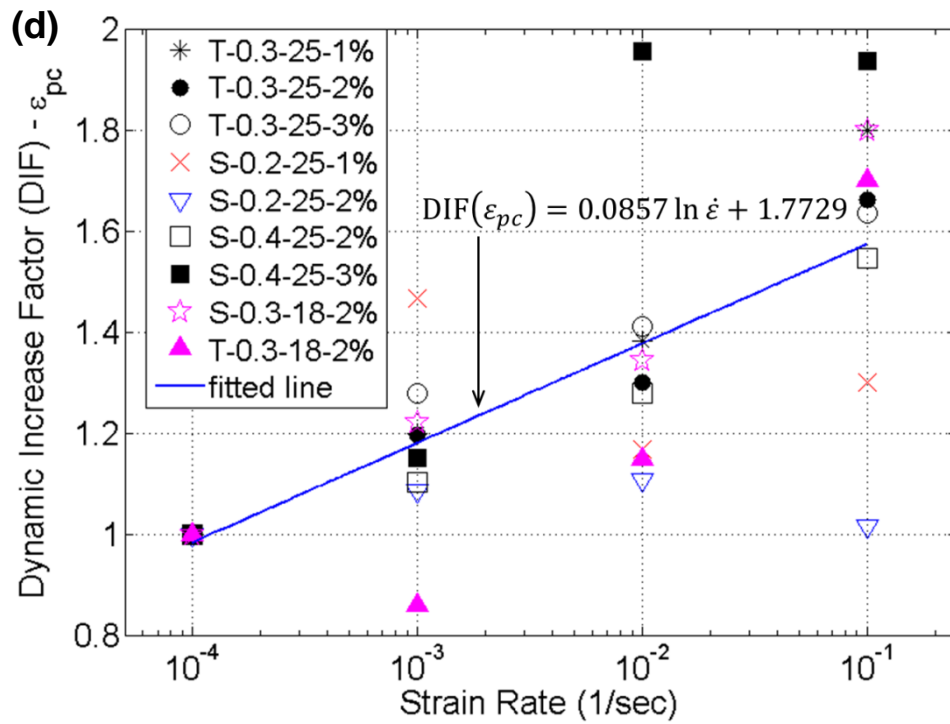
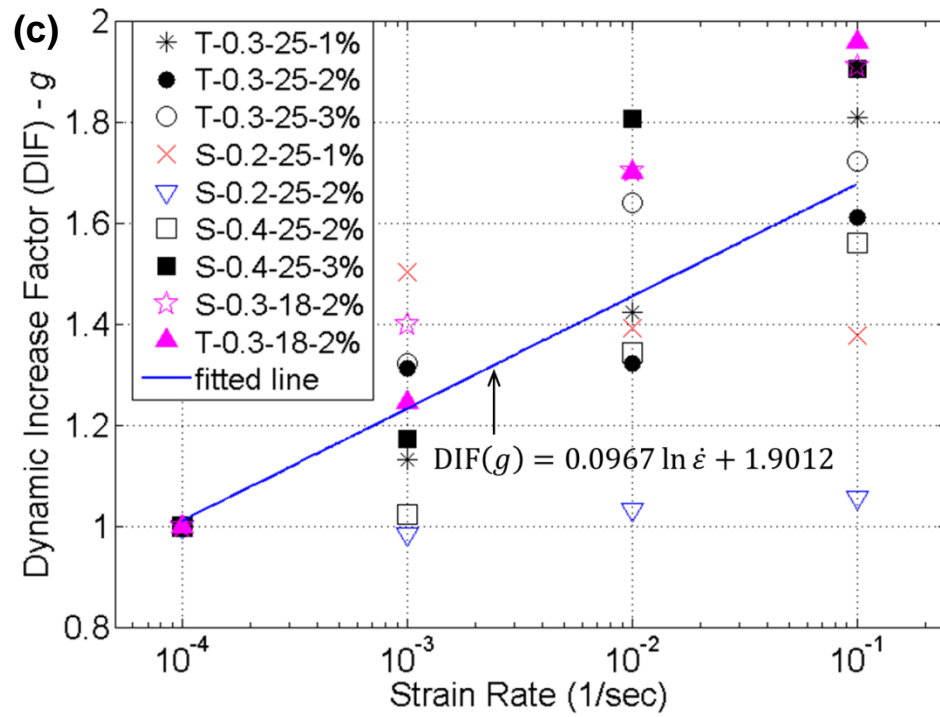


Figure 3.18. Continued

3.2.8 General Trends in the Test Data

Several general trends can be seen in the tension test results: (1) Tensile strength, energy absorption capacity and strain capacity all increase as fiber volume fraction increases for all fiber series under all strain rates; (2) While twisted fibers provided somewhat better performance than equivalent straight fibers, the mechanical anchorage advantage of twisted fibers over smooth fibers for post-cracking strength could be overcome by increasing fiber aspect ratio; (3) The fiber aspect ratio influences post cracking strength and fiber tensile stress, while fiber shape and length play important roles for strain capacity and energy absorption capacity; (4) Similar to other concretes, log-linear relationships of DIF of UHP-FRC are moderate and nearly linear at strain rates up to 0.1 /sec.; (5) Even though there is no rate sensitivity in the number of cracks (see Table 3.5), multiple cracks developed in all UHP-FRC specimens (see Figure 3.15) promoting strain hardening behavior of UHP-FRC under tension.

Twisted fibers lead to better overall mechanical performance than equivalent straight fibers, primarily because their mechanical anchorage mechanism is beneficial. However, the fact that the S-0.2-25 series shows similar mechanical performance to the T-0.3-25 series at the 2 % fiber content suggests that the mechanical anchorage advantage can be accounted for by changing fiber aspect ratio. This has practical significance because the price of straight fibers is generally cheaper than that of twisted fibers.

Unlike results reported for HPFRCC (e.g. in Yang and Li 2005 and Douglas and Billington 2011), the strain capacity does not decrease as strain rate increases. In fact, it almost doubles depending on fiber type and other mechanical properties such as tensile strength and energy absorption capacity also increase substantially as strain rate increases. These results indicate that UHP-FRC is particularly promising for applications that involve seismic, impact or blast.

3.3 CONCLUSIONS

The work reported on in this Chapter investigated the direct tensile behavior of UHP-FRC with five different steel fibers at strain rates ranging from quasi-static (0.0001 /sec) to seismic (0.1 /sec). The tests were conducted using a hydraulic servo-controlled testing machine and

results were evaluated in terms of first cracking strength, post-cracking strength, energy absorption capacity, strain capacity, elastic modulus, fiber tensile stress and number of cracks within the gage length. Log-linear relationships of DIF for first cracking strength, post-cracking strength, energy absorption capacity and strain capacity were presented based on the test data. The key observations and findings of this study can be summarized as follows:

- An increase in the fiber volume fraction led to increases in the composite tensile strength, energy absorption capacity, strain capacity and elastic modulus for all fiber tested under all strain rates. In contrast, the fiber tensile stress did not show a clear trend, likely because it was influenced by the fiber group effect.
- For the UHP-FRC tested in this study, the equivalent bond strength for the straight steel fibers seems to be of the same order as that of the twisted fibers.
- For similar equivalent bond strength, the observed post cracking strength of the composite varies linearly with the fiber reinforcing index ($V_f(l_f/d_f)$) as predicted theoretically from Equation (3.2).
- For similar equivalent bond, the observed energy absorption capacity up to peak load varies linearly with the product $V_f(l_f^2/d_f)$, as predicted from theory.
- For the range of strain rates used in this study (0.0001 to 0.1) both the post-cracking peak strength and the fracture energy up to peak load increase with an increase in strain rate. It was difficult to draw a firm conclusion regarding the rate sensitivity of the elastic modulus and the number of cracks because of observed large scatter in the test data.

The fact that UHP-FRC reported on in this Chapter shows substantial increases in energy absorption capacity as strain rate increases implies that the material is especially promising for blast and impact applications. The response of the material under high strain rates is investigated in Chapter 5.

CHAPTER 4

IMPACT TESTING OF STRAIN HARDENING CEMENTITIOUS COMPOSITES IN DIRECT TENSION USING RELEASED STRAIN ENERGY

Previous research by Kim et al. (2011) at the University of Michigan has shown that it is feasible to test concrete specimens under impact using suddenly released elastic strain energy. In this chapter, a refined set up is proposed to permit accurate and practical testing of ultra-high performance fiber reinforced concrete (UHP-FRC) specimens in direct tension, under high strain rate, capturing both hardening and post peak responses. A detailed finite element model is used to develop the test setup and proportion it. Among the advantages of the proposed setup is that it is relatively compact compared to existing test methods, can be easily adjusted to allow for a range of strain rates to be achieved, and permits the use of specimens that are similar in size and geometry to the specimens used in pseudo-static testing. The setup is used to successfully test UPH-FRC specimens at strain rates of 90 to 146 /sec. a discussion of the promise and limitations of the new testing scheme is provided.

4.1 BACKGROUND

As described in Chapter 2, the Split Hokinson Pressure Bar (SHPB) has been used for testing concrete at strain rates around 10^2 /sec. In spite of being used for more than a century, the SHPB has two key disadvantages when applied to cementitious materials: 1) it requires specimens with a completely different geometry compared to those used in pseudo static testing; and 2) it needs a large open space, e.g. for cementitious materials, a 75 mm thick SHPB can be 10 – 12 m long. The large size and cost of the SHPB coupled with the difficulty of fully assessing its results for concrete have hindered its wide spread use. As outlined in Section 2.3.2.3,

Kim et al. (2011) proposed an alternative to the SHPB for testing concrete, termed Strain Energy Impact Test System (SEITS). The device was subsequently modified and called Strain Energy Frame Impact Machine (SEFIM) by Tran and Kim (2012, 2013) and Kim et al. (2012). Both devices use energy bars and a coupler to store and suddenly release elastic energy for the purposes of rapidly loading concrete specimens. The energy-based devices are compact in size, cheap to build and permit testing of full scale specimens thereby alleviating the previously mentioned SHPB concerns. Details of these devices were provided in Sections 2.3.2.3.

4.2 MODIFIED SEFIM TO CAPTURE HARDENING AND POST PEAK RESPONSE

As mentioned in Section 2.3.2.3, the transmitter bar utilized in SEFIM, proposed by Tran and Kim (2012, 2013), is not long enough to fully capture the hardening and post peak response of strain hardening UHP-FRC tensile specimens. As discussed in detail later on, if the transmitter bar is short, the signal from the specimen reflects back too quickly, interfering with the ability to fully capture the incoming signal, which takes a relatively long time when substantial strain hardening is present. Hence, unlike conventional concrete or quasi-brittle materials, a minimum transmitter bar length is required to accommodate strain hardening concretes such as UHP-FRC.

In the conventional SHPB setup, researchers use a long transmitter bar to capture a clean stress signal, where there is no overlap between transmitted and reflected waves. For example, Reinhardt et al. (1986) used a 6.65 m transmitter bar and Cadoni et al. (2001) used a 2 m transmitter bar for quasi-brittle concrete. However, the length of the transmitter bar becomes important for a compact testing system, whose overall length is governed by the length of the transmitter bar.

The stress wave travel time can be visualized as shown in Figure 4.1. The time (t) between when the first incoming stress signal enters the strain gage (Figure 4.1a) and the reflected stress signal returns to the strain gage (Figure 4.1c) can be calculated as $t = 2(L - \delta)/C$, where δ denotes the strain gage location from the specimen. And wave speed in the transmitter bar, C , is

$$C = \sqrt{E/\rho} \quad (4.1)$$

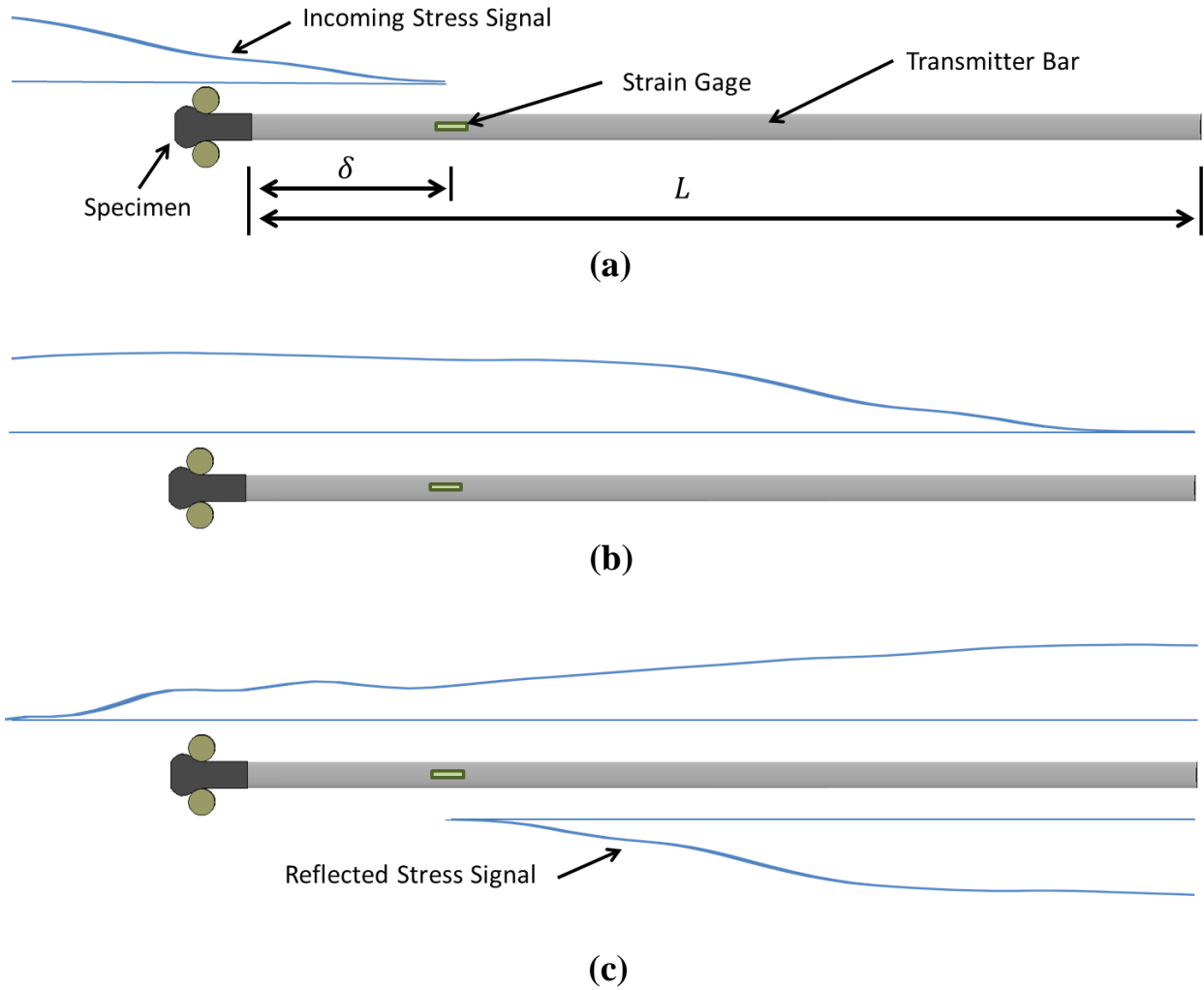


Figure 4.1. Stress signal travel: (a) approaching the strain gage; (b) reaching the end of the transmitter bar; (c) reflecting back to the strain gage

where, E and ρ are the elastic modulus and density of the transmitter bar, respectively. Table 4.1 shows the properties of three materials considered for the transmitter bar. The time duration (t') required to break the specimen is $t' = \bar{\epsilon}/\dot{\epsilon}$ for a constant strain rate, where $\bar{\epsilon}$ and $\dot{\epsilon}$ denote failure strain and strain rate, respectively. Here, the failure strain is defined as the strain below which the specimen can support stress, i.e. in the elastic, hardening and softening ranges. To capture the stress signal before signal overlapping, t must be longer than t' . Therefore, the minimum transmitter bar length (L) is

$$L \geq \frac{C \cdot \bar{\epsilon}}{2\dot{\epsilon}} + \delta \quad (4.2)$$

For example, for a specimen with a failure strain of 1 % at the strain rate of 35 /sec, $L = 0.95$ m if the transmitter bar is made of steel and $\delta = 0.2$ m.

Table 4.1. Transmitter bar material characteristics

Material	Elastic Modulus (GPa)	Density (kg/m ³)	Wave speed (m/sec)
Steel	200	8027	4992
Copper	117	8940	3617
Brass	96.5	8498	3370

Clearly, special attention must be paid to selecting a long enough transmitter bar or else the stress signal will be contaminated by unwanted reflections. With this consideration mind, a modified version of SEFIM (termed M-SEFIM, hereafter) is built as shown in Figure 4.2, with a substantially longer transmitter bar than used by Tran and Kim (2012, 2013). Like SEFIM, elastic energy is stored in the energy bars and released when the coupler breaks under increasing loads applied to the pull bar. Tensile load is transmitted from the energy bars to the UHP-FRC specimen via the load transfer member shown in Figure 4.3.

4.3 FE MODELING OF M-SEFIM

A detailed finite element model of the prototype system is developed as shown in Figure 4.3. The simulations are conducted using the commercial finite element program LS-DYNA within an explicit integration framework. Eight-node solid elements are used to model the system, and interpenetration between parts in the system is prevented by using the contact features in LS-DYNA. Tensioning of the pull bar is performed by applying displacement control at the end of the pull bar. An isotropic elastic-plastic material model, Mat-124: Mat_Plasticity_Compression_Tension, is used to model the behavior of UHP-FRC. The selected material model can represent separate stress versus plastic strain responses for compression and tension. While

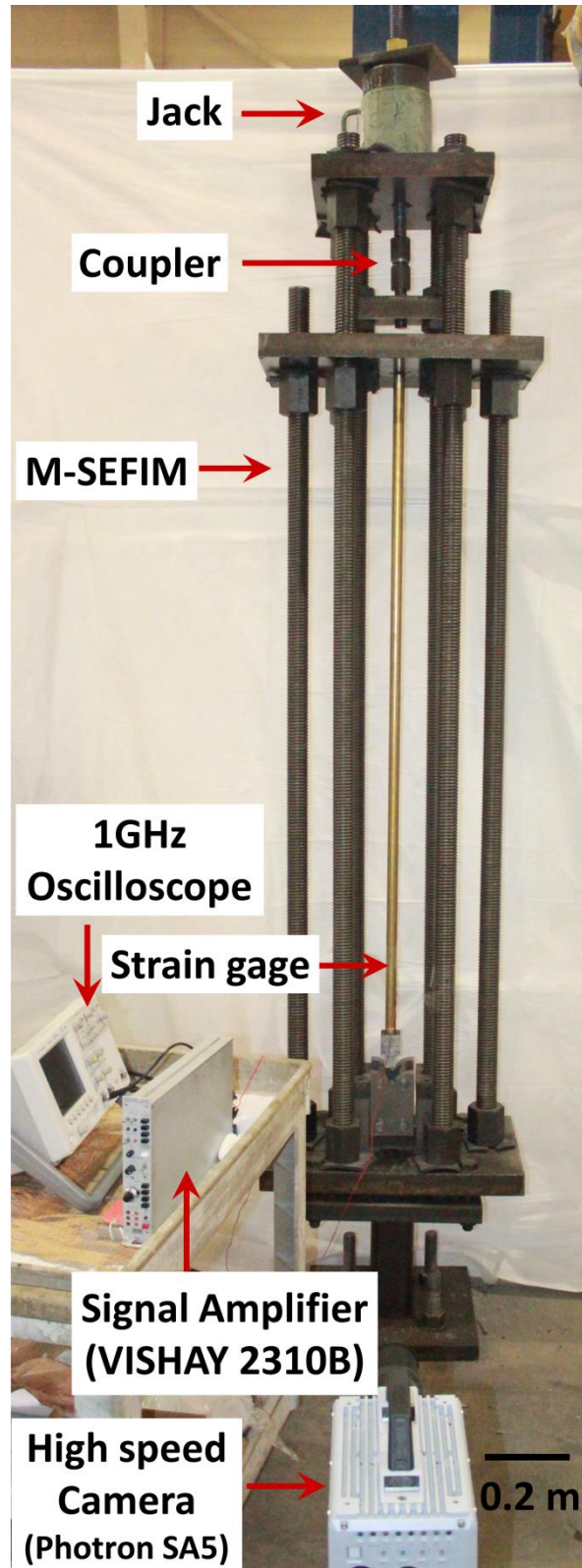


Figure 4.2. Prototype of the proposed impact testing system

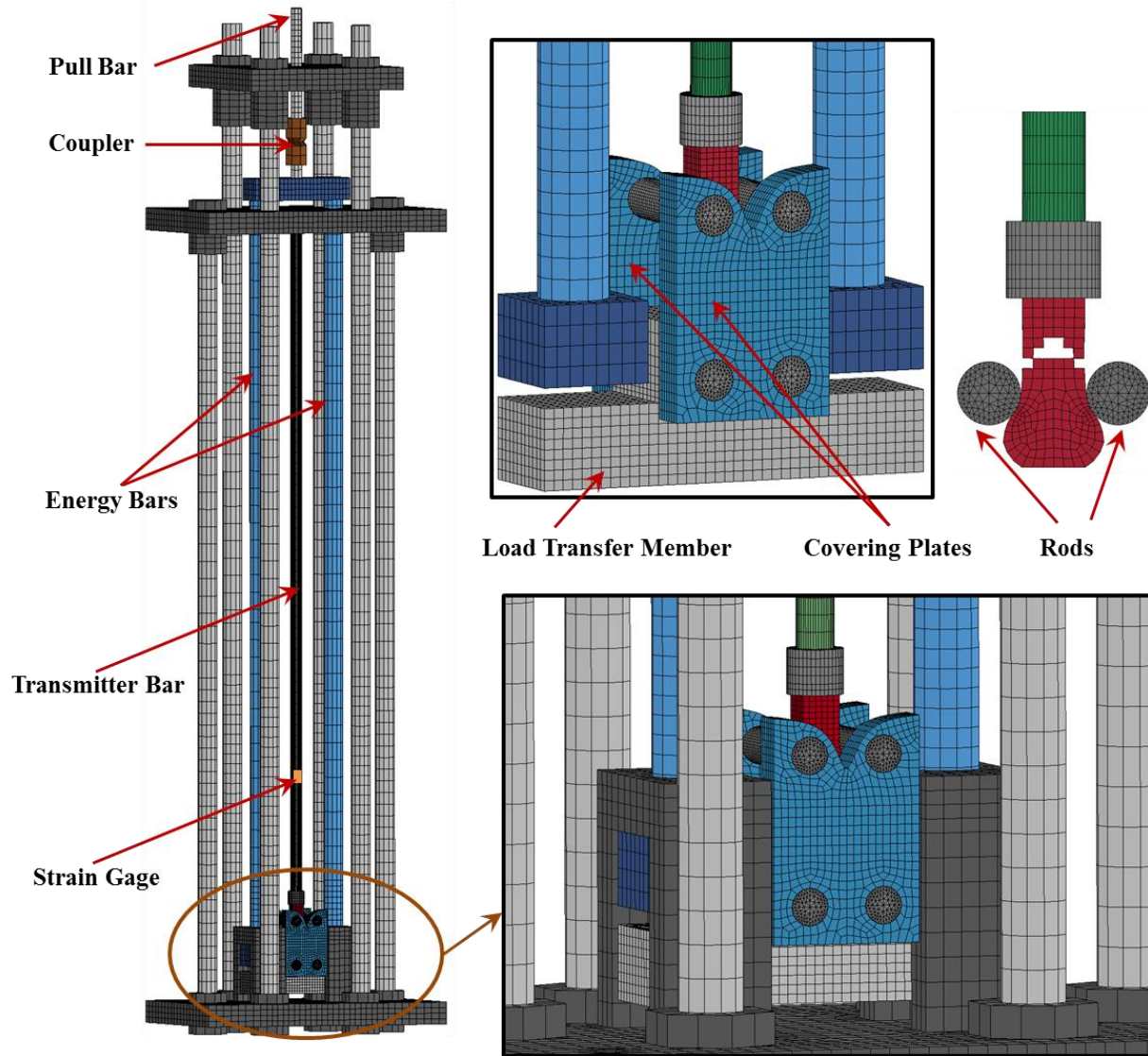


Figure 4.3. Finite element model of the proposed test setup

plasticity models, such as the one used, fail to fully represent the effect of confinement that is influential in compressively loaded concrete materials, they are deemed suitable here because the focus is primarily on uniaxial tensile material response, which is well represented by the selected modeling scheme. The dotted line in Figure 4.4a shows the computed tensile response, which compares reasonably to the measured uniaxial responses of UHP-FRC specimens as reported by Wille et al. (2012). The coupler is represented using Mat-3, which is a mixed isotropic-kinematic

hardening plasticity material model. Element erosion is activated when a pre-specified plastic strain is reached to represent fracture of the specimen and coupler.

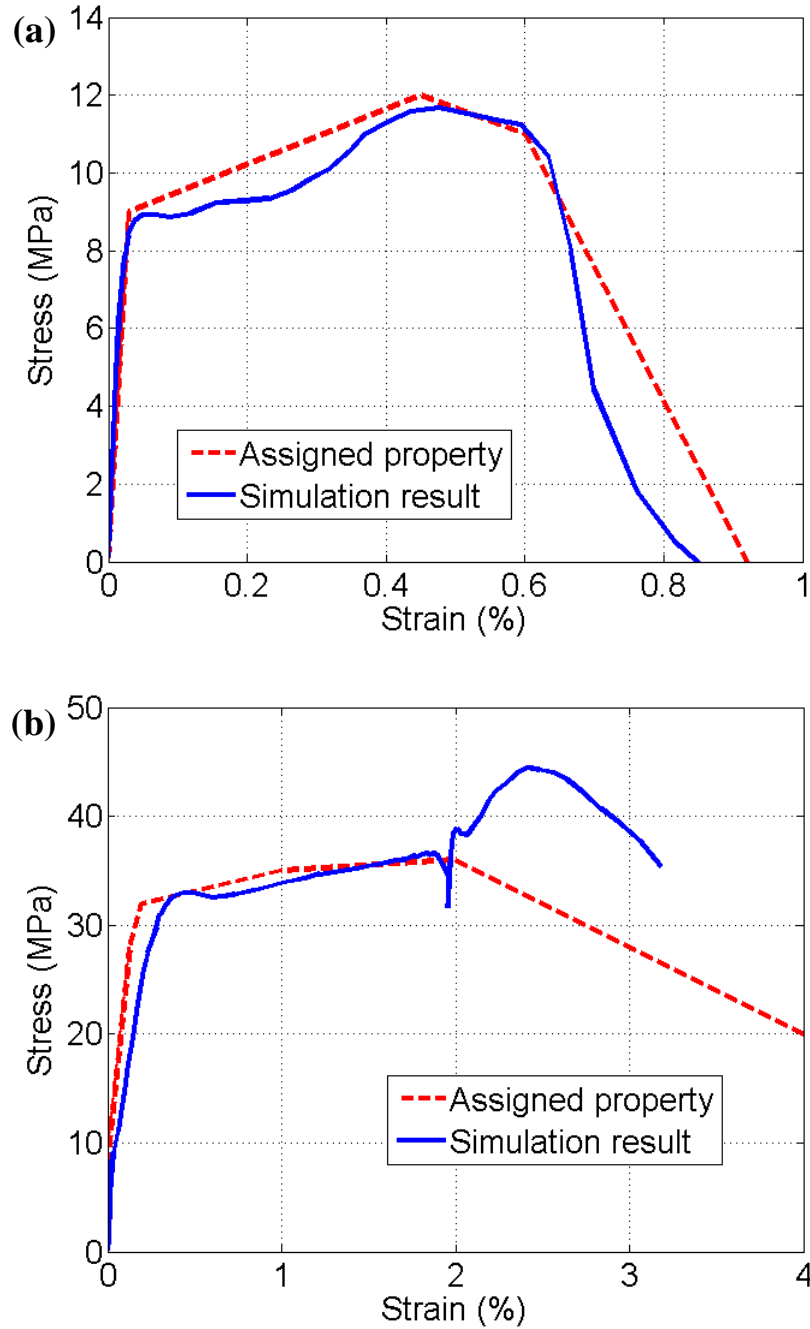


Figure 4.4. Stress-strain responses obtained from simulations: (a) material with small failure strain; (b) material with larger failure strain

4.4 PARAMETRIC SIMULATIONS

A series of parametric simulation studies of M-SEFIM were carried out to investigate the length and material of the transmitter bar. As calculated earlier, a 0.95 m long steel transmitter bar can theoretically capture the response of a specimen with a failure strain of 1 % at a strain rate of 35 /sec. Figure 4.4a shows a comparison between the assigned quasi-static stress-strain relation and the computed response of a specimen with a failure strain below 1 %. It should be noted that M-SEFIM setup with a 0.95 m long steel transmitter bar was used for this simulation as can be seen in Figure 4.5a. The specimen's response is computed as it would from the experiment, i.e. by measuring strain in the transmitter bar and converting that to stress, whereas strain is computed from the displacements of top and bottom points in the specimen's gage length. As shown in Figure 4.4a, the transmitter bar is clearly long enough to enable the full stress versus strain curve to be reasonably simulated. When a different material, with larger maximum strain is modeled, interference contaminates the signal as previously alluded to. This is clear from Figure 4.4b, where a material with a failure strain of $> 4 \%$ is simulated.

The material of the transmitter bar also plays an important role, because it influences stress wave speed through the bar. Selecting a material with slow wave speed would allow the transmitter bar to be smaller, reducing the size of the entire system. Brass and copper are feasible candidates for the transmitter bar. The wave speeds for those two materials are listed in Table 4.1, which shows that wave speed for both materials is about a third lower than steel.

Figure 4.6 shows another example in which a brass transmitter bar 1.55 m long (see Figure 4.3) is used instead of the 0.95 m steel bar in the previous example. As a result of using the longer brass bar, the new configuration is capable of capturing the stress strain response up to about 4 %. These observations suggest that the selected bar length and material are sufficient for capturing the required response of UHP-FRC specimens while keeping the device size as compact as possible.

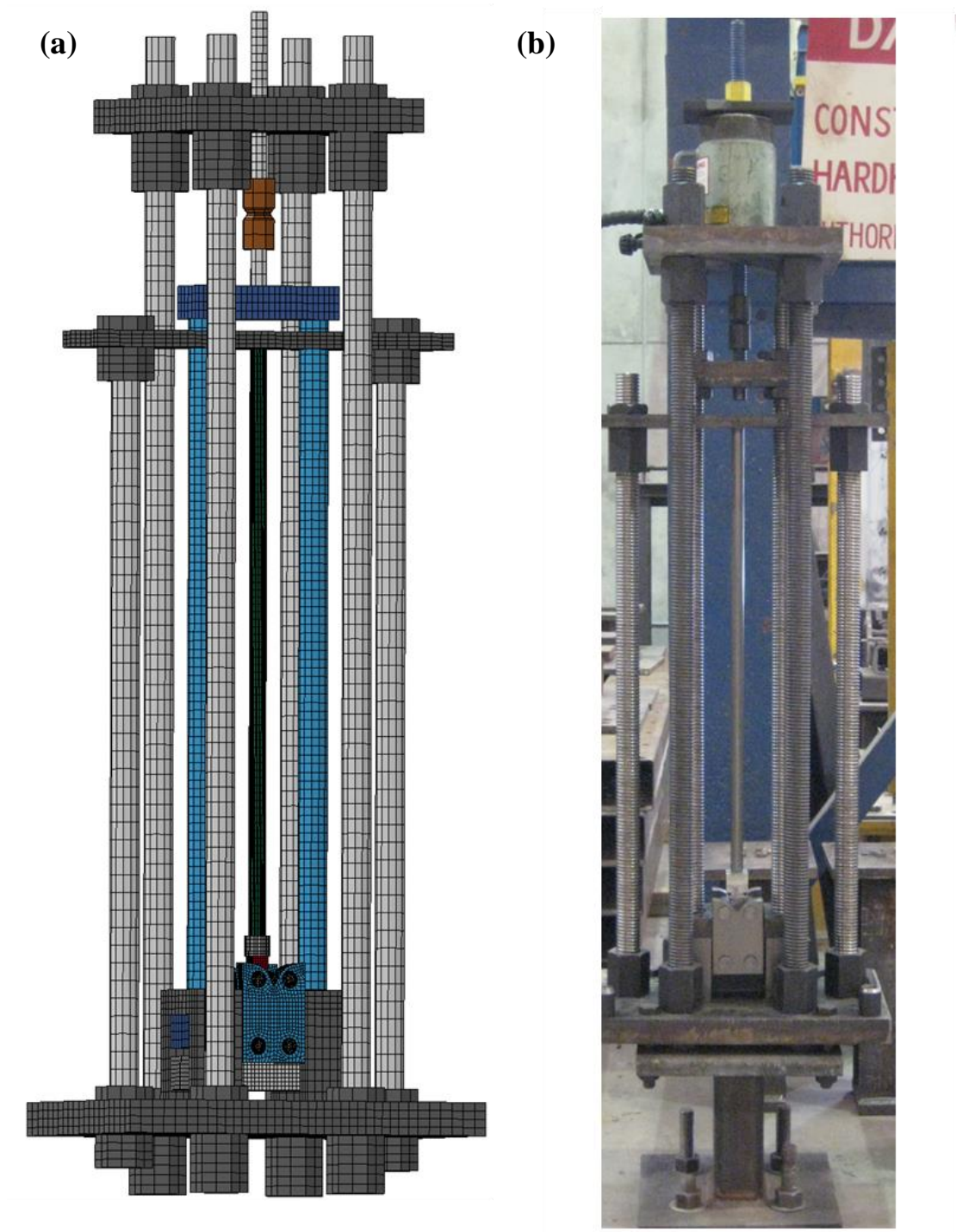


Figure 4.5. M-SEFIM with 0.95 m long steel transmitter bar: (a) finite element model; (b) installation of the proposed testing setup

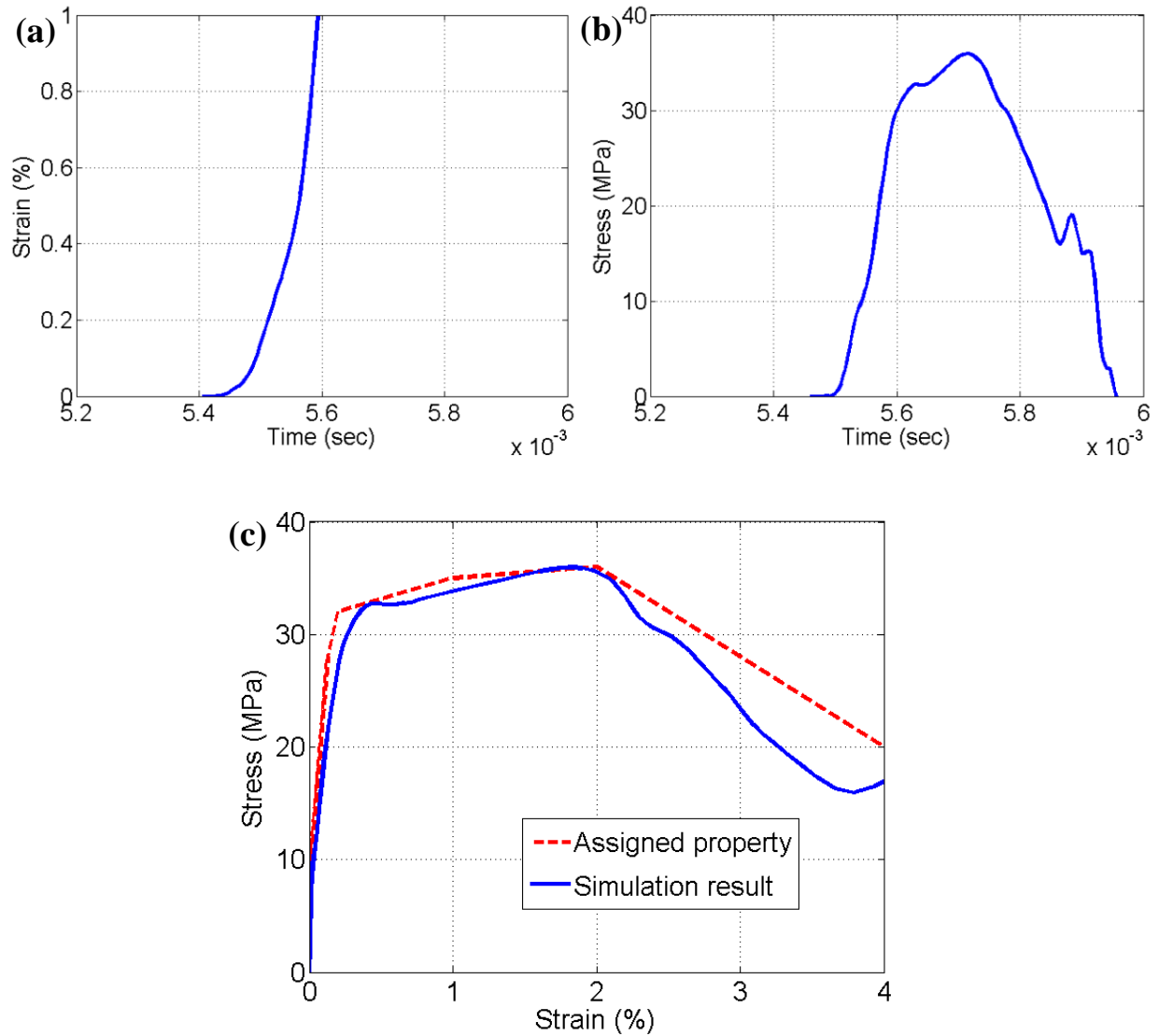


Figure 4.6. Computed material behavior from simulation results: (a) Strain data; (b) Stress data; (c) Stress-strain relationship in comparison with assigned constitutive model

4.5 SPECIMEN PREPARATION FOR IMPACT TESTING

UHP-FRC specimens for impact testing were fabricated as following. The same concrete molds were used to cast the UHP-FRC specimens discussed in Chapter 3 (see Figure 4.7a). After 28 days of water curing, the UHP-FRC specimens were left to dry in the laboratory environment for at least 24 hours (see Figure 4.7b). UHP-FRC specimens were then cut to the desired

specimen length using a diamond saw (see Figure 4.7c). The cut UHP-FRC specimens were glued into an aluminum housing using epoxy glue (Sikadur® 32, Hi-Mod), and dried for at least 24 hours. To apply the Digital Image Correlation (DIC) technique for strain measurement in the specimens (see Section 4.6), random speckle patterns were applied manually to all specimens. First, white paint (RUST-OLEUM Flat Protective Enamel) was sprayed on the specimen as can be seen Figure 4.8a. After the white paint dried, random speckle patterns were sprayed using black paint (RUST-OLEUM Flat Protective Enamel). Figure 4.8b shows an example of a prepared UHP-FRC specimen. The resulting specimen (within its aluminum housing) can then be screwed into the transmitter bar (see Figure 4.9) in preparation for impact testing.

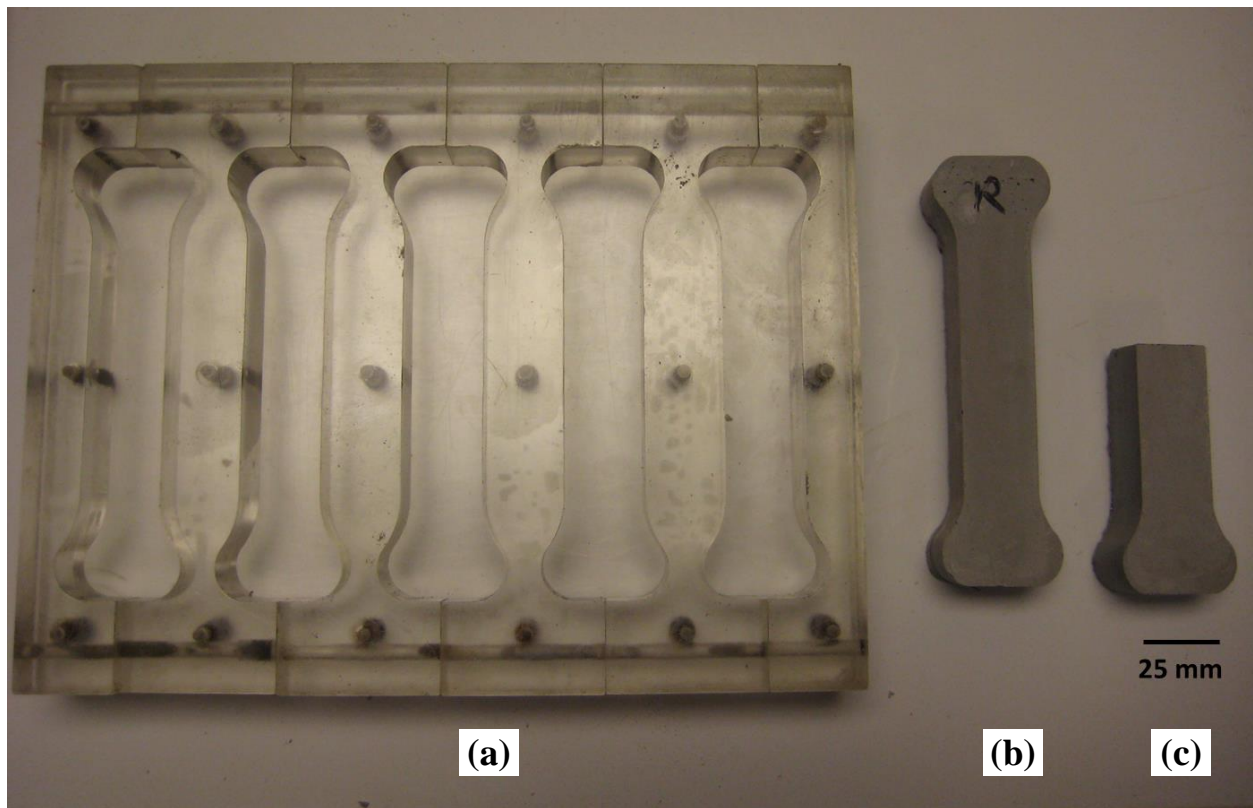


Figure 4.7. (a) UHP-FRC mold for tension testing; (b) A UHP-FRC specimen for low strain rates testing used in Chapter 3; (c) A UHP-FRC specimen cut to desired length

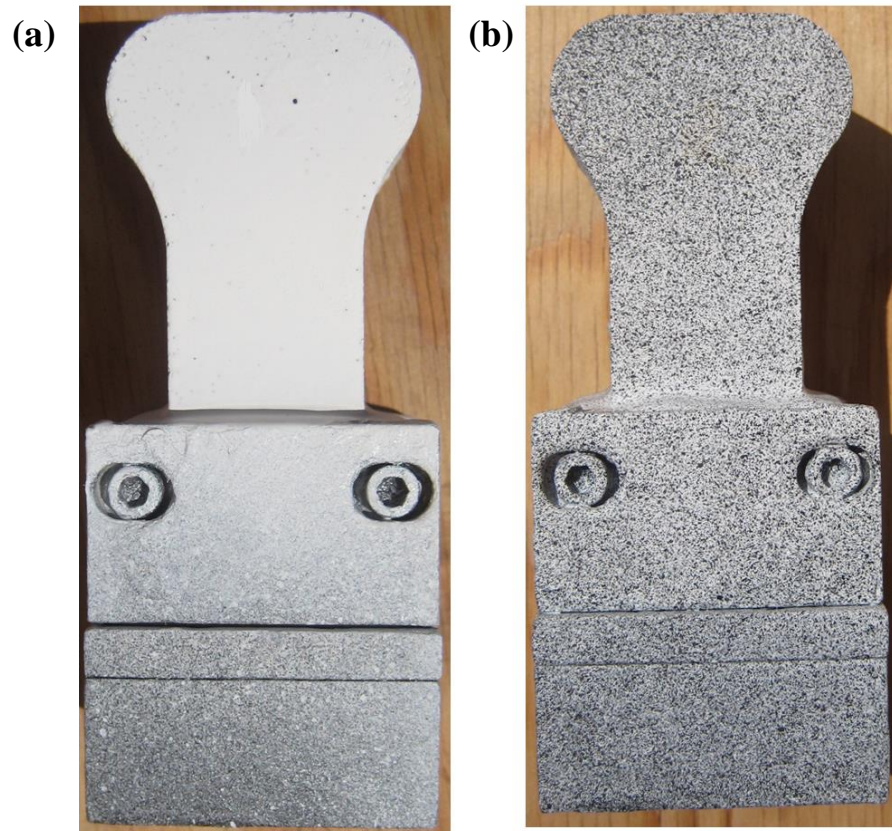


Figure 4.8. Example of speckle patterns in this study: (a) specimen sprayed with white paint; (b) random speckle patterns with black paint

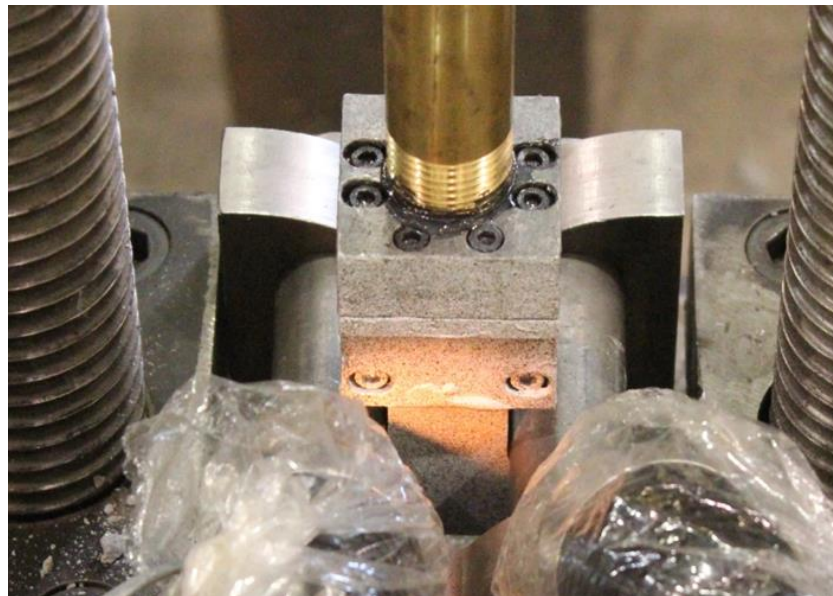


Figure 4.9. Connection between the transmitter bar and aluminum housing

4.6 STRAIN MEASUREMENT UNDER IMPACT LOADING

Strain in M-SEFIM is measured using DIC. DIC, proposed at the beginning of the 1980s (Peters and Ranson 1982; Sutton et al. 1983), is an optical, non-contact technique to measure deformation or movement of the surface of a specimen. The method requires application of random speckle patterns to the specimen surface by spraying it with white and black paints. Digital images of the specimen surface, obtained during testing, are processed to track unique speckle patterns as the specimen deforms. DIC can calculate full-field displacement on the surface of a specimen by tracking a non-uniform, random, high contrast pattern on the sample surface.

The DIC technique is a practical and effective tool that is widely accepted and commonly used in the field of experimental solid mechanics (Pan et al. 2009). In contrast to traditional measurement systems, e.g., strain gage and Linear Variable Differential Transformer (LVDT), the DIC technique provides domain-level information, not just local information. 2-D DIC can provide planar data with one camera, while 3-D DIC can measure 3-D strain fields when two synchronized cameras are used, although only a planar version of the technique is used herein. Pan et al. (2009) and Sutton et al. (2009) provide further details about the method and its application.

The DIC technique does not require an intrinsic length or time scale. As a result, it can be applied at length scales ranging from micro- to meter-scale depending upon the magnification level employed. For example, Verhulp et al. (2004) used the 3-D DIC technique for strain measurements in open-cell structures while Yoneyama et al. (2007) applied it to measure bridge deflections. Furthermore, because there is no time scale, the technique can be applied to situations that range from micro seconds to hours. In this research study, the DIC technique is used to measure rapidly varying strain fields in the UHP-FRC specimens. However, it should be noted that there are some important challenges when DIC technique is used for high speed applications. For example, since high speed cameras are a compromise between frame rate and resolution, the resolution may not sufficient for accurate strain measurement under high speed testing (Reu and Miller 2008).

For ductile metal specimens, strain in a gage length can be computed by averaging strain data at each speckle point. However, multiple cracking in the UHP-FRC specimen (see Figure 4.10) causes speckles to flake off around cracks, which contaminates the results as shown in Figure 4.11a. Therefore, strain is computed from displacements of the top and bottom points of the gage length. Figure 4.11a shows comparisons between strain readings obtained both ways, while Figure 4.11c shows corresponding stress strain relations computed using stress data in Figure 4.11b. It is clear that the averaging technique creates spurious results.

The stress versus strain relationship is only valid prior to crack localization and assuming a smeared cracking effect for the multiple cracking phase. Upon localization, the material's softening behavior is better characterized by a stress versus crack opening relationship. Nevertheless, including the softening portion in the stress strain relationship is commonly used by others, albeit with a length scale to enable continued use of the smeared cracking representation.

The strain rate in the test specimen can be calculated as (Gray 2000)

$$\dot{\epsilon} = \frac{\dot{u}_1 - \dot{u}_2}{l_s} \quad (4.3)$$

where l_s is gage length of the specimen, and \dot{u}_1 and \dot{u}_2 are the velocities at both ends of the gage length. The strain rate is not constant throughout the test because of the dynamic nature of the experiment. Therefore, an average strain rate is calculated and used for the duration of loading. Figure 4.12a shows an example of histories of stress, strain rate and strain during an impact test using M-SEFIM with 1.55 m long brass transmitter bar, which are similar in nature to those computed for SHPB data, e.g., Gilat et al. (2002). The average strain rate for the test shown in Figure 4.12a is 126 /sec. Figure 4.12b shows the stress-strain relations corresponding to the example in Figure 4.12a.

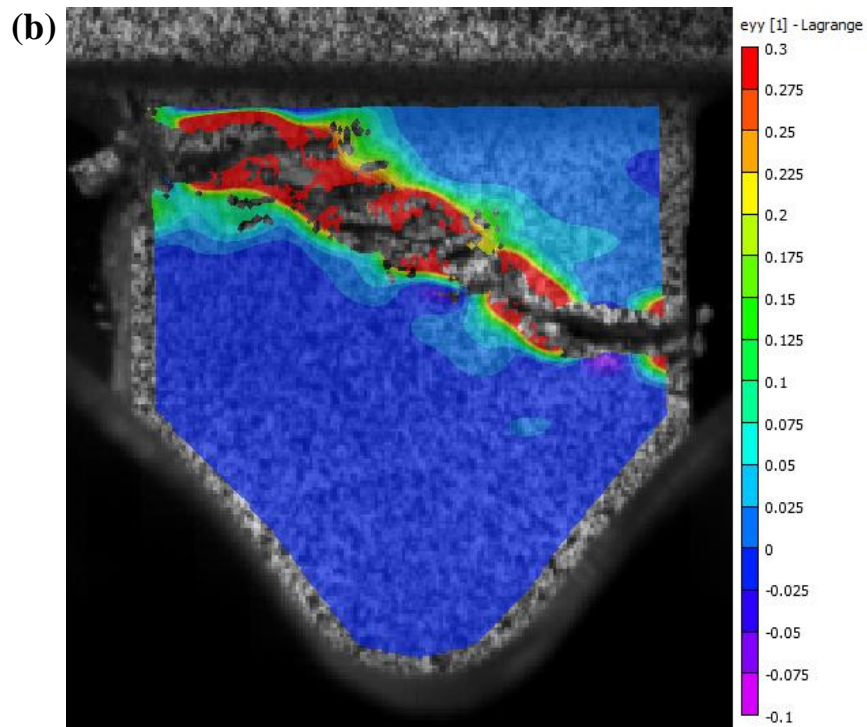
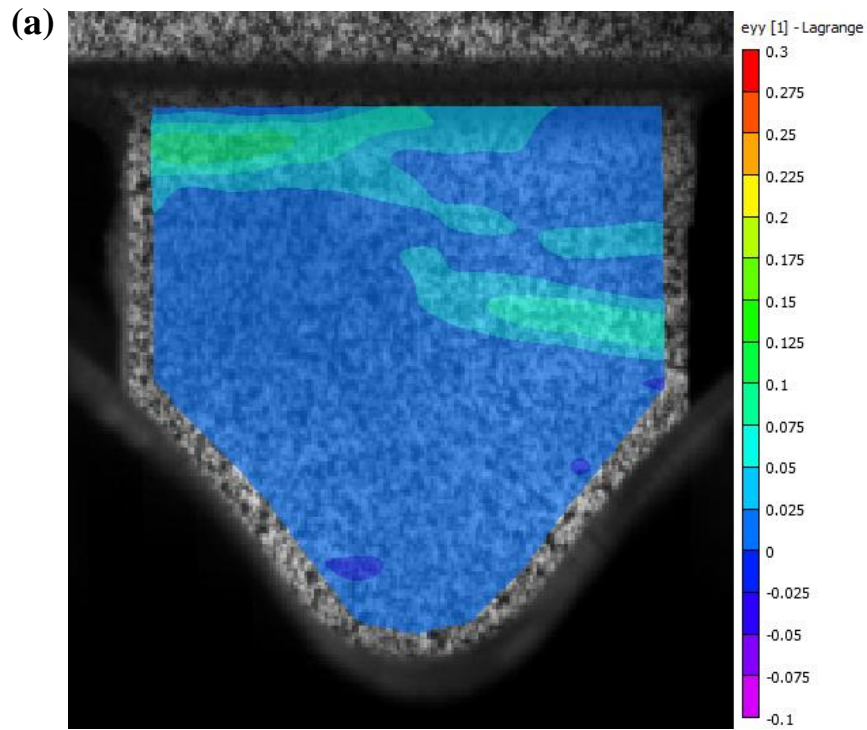


Figure 4.10. Example of strain field computed using the DIC technique: (a) before major crack development; (b) after crack localization

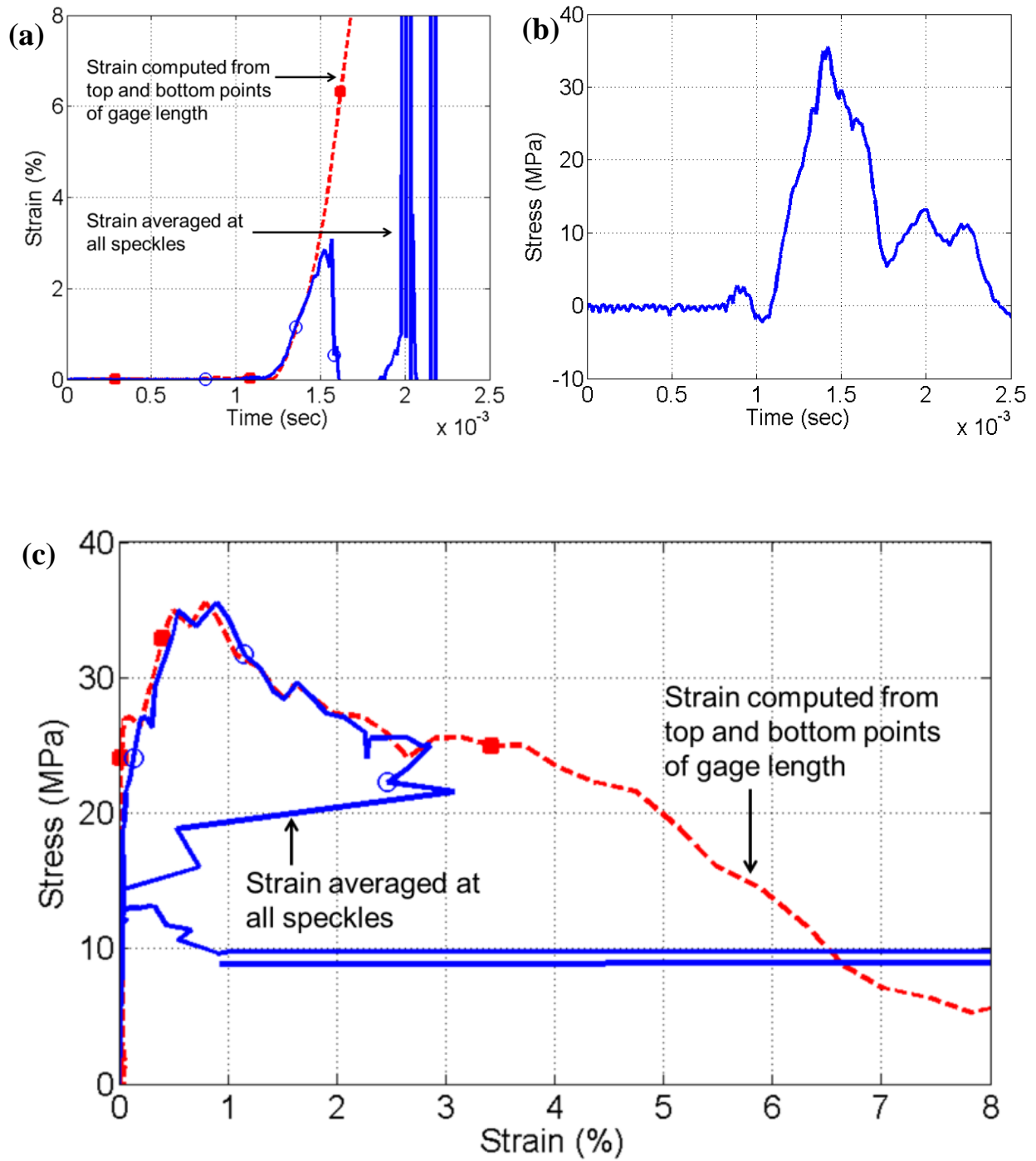


Figure 4.11. Example of DIC results: (a) comparison of strain calculations methods; (b) stress data; (c) comparison of stress-strain relationships obtained by various methods

4.7 EXERCISING THE M-SEFIM SETUP

The prototype M-SEFIM device is used to test a number of UHP-FRC specimens, the details of which are discussed in Chapter 5. Stress within the specimen is measured via a strain gage attached to the transmitter bar. The stress wave is amplified and conditioned using a signal amplifier (VISHAY 2310B) and then recorded using an oscilloscope. A high speed camera (Photron SA5) and the DIC technique, as described above, are employed to accurately measure strain in the specimen. The high speed camera is run at 75,000 frames per second with a resolution of 320×264 pixels.

When used with the shorter (0.95 m) steel transmitter bar, the results are contaminated by the reflected signal as seen in the simulations studies. This can be observed in Figure 4.13, which shows actual experimental results using the M-SEFIM setup in Figure 4.5b. As shown in Figure 4.14, the results are more meaningful when the longer brass transmitter bar is used instead, eliminating signal interference. The high strain rate experimental results shown in Figure 4.14 are the average of three tests, for which the average strain rate is 118 /sec. For comparison, Figure 4.14 shows corresponding experimental results for identical specimens tested at lower strain rates, ranging from 0.1 to 0.0001 /sec using a hydraulic servo-controlled testing machine (see Chapter 3). The high strain rate curves have distinctive hardening and then softening responses, very much like the low strain curves. However, comparing the slower rate data with high strain rate data, it is clear that there are substantial dynamic effects, specifically a marked increase in strength combined with a large increase in energy dissipation ability.

Figure 4.15 shows a failed specimen after testing. The specimens are made using mixes described in Chapter 3, which also lists material properties for the fibers. Figure 4.16 shows failure patterns of UHP-FRC specimens subjected to impact testing as recorded using the high speed camera. As can be seen from the figure, multiple cracking developed in most specimens.

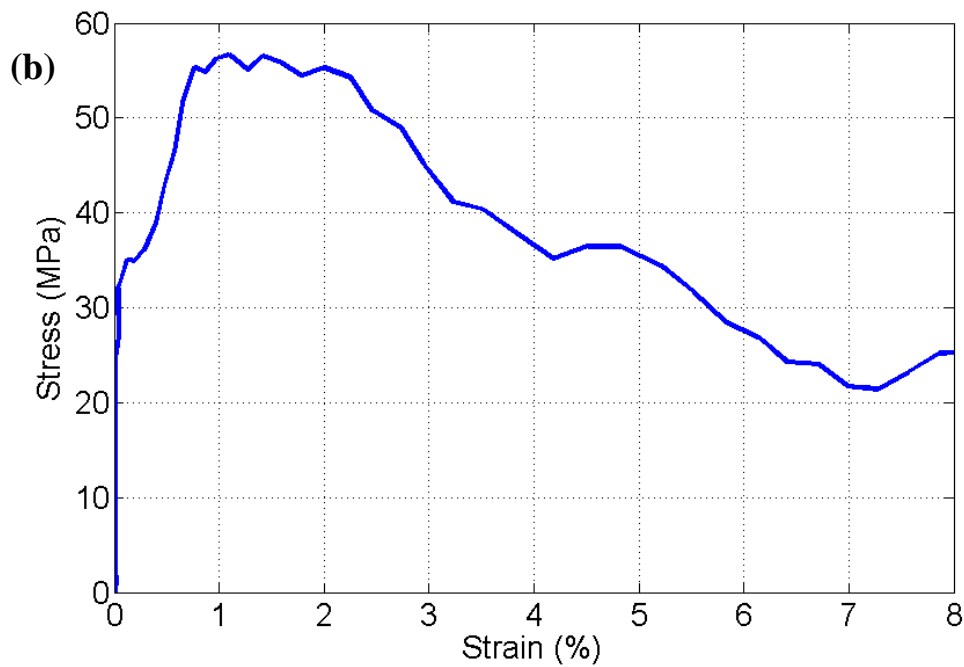
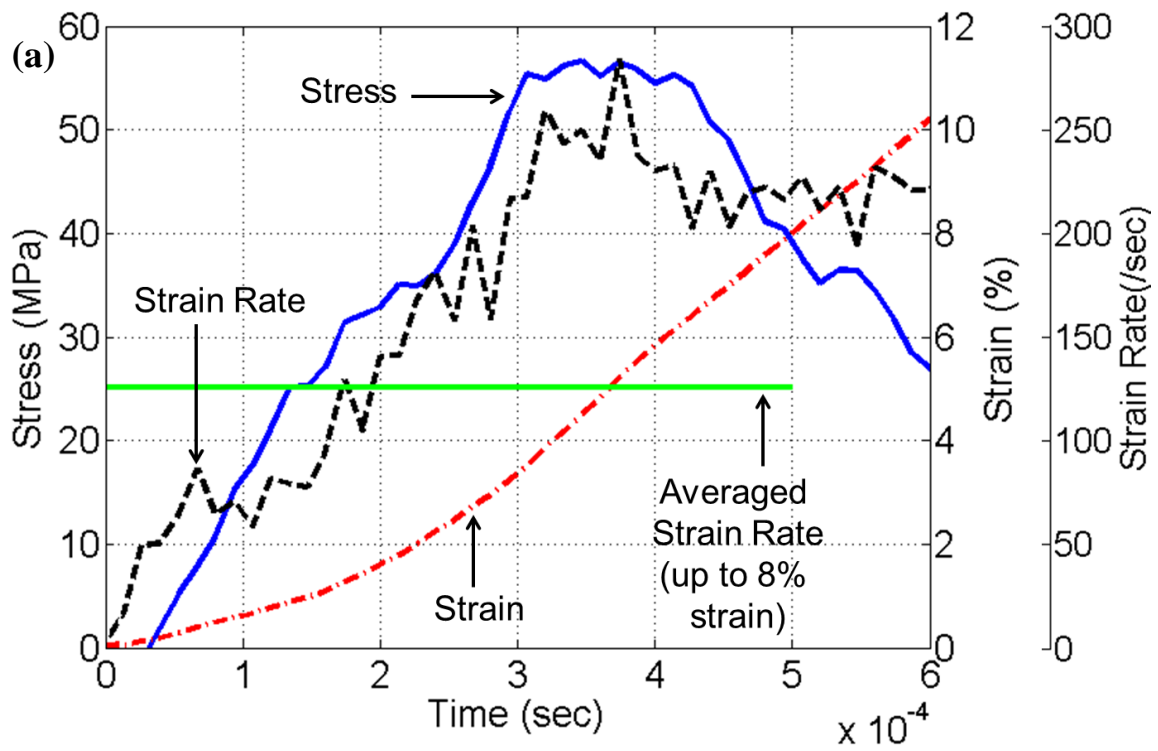


Figure 4.12. (a) Stress, strain rate and strain during an impact test; (b) Corresponding stress-strain relationship obtained from the data

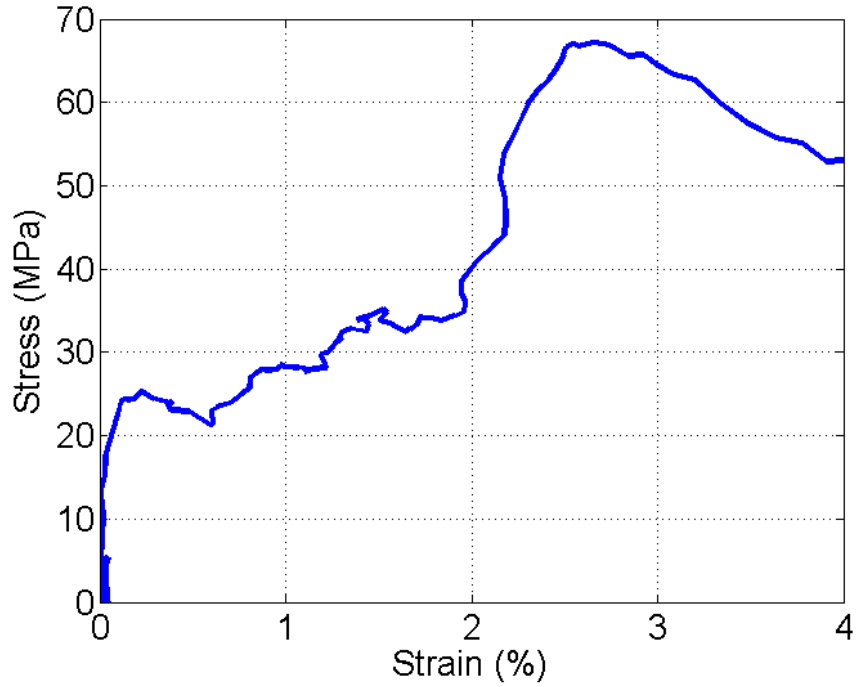


Figure 4.13. Experimentally obtained stress-strain relationship contaminated by signal interference

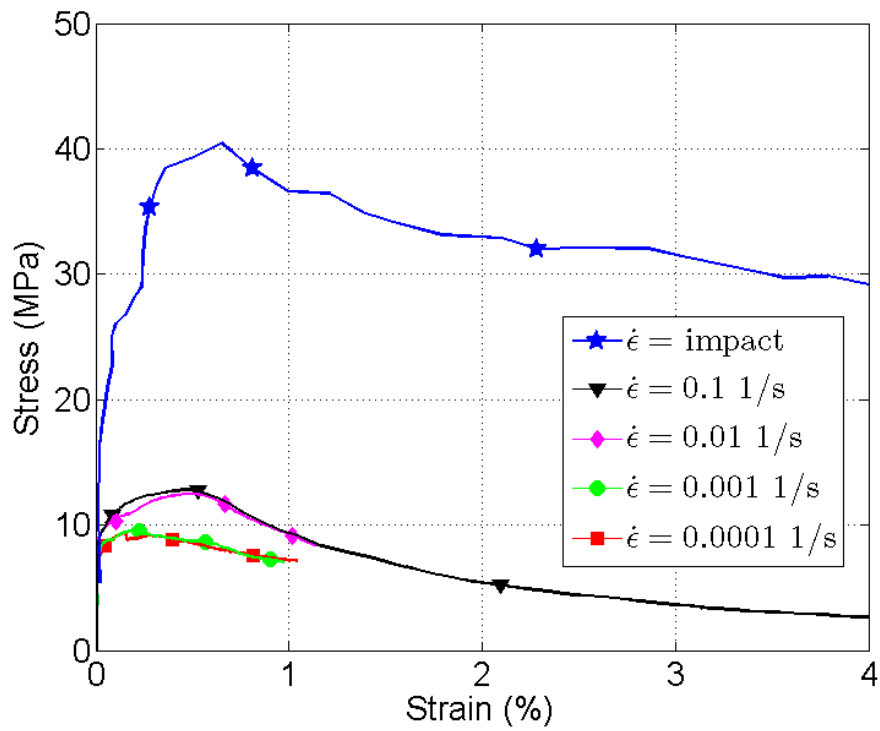


Figure 4.14. Experimentally obtained stress-strain responses under different strain rates for direct tension tests

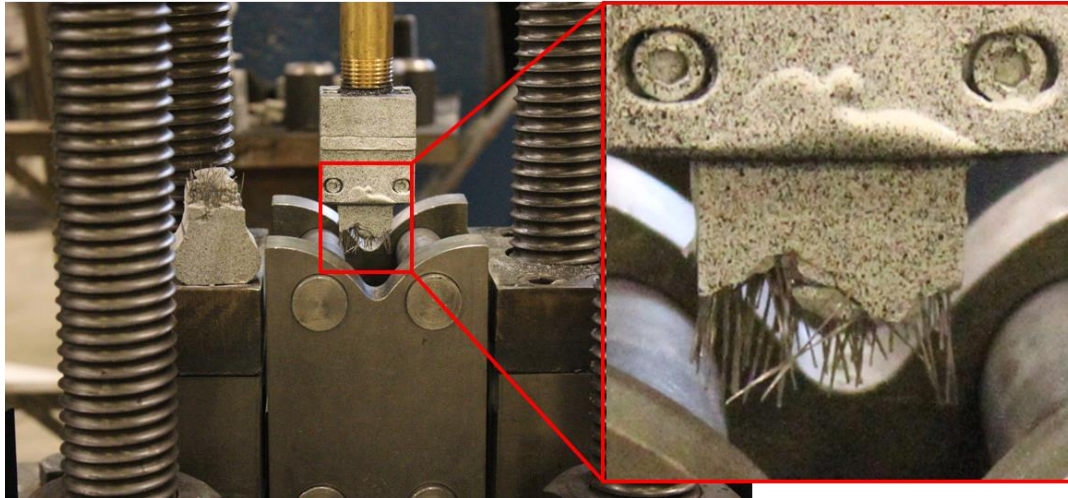
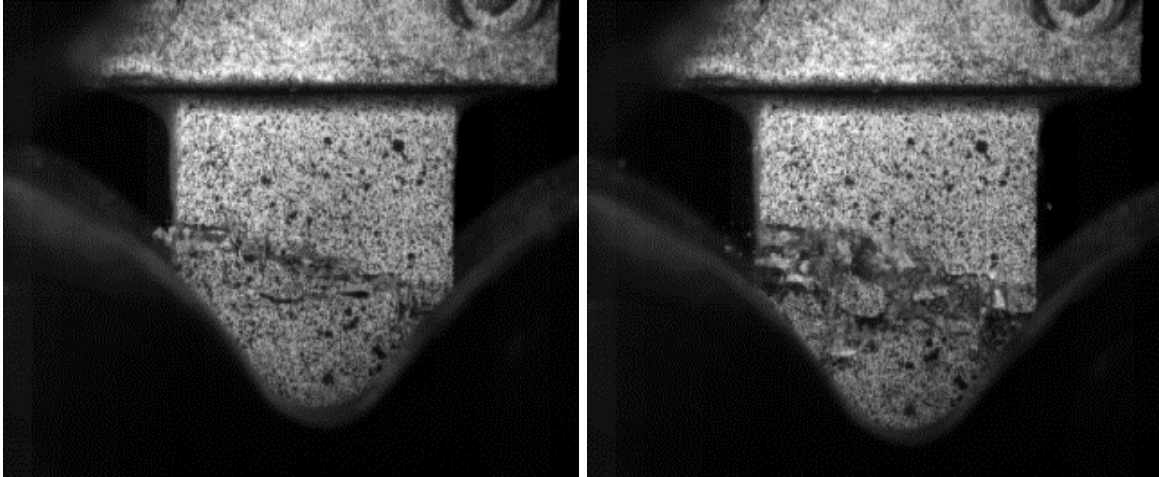
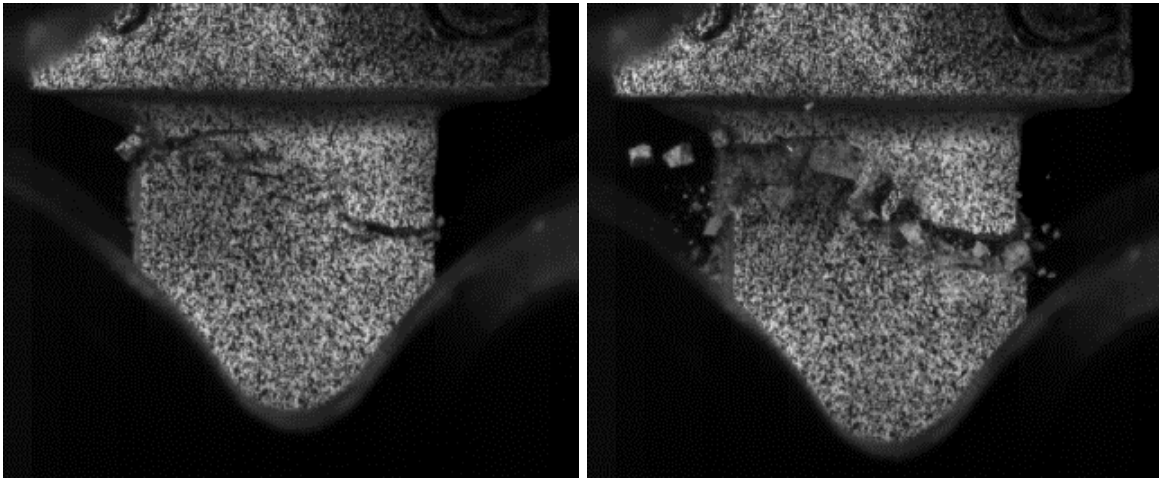


Figure 4.15. Failed specimen after testing

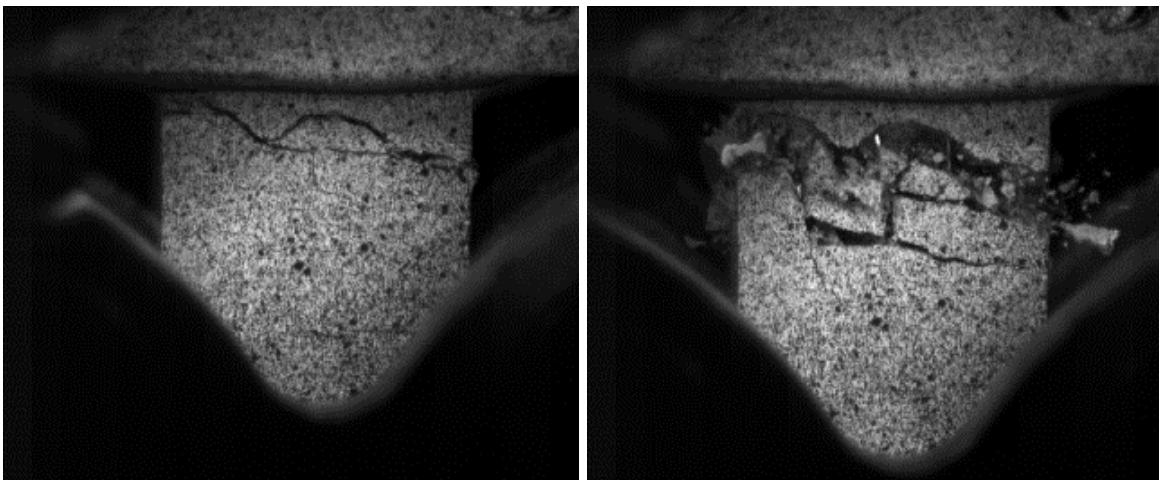
In addition, the effect of coupler net area on strain rate was investigated. Three types of couplers with different net areas are used, termed Type 1, 2 and 3. Type 2 and 3 couplers have net areas that are 86 % and 183 % larger, respectively, than Type 1, as can be seen in Figure 4.17. Figure 4.18 shows actual couplers and their cross sections after tests. Figure 4.19 shows how the applied strain rate can be changed by changing coupler characteristics. The figure shows the relationship between strain rate and coupler type using both simulation and experimental results. Simulation results indicate that strain rates attainable with Type 2 and 3 couplers increase when compared with those obtained from Type 1 by 41 % and 150 %, respectively. Twenty two experiments (discussed in Chapter 5) with Type 3 couplers suggest that the experimental results bound the simulation data as shown in Figure 4.19.



(a)

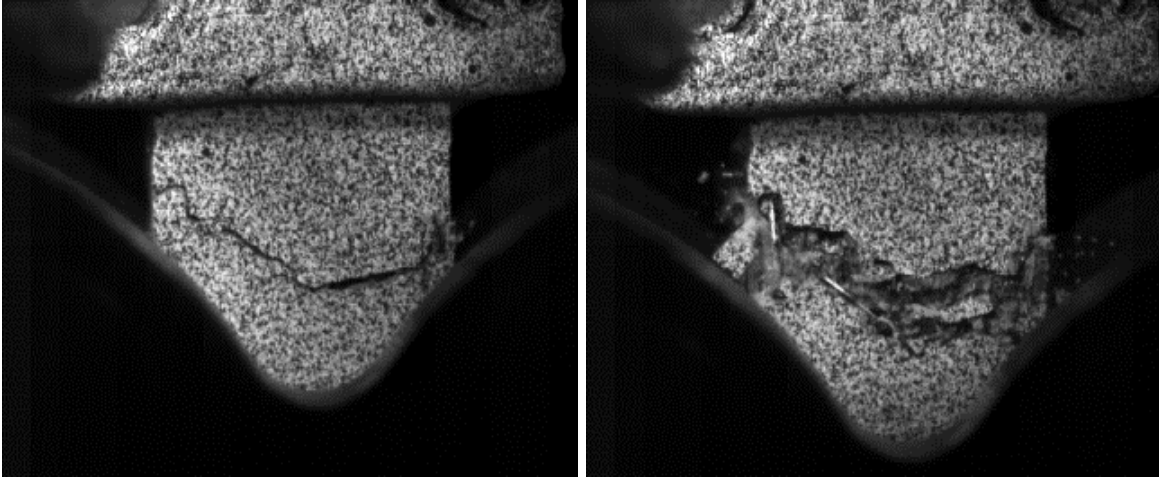


(b)

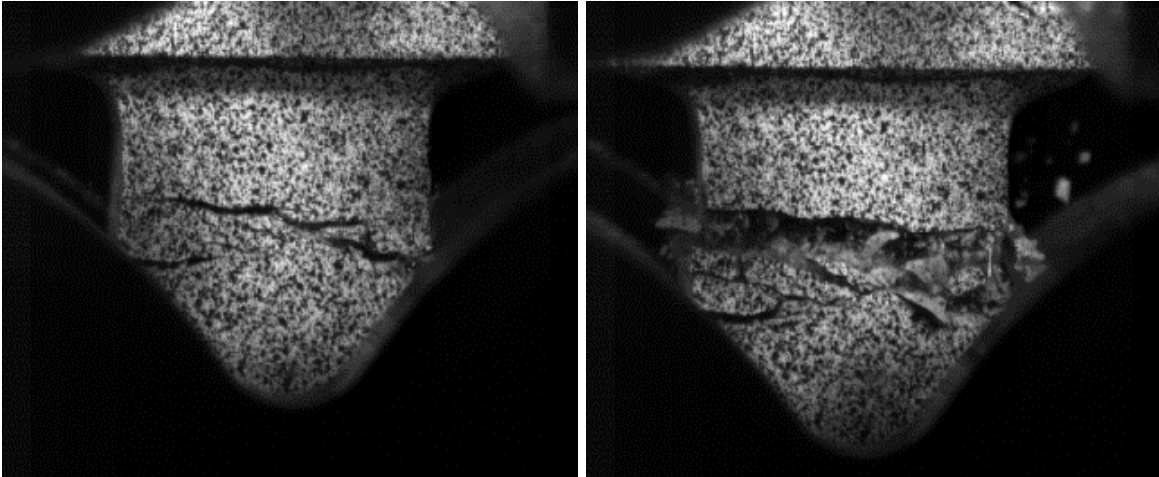


(c)

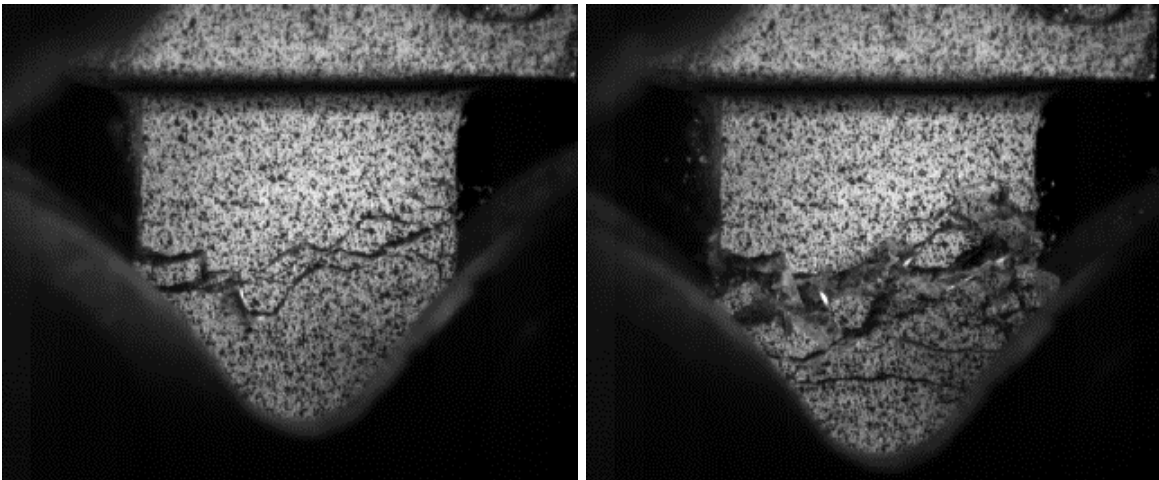
Figure 4.16. Examples of failed specimens: (a) S-0.2-25-1%; (b) S-0.2-25-2%; (c) S-0.4-25-2%; (d) S-0.4-25-3%; (e) T-0.3-25-1%; (f) T-0.3-25-2%; (g) T-0.3-25-3%



(d)

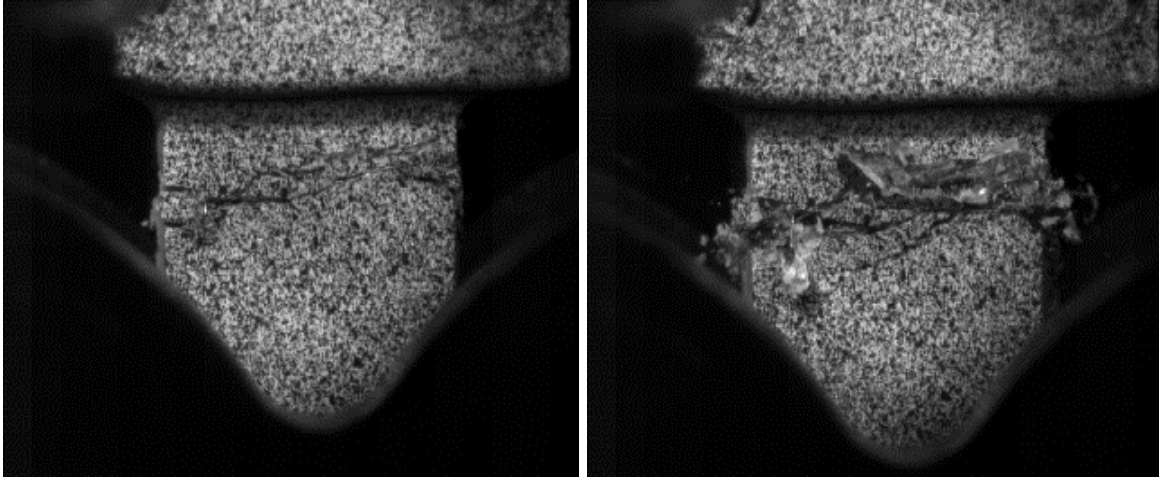


(e)



(f)

Figure 4.16. continued



(g)

Figure 4.16. continued

4.8 LIMITATIONS AND POTENTIAL OF M-SEFIM

Despite the promising results presented in this Chapter, M-SEFIM has a few limitations that should be enumerated. First, while the system itself is cheap to build, the electronics needed to obtain high quality measurements are expensive at the present time. Unlike the SHPB, which uses an incident bar to measure strain in the specimen, M-SEFIM requires the use of a high speed camera. High speed cameras are currently expensive, but their price is rapidly declining as the technology matures. Unlike SHPB, however, the new device is particularly suitable for tensile testing and is easily reconfigurable to enable compression testing. Various strain rates can be conveniently achieved by changing coupler characteristics. Yet, use of such couplers represents an added cost to each experiment. Each coupler costs about \$30 at present, but this cost can be alleviated by developing a reusable release mechanism, making the device truly customizable at low cost.

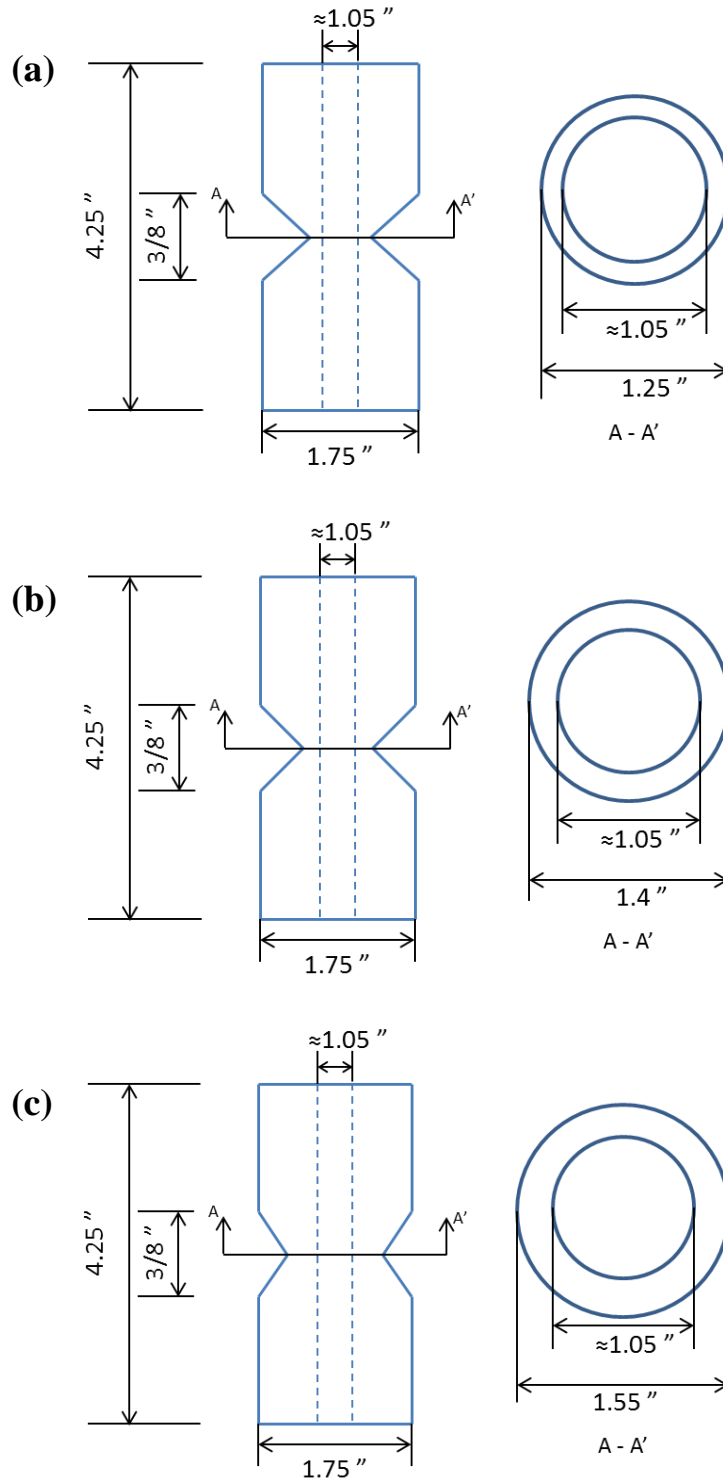
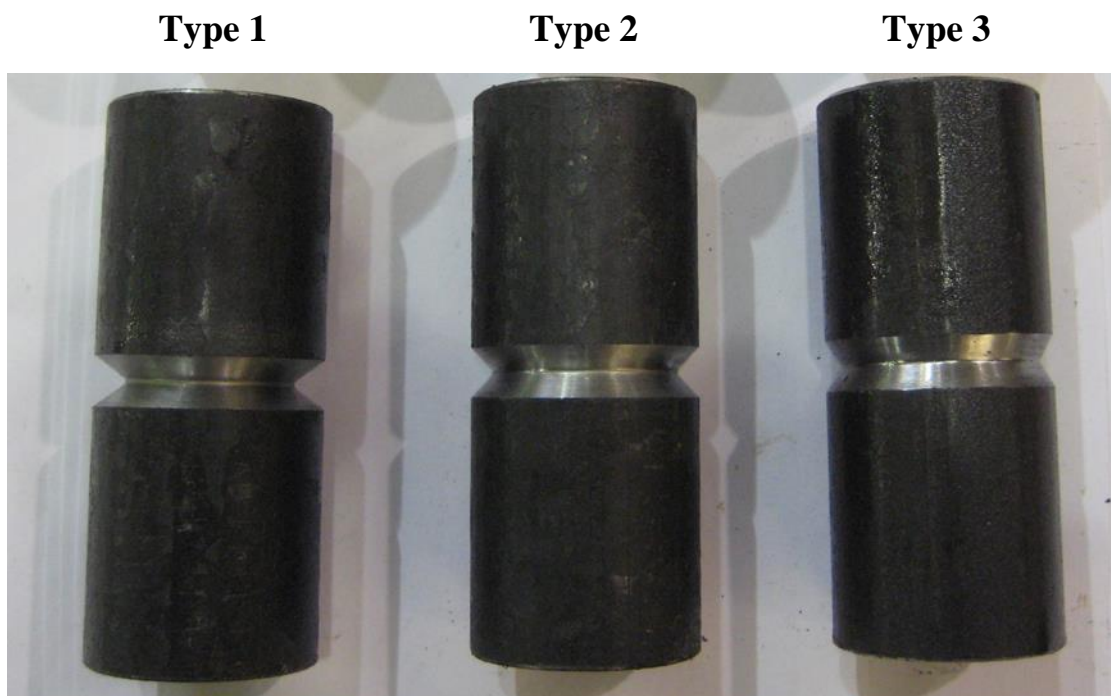


Figure 4.17. Detail dimensions of couplers: (a) Type 1; (b) Type 2; (c) Type 3



(a)



(b)

Figure 4.18. Three types of couplers: (a) couplers before test; (b) fractured couplers

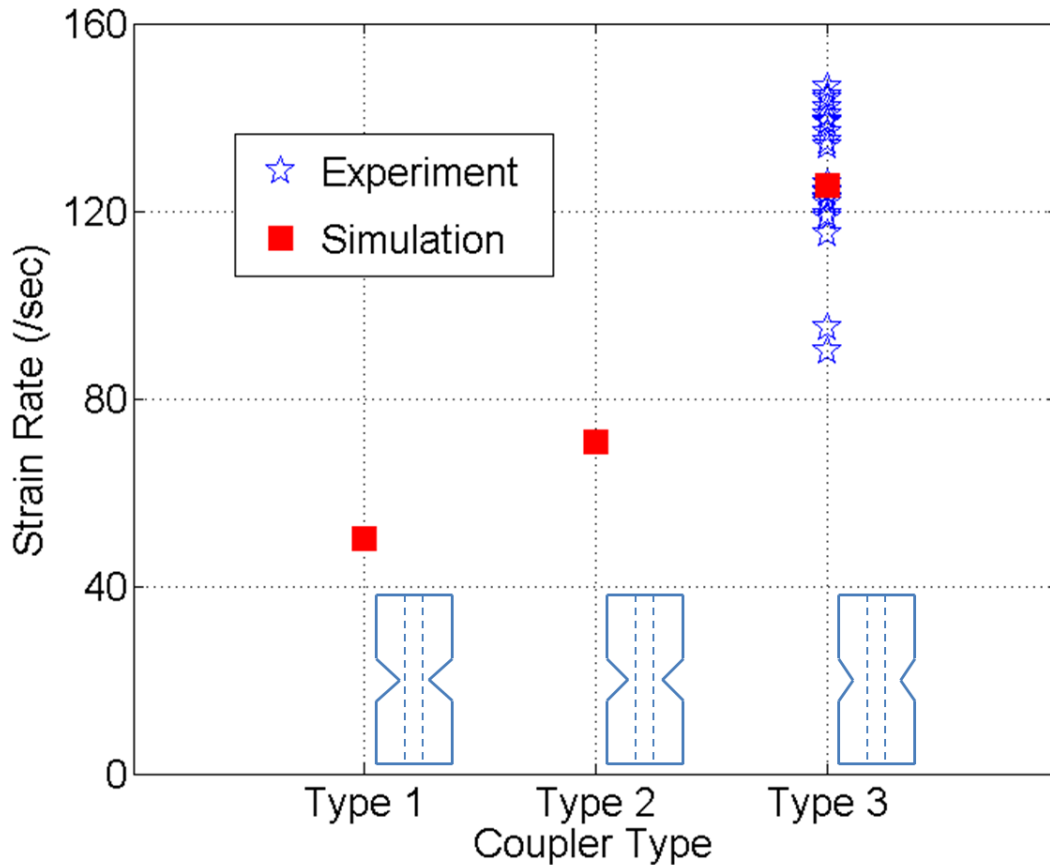


Figure 4.19. Effect of coupler characteristics on strain rate (computational and experiment data)

4.9 CONCLUSIONS

A compact and reliable impact testing system for direct tension testing of UHP-FRC specimens was refined in this study. The device requires the use of only a single specimen and uses energy bars and a coupler to store and suddenly release strain energy with the purpose of striking a specimen at high speed. A transmitter bar is employed to measure stress in the specimen and strain is measured using the DIC technique. The observations and findings of this study can be summarized as follows:

- The DIC technique can be successfully used to measure strain in UHP-FRC specimens. However, due to the fact that speckles are lost as cracks develop, especially during the multiple cracking phase of the material, the averaging scheme

for computing strain produces spurious results. Instead, strain should just be measured by using two points in the gage length, just like an LVDT.

- Analytical and detailed simulation studies showed the importance of using a long enough transmitter bar, made of an appropriate material. As a result of the studies described herein, a 1.55 m long brass transmitter bar is appropriate for capturing the strain hardening then softening behavior of UHP-FRC specimens, up to about 4 % strain.
- Strain rates ranging from 90 to 146 /sec were experimentally achieved. The simulation results indicated that various strain rates can be achieved by changing the net area of the coupler.
- The new setup allows the use of specimens that are similar in size to the specimens used in pseudo-static testing. This is particularly important because it allows direct comparison between specimen responses under widely differing strain rates without concerns about changes in specimen shape or size for low and high strain rate testing.
- The experiments conducted to date demonstrate that rate effects in UHP-FRC are substantial. Not only is the peak stress greatly influenced by strain rate, but the material maintains its strain capacity and has highly enhanced strain dissipation capacity. These results signify that UHP-FRC is particularly promising for blast and impact applications, an issue that will be explored in detail in Chapter 5.

CHAPTER 5

DIRECT TENSILE BEHAVIOR OF UHP-FRC AT HIGH STRAIN RATES

In this Chapter, the direct tensile behavior of UHP-FRC at strain rates ranging from 90 to 146 /sec is investigated. The tests are conducted using the impact testing system developed in Chapter 4. Three fiber types were considered in the experimental program, a twisted fiber and two other types of straight fibers, at various volume fractions. Specimen impact response was evaluated in terms of first cracking strength, post cracking strength, energy absorption capacity and strain capacity. The test results indicated that specimens with twisted fibers generally exhibit better mechanical properties than specimens with straight fibers for the range of strain rates considered. All UHP-FRC series tested in this study showed exceptional rate sensitivities in energy absorption capacity, generally becoming much more energy dissipative under increasing strain rates. This characteristic highlights the potential of UHP-FRC as a promising cement based material for impact- and blast-resistant applications.

5.1 EXPERIMENTAL PROGRAM

The impact testing system developed in Chapter 4 is used in this Chapter to characterize the mechanical properties of UHP-FRC under high strain rates. The UHP-FRC mixes used in this Chapter are same as those used in Chapter 3. The mechanical properties of the three steel fibers used in this study can be found in Table 3.3.

The same naming scheme used in Chapter 3 is employed here as well, where different fibers are designated by their type, diameter and length. Seven series, with 3 tensile specimens each, were prepared and tested as shown in Table 5.1. Each series is designated by fiber type as discussed above and appended with a number that reflects the volume fraction of the fiber. The

rate sensitivity of these materials in direct tension was evaluated in terms of their first cracking strength (σ_{cc}), post cracking strength (σ_{pc}), energy absorption capacity (g) and strain capacity that is the strain value at post cracking strength (ε_{pc}) as can be seen in Figure 3.4. It should be noted that g is the area under stress-strain curve up to $\sigma_u (= 0.95\sigma_{pc})$, as done in Chapter 3. Dynamic increase factors (DIFs), which are the ratio of the dynamic to static responses, are computed for three parameters (σ_{cc} , σ_{pc} , g , ε_{pc}) to illustrate the effect of strain rate on strength and other material parameters. In this study the values measured at the lowest strain rate of 0.0001/sec from Chapter 3 are considered to be static responses.

The average strain rate was calculated by averaging strain rate over the duration of loading as done in Section 4.6 (e.g. Equation 4.3). Figure 5.1 shows an example of the recorded stress and strain data for a T-0.3-25-1% specimen. In this example, the strain rate was calculated to be 119 /sec. Figure 5.2 shows how the average stress-strain response is computed from raw stress-strain responses of multiple specimens. The curve averaging process is discussed in detail in Section 3.1.3. It is clear, and this was generally observed throughout the test program, that specimen-to-specimen variability was reasonably low for all parameters considered in this work.

5.2 SELECTION OF SPECIMEN LENGTH

Specimen length is an important variable. Specimens that are too short or long may influence measurement of quantities sought in the experiment. Therefore, the finite element model developed in Chapter 4, is employed here to evaluate the effect of specimen length (l in Figure 5.3) on measured response. The red dashed line in Figure 5.4 is the assigned stress-strain curve for UHP-FRC under tension, which compares reasonably to the measured uniaxial responses of UHP-FRC specimens as reported in Chapter 4. The predicted stress-strain responses based on the simulation results of UHP-FRC under uniaxial tension for various specimen lengths are shown in Figure 5.4. Figures 5.5 and 5.6 show examples of how UHP-FRC specimen of various lengths fare in both simulations and experiments, respectively. It is clear from Figure 5.4 that no significant difference can be found in the computed stress-strain responses of the various specimens and that all compare well with the analytically specified stress-strain response.

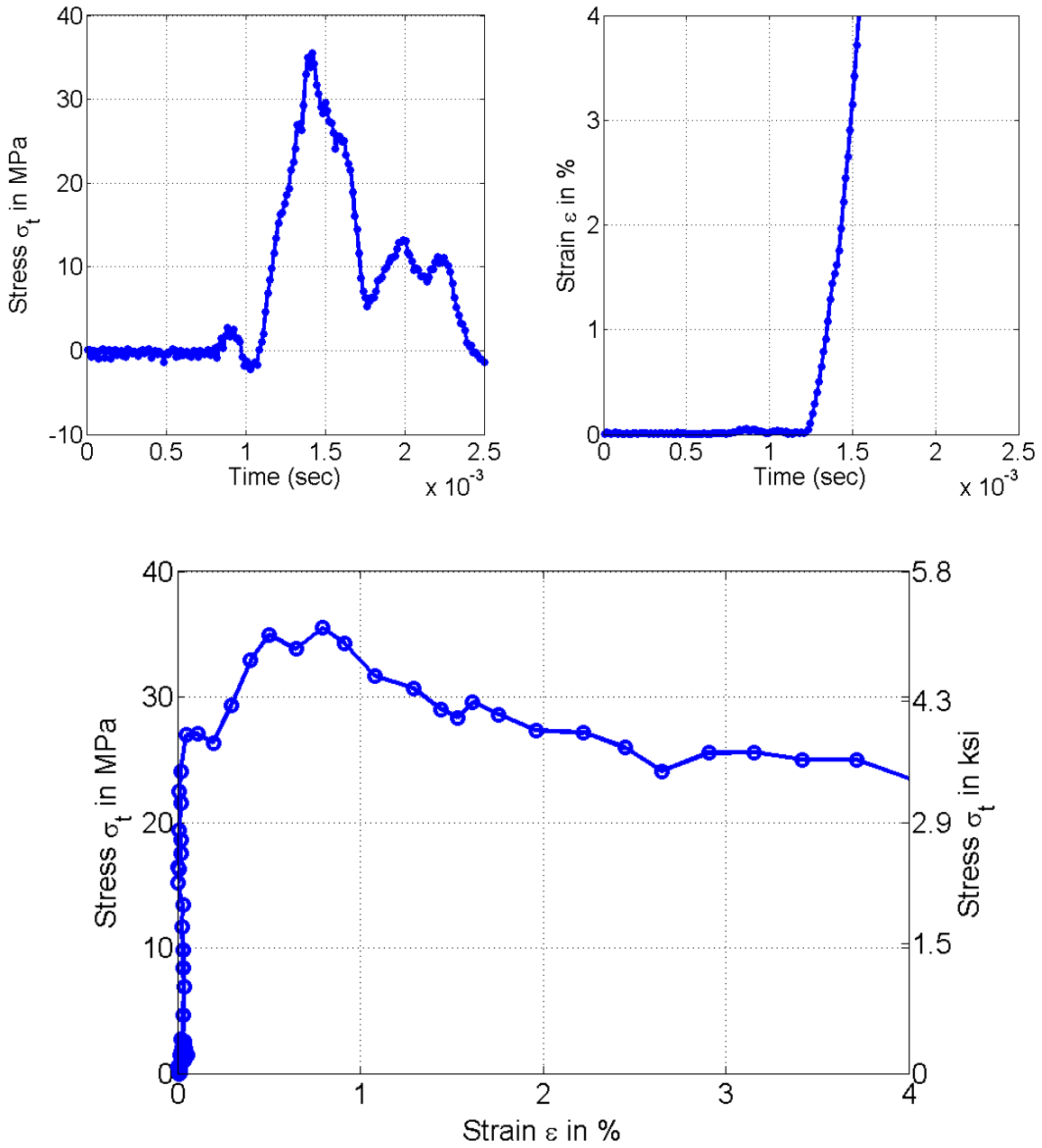


Figure 5.1. Example of data reading (T-0.3-25-1%): (a) Stress reading; (b) Strain reading; (c) Stress-strain relation (Note: strain valid up to peak stress only.)

Table 5.1. Summary of impact test results

Test series	Specimen length (ℓ) (mm)	Strain rate	First cracking strength (σ_{cc})		Post cracking strength (σ_{pc})		Energy absorption capacity (g)		Strain capacity (ϵ_{pc})		
			MPa	DIF	MPa	DIF	kJ/m^3	DIF	%	DIF	
S-0.2-25-1%	55		115.3	14.27	2.3	24.53	3.0	148.9	4.3	0.493	1.5
			122.4	14.54	2.3	25.98	3.2	156.5	4.5	0.417	1.3
			133.9	15.52	2.5	26.32	3.2	359.8	10.4	1.161	3.5
			136.8	14.24	2.3	24.33	3.0	329.7	9.5	1.219	3.7
	Average	127.1	14.64	2.4	25.29	3.1	248.7	7.2	0.823	2.5	
	60		78.87	18.14	2.9	23.69	2.9	382.5	11.1	0.865	2.6
			87.54	15.56	2.5	27.76	3.4	255.8	7.4	0.832	2.5
			114.8	13.15	2.1	25.64	3.2	257.5	7.5	0.779	2.4
		Average	93.72	15.61	2.5	25.70	3.2	298.6	8.6	0.826	2.5
	65		65.98	13.45	2.2	29.39	3.6	379.4	11.0	0.600	1.8
			78.42	13.88	2.2	27.92	3.4	240.8	7.0	0.546	1.7
			89.03	17.72	2.9	28.91	3.6	239.5	6.9	0.332	1.0
Average		103.3	16.17	2.6	30.81	3.8	414.0	12.0	1.087	3.3	
	84.18	15.31	2.5	29.26	3.6	318.4	9.2	0.641	1.9		
S-0.2-25-2%	55		139.1	26.19	2.7	47.92	3.2	860.3	10.2	1.999	3.7
			140.6	25.19	2.6	49.94	3.3	383.4	4.5	1.002	1.8
			143.8	29.86	3.1	36.24	2.4	252.4	3.0	0.466	0.9
		Average	141.1	27.08	2.8	44.70	3.0	498.7	5.9	1.156	2.1
S-0.4-25-2%	55		118.6	19.26	2.8	30.18	3.6	448.9	12.5	1.172	4.3
			136.6	17.21	2.5	24.74	3.0	280.0	7.8	0.435	1.6
			146.3	15.97	2.3	19.94	2.4	379.7	10.6	0.656	2.4
		Average	133.8	17.48	2.5	24.95	3.0	369.5	10.3	0.754	2.8
S-0.4-25-3%	55		95.22	23.50	3.1	40.57	4.3	302.5	7.3	0.786	3.3
			124.3	24.23	3.2	36.16	3.8	323.8	7.8	0.471	2.0
			134.8	21.90	2.9	44.67	4.7	439.5	10.6	0.697	2.9
		Average	118.1	23.21	3.0	40.47	4.3	355.3	8.6	0.651	2.7
T-0.3-25-1%	55		119.3	15.16	2.2	35.50	4.3	298.8	8.9	0.854	4.5
			123.9	18.10	2.6	20.81	2.5	238.2	7.1	0.335	1.8
			144.6	17.95	2.6	29.67	3.6	455.1	13.6	0.624	3.3
		Average	129.3	17.07	2.5	28.66	3.5	330.7	9.9	0.604	3.2
T-0.3-25-2%	55		90.14	21.24	2.3	46.64	4.0	643.7	10.1	0.762	1.8
			122.7	29.71	3.3	53.02	4.6	680.5	10.7	0.633	1.5
			139.3	21.16	2.3	38.10	3.3	877.6	13.8	1.840	4.4
		Average	117.4	24.04	2.6	45.92	4.0	733.9	11.6	1.078	2.6
T-0.3-25-3%	55		121.8	30.16	2.5	64.78	3.1	1167	10.8	1.615	3.4
			125.8	25.15	2.1	56.65	2.7	1133	10.5	1.098	2.3
			142.1	32.71	2.7	68.05	3.3	1153	10.7	0.927	1.9
		Average	129.9	29.34	2.5	63.16	3.0	1151	10.7	1.213	2.5

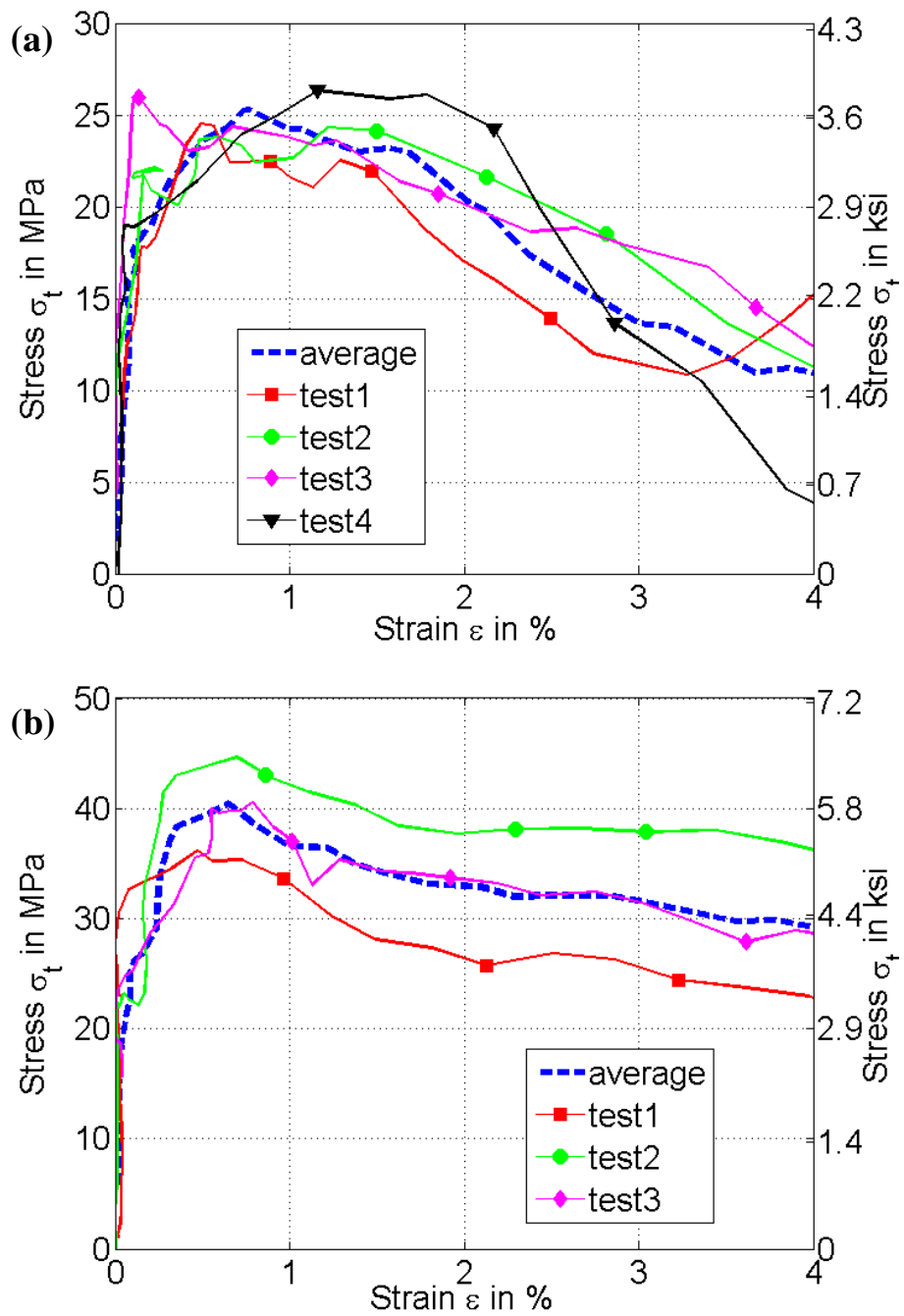


Figure 5.2. Examples of the averaging process for obtaining the stress-strain response: (a) S-0.2-25-1%; (b) S-0.4-25-3% (Note: strain valid up to peak stress only.)

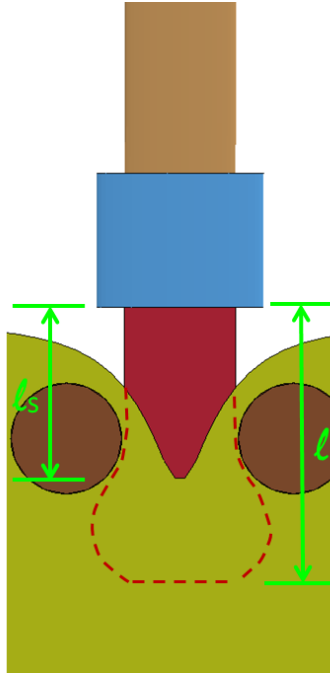


Figure 5.3. Specimen length of UHP-FRC specimens

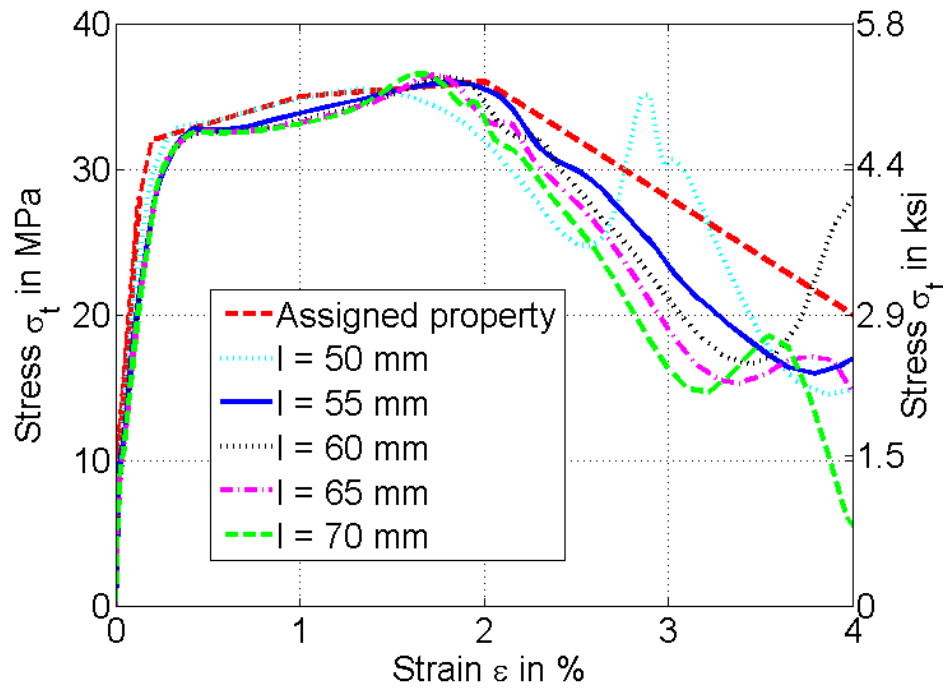


Figure 5.4. Stress-strain responses from the parametric study using simulations

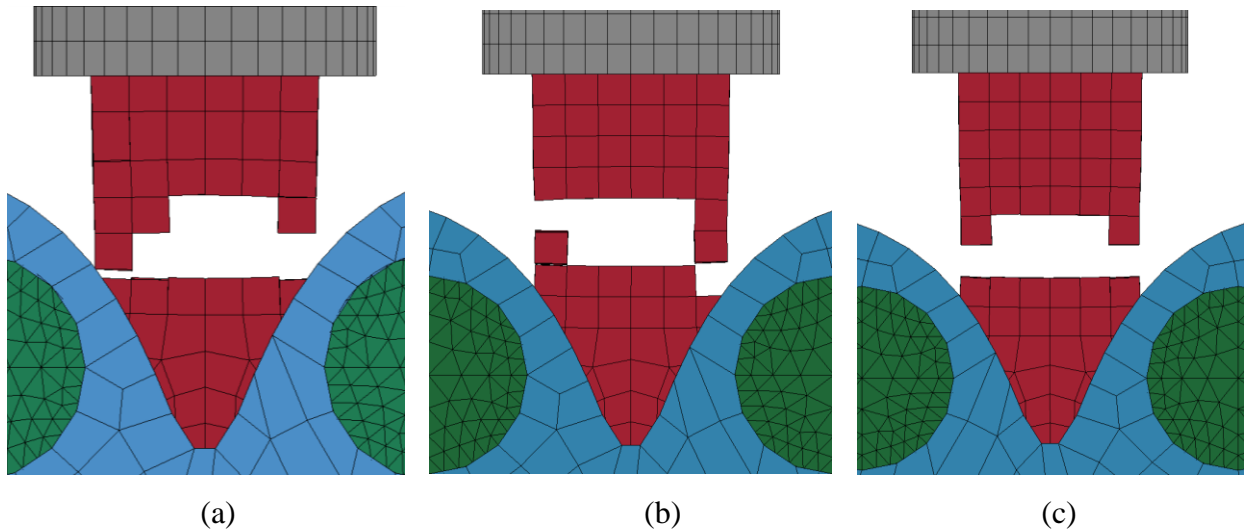


Figure 5.5. Examples of failure of UHP-FRC specimens in simulations: (a) $l = 55\text{mm}$; (b) $l = 60\text{mm}$; (c) $l = 65\text{mm}$

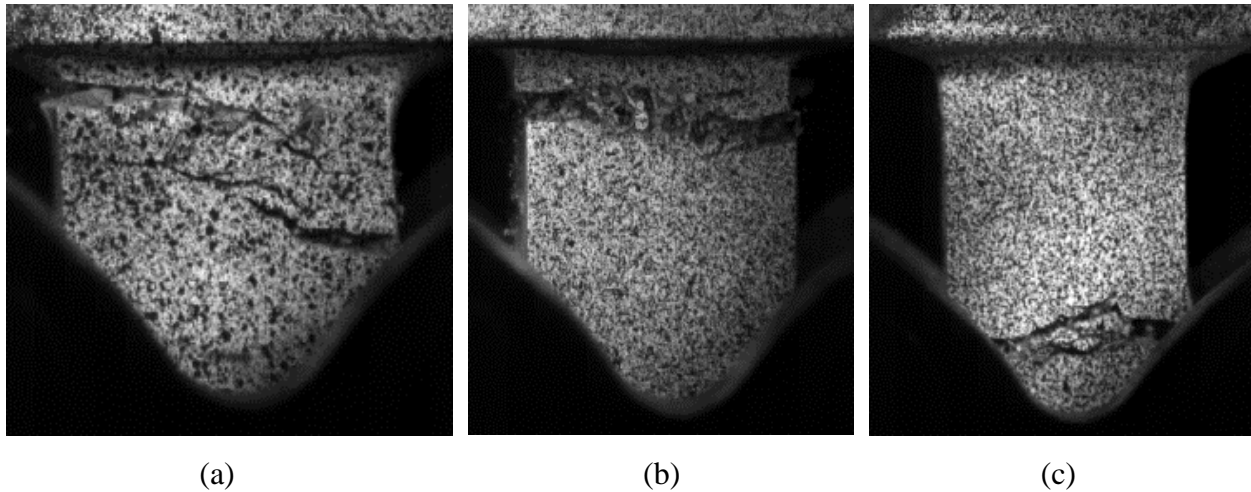


Figure 5.6. Examples of failure of UHP-FRC specimens in experiments: (a) $l = 55\text{mm}$; (b) $l = 60\text{mm}$; (c) $l = 65\text{mm}$ (note that the darker lower part of the photos is part of the gripping fixture of the machine)

Figure 5.7 illustrates the averaged stress-strain responses of UHP-FRC with various specimen lengths as obtained from the experiments. Table 5.1 summarizes the detail test results. As seen in the simulation studies, the effect of specimen length on stress-strain response is minor. Figure 5.8 shows the computed DIF versus specimen length for various mechanical properties: first cracking strength, post cracking strength, energy absorption capacity and strain capacity.

Similar to the overall stress-strain curves, no clear trend can be found for first cracking strength and strain capacity associated with increasing specimen length from 55 to 65 mm. However, the DIF for post cracking strength and energy absorption capacity increase by 15% and 28% as specimen length increases from 55 to 65 mm.

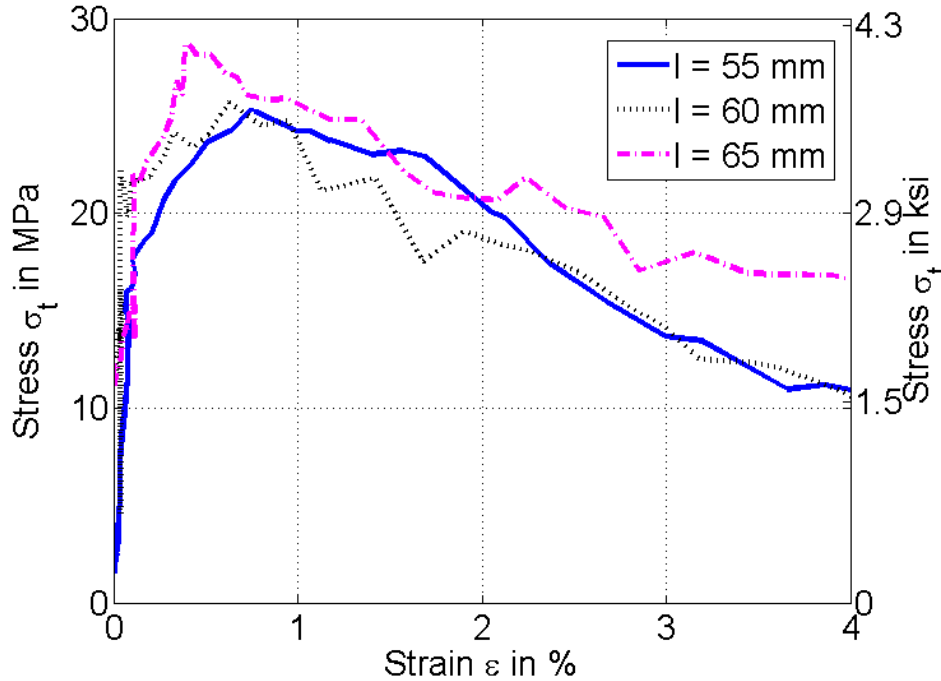


Figure 5.7. Stress-strain responses from the parametric study using experiments

The effect of specimen length on the strain rate recorded from both simulations and experiments is illustrated in Figure 5.9. Three trends are evident from the figure. First, there is large scatter in the experimental strain rate values. Second, simulation results for strain rate match reasonably well with their measured counterparts, especially given the large scatter. Third, both simulation and experimental data suggest that strain rates decrease as specimen length increases. While both simulation and experimental studies quantify the effect, the trend is indeed expected, i.e. the strain rate will decrease linearly as the gage length of the specimen increases, as suggested in Equation 4.3.

Dynamic testing requires that a short specimen be used to ensure that it is uniformly loaded during the experiment (Ravichandran and Subhash 1994, Chen and Song 2011). On the

other hand, a gage length that is too short compared to the least size of the constituents of the material being tested does not permit meaningful measurement of strain. For UHP-FRC

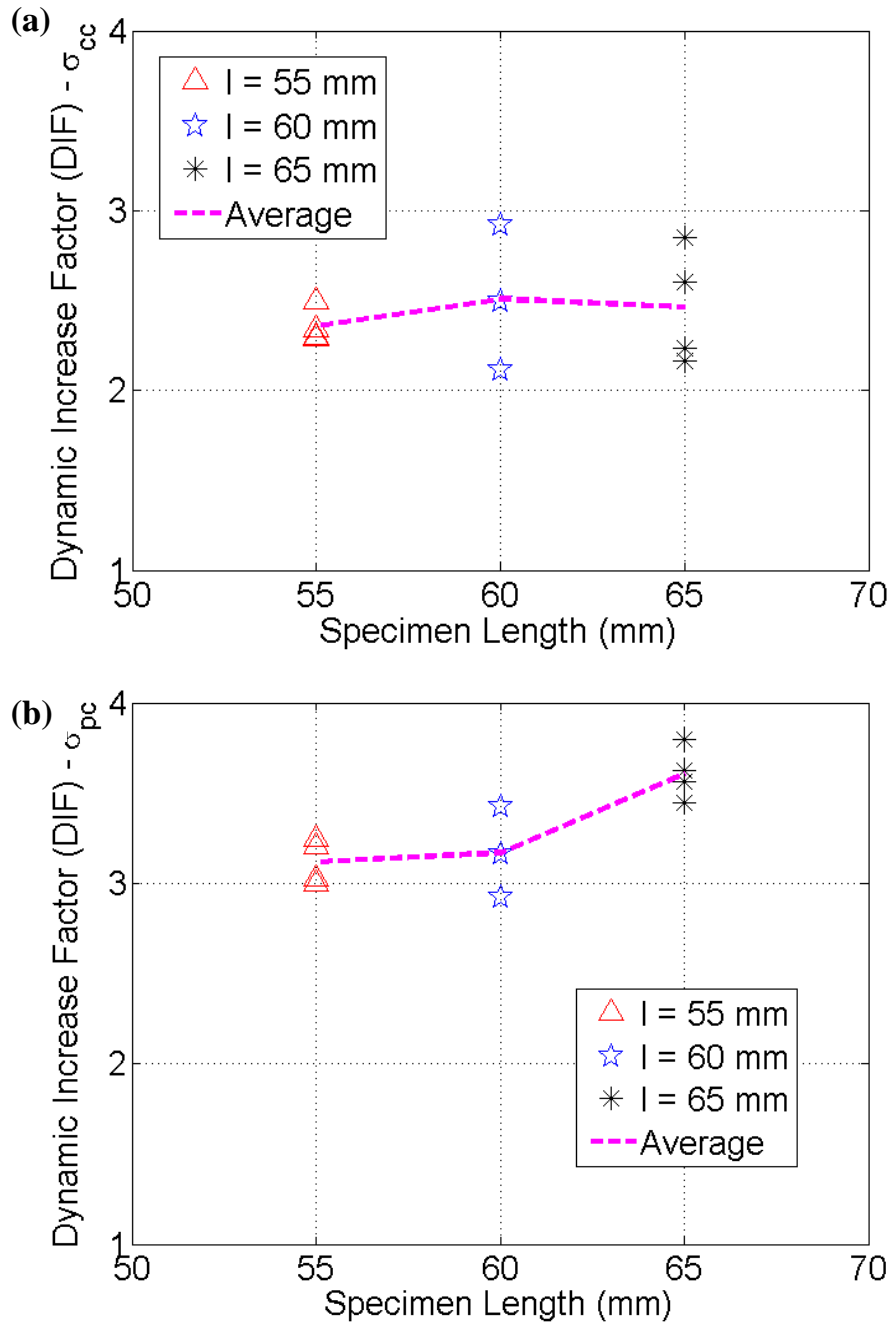


Figure 5.8. Experimentally obtained dynamic increase factor (DIF) of UHP-FRC specimens with different lengths: (a) First cracking strength; (b) Post cracking strength; (c) Energy absorption capacity; (d) Strain capacity

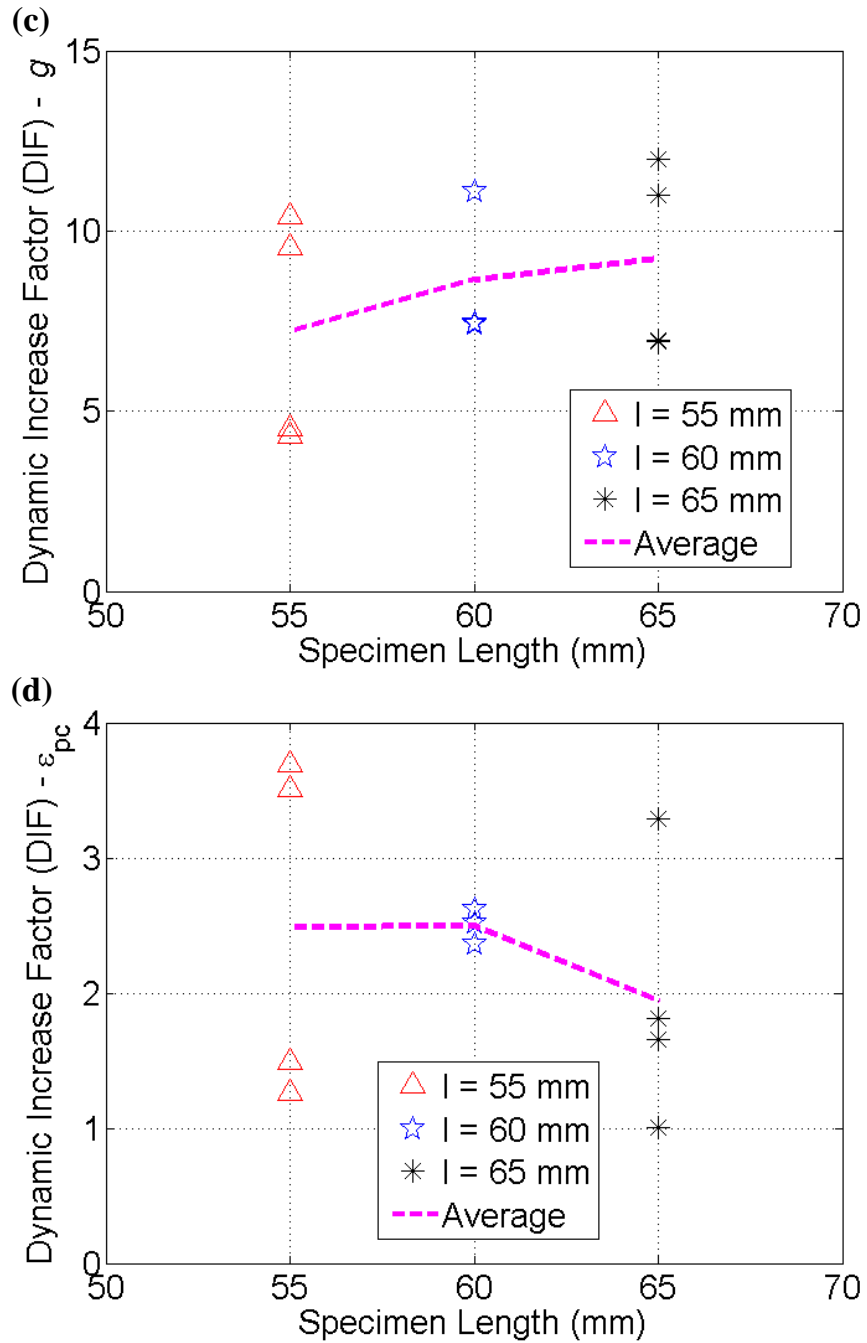


Figure 5.8. continued

specimens and the given experimental program, which employs 25 mm long fibers, specimen length was selected to be 55 mm. This length was deemed long enough for the fiber length and yet short enough to avoid non-uniform loading during the experiments.

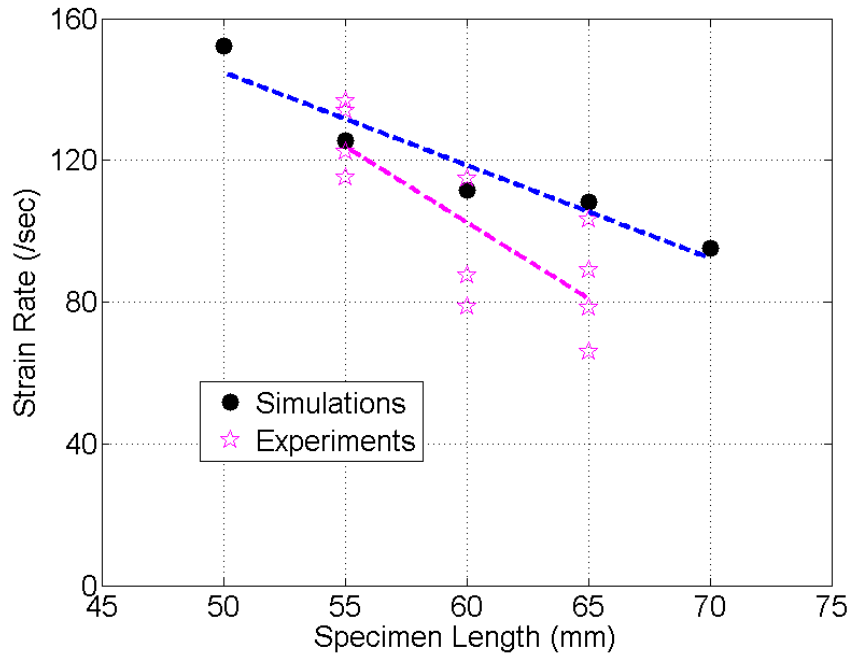


Figure 5.9. Strain rate versus specimen length

5.3 EVALUATION OF EXPERIMENTAL RESULTS

Table 5.1 summarizes test results including strain rates and the four basic parameters computed from the test data: σ_{cc} , σ_{pc} , g , and ε_{pc} . The table shows that strain rates ranging from 90 to 146 /sec are achieved. The DIF values are also listed in Table 5.1. The average tensile stress-strain curves for each series with different types of fiber and volume fractions are plotted in Figure 5.10. The stress-strain curves with lower strain rates obtained in Chapter 3 are also plotted in Figure 5.10 to allow a direct comparison of UHP-FRC responses under various loading rates. There is clear evidence from all test series described in Figure 5.10 that UHP-FRC specimens loaded at high strain rate show exceptional enhancement in both peak strength and strain capacity compared to specimens loaded at low strain rates (< 0.1 /sec) regardless fiber type. More importantly, the energy absorption capacity of UHP-FRC specimens under impact loading is remarkable (Figure 5.11c), about an order of magnitude higher than their quasi-static

counterparts. This latter observation suggests that UHP-FRC is likely a highly promising cement based material for impact and blast resistance applications.

Figure 5.11 depicts the effect of two parameters, fiber type and fiber volume fraction, on the strain rate sensitivity of UHP-FRC. Since the strain rate is bounded within a relatively narrow band, values that are averaged across all strain rates are used in Figure 5.11. From a qualitative perspective, Figure 5.11 suggests that increasing fiber volume fraction leads to an increase in first cracking strength, post cracking strength, energy absorption capacity and strain capacity for all fiber cases (S-0.2-25, S-0.4-25 and T-0.3-25). In general, all the parameters summarized in Table 5.1 show significant rate sensitivities.

Figure 5.12 shows examples of the captured cracking patterns for specimen. The figure clearly shows that the specimen exhibits multiple cracking. This is also evident in the computed stress strain curves, where hardening behavior after first cracking is observed. Multiple cracking with strain hardening behavior was observed in all specimens, even at 1% fiber content, and confirms observations made earlier for high performance fiber reinforced cementitious composites by Kim et al. (2011) for impact loaded specimens.

5.3.1 Effect of Fiber Type and Aspect Ratio

As seen in the tests at lower strain rate reported in Chapter 3, the twisted fiber series show generally better performance than the straight fiber series at high strain rates (see Figure 5.11). As surmised in Chapter 3 for low strain rates, it is believed that the additional anchorage effect associated with the untwisting action that occurs during pullout is the reason for the improved behavior. The enhanced behavior seen in twisted fiber specimens are not across the board. For example, the T-0.3-25 and the S-0.2-25 fibers show similar σ_{pc} and ε_{pc} for a volume fractions up to 2%. However, energy absorption capacity, g , is much higher in the former than the latter, i.e. T-0.3-25-2% shows 47% higher energy absorption capacity than S-0.2-25-2% at high strain rate loading. The higher aspect ratio, l_f / d_f , of the S-0.2-25 fibers, which translates into more fibers per unit volume, and its higher specific surface for bond, appear to compensate for the mechanical anchorage action of the twisted fibers when it comes to σ_{pc} and ε_{pc} , but not for energy absorption capacity.

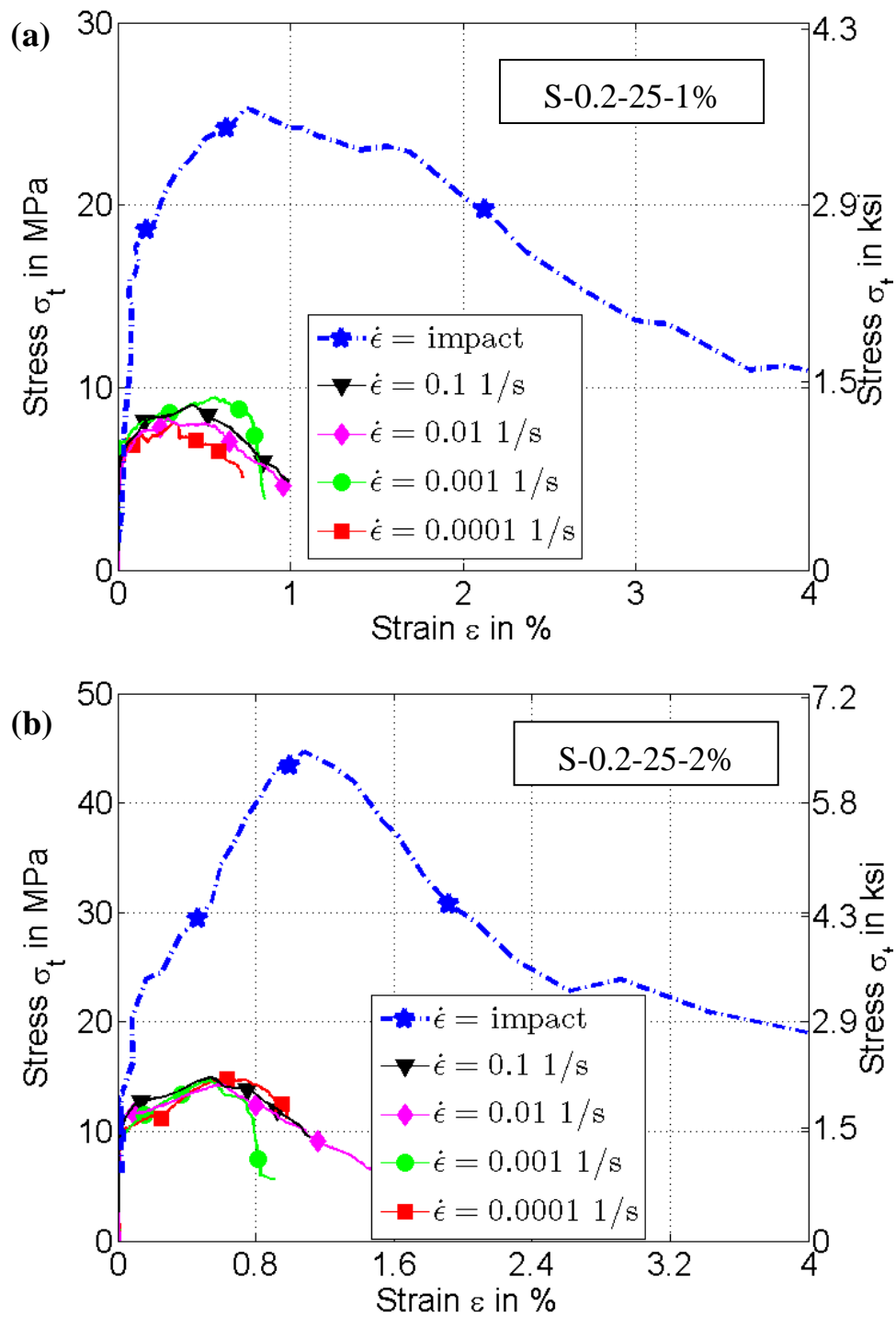


Figure 5.10. Rate effect on stress-strain response under tension of UHP-FRC using different fibers (Note: strain valid up to peak stress only.)

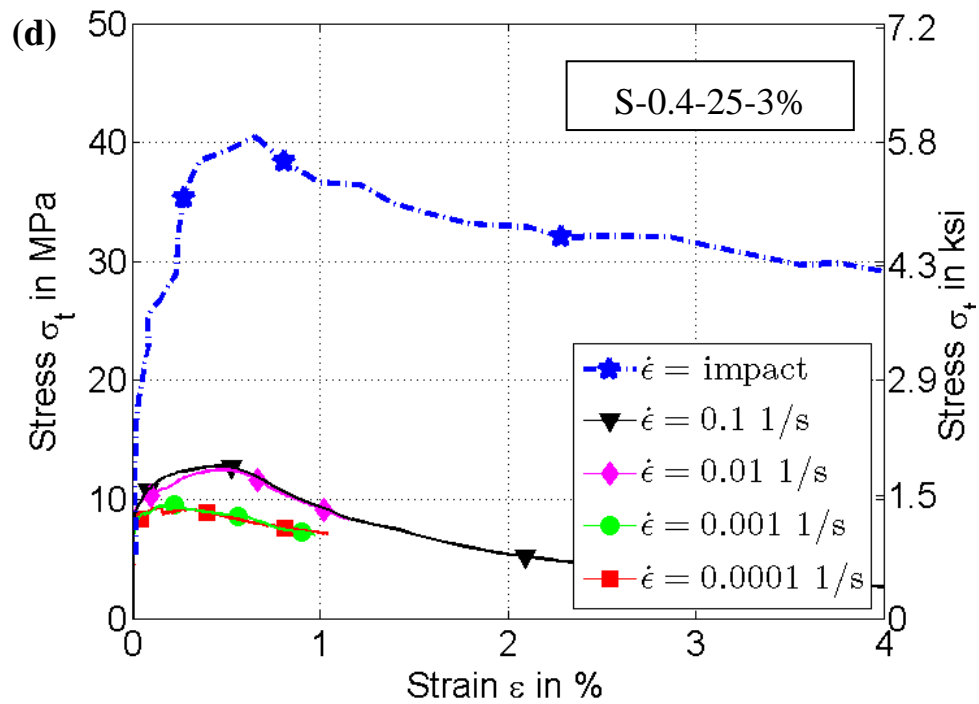
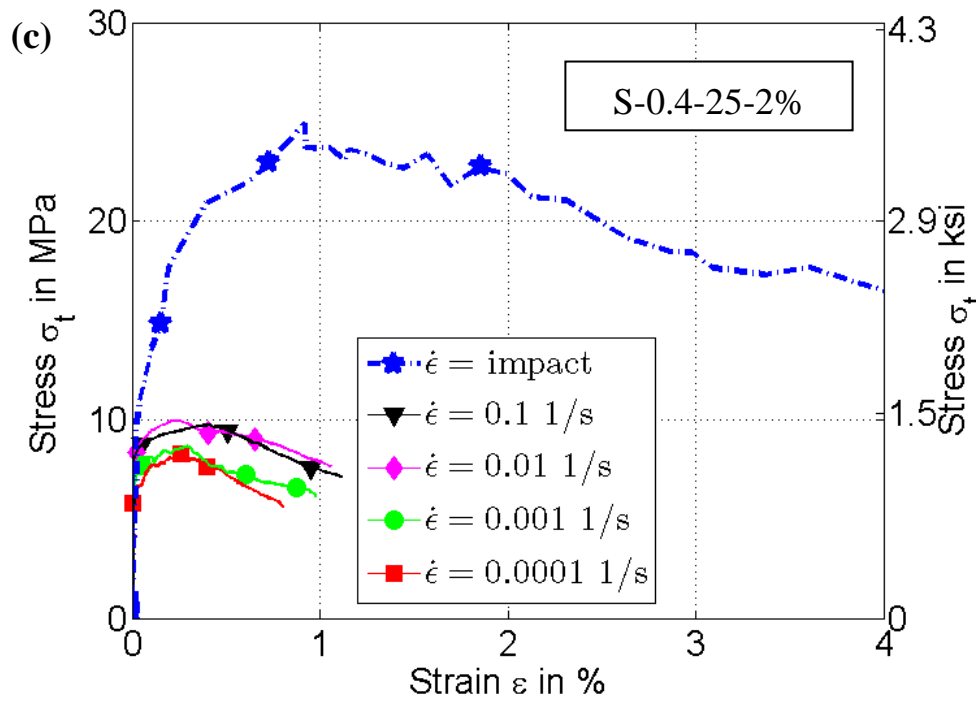


Figure 5.10. continued

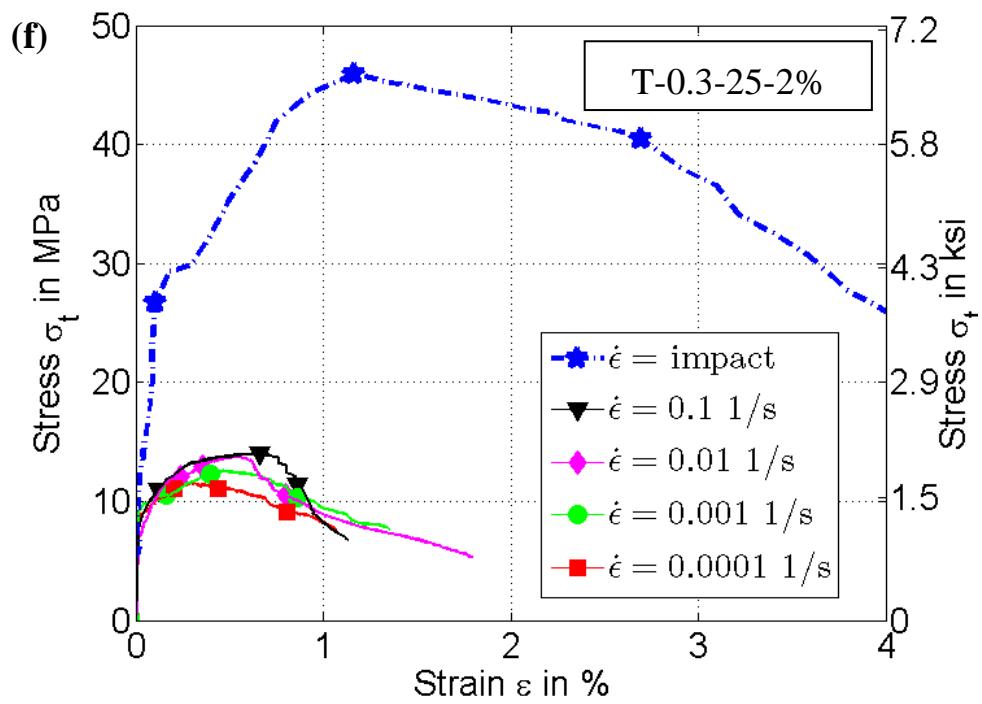
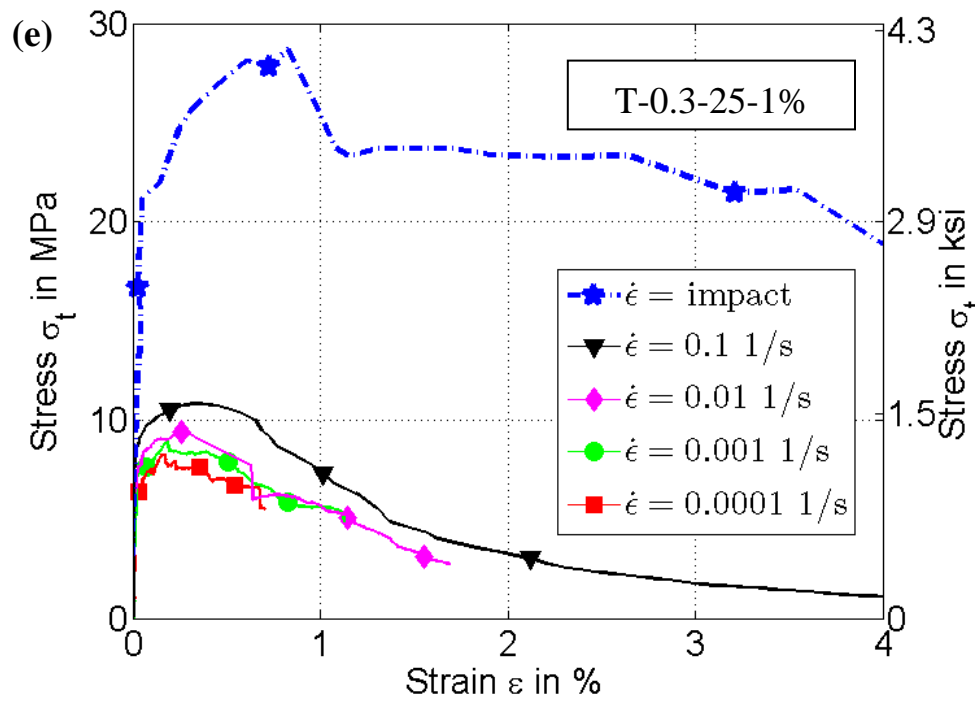


Figure 5.10. continued

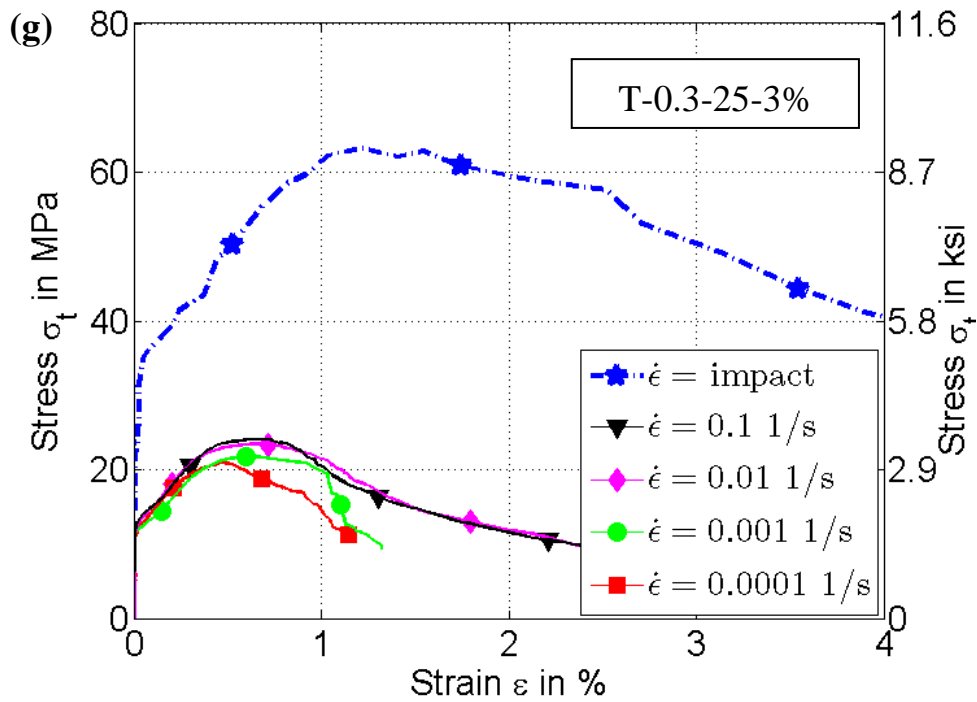


Figure 5.10. continued

As expected, the straight fibers with higher aspect ratio, S-0.2-25, show generally better performance than the corresponding straight fibers with lower aspect ratio, S-0.4-25. For example, the S-0.2-25-2% case shows 10%, 40% and 77% higher post cracking strength, energy absorption capacity and strain capacity, respectively, than S-0.4-25-3% under impact loading. These observations suggest that the fiber aspect ratio is a critical factor not only at low strain rates but also at higher strain rates.

The general trend from the test data under impact loading is that the post-cracking stress and corresponding strain increase substantially under impact loading for all fiber types. The increase is significantly more important for energy absorption capacity. For example, the strain capacity DIF for the T-0.3-25-2% series is 2.56 for impact (averaged across all strain rates achieved in the tests), whereas the corresponding energy absorption DIF for the same series is 11.55.

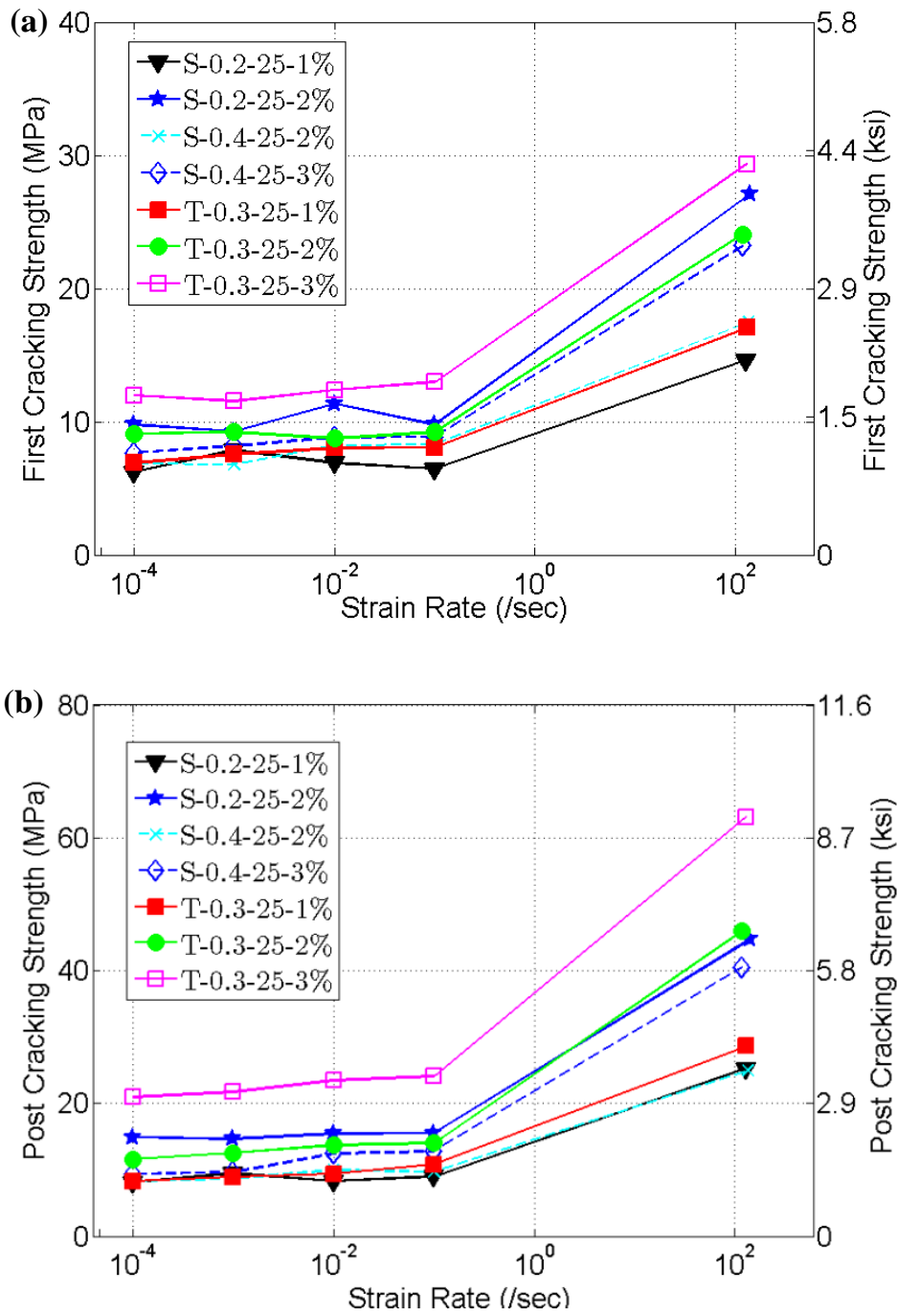


Figure 5.11. Rate effect of UHP-FRC using different fibers: (a) First cracking strength; (b) Post cracking strength; (c) Energy absorption capacity; (d) Strain capacity

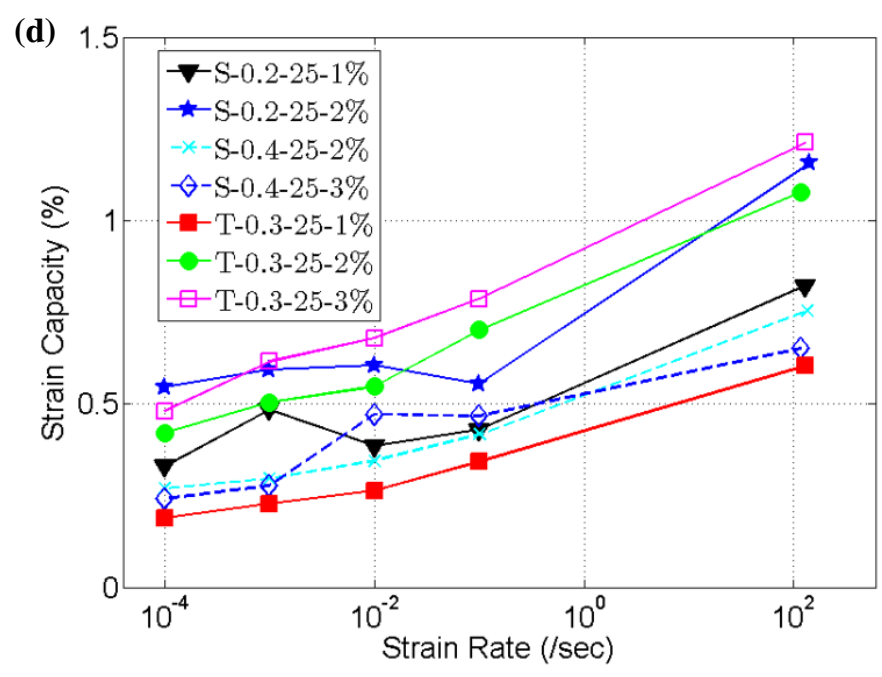
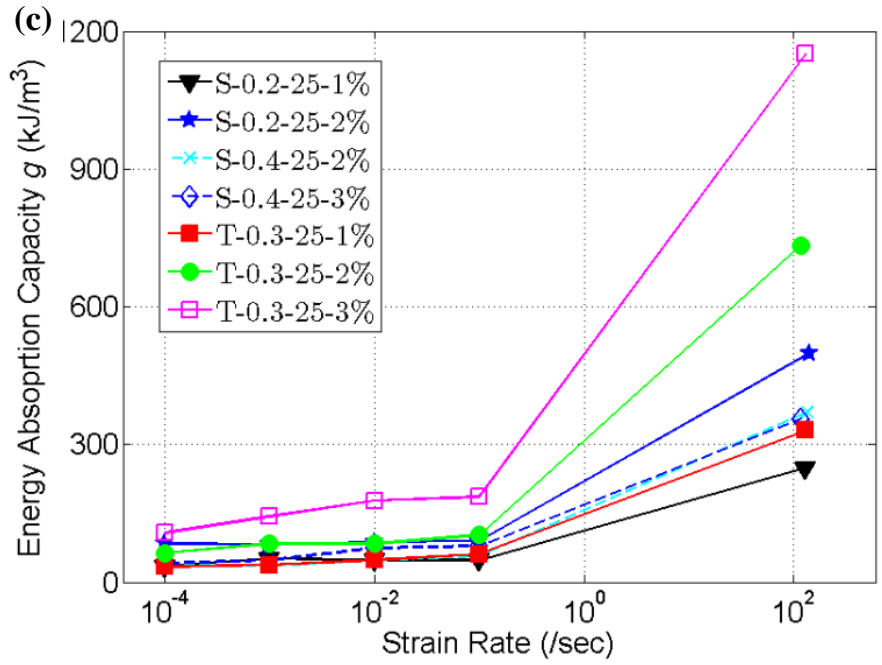


Figure 5.11. continued

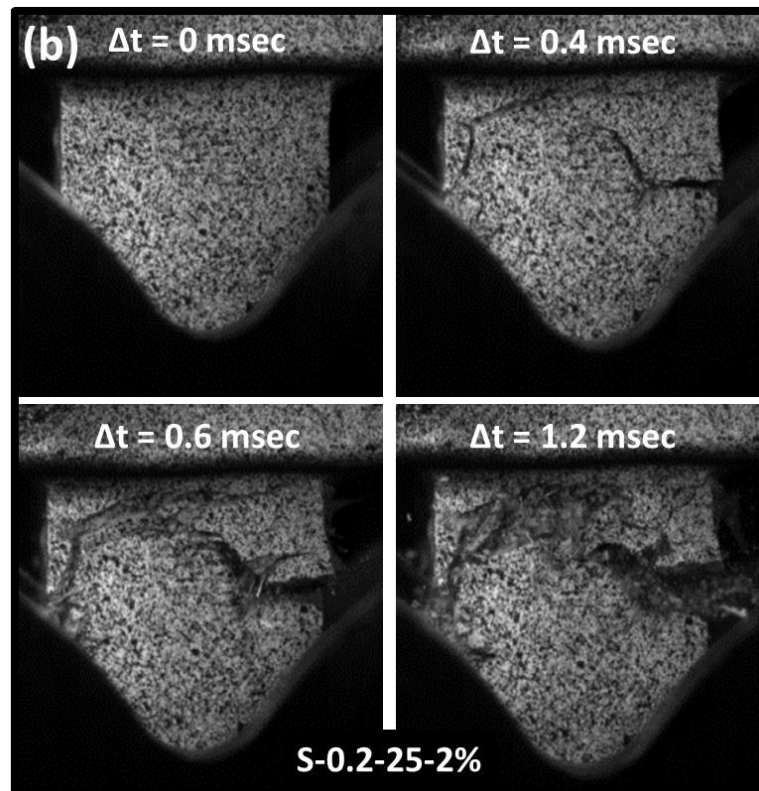
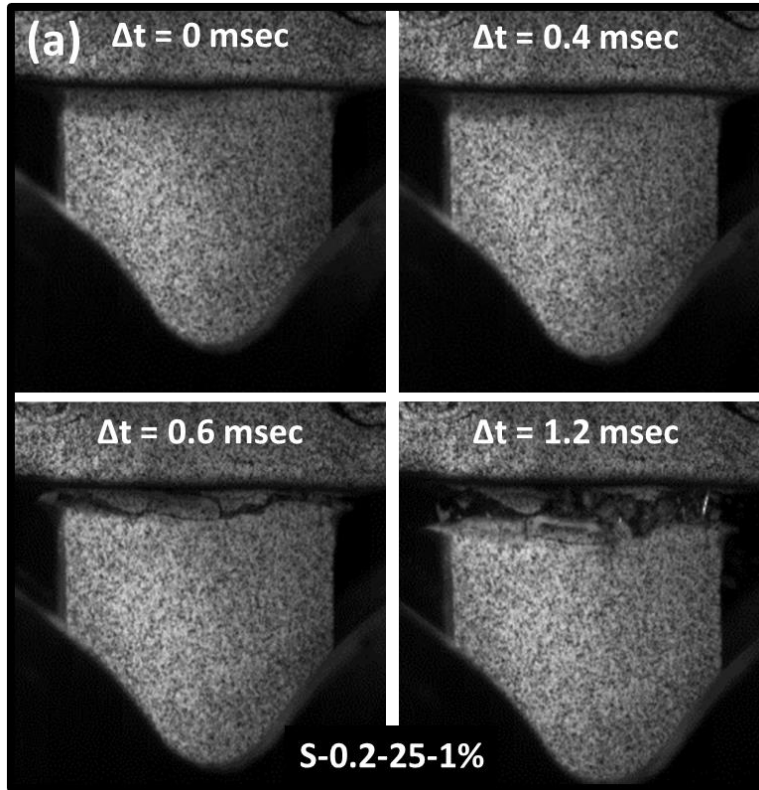


Figure 5.12. Examples of failed specimens: (a) S-0.2-25-1%; (b) S-0.2-25-2%; (c) S-0.4-25-2%; (d) S-0.4-25-3%; (e) T-0.3-25-1%; (f) T-0.3-25-2%; (g) T-0.3-25-3%

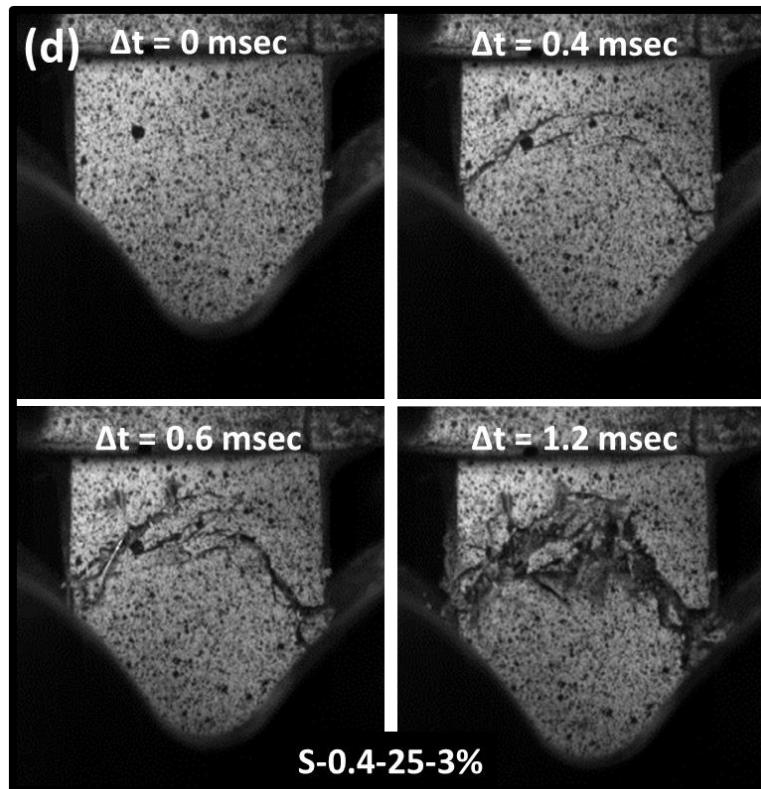
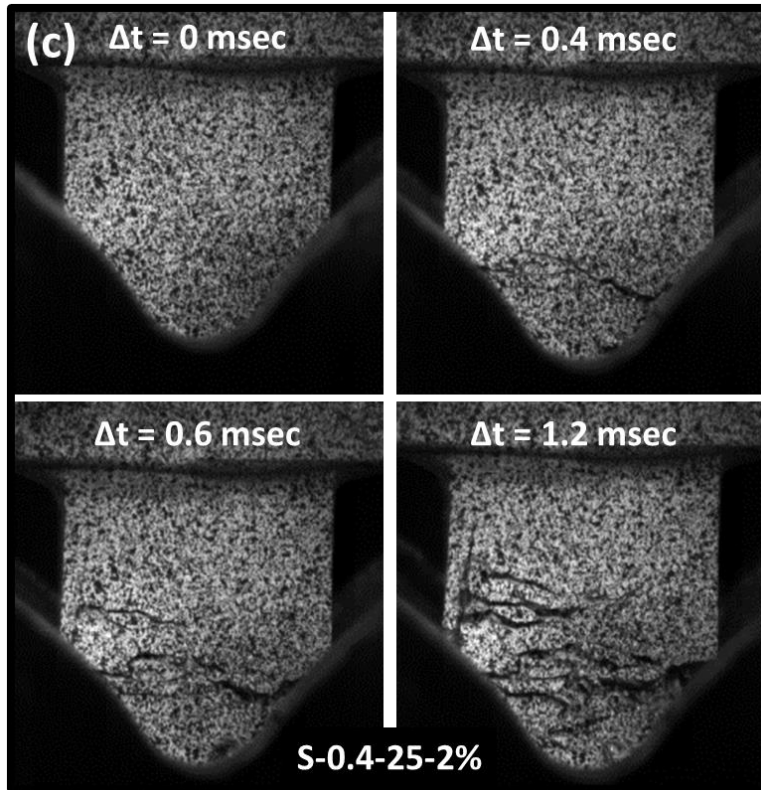


Figure 5.12. continued

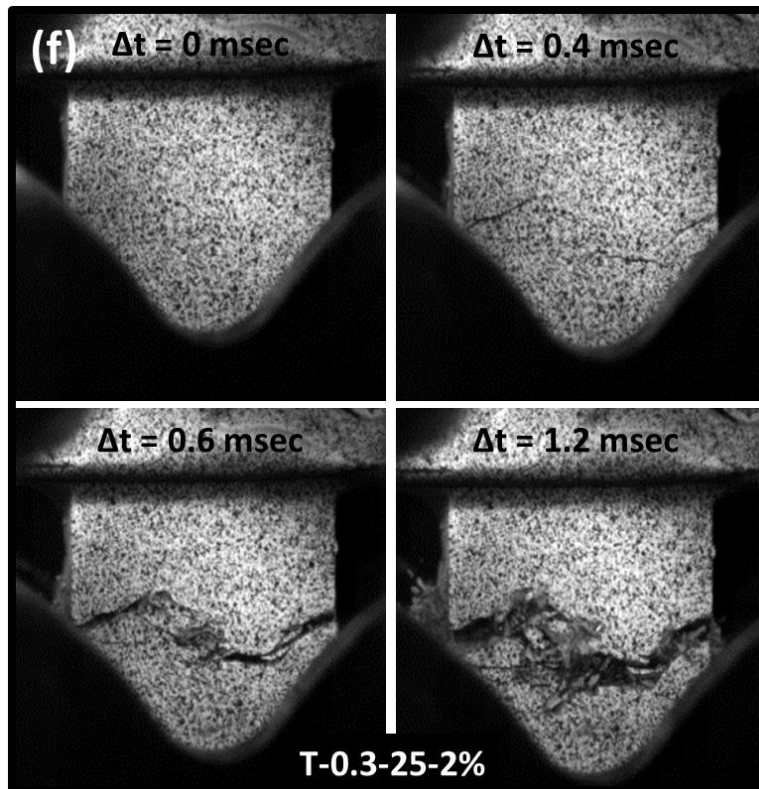
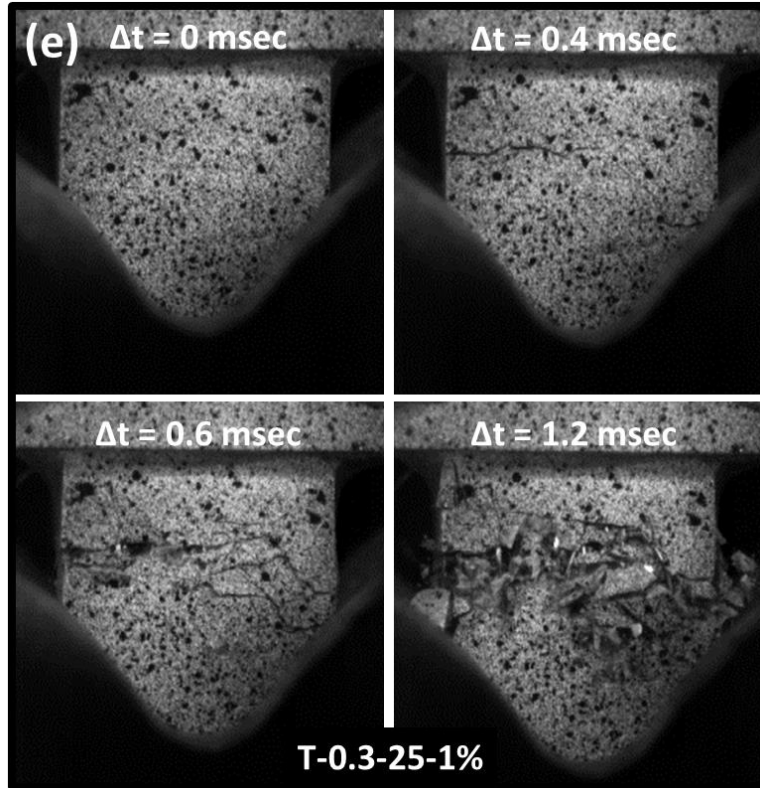


Figure 5.12. continued

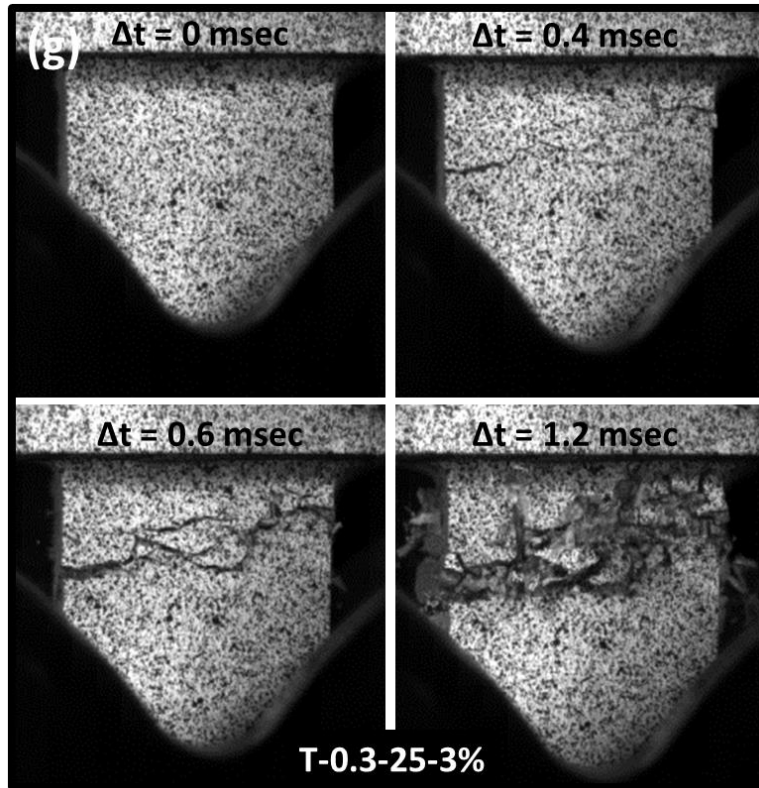


Figure 5.12. continued

5.3.2 DIF

Overall, the DIF results in Table 5.1 along with the plots in Figures 5.13 and 5.14 highlight the impact resistance of UHP-FRC under tensile loading. DIF was evaluated for four key parameters, first cracking strength, post cracking strength, energy absorption capacity and strain capacity. Plots of DIF versus strain rate for different fiber types and volume fractions are compared in Figure 5.14. The increases in DIF of the four parameters follow a log-linear relationship at lower strain rates and rise exponentially at high strain rates. This follows general trends for regular concrete under tension, where the DIF for tensile strength increases mildly up to strain rates between 1 or 30/sec then much rapidly thereafter (Malvar and Crawford 1998, Hentz et al. 2004, Leppanen 2006, Pyo and El-Tawil 2013).

The S-0.4-25-3% series shows the highest rate sensitivity for post cracking strength. The DIF for this parameter is 4.3 on average. In contrast, the S-0.2-25-2% series shows the lowest rate sensitivity for post cracking strength, i.e. 3.0 on average. The T-0.3-25-1% series shows the

highest rate sensitivity for strain capacity. The DIF for this parameter was 3.2 on average. In contrast, the S-0.2-25-2% series shows the lowest rate sensitivity for strain capacity, i.e. 2.1 on average. It appears that the range is narrow enough to attribute the differences to experimental scatter.

It should be noted that as can be seen in Figures 5.14e and 5.14f twisted fibers show a somewhat higher increase in energy absorption capacity DIF than straight fibers. However, it is noteworthy that straight fiber series still exhibit impressive increases in energy absorption capacity. It is difficult to draw a firm conclusion about the increase in strain capacity due to scatter data in strain capacity.

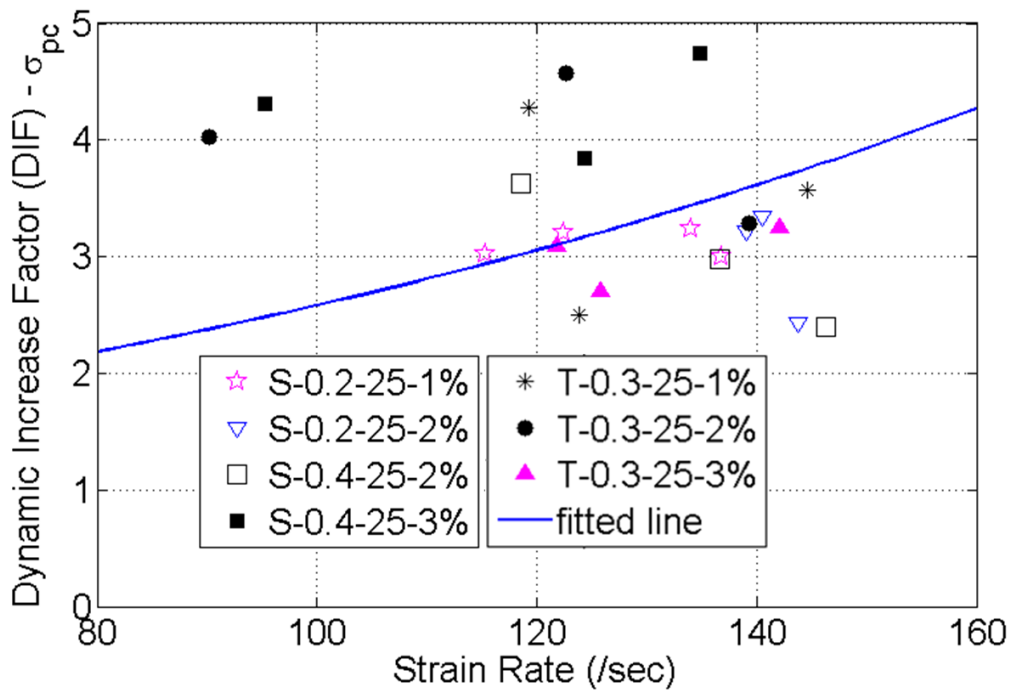


Figure 5.13. Dynamic increase factor (DIF) for post cracking strength (excluding lower strain rate data)

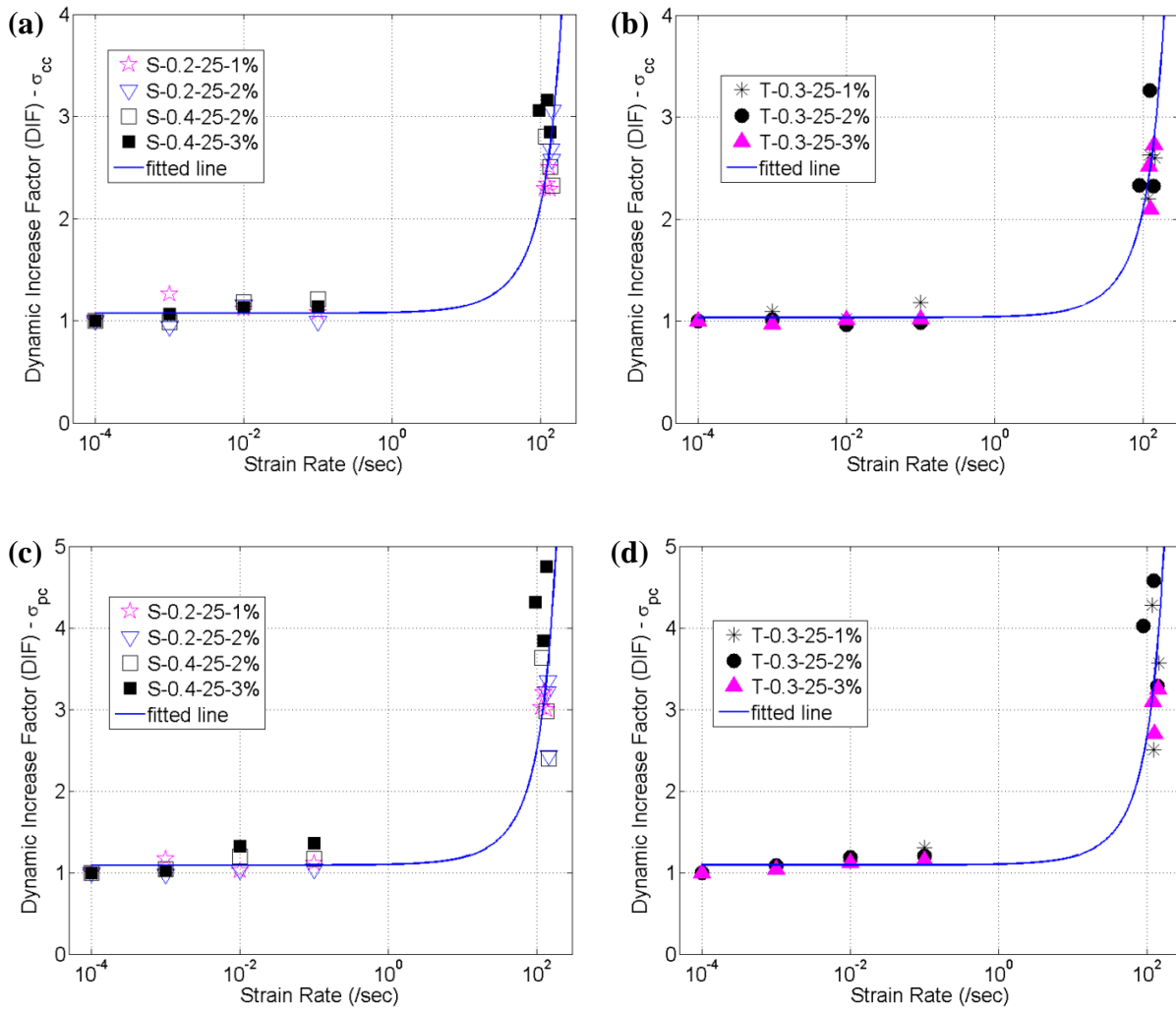


Figure 5.14. Dynamic increase factor (DIF) of UHP-FRC: (a) First cracking strength of smooth fiber; (b) First cracking strength of twisted fiber; (c) Post cracking strength of smooth fiber; (d) Post cracking strength of twisted fiber; (e) Energy absorption capacity of smooth fiber; (f) Energy absorption capacity of twisted fiber; (g) Strain capacity of smooth fiber; (h) Strain capacity of twisted fiber

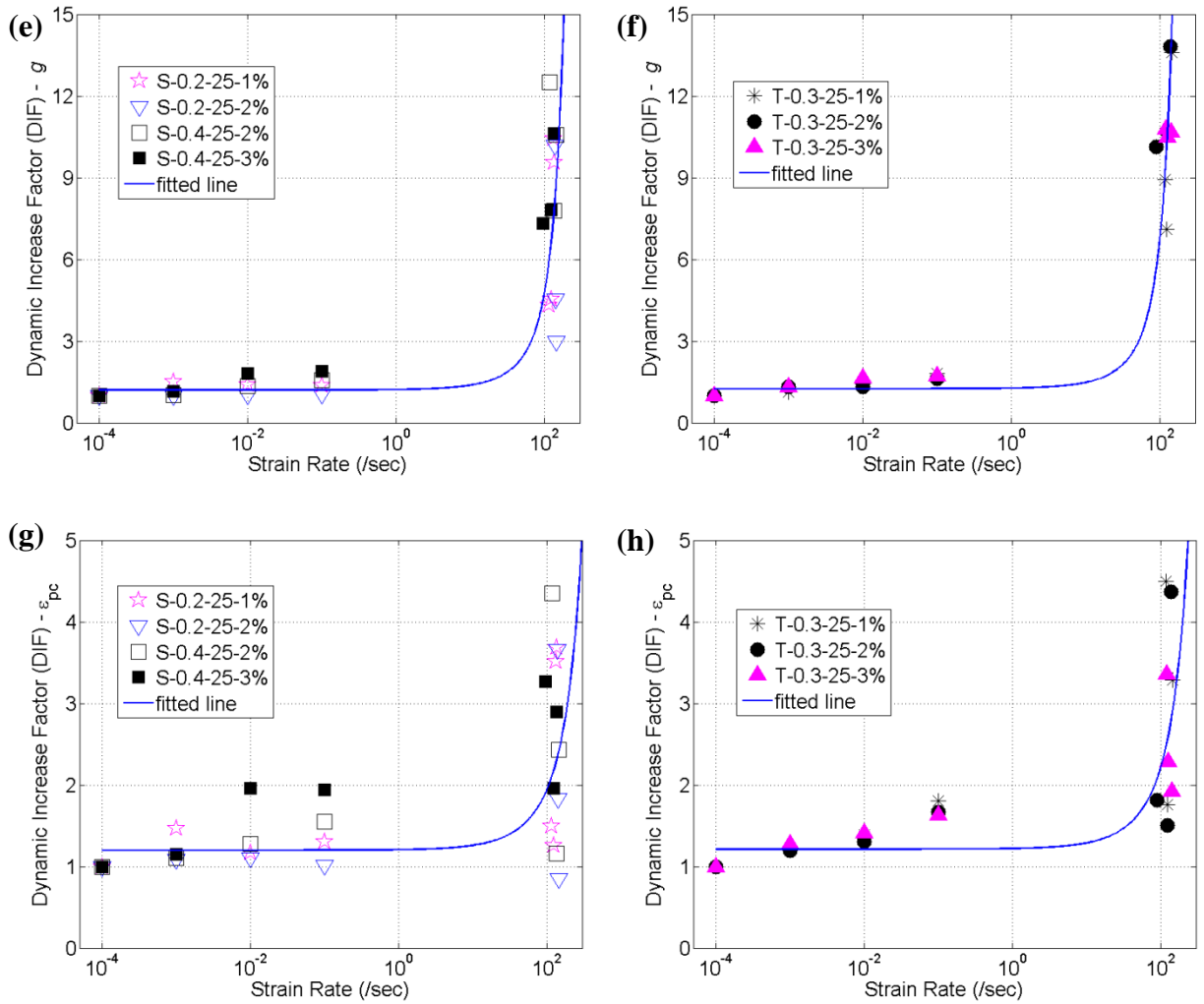


Figure 5.14. continued

5.3.3 Comparison with Theoretical Predictions

Experimental data for high strain rates is compared with theoretical predictions for cement based composites reinforced with short discontinuous fibers to assess whether the theoretical predictions are applicable to impact loading situations. The same theoretical predictions used in Chapter 3 (Equations 3.1, 3.2 and 3.3).

Figures 5.15 and 5.16 illustrate the measured post-cracking strength versus the reinforcing index, and energy absorption capacity versus the product of the fiber length and the reinforcing

index, respectively. The data is plotted for 3 strain rates (0.0001 /sec, 0.1 /sec and impact) and for both twisted and straight fibers. The linear trend predicted by Equation 3.2 is clearly evident in Figure 5.15 for all strain rates. Similarly, as predicted by Equation 3.3, the energy absorption capacity increases linearly with $V_f(l_f^2/d_f)$ for all 3 strain rates considered and for both fiber types. The higher slopes associated with twisted fibers in Figures 5.15b and 5.16b compared to smooth fibers in Figures 5.15a and 5.16a, respectively are an indication that fiber twisting enhances the mechanical properties of UHP-FRC, especially at higher strain rates. The effect is modest for post cracking strength, where the coefficient at impact loading increases from 19.01 (smooth) to 26.18 (twisted), a 37.7% increase (see Figure 5.15). The effect is substantially larger for energy absorption; the coefficient at impact loading increases from 8.26 (smooth) to 18.8 (twisted), a 227.6% increase (see Figure 5.16).

Table 5.2 summarizes fiber tensile stress and equivalent bond strength for impact conditions for different fiber types and volume fractions. It is clear that σ_{fpc} depends on fiber type but is somewhat independent of fiber volume fraction. Smooth fibers with high aspect ratio (S-0.2-25) and twisted fibers (T-0.3-25) show higher σ_{fpc} than smooth fibers with low aspect ratio (S-0.4-25), indicating that fibers are better mobilized in those situations. The high values of σ_{fpc} suggest that the fibers are heavily loaded during impact. In fact, Table 5.2 shows that the average fiber stress, σ_{fpc} , exceeds the static tensile strength as listed in Table 3.3 suggesting that fibers likely see high demands under impact conditions. A close examination of the tested specimens did not clearly show fiber breakage, which implies that Equation 3.1 may not fully capture the mechanics of the impact situation and that some other mechanisms may be at play under impact conditions. Until these mechanisms are clarified through new research, the numbers in Table 5.2 suggest at least one conclusion, that is, it is likely necessary to use high strength fibers with UHP-FRC to ensure good impact response.

Also of note from Table 5.2 is that $\lambda\tau_{eq}$ is independent of fiber volume fraction and aspect ratio for smooth fibers. Twisted fibers, however, showed some dependency on fiber volume fraction and exhibited, on average, a higher equivalent bond strength than smooth fibers. Unlike the lower strain rate cases in Chapter 3, where $\lambda\tau_{eq}$ was seen to be independent of fiber type, the

higher numbers for twisted fibers seen here is likely a manifestation of the greater strain rate sensitivity generally seen in specimens with twisted fibers at high strain rates.

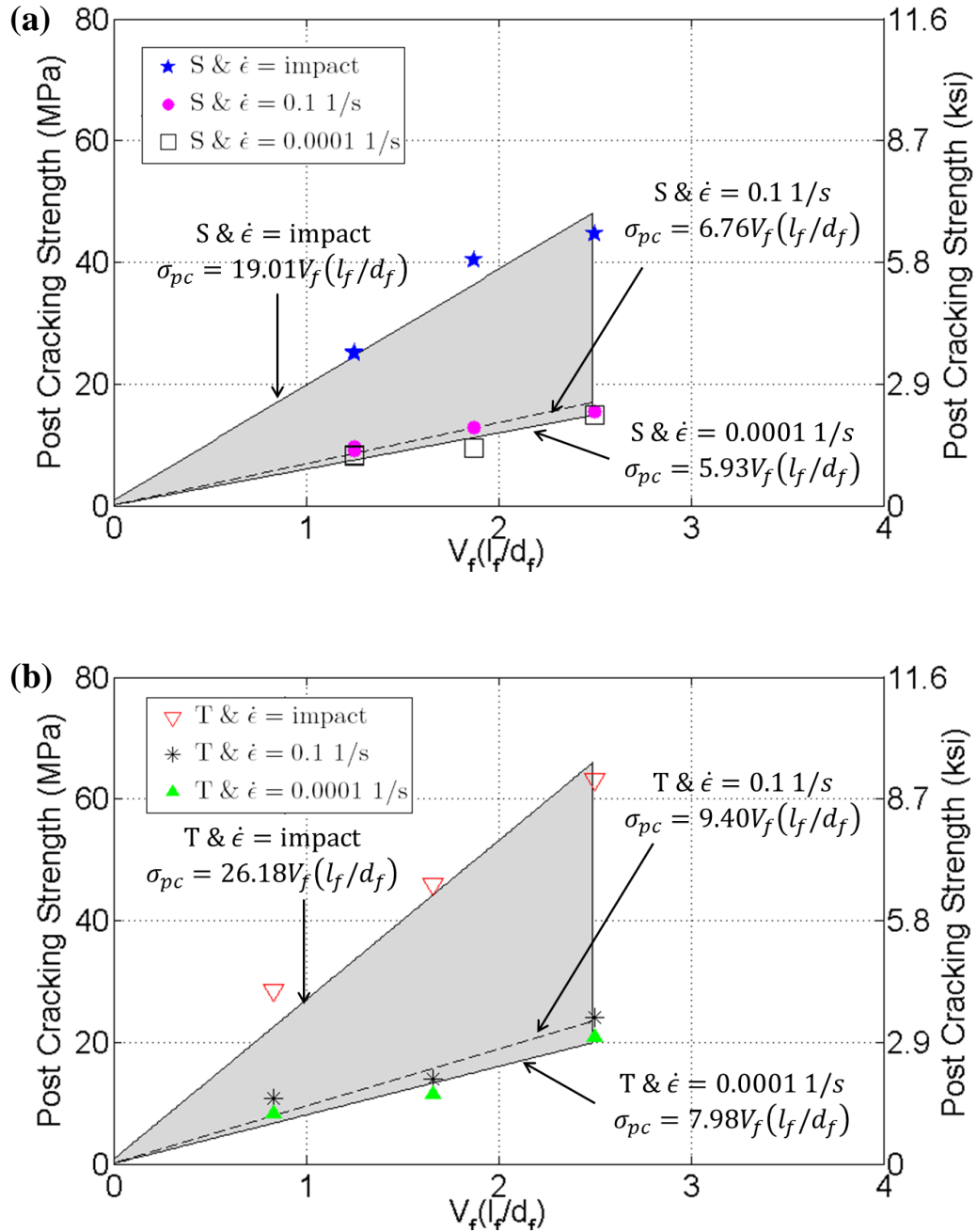


Figure 5.15. Effects of the fiber reinforcing index on post cracking strength: (a) Smooth fibers; (b) Twisted fibers

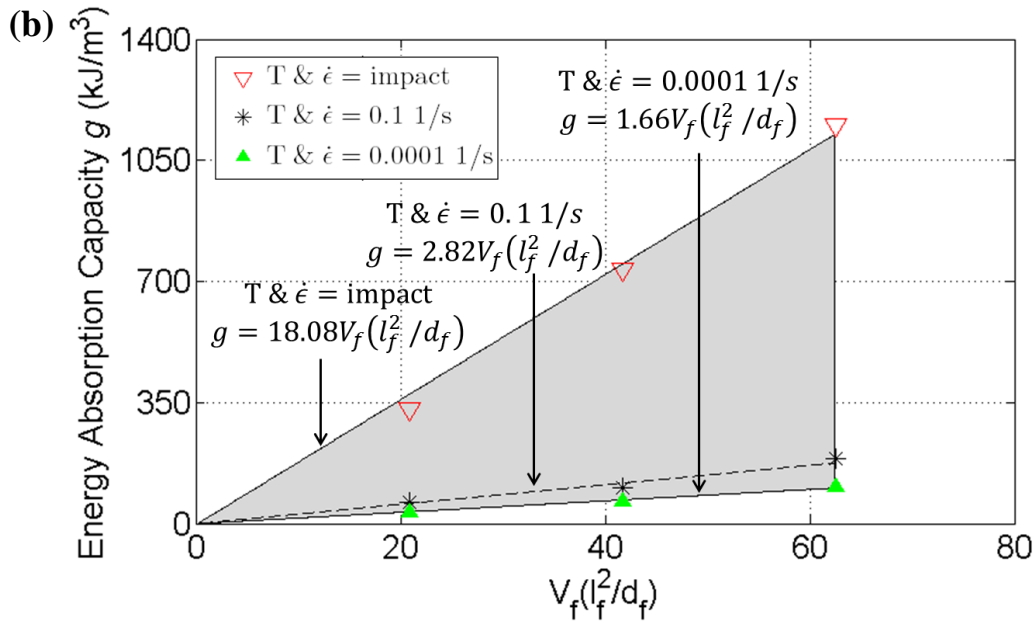
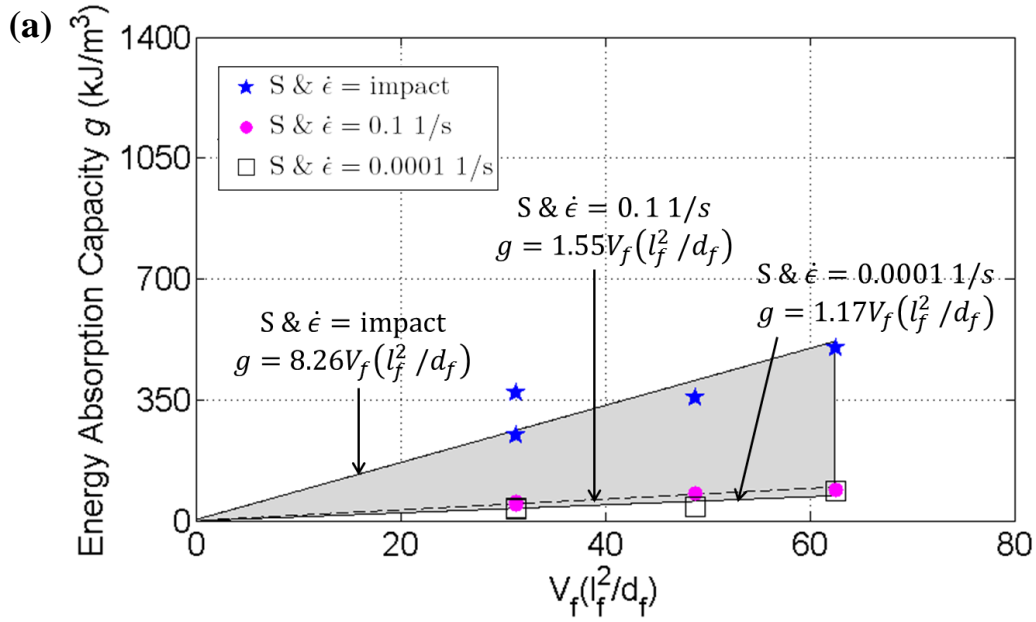


Figure 5.16. Effects of $V_f(l_f^2/d_f)$ on energy absorption capacity of UHP-FRC: (a) Smooth fibers; (b) Twisted fibers

Table 5.2. Fiber tensile stress and equivalent bond strength of UHP-FRC under impact loading

Test series	l_f / d_f	σ_{pc} (MPa)	σ_{fpc} (GPa)	$\lambda\tau_{eq}$ (MPa)
T-0.3-25-1%	83	28.66	3.18	34.5
T-0.3-25-2%	83	45.92	2.55	27.7
T-0.3-25-3%	83	63.16	2.34	25.4
S-0.2-25-1%	125	25.29	2.81	20.2
S-0.2-25-2%	125	44.70	2.48	17.9
S-0.4-25-2%	62.5	24.95	1.39	20.0
S-0.4-25-3%	62.5	40.47	1.50	21.6

5.3.4 Discussion

Many engineering materials become stronger, but more brittle and less energy absorbent, when loaded at high strain rates. Yang and Li (2005) found that the tensile strength of Engineered Cementitious Composite (ECC) reinforced with polyvinyl alcohol (PVA) fibers doubled whereas its strain capacity decreased from 3 % to 0.5 % as strain rate increased from 10^{-5} to 10^{-1} /sec. Sun et al. (2005) concluded that the failure strain of E-Glass/epoxy composites decreased from 16.8% to 9.6% as the strain rate increased to 1600 /sec. Smerd et al. (2005) carried out high strain rate tensile testing of aluminum alloys and found out that energy absorption capacity under high strain rates decreased by up to half of that under quasi-static cases. In contrast, the UHP-FRC material studied in this paper exhibits very different trends. It becomes stronger, more ductile and energy absorbent as strain rate increases. These substantial, and indeed remarkable, improvements at high strain rates suggest that UHP-FRC is a highly damage tolerant material that is well suited for mitigation of blast and impact hazards.

5.4 CONCLUSIONS

This experimental study investigated strain rate effect of UHP-FRC under direct tension using M-SEFIM, developed in Chapter 4. The effect of specimen length on measured properties was investigated and a proper specimen length was identified based on the series of computational and experimental parametric studies. The rate sensitivity of UHP-FRC specimens with three different types of steel fibers, three different lengths, and three different volume

fractions was evaluated in terms of their first cracking strength, post cracking strength, energy absorption capacity and strain capacity under direct tensile loading. The experimental study utilized specimens that were similar in cross-section and material properties to those used in Chapter 3 that focused on pseudo-static loading. That way, the data from both studies covered a large range of strain rates, allowing for a more comprehensive picture of strain rate sensitivity to emerge. The observations and findings of this study can be summarized as follows:

- Strain rates of 90 to 146 /sec were achieved in this study. Crack localization and eventual failure occurred within the gage length in all UHP-FRC specimen and both hardening and softening segments of the stress-strain response were captured. These results demonstrate M-SEFIM's unique capability to conduct impact testing for UHP-FRC and other cementitious composites under direct tension loading, while requiring a minimal footprint.
- The general trend from the test data under impact loading is that strain capacity increases substantially under impact loading for all fiber types. Post cracking strength and energy absorption capacity increase greatly under impact loading.
- Analysis of the experimental data shows that fiber aspect ratio and twisting play important roles in the response of UHP-FRC under tension at high strain rates. Specimens with more slender smooth fibers and with twisted fibers were better able to mobilize the fibers than specimens with stubbier fibers – as evidenced by higher σ_{fpc} values. Moreover, specimens with twisted fibers saw greater increases in post cracking strength and energy absorption capacity compared to those with smooth fibers.
- Extremely high values of σ_{fpc} (maximum stress in the fiber at failure of the composite) were computed, suggesting that the fibers are highly loaded during impact. The high σ_{fpc} values suggest the need to use high strength fibers in UHP-FRC to achieve good performance under impact.
- As with other cement based materials, UHP-FRC exhibits log-linear increases in the DIFs associated with post cracking strength under low strain rates and dramatic

increases in DIFs at high strain rates. Because of the material's unique strain hardening behavior under high strain rate, this trend also translates directly to energy dissipation capacity. These substantial, and indeed remarkable, improvements in mechanical properties at high strain rates suggest that UHP-FRC is a highly damage tolerant material that is well suited for mitigation of blast and impact hazards.

CHAPTER 6

CRACK PROPAGATION SPEED IN ULTRA HIGH PERFORMANCE CONCRETE (UHPC)

The objective of this chapter is to investigate crack speed in UHPC. The experimental parameters are fiber volume fraction, rate of loading and applied strain rate. The tests are conducted on pre-notched three-point bending specimens. A hydraulic servo-controlled testing machine is used to apply lower notch tip strain rates, in the range of 0.0255 to 1.04 /sec, while M-SEFIM is used to achieve higher notch tip strain rates, ranging from 6.79 to 41.1 /sec. As done in Chapters 4 and 5, a high speed camera is used to record UHPC images during testing. The recorded images are used to evaluate notch tip strain and crack speed using the Digital Image Correlation (DIC) technique and the Canny edge detection algorithm, respectively. The critical stress intensity factors for UHPCs with different fiber volume fractions are computed for the low strain rate tests and used to evaluate the effectiveness of fiber reinforcement in improving fracture toughness. The relationships between crack speed and notch tip strain rate of UHPC with different fiber volume fractions are computed from the test data. It is shown that crack speed increases asymptotically as notch tip strain rate increases.

6.1 EXPERIMENTAL PROGRAM

An experimental program was carried out to investigate the crack propagation in ultra high performance concrete (UHPC) as a function of notch tip strain rate. The mix proportions of UHPC with three different volume fractions of fiber are given in Table 6.1. These mixes are different than those used in the previous Chapters, primarily because they have low fiber volume fractions, i.e. 0%, 0.5% and 1% versus 2% or more in other Chapters. Mixes with no fibers were

selected to focus attention on the matrix itself. Matrices with higher fiber volume fractions were not considered because of concern that the crack speed would be too slow to capture with the high speed camera. The mixing technique can be found in Chapter 3. Table 6.2 lists the properties of the steel fibers used in this study. Note that the fiber type is also different from those previously tested. It is a brass coated, smooth fiber, obtained from a South Korean manufacturer (Jiyang Technology).

Table 6.1. Mixtures proportions by weight (based on Wille et al. (2011b))

Fiber Volume Fraction	0 %	0.5 %	1.0 %
Cement	1.00	1.00	1.00
Silica Fume	0.25	0.25	0.25
Glass Powder	0.25	0.25	0.25
Water	0.22	0.22	0.22
Superplasticizer	0.005	0.005	0.005
Sand A [†]	0.28	0.27	0.27
Sand B [§]	1.10	1.09	1.07

[†] Maximum grain size = 0.2 mm (1/128 in.).

[§] Maximum grain size = 0.8 mm (1/32 in.).

Table 6.2. Properties of steel fiber used in this study

Material	Brass coated high carbon steel wire
Shape	Cross section: round / length: straight
Diameter (mm)	0.2 ± 0.01
Length (mm)	19.5
Tensile Strength (MPa)	2450 ~ 2750

Each test series is designated by its fiber volume fraction; e.g. CS-0.5% represents a crack speed (CS) mix with 0.5% fiber volume fraction. Four loading rates are considered in this study. The two lower loading speeds are achieved by using the hydraulic servo-controlled testing system running at 0.0076 and 7.6 mm/sec. The two faster speeds are achieved by M-SEFIM, employing couplers Type 1 and Type 2, as discussed in Section 4.7. The selected loading rates cover a large range of loading speeds allowing for a wide range of crack tip strain rates to be achieved. At least three specimens for each series are tested as summarized in Table 6.3. The

lowest loading speed, 0.0076 mm/sec, is used just for the plain UHPC specimens, i.e. CS-0%, since crack propagation in the fiber reinforced UHPC specimens was too slow to record using the high speed camera.

After 27 days of water curing, the UHPC specimens were left to dry in the laboratory environment for at least 24 hours. Prior to three-point bending testing, additional compressive testing of each series was carried out using cubic specimens with dimensions of 50 x 50 x 50 mm (2 x 2 x 2 in) (see Figure 6.1). The compressive strengths were averaged from at least three specimens and are summarized in Table 6.4.

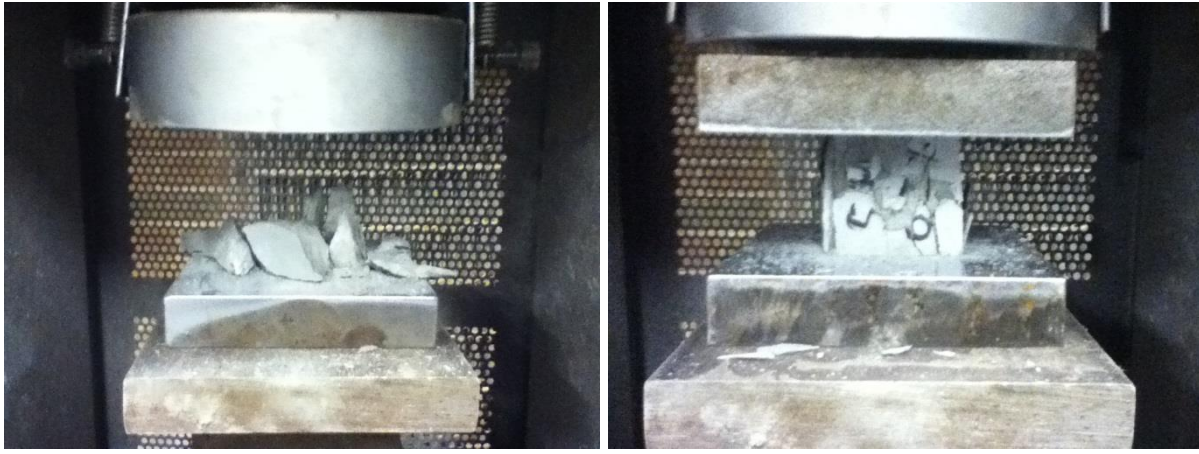
Table 6.3. Number of UHPC specimens investigated in this study

Test series	MTS		Impact Testing Machine	
	0.0076 mm/sec	7.6 mm/sec	Type 1 coupler	Type 2 coupler
CS-0%	3	4	4	3
CS-0.5%	X	3	4	3
CS-1.0%	X	3	4	3

Table 6.4. Mechanical and fracture properties of UHPC

Test series	Compressive stress (MPa)	Critical stress intensity factor, K_{IC} , (MPa \sqrt{m})	
		0.0076 mm/sec	7.6 mm/sec
CS-0%	150.8	5.00	5.46 [†]
CS-0.5%	171.3	N/A	7.19
CS-1.0%	191.2	N/A	14.3

[†] Calculated from one only experiment because of an error in the data acquisition system while testing.



(a)

(b)

Figure 6.1. Specimen failure after compression test: (a) CS-0 %; (b) CS-0.5 %

Figure 6.2 shows a schematic of the pre-notched three-point bending specimen used in this study. The specimen is sized after John et al. (1987), who used it in a 3 point bending configuration for measurement of crack speed in mortar. Figure 6.3 shows a typical UHPC specimen. The specimen is painted white to enhance crack detection. Random speckle patterns are applied around the notch tip to permit usage of the Digital Image Correlation (DIC) technique for measuring notch tip strain (see Chapter 4.6 for details of the DIC technique). The

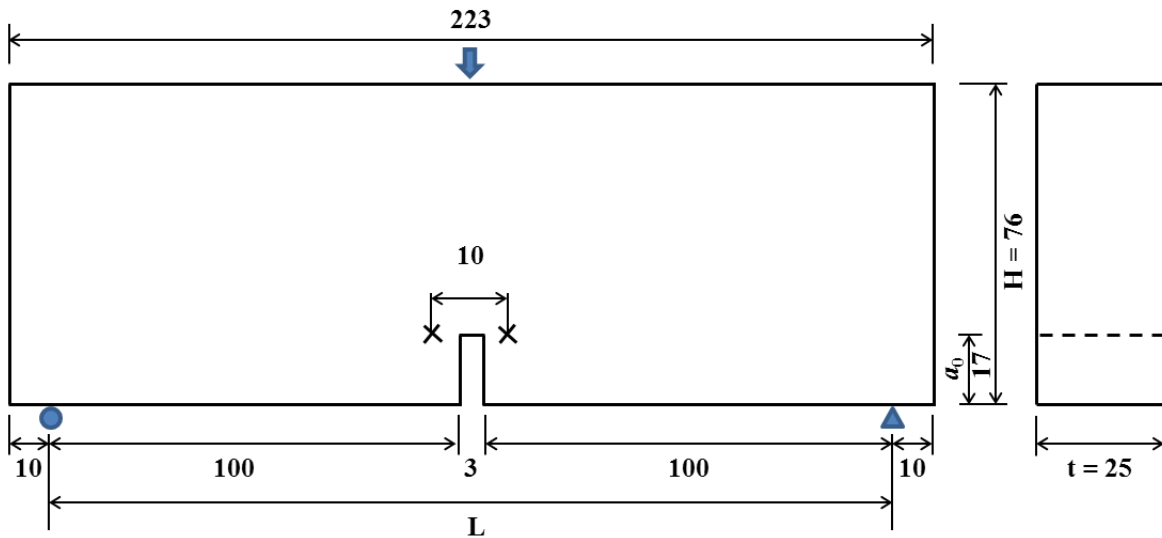


Figure 6.2. Schematic of the specimen employed in the crack speed study (unit: mm)

DIC data allows measurement of displacement along the gage length shown in Figure 6.2. Notch tip strain is then computed from the displacement data by simply dividing displacement by gage length (10 mm). This follows, in spirit, the process used by John et al. (1987), although they used a strain gage attached to the notch tip to measure strain. Figure 6.4 shows the test setup within the hydraulic servo-controlled testing system.

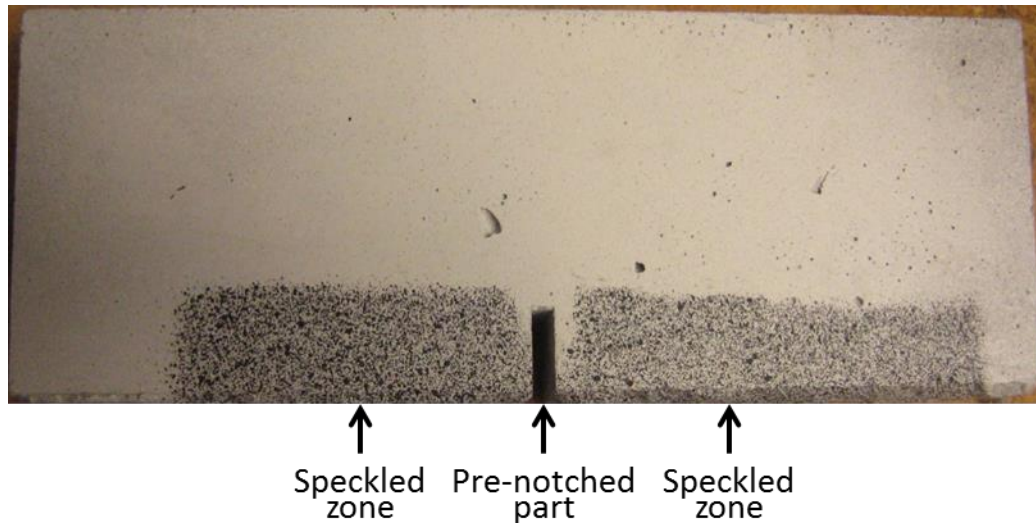


Figure 6.3. Actual UHPC specimen

The impact testing system, M-SEFIM, developed in Chapter 4, was modified to accommodate the new three-point bending test. As previously done, finite element analysis (Figure 6.5a) was conducted to optimize the system and ensure that it works prior to building it. Figure 6.5b shows the modified impact testing setup. The way in which the modified setup works is similar to the basic M-SEFIM. When displacement is applied to the pull bar, the energy bar stores elastic energy. After sudden failure of the coupler, the stored elastic energy in the energy bar is suddenly released and transmitted to the specimen in the form of a load pulse. Notch tip strain and crack speed are calculated by post-processing images of the specimen obtained using the high speed camera.

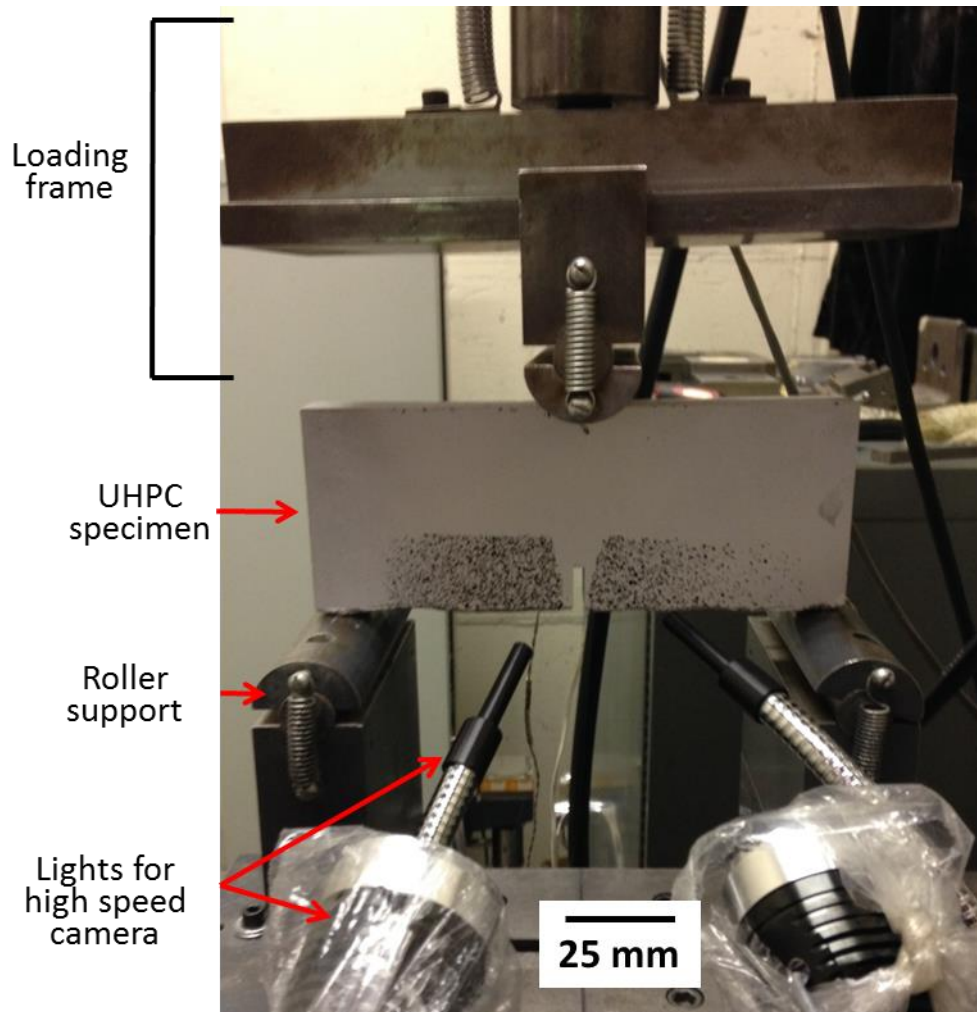


Figure 6.4. Test setup for three-point bending testing using a MTS

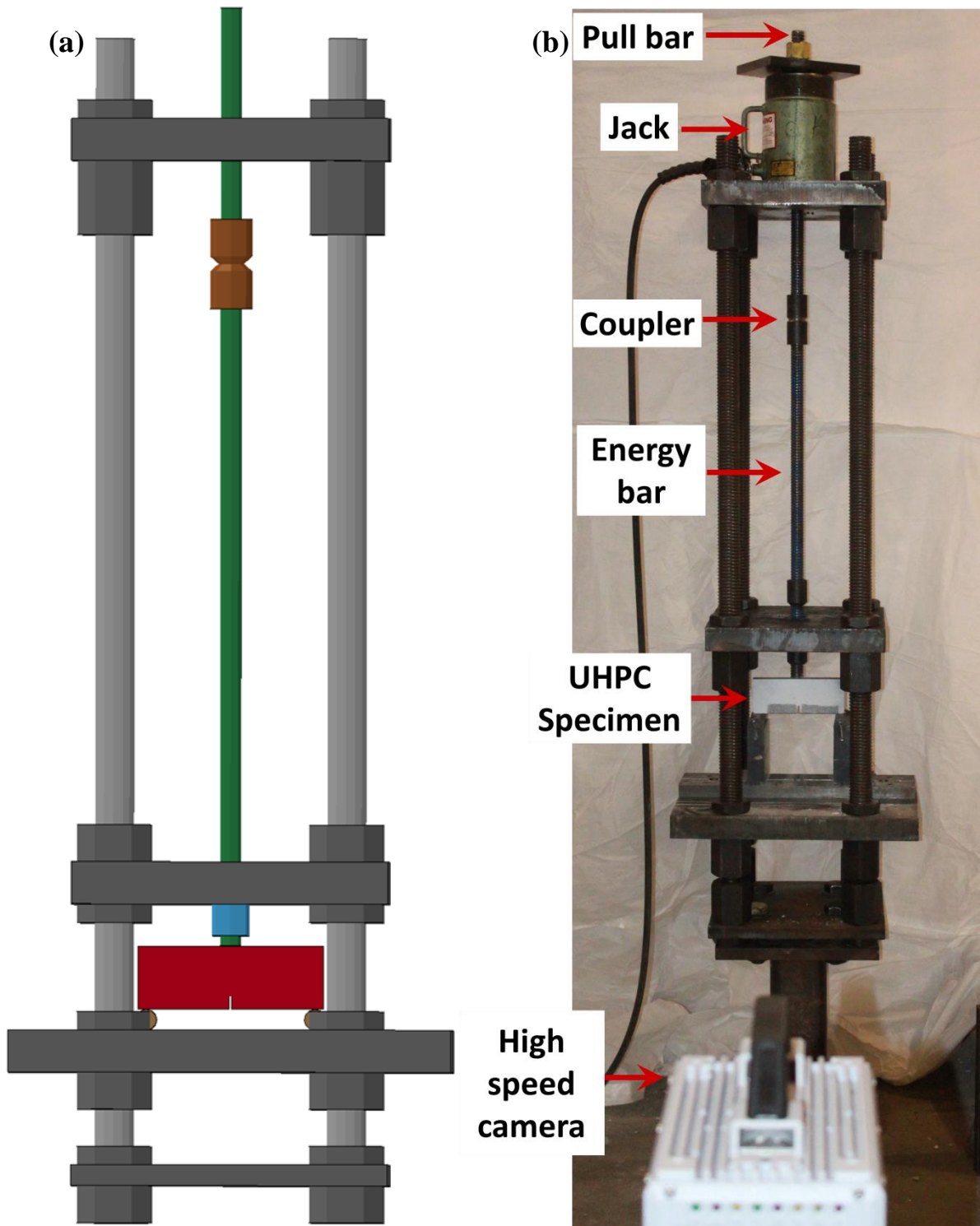


Figure 6.5. Impact testing system for crack propagation: (a) finite element model of the system; (b) as-built setup

6.2 REVIEW OF EDGE DETECTION AND CRACK SPEED ANALYSIS

The images obtained from the high speed camera are post-processed to measure crack tip displacement, which enables calculation of the crack tip speed. In order to extract crack length data from the images, each frame is first queued into an image processing program that runs an edge detection algorithm. Edge detection is achieved using a set of mathematical methods which aim at identifying points in a digital image at which the image brightness changes sharply or, more formally, has discontinuities. Marr and Hildreth (1980) first introduced the theory of edge detection based on zero-crossings of the Laplacian of the Gaussian operator applied to the image. Haralick (1984) determined edges by fitting polynomial functions. Canny (1986) proposed an approximation to the optimal detector as the maxima of the gradient magnitude of a Gaussian-smoothed image. For this study, the Canny edge detection algorithm (Canny 1986) was implemented because it has been shown that it performs better than all these operators under almost all scenarios (Maini and Aggarwal 2009).

The Canny edge detector is an operator capable of detecting a wide range of edges in an image. The Canny algorithm can be divided into five steps. The first step is noise reduction. The Canny method is susceptible to noise present in a raw unprocessed image. The method utilizes a filter, in which the raw image is convolved with a Gaussian. This in turn produces an image that is slightly blurred, minimizing the effect of a single noisy pixel. Step two of the algorithm finds the intensity gradient of the image. Step three finds the direction of the edge (each pixel can be located in only 4 different direction in relation to an adjacent pixel (0, 45, 90, 135) from the gradient. Directions in between those are rounded to the closest angle. Step four applies a non-maximum suppression (edge thinning) technique. Non-maximum suppression is used to trace along the edge in the edge direction and suppress any pixel value (i.e. it sets the pixel equal to 0) that is not considered to be an edge. This will give a thin line in the output image. The final step includes thresholding, requiring two thresholds, one high and one low. The algorithm first applies the high threshold, marking out the real edges. Using the directional information derived earlier, those edges can then be traced through the image. While tracing the edge, the algorithm applies the lower threshold, allowing the algorithm to trace faint sections of edges.

At the completion of the algorithm, the output binary image contains a matrix of pixels marked as either an edge pixel or a non-edge pixel. This binary image can then be plotted, and the image edges can be seen. Since the image outputted from the Canny algorithm is a binary (the pixel values are either 1 or 0), a simple count of the “on” or “1” pixels can be accomplished, with the total numbers of “on” pixels are directly related to the total length of the crack. The total image resolution (x pixels by y pixels) can be converted to the length and width of the specimens, making the calculation for the length of the crack very simple. Since the frame rate at which the camera recorded the images is known, then the time in between increments in crack length can be determined. From this, the crack tip speed can be easily recorded.

6.3 EVALUATION OF EXPERIMENTAL RESULTS

6.3.1 Critical Stress Intensity Factor

Experimental results from the slow rate tests are used to determine the critical stress intensity factor, K_{IC} , which is a key parameter that characterizes crack stability under service loads and provides a measure of the effectiveness of steel fiber reinforcement in UHPC. The critical stress intensity factor for a pre-notched three-point bending specimen is calculated using Equation (6.1) (Shah 1990, Wardeh and Ghorbel 2013):

$$K_{IC} = \sigma_{NC} \sqrt{\pi a_0} f_1(\alpha_0) \quad (6.1)$$

in which

$$f_1(\alpha) = \frac{1.99 - \alpha(1 - \alpha)(2.15 - 3.93\alpha + 2.7\alpha^2)}{\sqrt{\pi}(1 + 2\alpha)(1 - \alpha)^{3/2}} \quad (6.2)$$

and $\alpha_0 = \frac{a_0}{H}$, $\sigma_{NC} = \frac{3P_{max}L}{2tH^2}$ and P_{max} is the maximum measured load plus the self-weight of the tested beam. All dimensions are given in Figure 6.2.

The computed results of the critical stress intensity factor are given in Table 6.4. It should be noted that only one value for the load data was recorded in CS-0% for the 7.6 mm/sec loading speed because of error in the data acquisition system while testing. Based on the calculated values, it is clear that the effect of loading rate on the critical stress intensity factor is not significant. It can also be seen that the critical stress intensity factor increases substantially as fiber volume fraction increases, i.e. 31.8% and 162% increase for CS-0.5% and CS-1.0% series compared to CS-0%, respectively. In contrast, the compressive strength increases by 13.6% and 26.8% in CS-0.5% and CS-1.0% compared to CS-0%. These results indicate that fiber reinforcement has a greater effect on fracture toughness than on compressive strength.

Figure 6.6 shows examples of load curves for the slow loading rate cases. It can be seen from Figure 6.6 that CS-0% shows brittle failure without a significant softening region, and thus shows fast crack speed even under slow loading rates. In contrast, CS-0.5% and CS-1.0%, show somewhat more ductile failure patterns, which allows large energy dissipation and leads to slower crack speed under slow loading rates.

6.3.2 Crack Speed in UHPC

The high speed camera used to capture images of crack growth runs at 75,000 frames per second with a resolution of 256×256 pixels when slow loading is applied (during testing with the hydraulic servo-controlled testing machine) and at 150,000 frames per second with a resolution of 256×144 pixels when fast loading is applied (M-SEFIM testing). Figures 6.7 to 6.9 show examples of the captured crack propagation images in CS-0%, CS-0.5% and CS-1.0% under various loading speeds. Multiple cracking patterns developed in many CS-1.0% specimens. For specimens with multiple cracking patterns, crack speeds are calculated by only tracking the initial crack. For example, two major cracks developed in the specimen shown in Figure 6.9a in a sequential manner, i.e. the right side crack developed first followed by the left side crack. Per the protocol discussed above, only the right side crack is accounted for in the crack speed calculation. Strain rate is computed as an average of the strain time history during which strain increases from zero to the point where the first crack initiates, typically at about 0.0165 % strain. This also follows in spirit the process used by John et al. (1987). Figure 6.10 shows examples of the strain rate calculations, while Table 6.5 summarizes the obtained rate results.

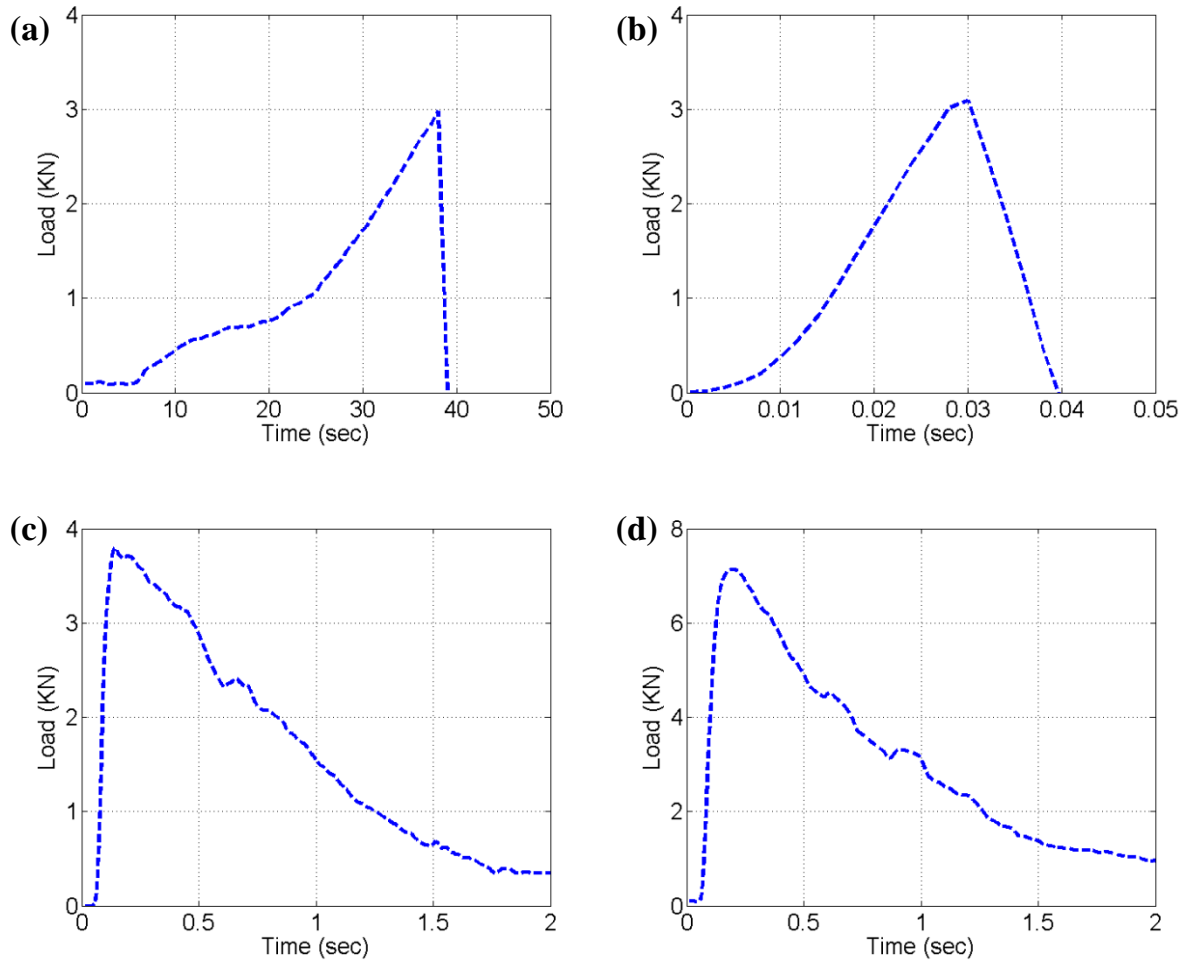


Figure 6.6. Examples of load curves for the slow loading cases: (a) CS-0% tested at 0.0076 mm/sec; (b) CS-0% tested at 7.6 mm/sec; (c) CS-0.5% tested at 7.6 mm/sec; (d) CS-1% tested at 7.6 mm/sec

Crack speed is calculated by averaging the slope of the crack length curves in this study (see Figure 6.15). Figure 6.11 shows an example of crack edge detection using the Canny edge detector. It is clear from the figure that the Canny edge detector algorithm works well for calculating crack speed from the experimental data. Figures 6.12 to 6.14 show examples of the final crack stages for CS-0%, CS-0.5% and CS-1.0% specimens under various loading speeds. Figure 6.15 illustrates examples of crack speed histories and averaged speeds. Table 6.5 summarizes all crack speed results from the experiments while Figure 6.16 shows the calculated relationships between crack speed and notch tip strain rate for UHPC.

Table 6.5. Summary of crack speed results

Test series	Loading speed in MTS (mm/sec)	Notch tip strain rate (/sec)	Crack speed (m/sec)	Test series	Coupler type in the impact testing machine	Notch tip strain rate (/sec)	Crack speed (m/sec)
CS-0%	0.0076	0.0255	135	CS-0%	Type 1	16.0	1117
		0.0424	206			19.3	1420
		0.0589	306			20.9	876
		0.102	514			24.9	1058
	7.6	0.205	510		Type 2	14.5	1201
		0.364	255			18.3	963
		1.04	283			32.5	1013
		CS-0.5%	7.6			0.0347	3.61
0.0798	15.0			13.7	1079		
0.203	3.98			20.1	1454		
0.0347	3.61			21.3	1123		
7.6	0.0798		15.0	Type 2	12.5	1442	
	0.203		3.98		20.9	1302	
	0.0408		1.90		41.1	827	
	CS-1.0%		7.6		0.108	1.32	CS-1.0%
0.200		4.12		13.8	1380		
0.0408		1.90		17.2	1126		
0.108		1.32		20.5	1406		
7.6		0.200	4.12	Type 2	18.6	1009	
		0.0408	1.90		23.1	1072	
		0.108	1.32		33.0	1127	
		0.200	4.12				

For the purpose of reference, the theoretical crack speed (i.e. the Rayleigh wave speed) is also plotted in the figure. The Rayleigh wave speed for compressible isotropic elastic solids can be calculated by Equation (6.3) (Rayleigh 1885, Vinh and Ogden 2004):

$$(2 - x)^2 = 4\sqrt{1 - x}\sqrt{1 - \gamma x} \quad (6.3)$$

where

$$x = \frac{c^2}{c_2^2}, \quad c_2^2 = \frac{\mu}{\rho}, \quad 0 < x < 1, \quad 0 < \gamma \equiv \frac{\mu}{\lambda + 2\mu} < 1 \quad (6.4)$$

and ρ is the mass density of the material, c is the Rayleigh wave speed and μ and λ are the classical Lamé moduli. For UHPC with $E = 50$ GPa, $\nu = 0.18$, $\rho = 2,550$ kg/m³ (Graybeal 2006), the Rayleigh wave speed is 2616 m/s, where E is Young's modulus and ν is Poisson's ratio.

Several observations can be made from Figure 6.16. The UHPC series with fiber reinforcement show much lower crack speed than UHPC without fibers at the lower loading speeds (achieved using the MTS hydraulic machine), which indicates that steel fiber reinforcement plays an important role in resisting crack opening at such speeds. In contrast, all UHPC series show similar crack speeds at higher loading rates, suggesting that cracking is independent of fiber reinforcement at these higher loading rates – although the CS-0% series failed right after crack propagation, while CS-0.5% and CS-1.0% series continued to resist load after matrix cracking up to the point where fibers are pulled-out from the matrix. Figure 6.16 also shows that crack speed increases asymptotically as strain rate increases and that the maximum asymptotic crack speed is below the theoretical maximum. The experimentally obtained data can be fitted as:

$$\begin{aligned}
 v &= 323 \log(\dot{\epsilon}) + 657 && \text{for CS} - 0\% \\
 v &= 470 \log(\dot{\epsilon}) + 567 && \text{for CS} - 0.5\% \\
 v &= 494 \log(\dot{\epsilon}) + 535 && \text{for CS} - 1.0\%
 \end{aligned}
 \tag{6.5}$$

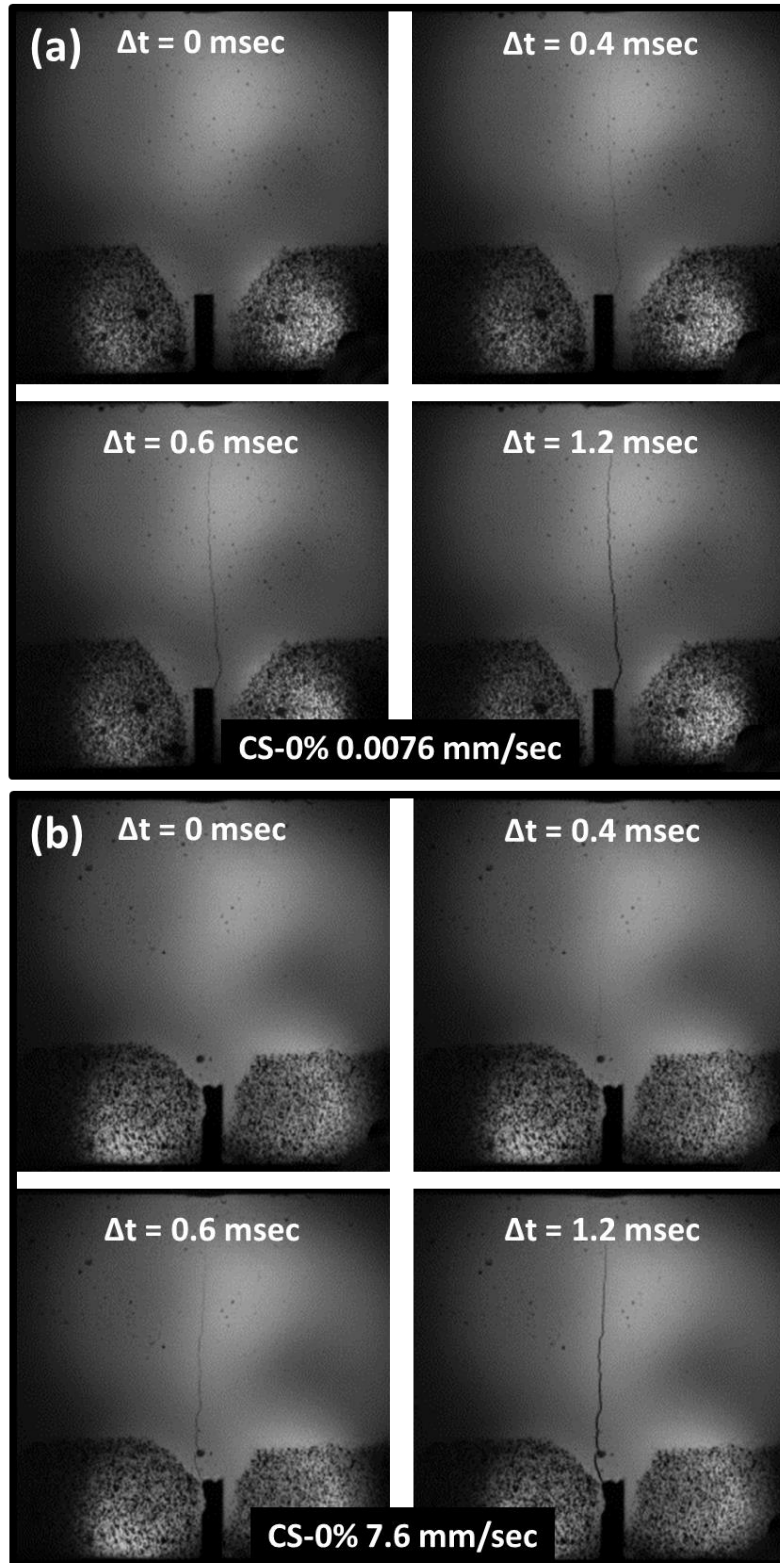


Figure 6.7. Examples of crack propagation in CS-0% specimens under various loading speed: (a) 0.0076 mm/sec (using MTS machine); (b) 7.6 mm/sec (using MTS machine); (c) Type 1 coupler (M-SEFIM); (d) Type 2 coupler (M-SEFIM)

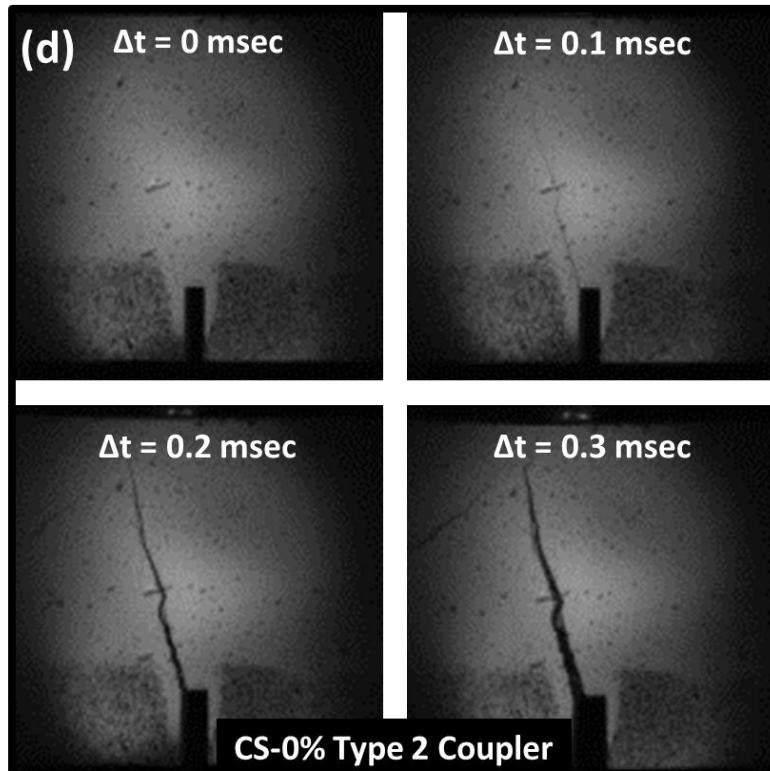
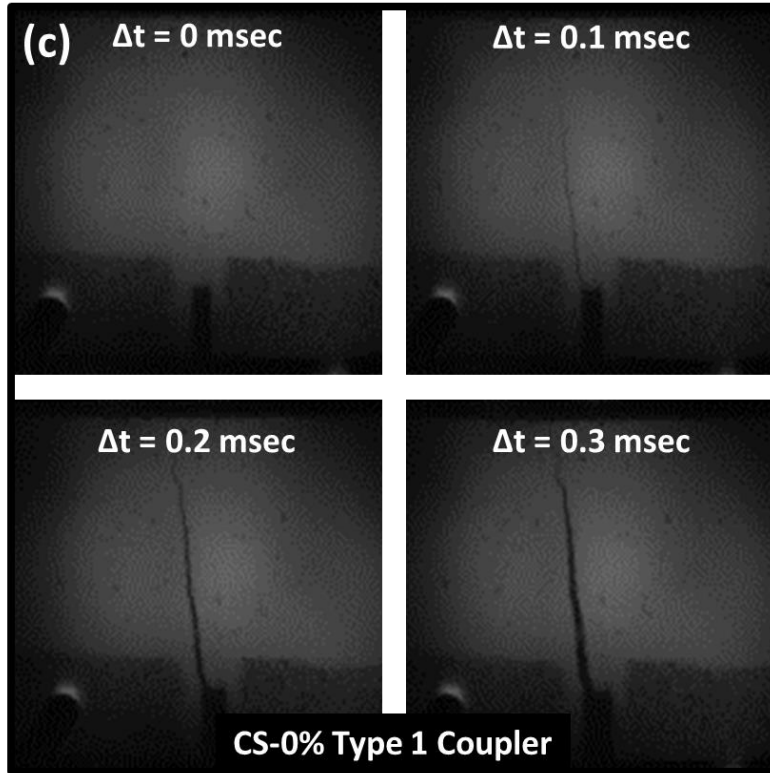


Figure 6.7. continued

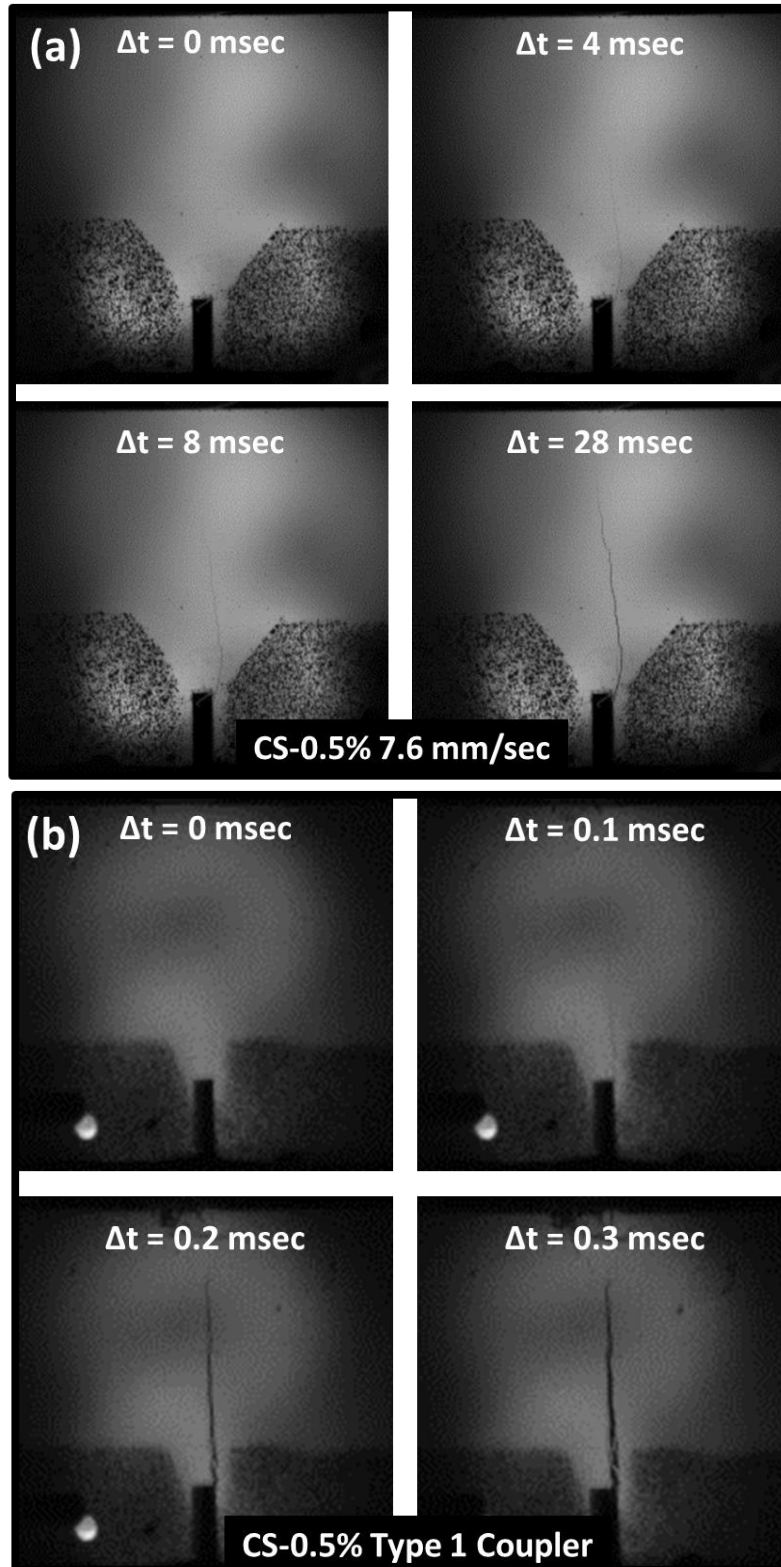


Figure 6.8. Examples of crack propagation in CS-0.5% specimens under various loading speed: (a) 7.6 mm/sec using MTS; (b) Type 1 coupler using the impact testing system; (c) Type 2 coupler using the impact testing system

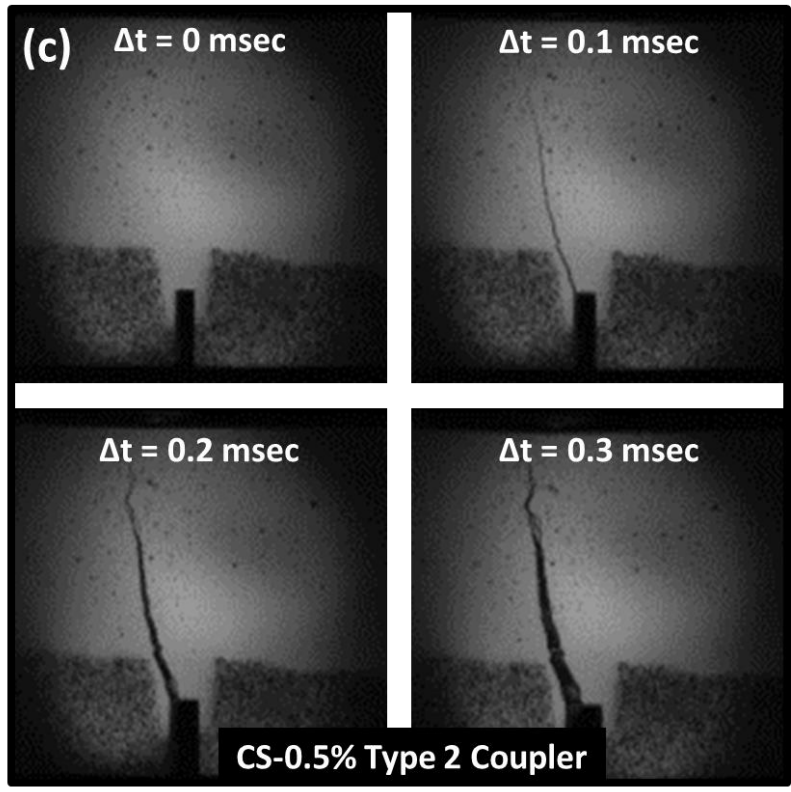


Figure 6.8. continued

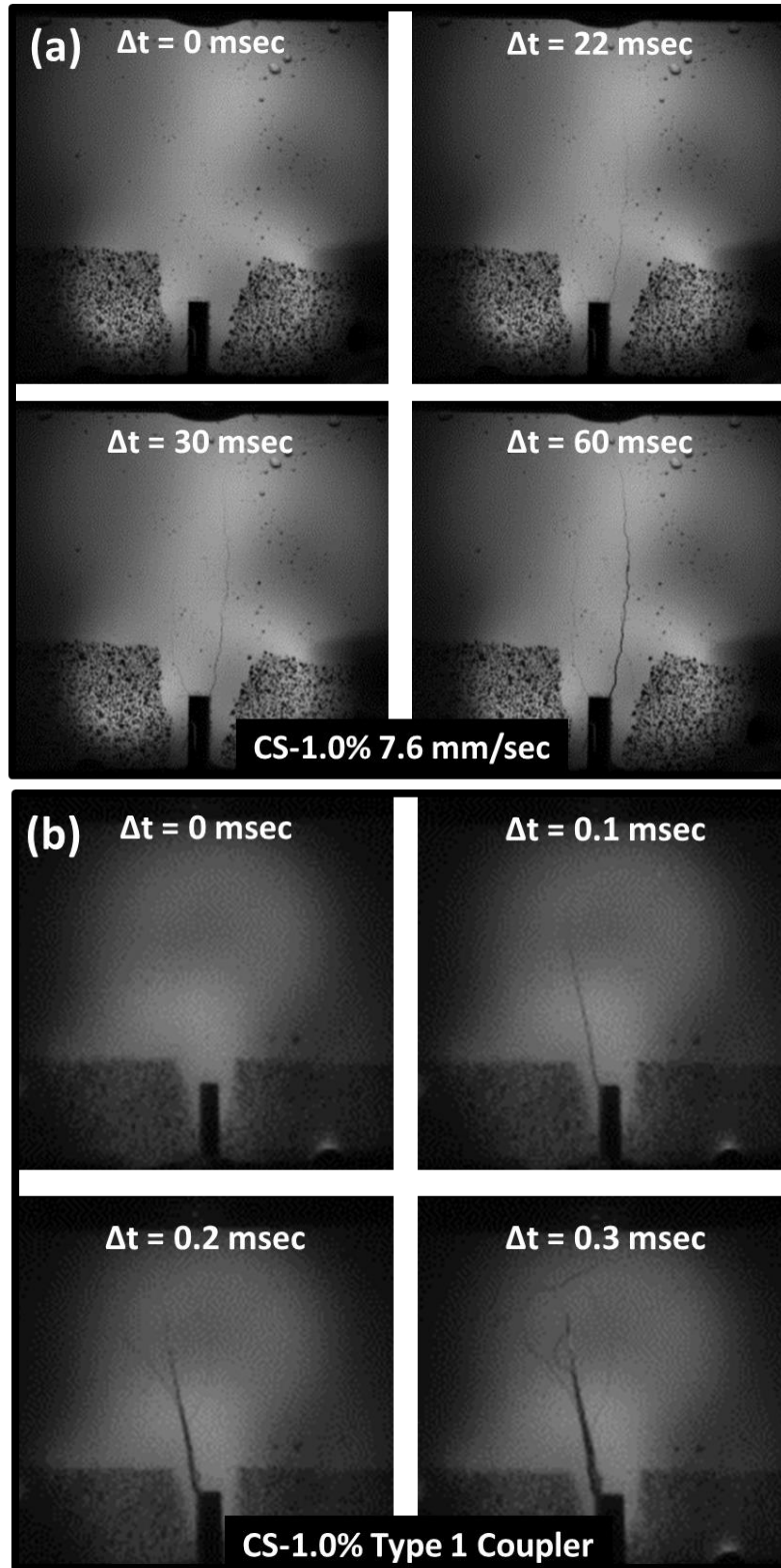


Figure 6.9. Examples of crack propagation in CS-1.0% specimens under various loading speed: (a) 7.6 mm/sec (using the MTS machine); (b) Type 1 coupler (using M-SEFIM); (c) Type 2 coupler (using M-SEFIM)

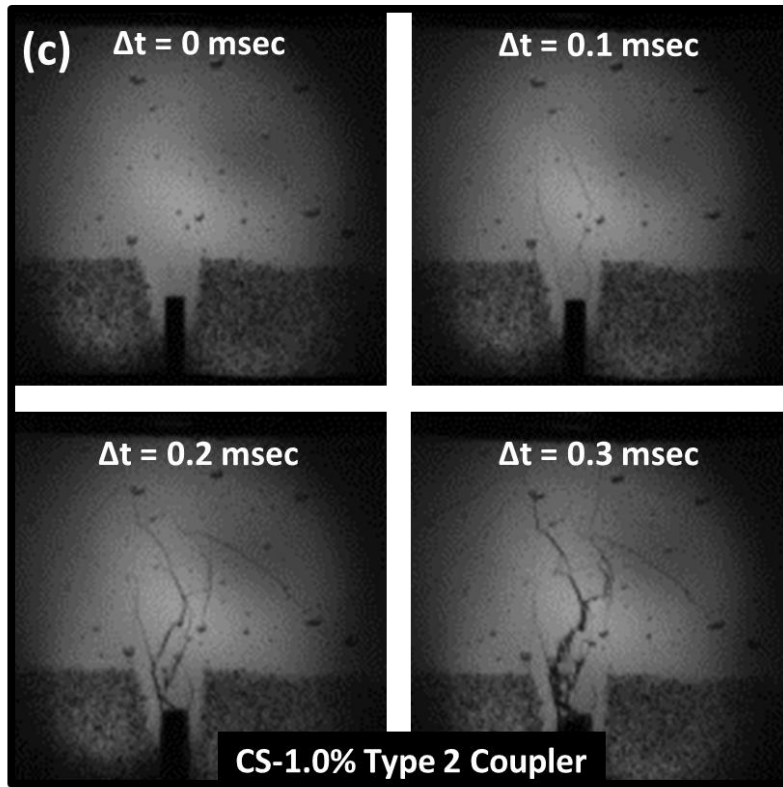


Figure 6.9. continued

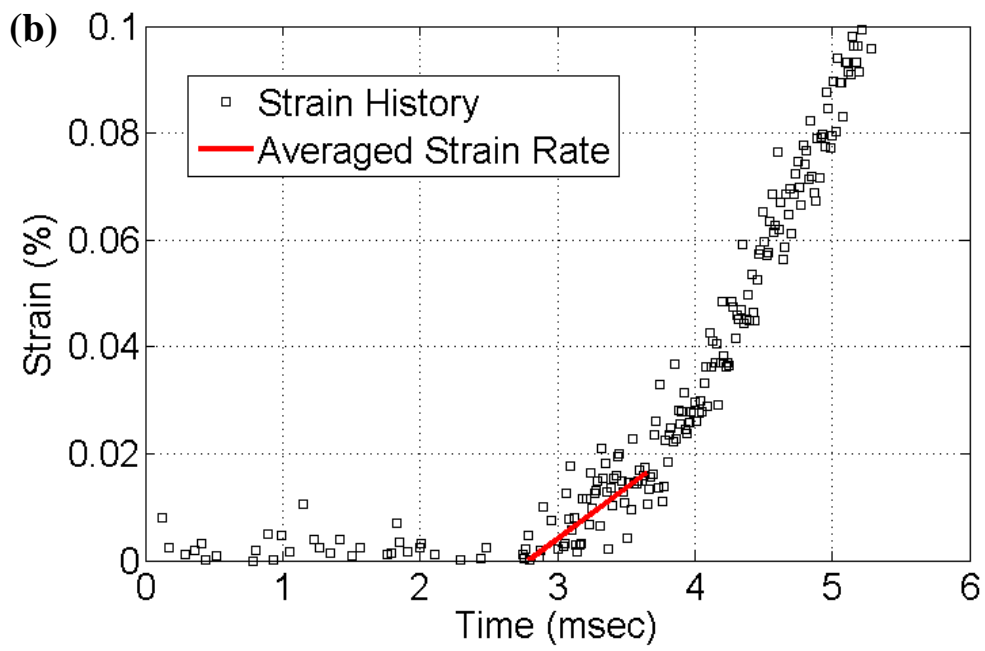
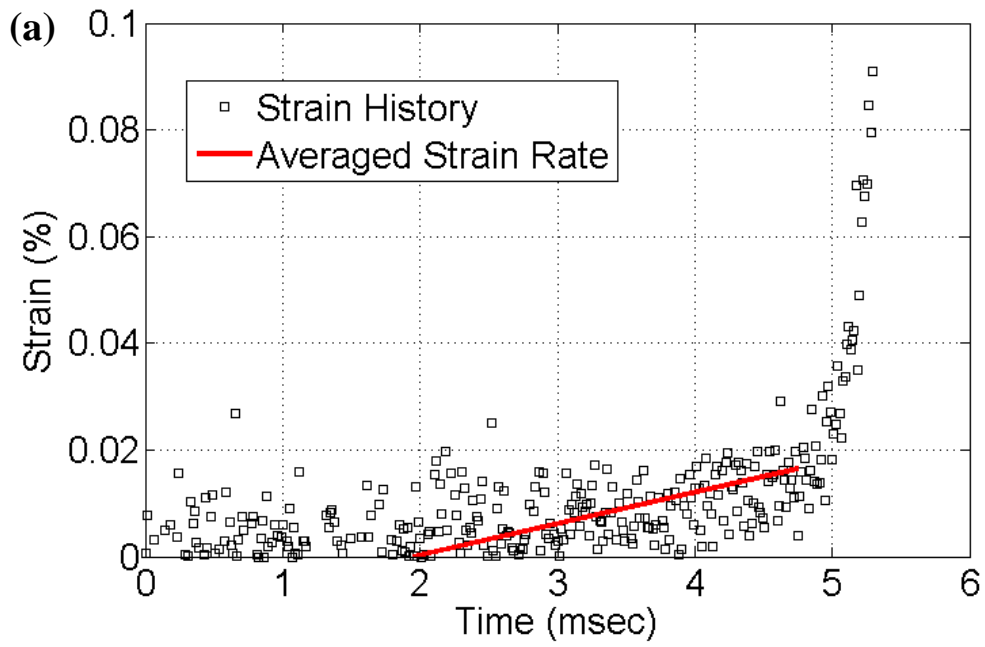


Figure 6.10. Examples of strain rate calculations: (a) CS-0% tested at 0.0076 mm/sec (0.0589 /sec); (b) CS-0.5% tested at 7.6 mm/sec (0.203 /sec)

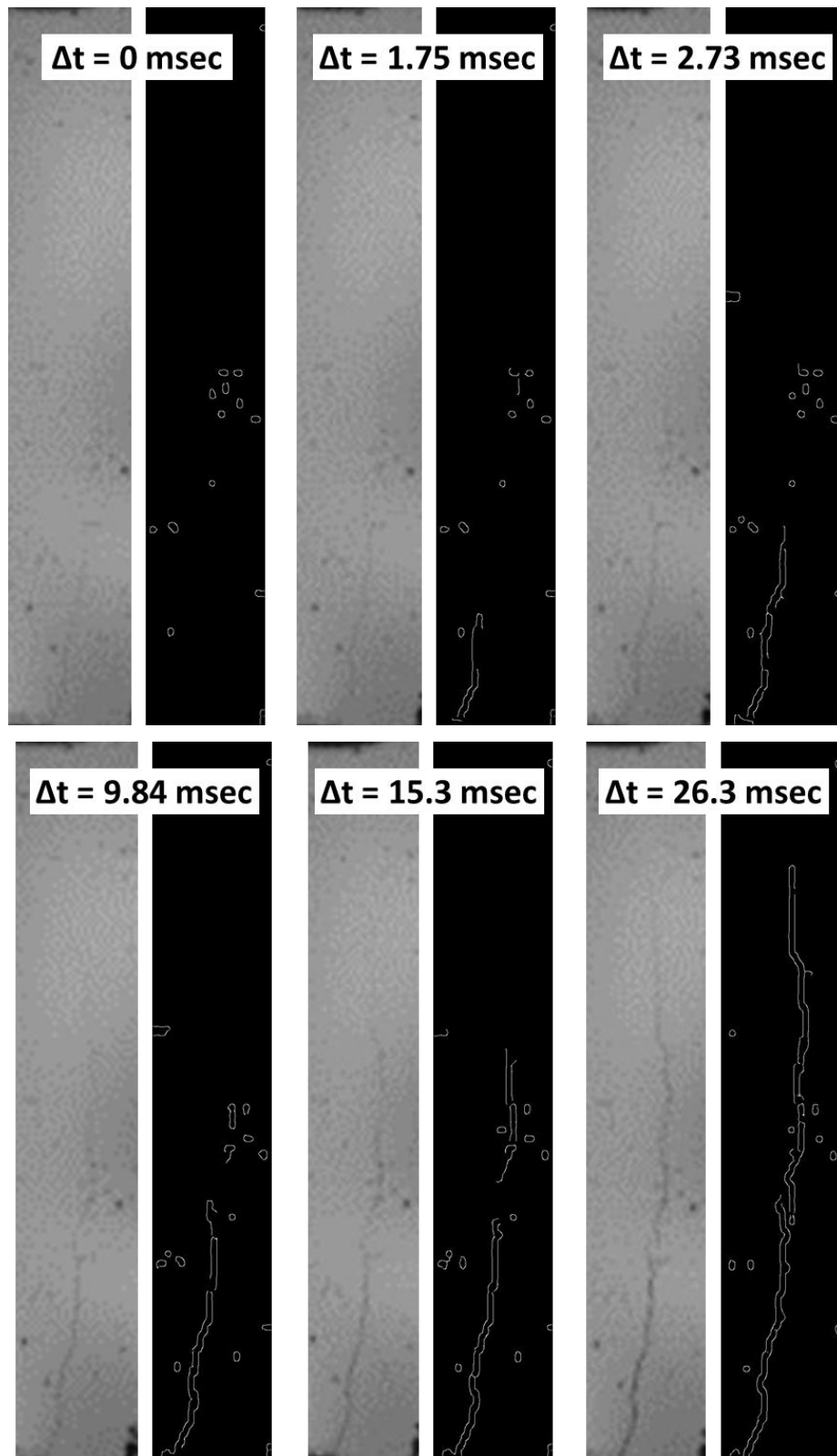


Figure 6.11. Example of crack edge detection in a CS-1.0% specimen for 7.6 mm/sec loading speed (using the MTS machine)

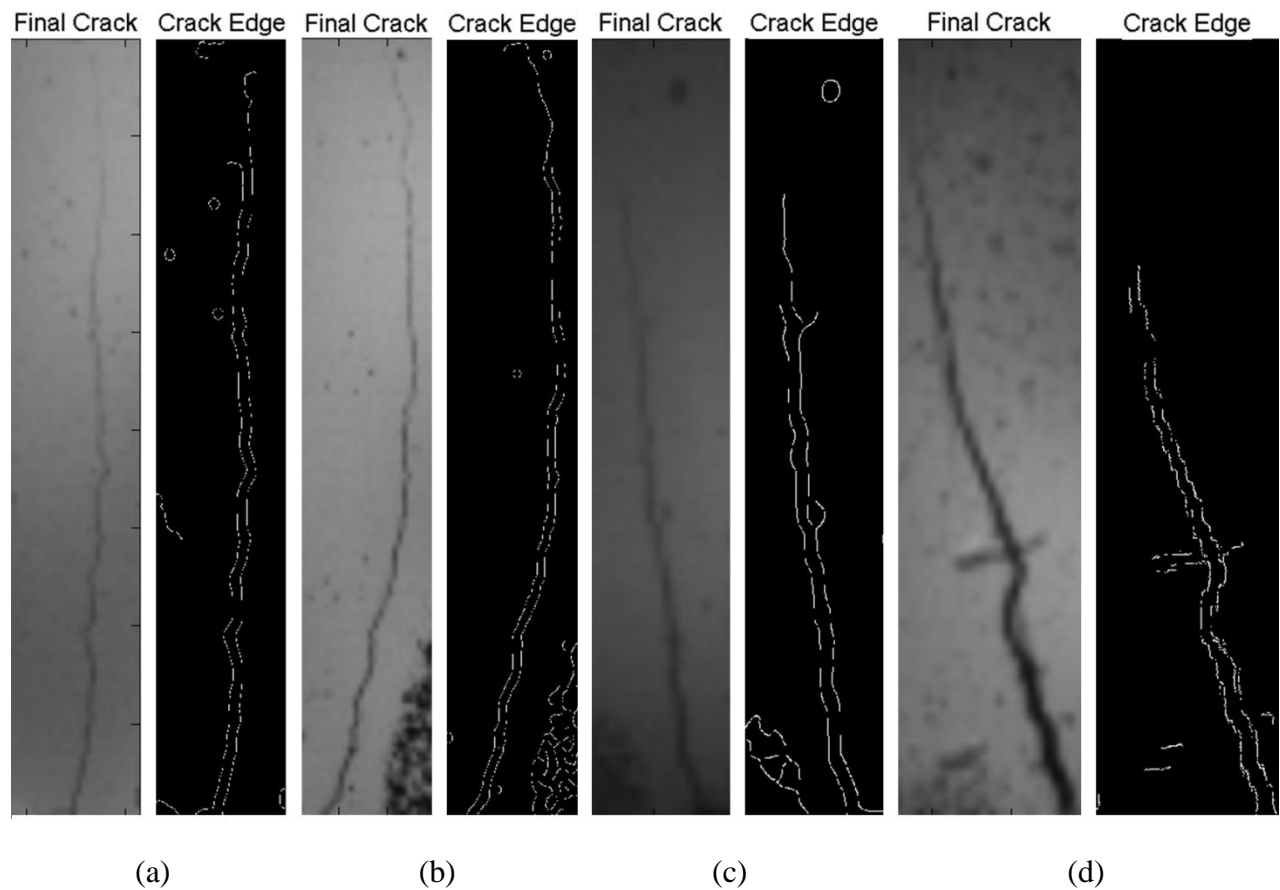


Figure 6.12. Examples of the final crack stage in captured and calculated images for CS-0% specimens under various loading speed: (a) 0.0076 mm/sec (using the MTS machine); (b) 7.6 mm/sec (using the MTS machine); (c) Type 1 coupler (using M-SEFIM); (d) Type 2 coupler using (M-SEFIM)

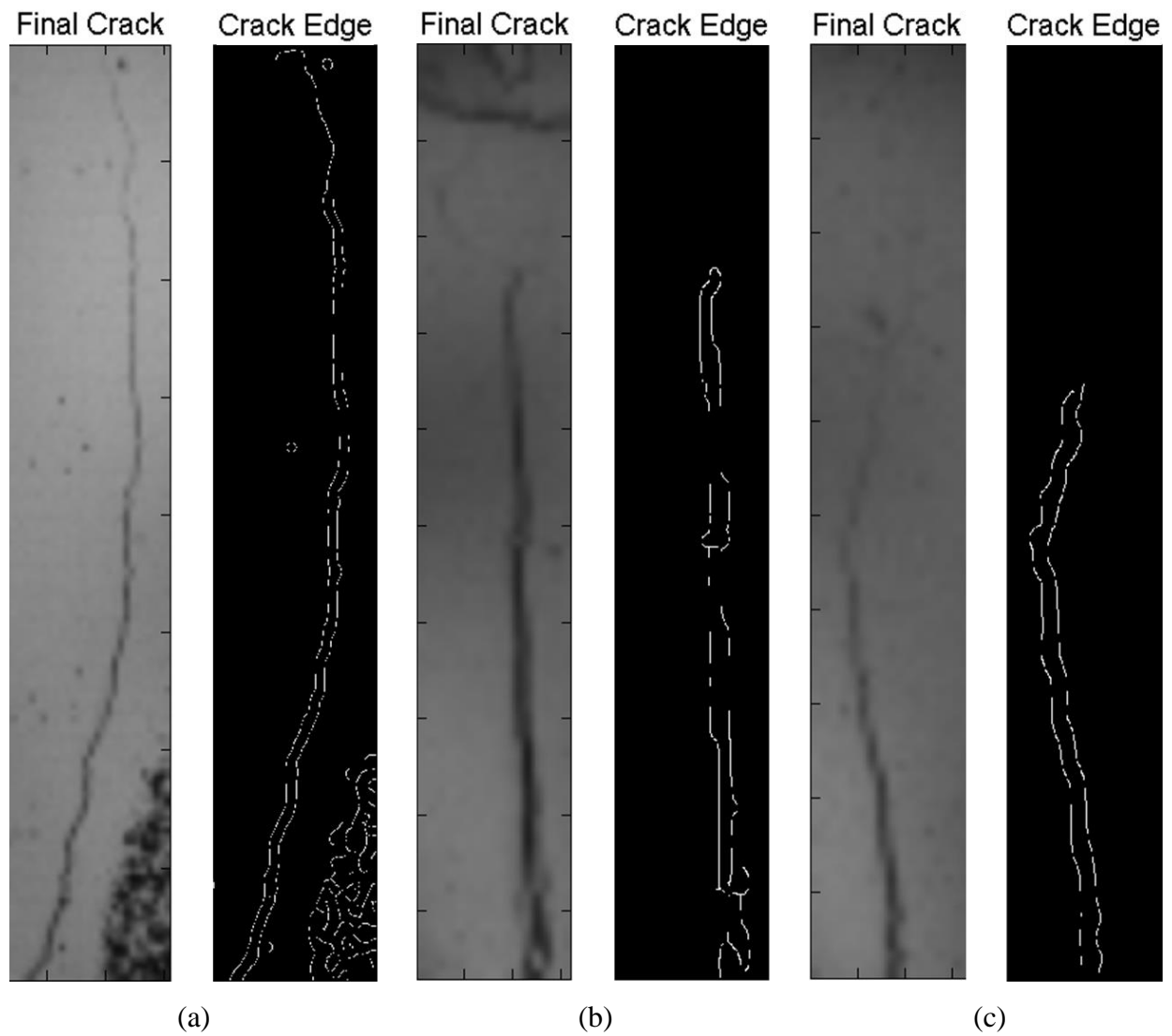


Figure 6.13. Examples of the final crack stage in captured and calculated images for CS-0.5% specimens under various loading speed: (a) 7.6 mm/sec (using the MTS machine); (b) Type 1 coupler (using M-SEFIM); (c) Type 2 coupler (using M-SEFIM)

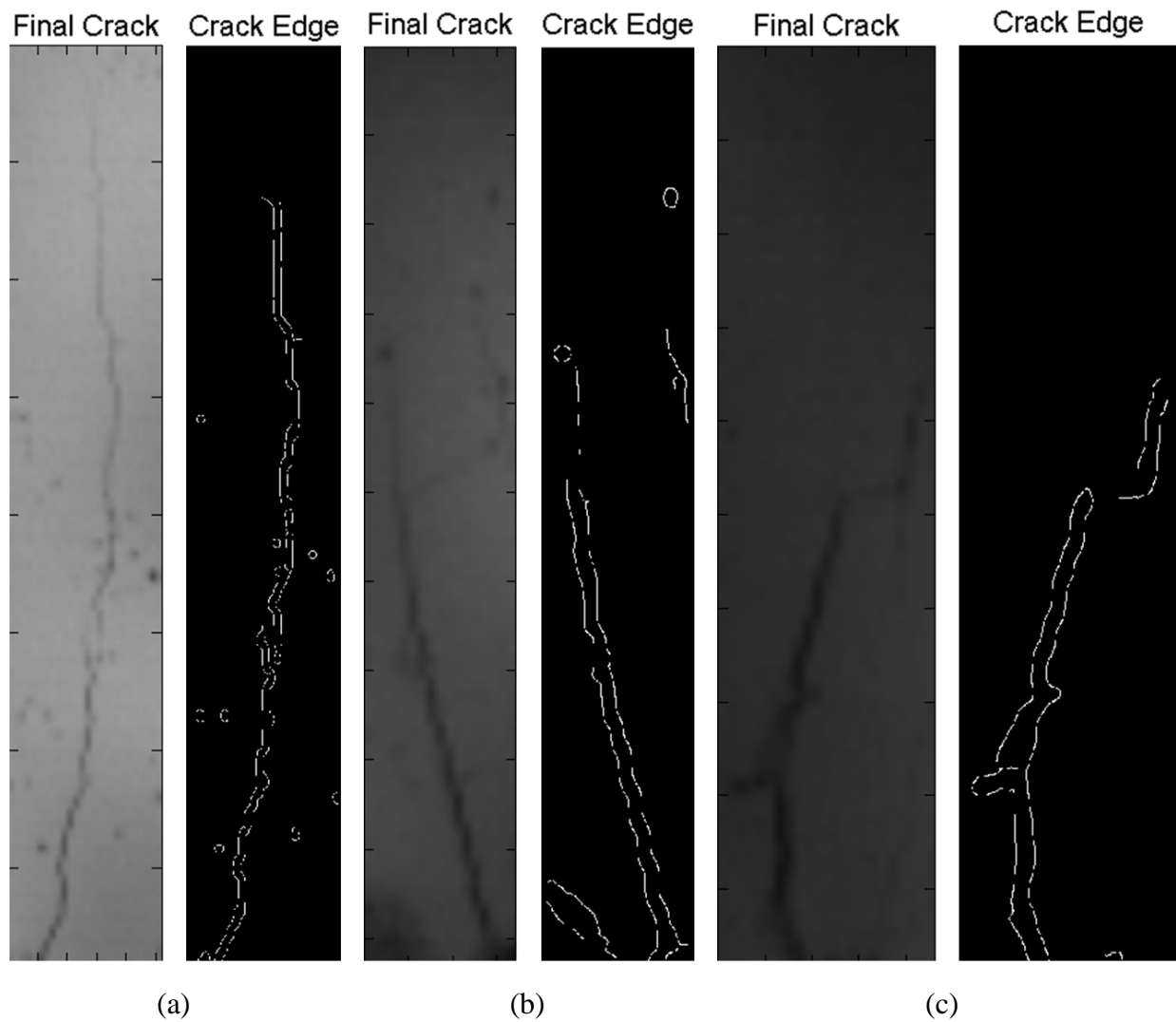


Figure 6.14. Examples of the final crack stage in captured and calculated images for CS-1.0% specimens under various loading speed: (a) 7.6 mm/sec (using the MTS machine); (b) Type 1 coupler (using M-SEFIM); (c) Type 2 coupler (using M-SEFIM)

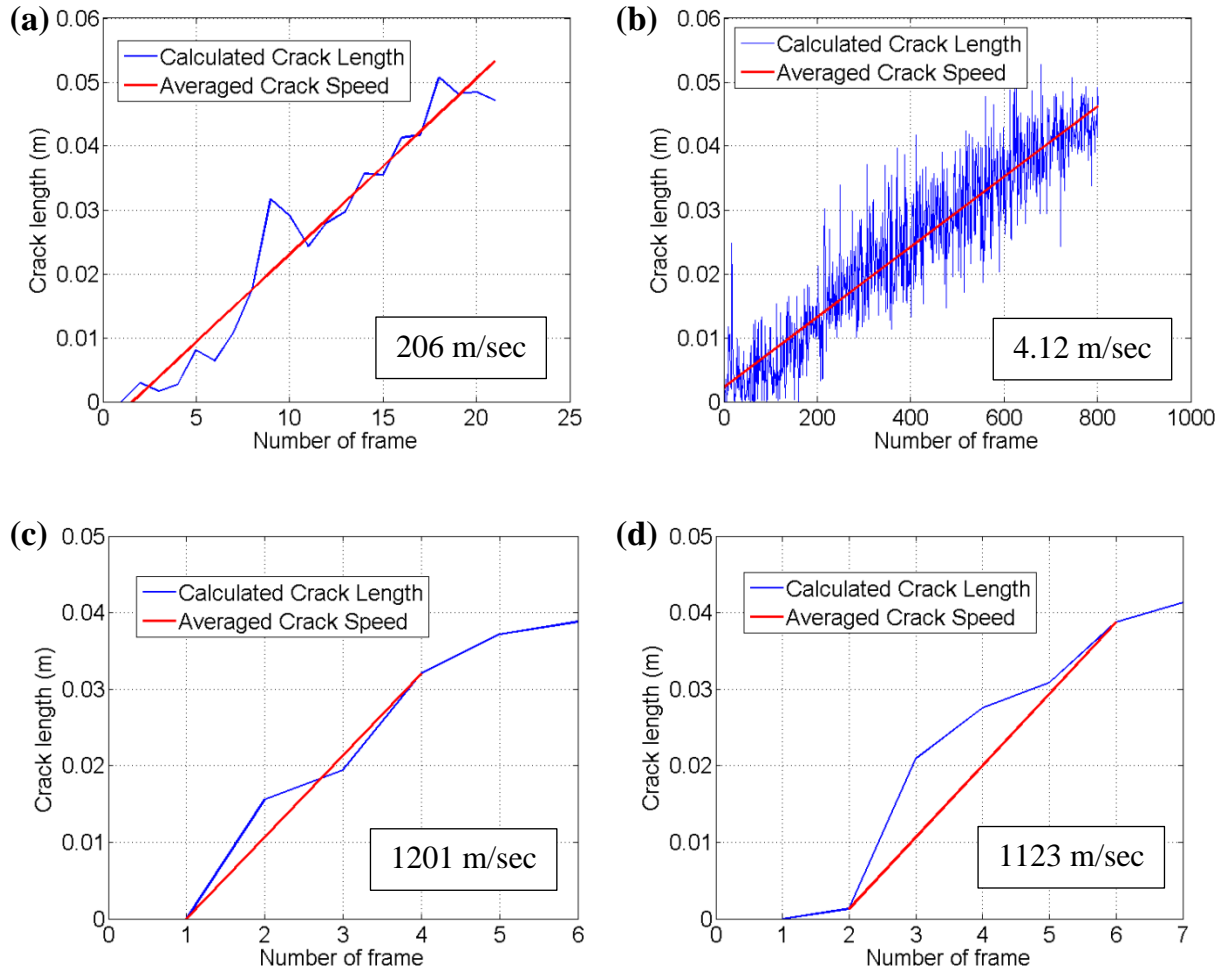


Figure 6.15. Examples of calculated crack speeds: (a) CS-0% tested at 0.0076 mm/sec; (b) CS-1.0% tested at 7.6 mm/sec; (c) CS-0% tested using Type 2 coupler in M-SEFIM; (d) CS-0.5% tested using Type 1 coupler in M-SEFIM

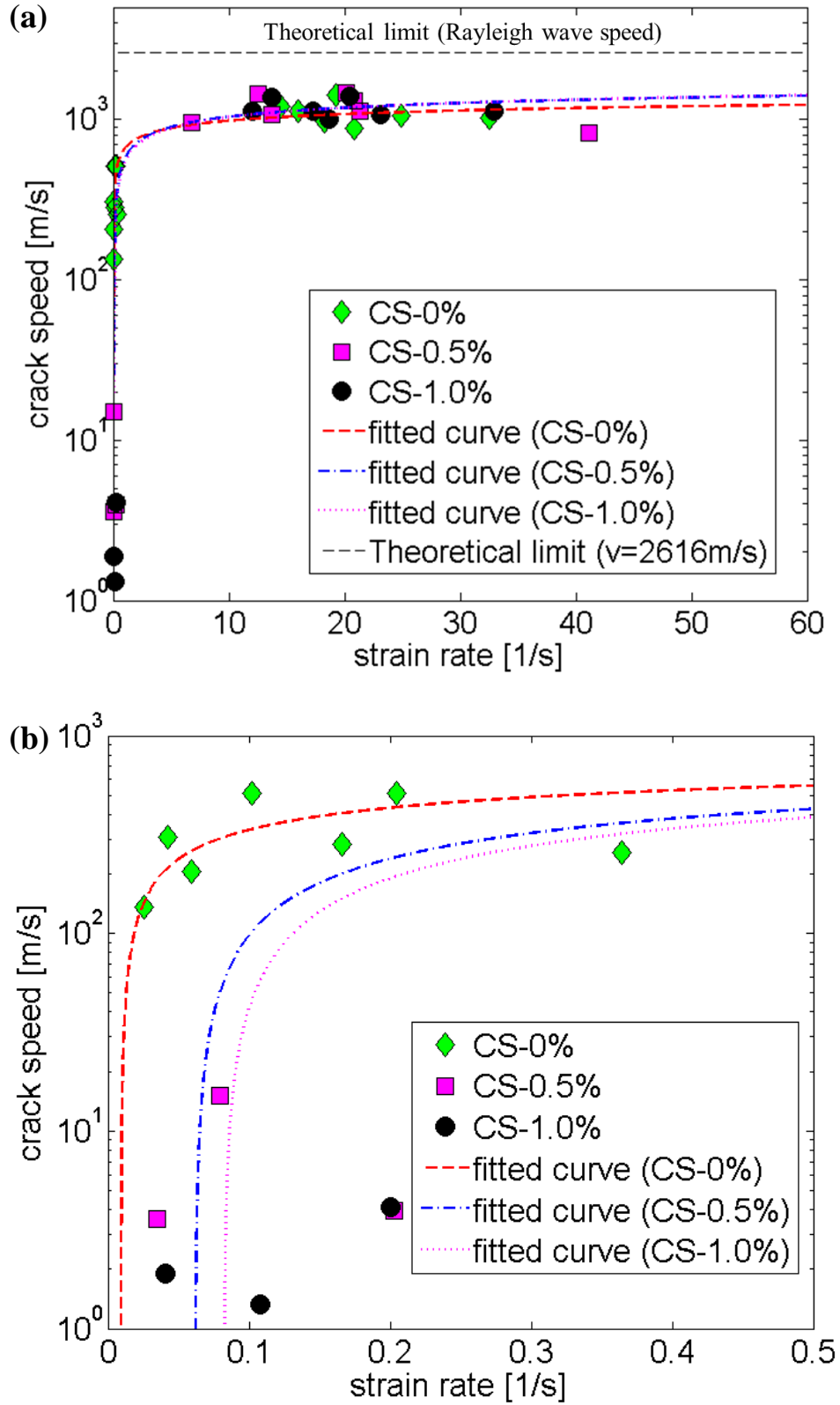


Figure 6.16. Calculated crack speed as a function of notch tip strain rate: (a) with high strain rate results; (b) without high strain rate results

6.3.3 Discussion

It is found after carefully examining the crack surfaces of all UHPC specimens that there are no noticeable changes in the features of the crack surfaces as a function of crack speed. This is unlike brittle plastic, e.g. polymethylmethacrylate (PMMA) where the fracture surface is featureless up to a certain crack speed and appears jagged thereafter (Fineberg et al. 1991). Figures 6.17 to 6.19 show examples of specimens after the three-point bending test for various loading rates. It can be seen from the figures that single straight cracks developed predominantly in CS-0% specimens. In contrast, cracks followed an irregular path occur in CS-1.0% specimens, which is attributed to the effects of the fibers.

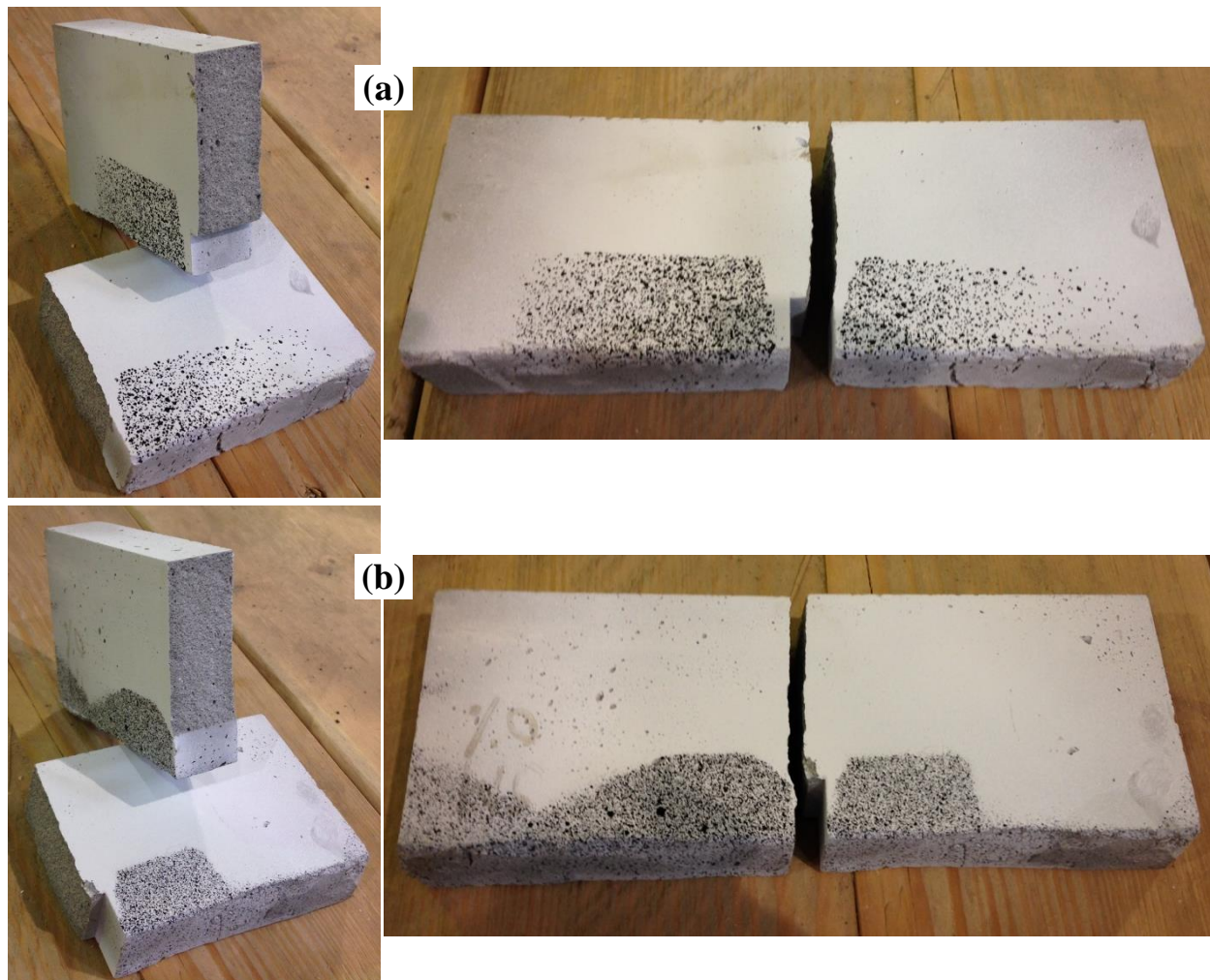
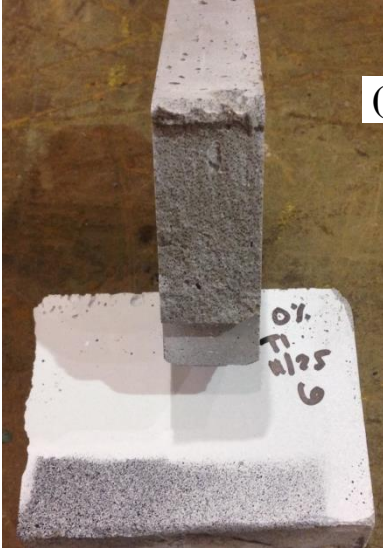
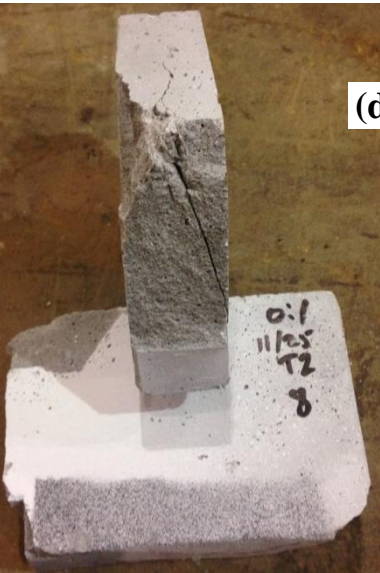
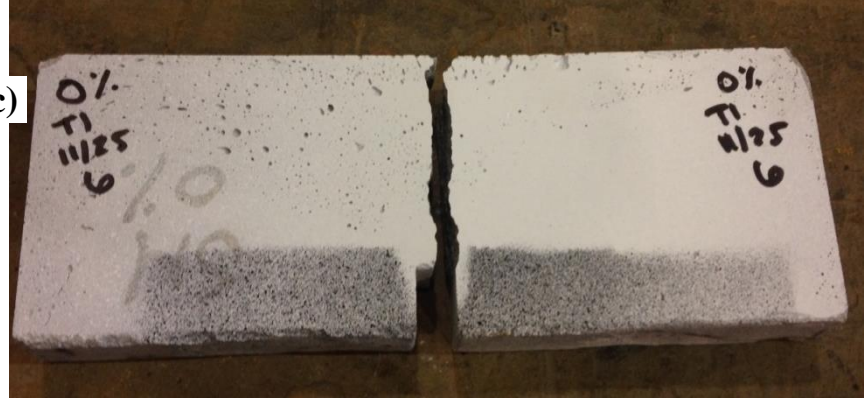


Figure 6.17. Examples of CS-0% specimens after testing: (a) 0.0076 mm/sec (using the MTS machine); (b) 7.6 mm/sec (using the MTS machine); (c) Type 1 coupler (using M-SEFIM); (d) Type 2 coupler (using M-SEFIM)



(c)



(d)



Figure 6.17. Continued

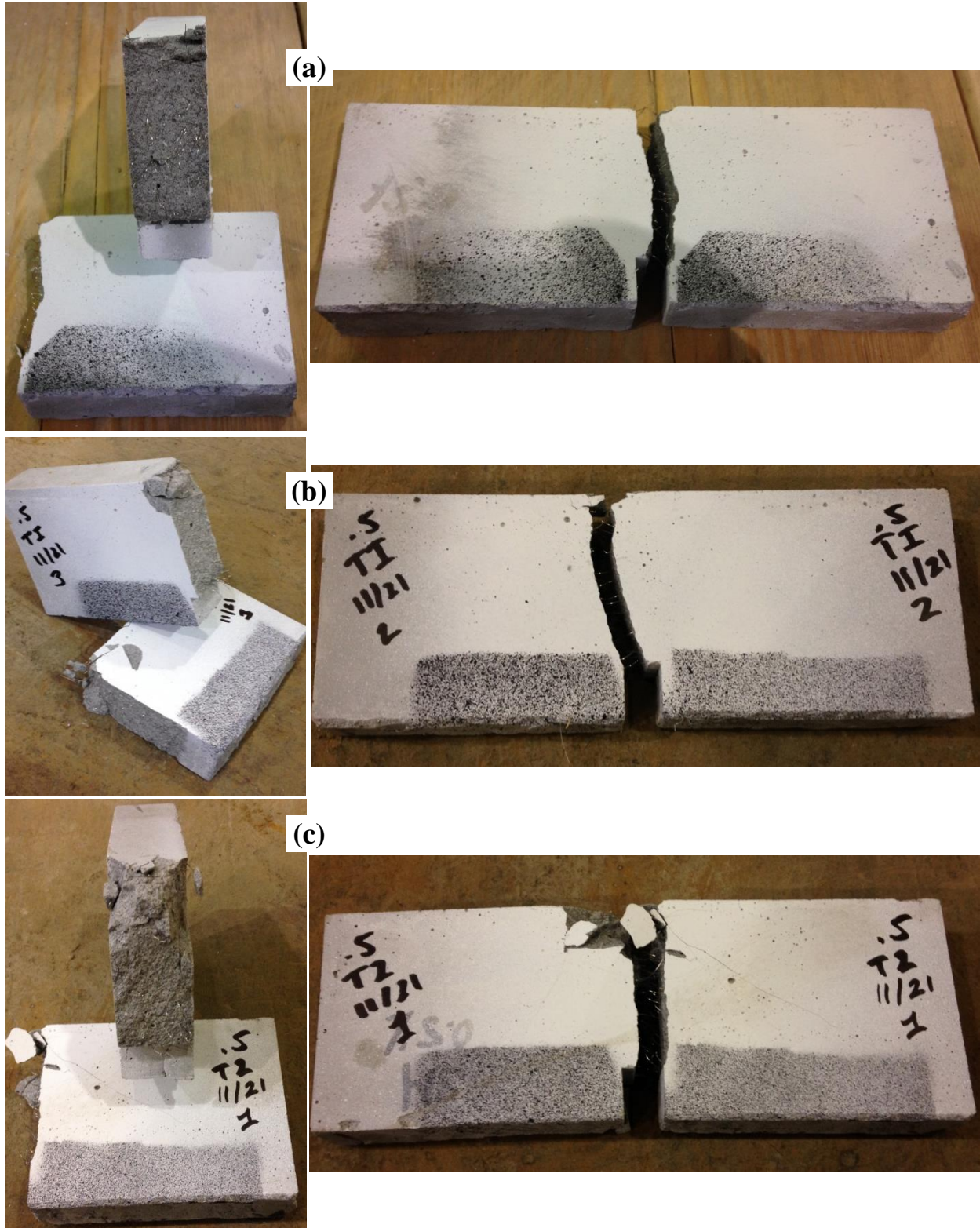


Figure 6.18. Examples of CS-0.5% specimens after testing: (a) 7.6 mm/sec (using the MTS machine); (b) Type 1 coupler (using M-SEFIM); (c) Type 2 coupler (using M-SEFIM)

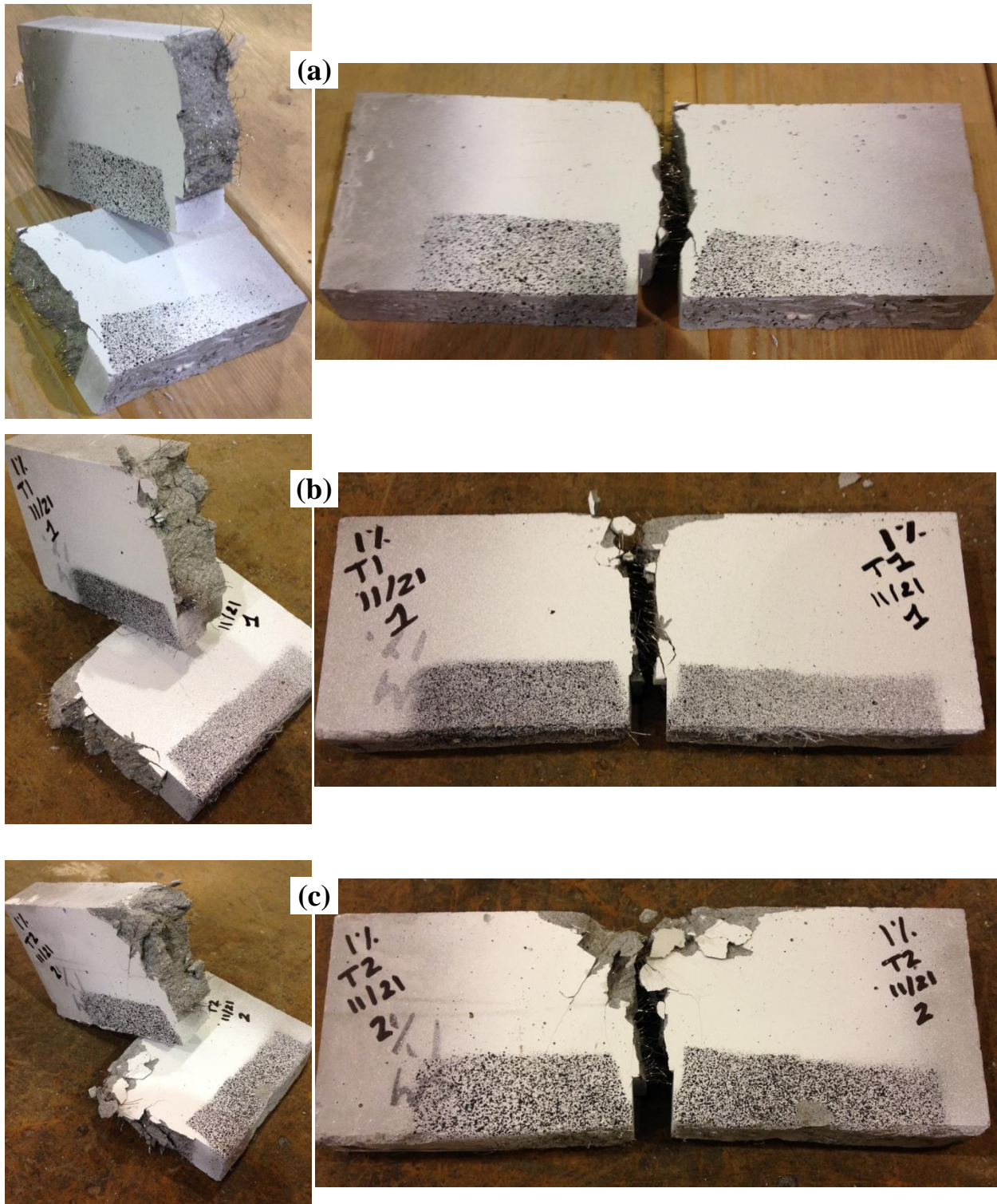


Figure 6.19. Examples of CS-1.0% specimens after testing: (a) 7.6 mm/sec (using the MTS machine); (b) Type 1 coupler (using M-SEFIM); (c) Type 2 coupler (using M-SEFIM)

In the initial design stages of the experimental program, there was a desire to use Type 3 couplers (see Chapter 4) to yield even greater impact speeds. Type 3 couplers have the greatest net area and therefore can lead to storage of the largest elastic energy. However, the use of Type 3 couplers caused the loading hammer to move so forcefully that it crushed the top half of specimens before notch tip cracking commenced, rendering the tests useless. Figures 6.20 and 6.21 show examples of specimens with crushing damage due to the use of Type 3 couplers.



Figure 6.20. Examples of CS-0.5% specimens with crushing failure tested in M-SEFIM with Type 3 coupler

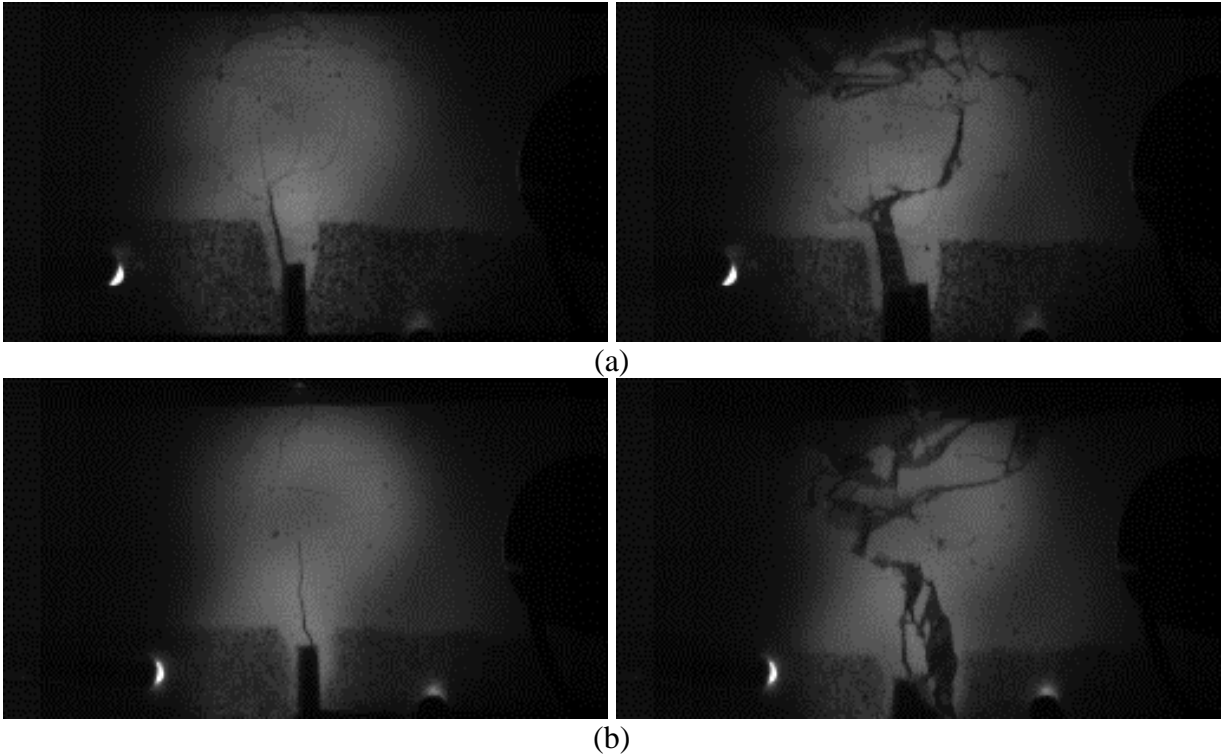


Figure 6.21. Examples of specimens with crushing failure tested in M-SEFIM with Type 3 couplers: (a) CS-0.5%; (b) CS-1.0%

6.4 CONCLUSIONS

This experimental study investigated crack propagation in UHPC using three-point bending specimens subjected to a wide range of loading speeds. A hydraulic servo-controlled testing machine was used to generate slow loading speeds, while M-SEFIM, developed in Chapter 4, was modified to achieve higher loading speeds. The DIC technique and the Canny edge detector technique were used to evaluate notch tip strain and crack speed, respectively. The relationships between crack speed and strain rate for UHPC were presented based on the test data. Critical stress factors for UHPC were computed to show the effectiveness of fiber reinforcement in UHPC under bending loading. The observations and findings of this study can be summarized as follows:

- The modified M-SEFIM was able to successfully perform three-point bending testing of UHPC under impact loading.

- Strain rates ranging from 0.0255 to 1.04 /sec and from 6.79 to 41.1 /sec were experimentally achieved using a hydraulic servo-controlled testing machine and the modified M-SEFIM, respectively.
- The frame rates of the high speed camera were fast enough to record sufficient images for both strain and crack speed calculations. The Canny edge detector employed herein properly captured the crack edges.
- There is no noticeable difference in the features of the crack surface of unreinforced specimens as crack speed increases.
- Crack speed asymptotically increases as strain rate increases. At low loading speed, the steel fiber reinforcement significantly slowed down crack propagation. This resulted in much slower crack speeds in the fiber reinforced cases than the case without fibers. However, at high loading speeds, crack speeds were insensitive to the amount of fibers in the specimens
- The stress intensity factor increases substantially as fiber volume increases from 0.5% to 1.0%. However, the experimental results showed that fiber reinforcement is more effective in improving fracture toughness than compressive strength.

The achieved relationships between crack speed and strain rate will be used in Chapter 7 to propose an explanation for the origins of the dynamic increase factor (DIF).

CHAPTER 7

CRACK VELOCITY-DEPENDENT DYNAMIC TENSILE BEHAVIOR OF CONCRETE

Experiments have consistently shown that the tensile strength of concrete increases with increasing strain rate. The reasons for this phenomenon are not yet well understood and several hypotheses have been proposed in the past to explain it. This study offers additional insight through the application of dynamic fracture mechanics. The relationship between crack velocity and strain rate of concrete is first investigated using a cohesive zone model and fitted to available experimental data. The obtained relationship is then implemented into two different versions of crack-velocity dependent dynamic fracture models. Both models show that computed strength versus strain rate responses compare favorably to well-established test data, suggesting that strain rate sensitivity is strongly associated with the characteristics of dynamic crack growth and inertial effects at the boundaries of the crack. A constitutive modeling scheme that incorporates the obtained dynamic fracture models into a meso-mechanical model is also proposed to predict stress-strain behavior of concrete under dynamic tensile loading. Comparisons between model predictions and published experimental data are provided to show the accuracy of the proposed framework.

7.1 EXPRESSION FOR CRACK VELOCITY IN CONCRETE

Figure 7.1 shows a bilinear cohesive traction-displacement curve. With increasing interfacial displacement, the traction across the interface increases linearly with stiffness E_n . When the traction reaches its peak value (T), the displacement reaches the damage initiation displacement (δ_0). Afterwards, the traction decreases linearly until an ultimate displacement (δ^F),

eventually vanishing and signifying complete decohesion. The area under the traction-displacement curve represents energy release rate.

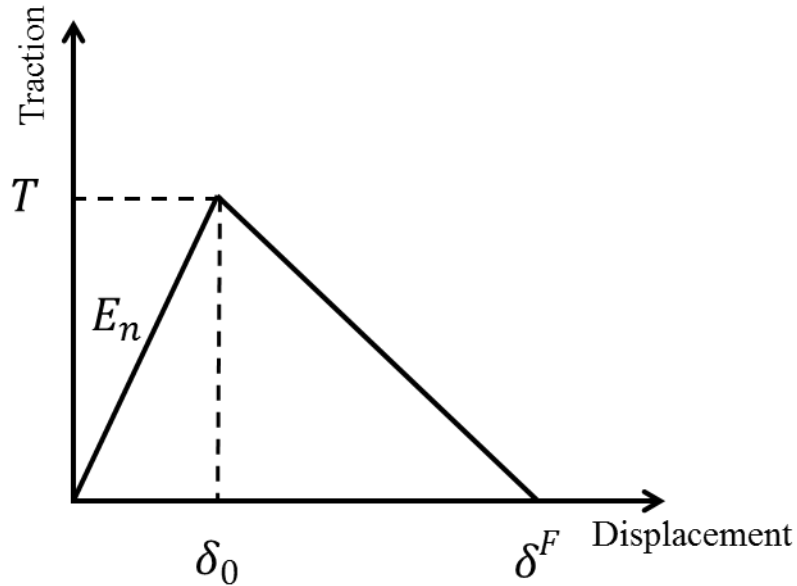


Figure 7.1. Bilinear cohesive traction-displacement curve

In this study, dynamic fracture in concrete is analyzed using the commercial code LS-DYNA (Livermore Software Technology Corporation 2007), employing MAT_138, which can represent a material with cohesive mixed mode behavior. Thin cohesive elements are used to connect solid elements and all fracture processes are assumed to be developed only within the cohesive elements. The geometry of the simulated specimen is adopted from John et al. (1987) as shown in Figure 6.2 and strain is measured at the notch tip over an 18 mm gage length as done in John et al. (1987). An average strain rate is then computed from the initial slope of the notch-tip strain versus time plot following John et al. (1987) and crack velocity is extracted from the slope of the relation between the crack tip position and time.

Three different mesh sizes are used in this study. Figure 7.2 shows a portion of the medium mesh when the crack tip length is 6mm. The triangular-shaped elements and thin-shaped elements are non-breakable solid and cohesive elements, respectively. To investigate the effect of mesh refinement, the lengths of cohesive element are taken as 0.375mm, 0.75mm and 1.5mm

for fine, medium, coarse mesh cases, respectively. All diagonal elements are oriented at 45 degree angles. To minimize the number of elements employed the model, only a single plane strain slice of the beam is considered. The slice is as wide as the characteristic element size (i.e. 0.375mm, 0.75mm and 1.5mm) to ensure that the elements employed have a good aspect ratio.

John et al. (1987) did not report the fracture properties required for the analyses presented herein. Therefore, reasonable assumptions were made with the objective of obtaining meaningful qualitative results. For simplicity, the energy release rates for mode I (G_{IC}) and mode II (G_{IIC}) are assumed to be the same and equal to 10 N/m. This is equivalent to $0.50 \text{ MPa}\cdot\text{m}^{1/2}$ for stress intensity factors K_{IC} (mode I) and K_{IIC} (mode II) when E is 25 GPa (E is Young's modulus of concrete). The fact that mode II properties were approximated as equal to mode I properties is not expected to play a significant role given the expectation that the fracture process will be primarily governed by mode I behavior.

There is consensus in the literature that the maximum possible crack velocity is the Rayleigh wave speed (Freund 1972, Curbach and Eibl 1990, Özbolt et al. 2011). However, it

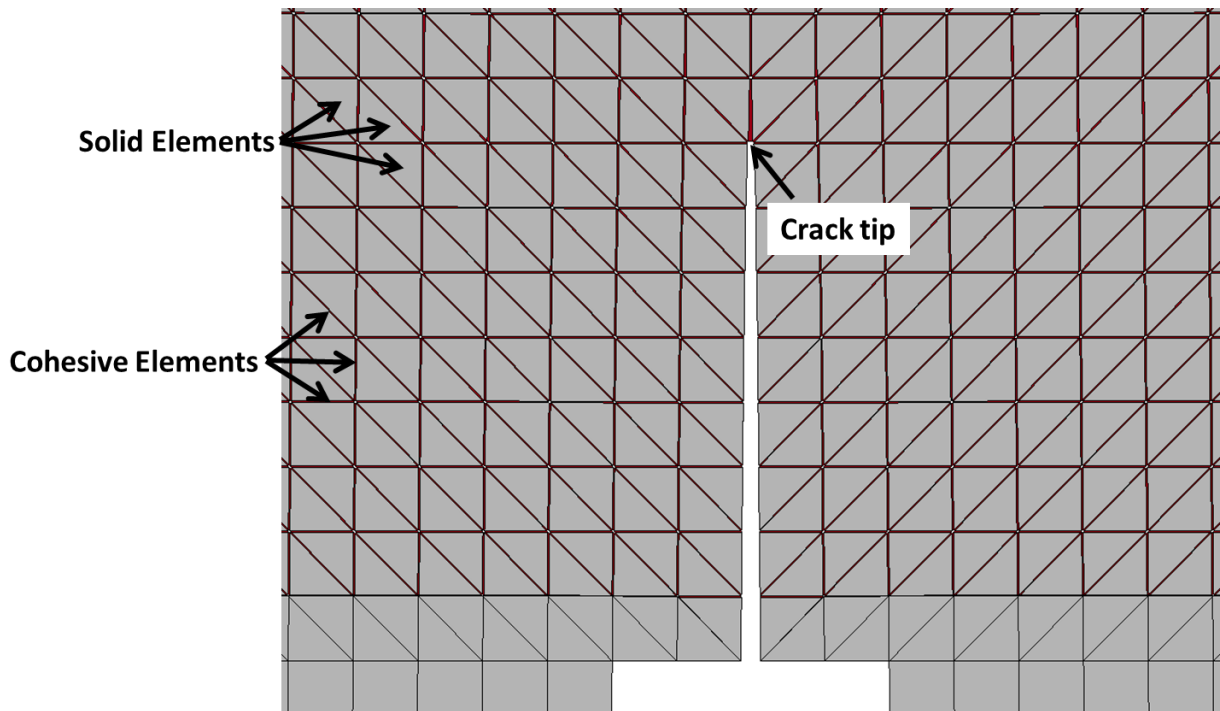


Figure 7.2. Medium mesh used in the simulation near the crack tip when crack length is 6 mm

should be noted that in a number of situations, cracks can actually travel faster than this, e.g. (i) at the boundary of two different materials (Wang et al. 1998, Sibiriakov 2002, Liu and Lapusta 2008), (ii) if there are large tensile residual stresses (Chaudhri 2009, 2011), and (iii) under shock wave loading (Bourne et al. 1999). For the material parameters considered herein, the Rayleigh wave velocity is 1940m/s. Takeda et al. (1982), using very high loading rates, found crack velocities of less than 1000 m/s in mortar and concrete (Mindess et al. 1986). Curbach and Eibl (1990) also noted velocities of less than 1000 m/s in their tests. Ruiz et al. (2000) conducted simulations of dynamic Brazilian tests with a split-Hopkinson pressure bar (SHPB) configuration using cohesive elements and computed crack velocities of 1320m/s at strain rates of 19/sec.

Figure 7.3 shows plots of crack velocity versus strain rate obtained from the 3 meshes used. The results are plotted along with the experimental results from John and Shah (1986), Muria Vila and Hamelin (1987) and Curbach and Eibl (1990). Several observations can be made from Figure 7.3: 1) all meshes show a similar trend, i.e. asymptotic crack velocity as the strain rate increases, 2) crack velocity slows as the mesh is refined, 3) the maximum asymptotic crack velocities are below the theoretical maximum.

Asymptotic crack velocity is attributed to the appearance of more distributed cracking and crack branching, both of which appear to occur more frequently as the mesh is refined and as the strain rate increases. The observed crack branching is consistent with test data in the literature and observations made by other researchers. As the mesh is refined, the increased cracking activity (branching and denser cracks) attenuates the crack velocity as the strain rate increases, by providing more opportunities for energy to be dissipated at the crack tip. Johnson (1992) concluded that as loading speed increases, the size of the fracture process zone increases and thereby energy dissipation per unit of crack growth increases. He surmised that this is the reason for asymptotic crack velocity. Shet and Chandra (2002) concluded from their simulation studies that the cohesive zone method allows the energy to flow into the fracture process zone, where a part of the energy is spent in the forward region and the rest in the wake region. Crack growth is generally promoted by extrinsic dissipation in the forward region resulting from microstructural damage mechanisms (e.g. microcracking initiation, micro void growth/coalescence, or phase transformation), while completion the gradual separation process is impeded by intrinsic

dissipation (e.g. crack deflection, crack meandering or grain bridging) that takes place in the wake region (Shet and Chandra 2002).

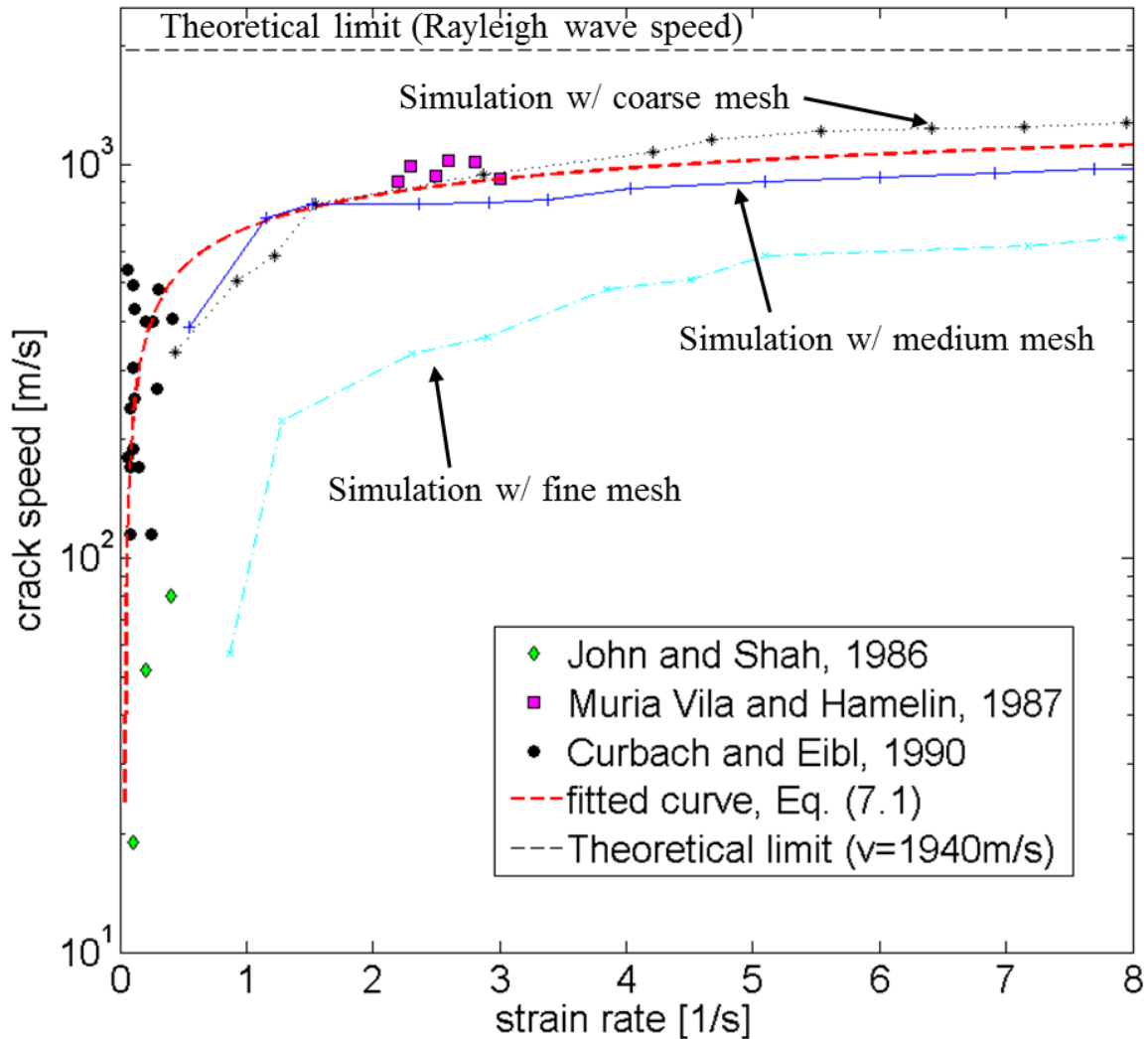


Figure 7.3. Crack velocity of concrete as a function of strain rate

The phenomenon of fracture process zone growth with increase in strain rate increase is also observed in this study. Figure 7.4 shows a comparison of the von Mises stresses within the cohesive elements (obtained from the medium mesh) when the crack length is 6 mm for 3 cases in which strain rate is 7.70 /sec, 14.6 /sec and 20.9 /sec, corresponding to crack velocities of 971 m/s, 1060 m/s and 1080 m/s, respectively. Coordinate (0, 0) indicates the crack tip for each case

in Figure 7.4, where it is clear that the demands are greater and more widespread in the forward region, leading to greater energy dissipation, as the strain rate increases.

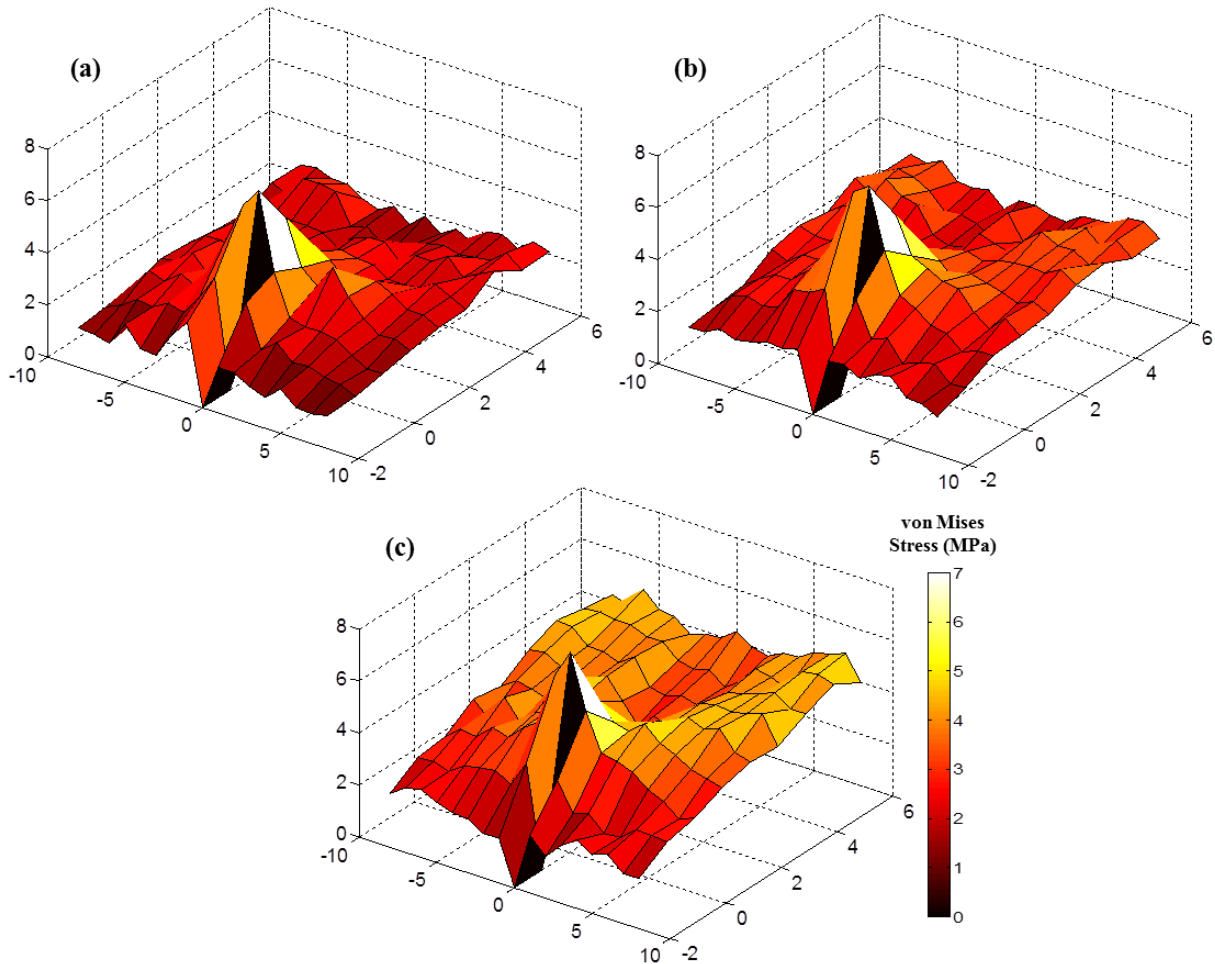


Figure 7.4. Stress profile within cohesive elements when crack length is 6 mm (a) $\dot{\epsilon}=7.70$ /sec; (b) $\dot{\epsilon}=14.6$ /sec; (c) $\dot{\epsilon}=20.9$ /sec

The softening nature of the cohesive zone model employed implies that the solution is mesh-dependent. Given that John et al. (1987) did not report the maximum aggregate size in their specimens, it is not clear what the characteristic length of the problem is and, in turn, which mesh best represents the problem at hand. The closer match to experimental data in Figure 7.3 suggests that the medium and coarse meshes produce a better representation of the problem than the fine mesh does. However, given the simplifications made in this study and uncertainties

about the material properties employed, it is not proper to draw such a conclusion. Nevertheless, it can be argued that since: 1) all 3 meshes exhibit asymptotic crack velocities with increasing strain rates, and 2) the results of other researchers support this observation as discussed above, it is reasonable to fit the experimental data with Equation (7.1), which relates crack velocity to strain rate, and extrapolate it as shown in Figure 7.3.

$$v = 207.2 \ln(\dot{\epsilon}) + 687.8 \quad (7.1)$$

7.2 CRACK VELOCITY-DEPENDENT MODEL FOR CONCRETE UNDER TENSILE LOADING

Two approaches (Broberg (1960) and Freund (1972)) are considered to model the DIF in concrete under tensile loading.

7.2.1 Broberg (1960)'s Approach

Broberg (1960) solved a *self-similar crack propagation* problem. The essential features of this problem are that: 1) two crack tips move at constant velocity symmetrically from a zero initial length, and 2) mechanical fields are invariant with respect to an observer moving steadily away from the crack nucleation point under the action of remote tensile loading in a direction perpendicular to the plane of the crack (Freund 1990). If crack growth begins at time $t=0$, the stress intensity factor increases in proportion to \sqrt{t} .

According to Freund (1990), the time history of the dynamic stress intensity factor $K_I^d(t, v)$ can be expressed as:

$$\frac{K_I^d(t, v)}{K_I^*} = - \frac{I(b/h)R(h)}{b^2 h \sqrt{h^2 - a^2}} = c \quad (7.2)$$

where $K_I^* = \sigma_\infty \sqrt{\pi l/2}$ denotes the static stress intensity factor, σ_∞ is the far-field loading, v is the crack velocity, $h = 1/v$, $a = 1/c_d$, $b = 1/c_s$, c_d is the dilatational wave speed, c_s is shear wave speed. The dilatational wave speed and shear wave speed can be written as (Broberg (1960) and Freund (1990)):

$$c_s = \sqrt{\frac{E}{2\rho(1+\nu)}}, \quad c_d = c_s \sqrt{\frac{2(1-\nu)}{1-2\nu}} \quad (7.3)$$

$R(\xi) = (b^2 - 2\xi^2)^2 + 4\xi^2 \sqrt{a^2 - \xi^2} \sqrt{b^2 - \xi^2}$ is the Rayleigh function. The function $I(b/h)$ can be expressed as (Broberg (1960) and Xia et al. (2006)):

$$I(b/h) = \frac{b^2}{h} \int_0^\infty \frac{R(i\eta)}{(h^2 + \eta^2)^{3/2} \sqrt{a^2 + \eta^2}} d\eta \quad (7.4)$$

For a conventional concrete material ($E = 25.0 \text{ GPa}$, $\nu = 0.2$, $\rho = 2300 \text{ kg/m}^3 = 2300 \text{ N s}^2/\text{m}^4$), one can plot the relationship between normalized stress intensity factor, K_I^d/K_I^* and normalized crack velocity, v/c_s as Figure 7.5.

7.2.2 Freund (1972)'s Approach

Freund (1972) considered a semi-infinite mode I crack running in an infinite block of prestressed material. In this problem the dynamic stress intensity factor only depends on the current crack tip speed as

$$K_I^d = k(v)K_I^* \quad (7.5)$$

Gao (1993) suggested a useful approximation for $k(v)$ as

$$k(v) = (1 - v/c_R) \sqrt{1 - v/c_d} \quad (7.6)$$

where c_R is Rayleigh surface wave speed and can be expressed as (Gao 1993)

$$c_R = \frac{0.862 + 1.14\nu}{1 + \nu} c_s \quad (7.7)$$

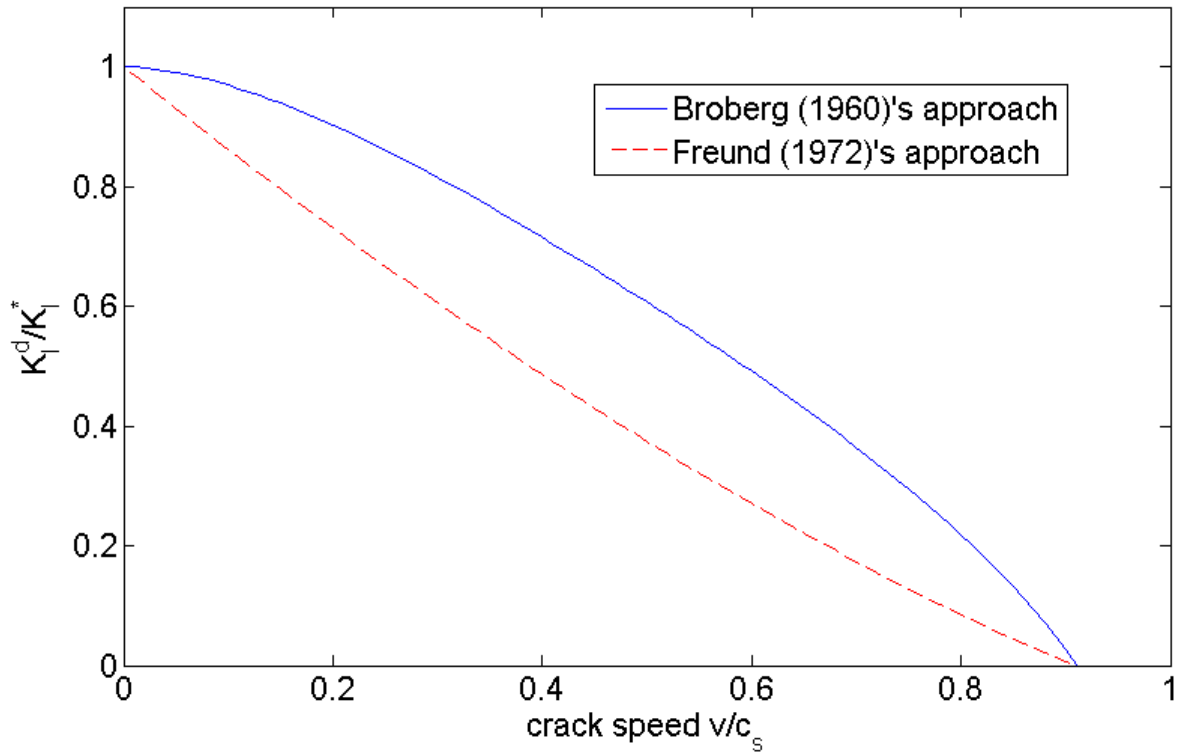


Figure 7.5. Normalized dynamic stress intensity factor versus normalized crack speed using Broberg (1960)'s and Freund (1972)'s approaches

Figure 7.5 depicts the relationship between the normalized stress intensity factor and normalized crack velocity for both approaches. Broberg's approach shows a parabolic relationship, whereas Freund's gives an almost linear relationship. According to Eibl and Curbach (1989), the stress intensity at the crack tip is much higher under static loading than under dynamic loading due to inertial effects at the boundaries of the crack. This is evident for both approaches in Figure 7.5 providing some measure of confidence in the derivations presented.

From Equations (7.2) and (7.5), K_I^d , can be generally written as $K_I^d = \zeta K_I^*$, where ζ is either c or $k(v)$ depending on which approach is employed. At the critical stress, the DIF can therefore be expressed as

$$DIF = \frac{\sigma_c^d}{\sigma_c^*} = \frac{K_{Ic}^d / \zeta \sqrt{\pi l / 2}}{K_{Ic}^* / \sqrt{\pi l / 2}} = \frac{1}{\zeta} \quad (7.8)$$

where σ_c^d and σ_c^* are the critical stresses in the dynamic and static cases, respectively. In this chapter, the critical stress intensity factors, K_{Ic}^d and K_{Ic}^* , are assumed to be the same following Ravichandrana and Subhash (1995), Paliwal and Ramesh (2008) and Lu and Li (2011). Figure 7.6 shows relationship between DIF and normalized crack velocity for both approaches.

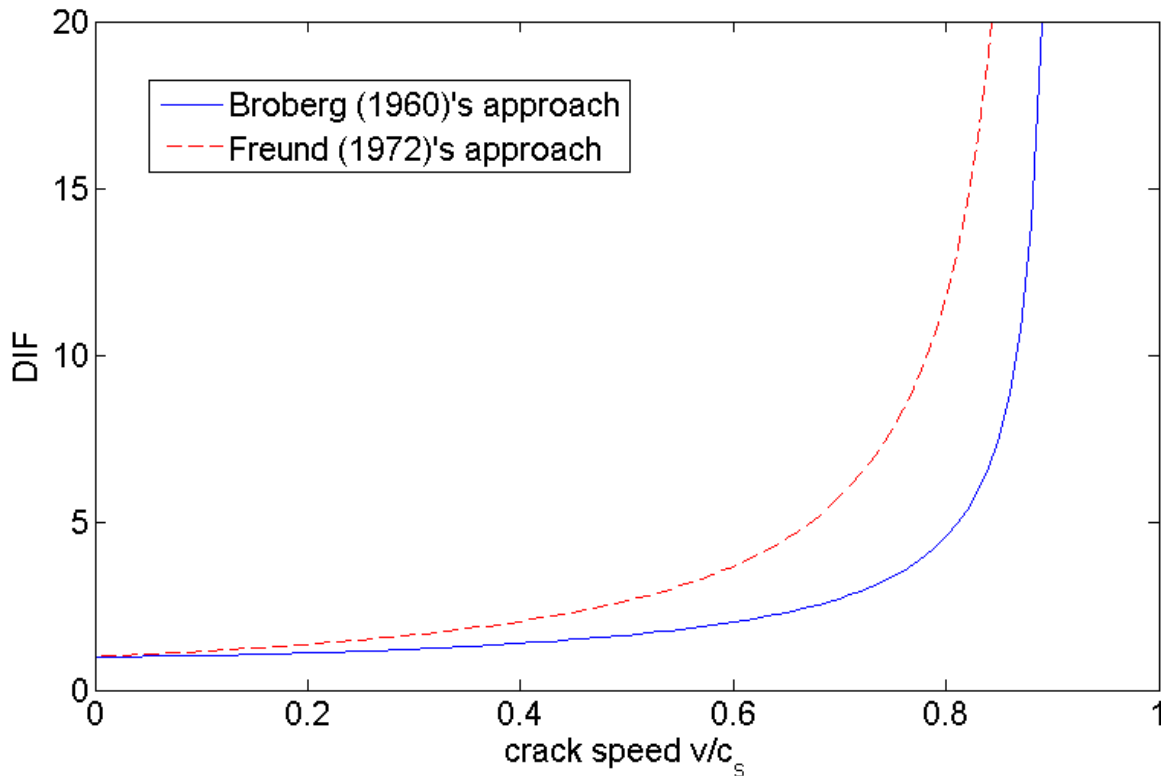


Figure 7.6. Dynamic intensity factor (DIF) versus normalized crack velocity using Broberg (1960)'s and Freund (1972)'s approaches

By substituting Equations (7.1), (7.2) and (7.6) into Equation (7.8), one may also plot the relationship between DIF and strain rate for a typical concrete as shown in Figure 7.7. Experimental results in the literature (Leppanen 2006) are also plotted in the Figure 7.7 for comparison. It is clear from Figure 7.7 that the proposed models capture well the observed trends and are close to the experimental values. In particular, application of Freund's approach shows better agreement with experimental results for this specific application and set of parameters.

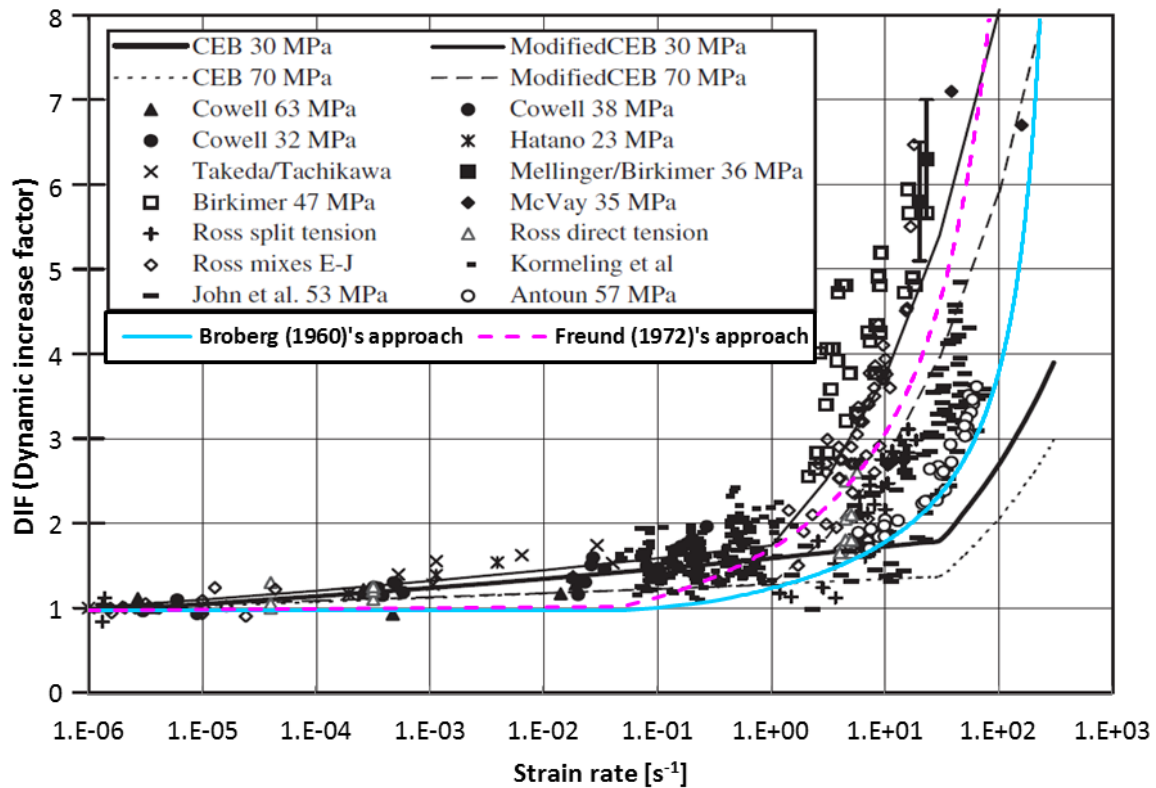


Figure 7.7. Comparison between the proposed models and experimental data in Leppanen (2006)

7.2.3 Application of the DIF Model to UHPC

The proposed dynamic fracture model is also used to estimate the DIF of ultra high performance concrete (UHPC). Freund (1972)'s approach is only considered in this subsection since it was found to better match the test data above. Using the crack speeds documented in Chapter 6, Freund's approach is used to plot the curve in Figure 7.8 for the experimental DIF

results obtained in Chapters 3 and 5. Clearly, there is reasonably good correlation between the prediction and the experimentally measured DIF data.

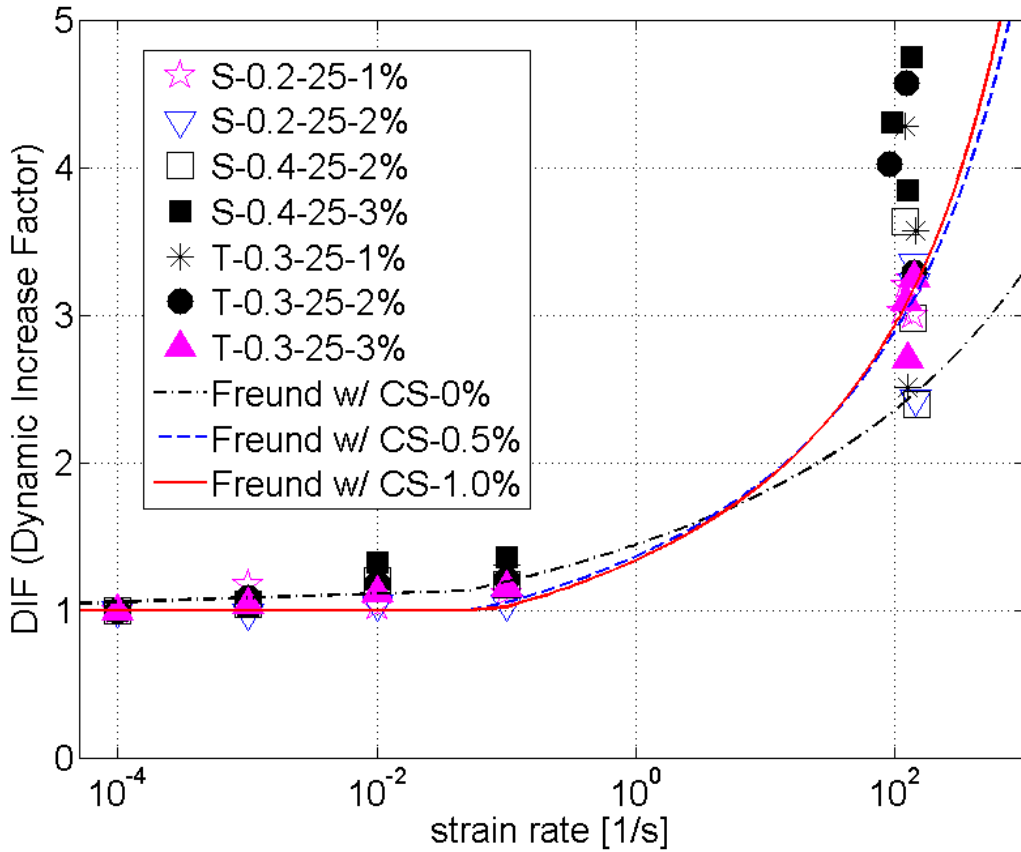


Figure 7.8. Comparison between experimental data obtained in Chapters 3 and 5 and the Freund approach incorporated with crack speed data obtained in Chapter 6

7.3 CONSTITUTIVE MODELING

To predict the stress-strain behavior of concrete under dynamic uniaxial tensile loading, a constitutive modeling scheme is proposed herein based on the model by Huang and Li (1989). Huang and Li (1989) proposed analytical expressions for inelastic deformation of concrete under static loading as functions of maximum aggregate size, aggregate volume fraction and cement matrix toughness. They achieved this by considering the opening of stably propagating interfacial cracks at interfaces to estimate inelastic deformation of concrete. Circular aggregates

in concrete are assumed to be randomly distributed following the Fuller distribution of aggregate size in the mixture, i.e. $R_{avg} = (1/3)R_{max}$, where R_{avg} and R_{max} are the average and maximum radii of aggregates, respectively (see Figure 7.9a). An initial crack is assumed to begin at the interface between the largest aggregate and matrix, and propagate through the matrix. Crack interactions are considered with $\lambda \equiv [1 + f(R_{max}, R_{avg})]/[1 - f(R_{max}, R_{avg})f(R_{avg}, R_{max})]$, where λ is the crack interaction parameter and $f(R_{avg}, R_{max})$ is the interaction function. Details of the methodology and equations can be found in Huang and Li (1989).

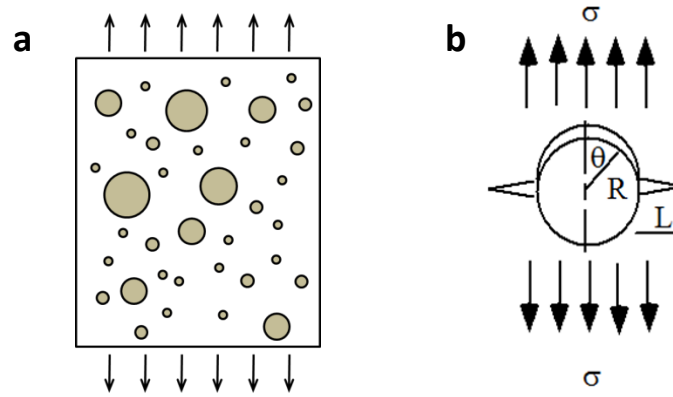


Figure 7.9. (a) Schematic of concrete with randomly distributed circular aggregates; (b) Schematic of interfacial crack between aggregate and matrix

The relation between the applied tensile load σ and the angle θ , which defines the crack size (see Figure 7.9b) is given as

$$\sigma = K_{Ic}^{if} F(\theta) / \sqrt{R} \quad (7.9)$$

$$F(\theta) = \frac{4(3 - \cos \theta) / \sqrt{\pi}}{\sqrt{\sin \theta (44 + 12 \cos \theta + 12 \cos^2 \theta - 4 \cos 4\theta + \sin^4 \theta)}} \quad (7.10)$$

Following Zaitsev (1985), it is assumed that K_{Ic}^{if} / K_{Ic}^m is 0.6, where K_{Ic}^{if} and K_{Ic}^m are toughnesses of the interface and cement matrix, respectively. Interfacial crack propagation follows the schematic in Figure 7.9b and Equations (7.9) and (7.10).

For multiple aggregates, the total stress-strain relation under static loading can be written as (Huang and Li, 1989)

$$\frac{\varepsilon}{\varepsilon_{el}} = \frac{\sigma}{\sigma_{el}} \left\{ 1 + 2V_{fa} \frac{(1-\nu^2)}{F(\theta)} \left[(\theta^2 - \theta_1^2)F(\theta) - 2 \int_{\theta_1}^{\theta} \xi F(\xi) d\xi \right] \right\} \quad (7.11)$$

where $\frac{\sigma_{el}\sqrt{R_{max}}}{K_{Ic}^{if}} = F(\theta_1)$ and $\frac{\sigma\sqrt{R_{max}}}{K_{Ic}^{if}} = F(\theta)$. In Equation (7.11) V_{fa} denotes the volume fraction of aggregates, θ varies from $\theta_1 \approx \pi/4$ to $\theta_2 \approx \pi/2$, and σ_{el} and ε_{el} are the stress and strain corresponding to the limit of proportionality, respectively. Including the effect of crack interaction, the tensile strength can be expressed as (Huang and Li, 1989)

$$f_t = \frac{\lambda K_{Ic}^{eff}}{\sqrt{\pi R_{max}}} \quad (7.12)$$

where K_{Ic}^{eff} is the effective toughness of concrete and $K_{Ic}^{eff}/K_{Ic}^m = \sqrt{\frac{1.0+0.87V_{fa}}{1-(\pi^2/16)V_{fa}(1-\nu^2)}}$

Similar to Equation (7.8), one may derive the stress-strain relation for dynamic loading with the following modifications.

$$\frac{\zeta \sigma_{el}^d \sqrt{R_{max}}}{K_{Ic}^{if}} = F(\theta_1), \quad \frac{\zeta \sigma^d \sqrt{R_{max}}}{K_{Ic}^{if}} = F(\theta), \quad f_t = \frac{\lambda K_{Ic}^{eff}}{\zeta \sqrt{\pi R_{max}}} \quad (7.13)$$

The assumption that $K_{Ic}^d = K_{Ic}^*$ still holds for the stress-strain predictions.

A series of simulations are conducted using the previously used material properties with the following additional material parameters: $R_{max} = 10mm$, $K_{Ic}^m = 0.3MPa \cdot m^{1/2}$. Figure 7.10 shows the stress-strain relations for concrete under static as well as dynamic uniaxial tensile loading with different volume fractions of aggregate ($V_{fa} = 0.3$ and $V_{fa} = 0.5$). It should be noted that Young's modulus for dynamic loading (E^d) of the concrete is assumed to be same as that for static loading (i.e. $E = E^d = 25.0 GPa$) in these simulations. It is clearly shown in

Figure 7.10 that as the strain rate increases, the concrete material shows not only a higher proportional limit (i.e. elastic limit) but also higher tensile strength. In addition, Freund (1972)'s approach gives a slightly higher stress-strain response and higher tensile strength than Broberg (1960)'s approach for the same crack propagation velocity and strain rate. Moreover, a higher volume fraction of aggregate is shown to lead to a higher stress-strain response for both static and dynamic loading cases.

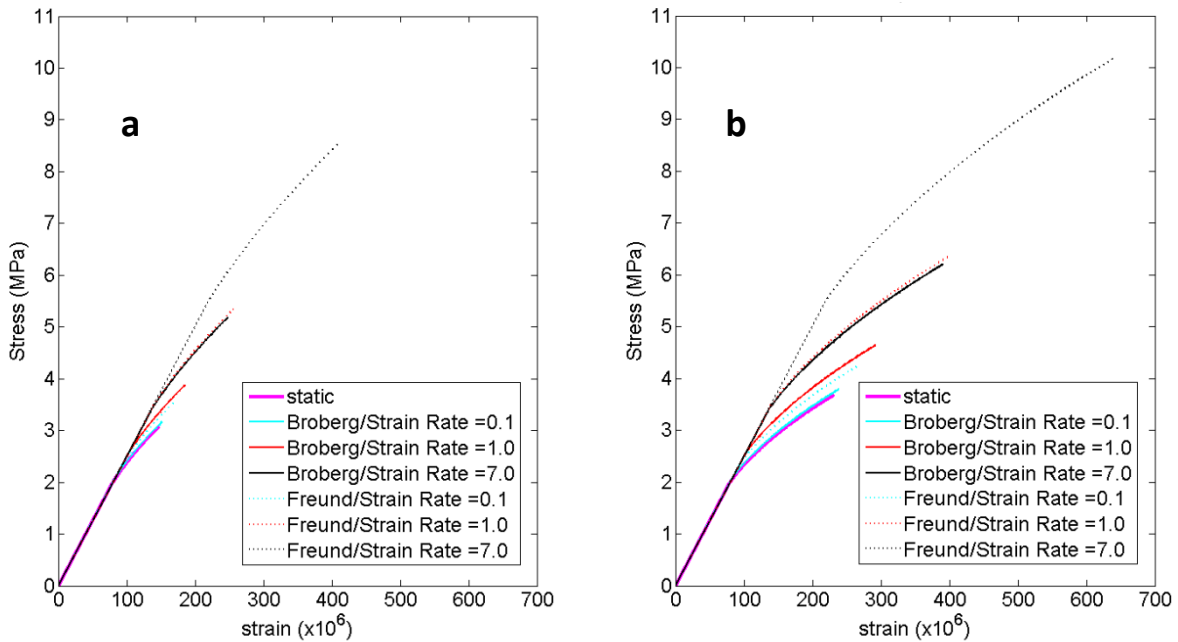


Figure 7.10. Stress-strain response under uniaxial tensile loading using Broberg (1960)'s and Freund (1972)'s approaches with various strain rate values: (a) $V_{fa} = 0.3$; (b) $V_{fa} = 0.5$

Comparison between the present predictions and experimental data reported by Zielinski et al. (1981) on stress-strain behavior of concrete under tensile loading is made to assess the predictive capability of the proposed models as shown in Figure 7.11. The material properties of the concrete are taken from Zielinski et al. (1981): $E = 25$ GPa, $E^d = 34$ GPa, $R_{max} = 16$ mm. The stress rate for impact test is reported as $\dot{\sigma} = 30$ N/mm²/ms. Since volume fraction of aggregate and cement matrix toughness, K_{Ic}^m , were not reported by Zielinski et al. (1981), the values are estimated by fitting the experimentally obtained stress-strain curve in the static case to

the present prediction as: $V_{fa} = 0.35$ and $K_{Ic}^m = 0.47 \text{MPa} \cdot \text{m}^{1/2}$. It is noted from the figure that the prediction with the Freund (1972)'s approach shows a good correlation with the experimental data compared to the Broberg (1960)'s approach for this specific case.

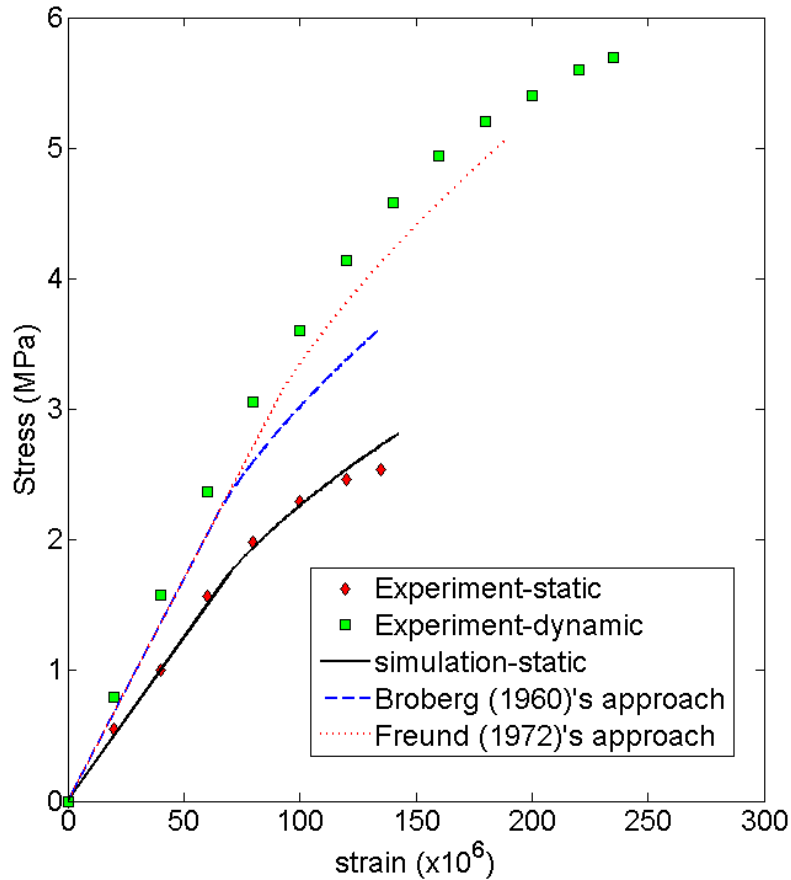


Figure 7.11. Comparison between the predicted and experimental data (Zielinski et al. 1981) for overall uniaxial tensile response of concrete under static and dynamic loading

7.4 CONCLUSIONS

The relationship between crack velocity and strain rate of concrete was investigated using a cohesive zone model and fitted to available experimental data. Using the obtained relationship, dynamic fracture models considering crack velocity dependency were presented and used to predict the DIF of concrete under tension. Good correlation to test results was achieved. A

constitutive modeling scheme was also presented to predict the stress-strain response of concrete under dynamic tensile loading. Numerical examples corresponding to dynamic uniaxial tensile loading were solved to illustrate the potential of the proposed dynamic fracture models. The observations and findings of this study can be summarized as follows:

- The cohesive zone model employed herein properly captured the increasing demands in the fracture process zone as the strain rate increased. The increasing process zone caused the crack velocity to attenuate as strain rate increased, in accord with previously published experimental data.
- The proposed dynamic fracture models predicted well the DIF of concrete under tension, suggesting that strain rate sensitivity is strongly associated with the characteristics of dynamic crack growth, and specifically, inertial effects at the boundaries of the crack.
- The proposed model incorporating with crack speeds documented in Chapter 6 properly predicts the DIF of UHPC obtained in Chapters 3 and 5.
- Higher volume fraction of aggregate can lead to higher stress-strain response for both static and dynamic loading cases. Also, the proposed constitutive models can capture important attributes of concrete behavior under high strain rate, in particular, a higher proportional limit and higher tensile strength.
- Freund (1972)'s approach gives a relatively higher stress-strain response and higher tensile strength than Broberg (1960)'s approach given the same crack propagation velocity and strain rate.

The conclusions drawn above are subject to the assumptions that were necessarily made for convenience, computational expediency and lack of pertinent experimental data. In particular, studies on dynamic fracture toughness are needed to resolve the controversy around the fracture toughness of concrete and its dependency on strain rate. Although dynamic fracture toughness is assumed to be the same as static fracture toughness in this study following the work of Ravichandrana and Subhash (1995), Paliwal and Ramesh (2008) and Lu and Li (2011), Lambert

and Ross (2000) claimed that dynamic fracture toughness does increase with strain rate in a nearly linear manner. Clearly such data may affect some specific findings of the research reported herein. However, the proposed general formulations and methodologies can be easily adjusted to account for the new data.

CHAPTER 8

RESEARCH SUMMARY AND DIRECTIONS OF FUTURE RESEARCH

8.1 SUMMARY OF RESEARCH

The aim of this dissertation was to investigate and characterize the mechanical response of Ultra High Performance Concrete (UHPC) and Ultra High Performance-Fiber Reinforced Concrete (UHP-FRC) under dynamic loading. As such, the research reported in this dissertation addressed five inter-related topics: (1) characterization of UHP-FRC under direct tension at low strain rates, (2) development of a new impact testing system for UHP-FRC, (3) characterization of UHP-FRC under direct tension at high strain rates, (4) characterization of crack propagation in UHPC, and (5) development of a theoretical modeling scheme for concrete under dynamic tension. A summary of this research and the most important conclusions in each of these areas follow.

8.1.1 Characterization of UHP-FRC under Direct Tension at Low Strain Rates

In Chapter 3, the tensile behavior of UHP-FRC under low strain rates, ranging from 0.0001 /sec to 0.1 /sec, was investigated using a hydraulic servo-controlled actuator. To provide fundamental information on discontinuous fiber reinforcement in UHP-FRC, the effects of deformed shape, fiber aspect ratio and fiber volume fraction were investigated. The rate sensitivity of UHP-FRC under direct tension was evaluated in terms of its first cracking strength, post-cracking strength, energy absorption capacity, strain capacity, elastic modulus, fiber tensile stress and number of cracks. The experimental results demonstrated that UHP-FRC experiences pronounced rate effects in post-cracking strength and energy absorption capacity.

All UHP-FRC series maintained performance Level 3 as classified in Naaman and Reinhardt (2003) for all low strain rates, i.e., strain hardening was observed for all strain rates. Furthermore, T-0.3-25-2%, T-0.3-25-3%, and S-0.2-25-2% series maintained performance Level 4 as classified by Naaman and Reinhardt (2003), which is defined as high energy absorption with $g \geq 50 \text{ kJ/m}^3$ as suggested by Wille et al. (2014) for all strain rates. It was observed that post-cracking strength and energy absorption capacity generally increase with an increase in both volume fraction of fiber and strain rate. However, the fiber tensile stress, which represents the effectiveness of incorporating fibers, generally decreases, from a qualitative perspective, as fiber volume fraction increases, likely due to the fiber-group effect.

The twisted fiber series showed better performance than the straight fiber series because of the additional anchorage effect associated with the untwisting action that occurs during pullout. While twisted fibers provided somewhat better performance than equivalent straight fibers, the mechanical anchorage advantage of twisted fibers over straight fibers for post-cracking strength could be acquired by using straight fibers with higher aspect ratios. However, the good performance of the fibers with high fiber aspect ratio comes at a price because the larger number of the fibers makes the concrete more difficult to mix. In general, it was not possible to make mixes with more than 2 % volume fraction of S-0.2-25 fibers.

As predicted by theory, the post-cracking strength and observed energy capacity increase with the fiber reinforcing index, $V_f(l_f/d_f)$, and $V_f(l_f^2/d_f)$, respectively. It should be noted that the equivalent bond strength between brass coated steel fibers and cement matrix is almost independent of fiber deformed shape, diameter and length. This unexpected result may be attributed to the use of a UHPC matrix where the bond for smooth straight fiber is reported to be excellent due to surface abrasion, and is likely due to the very high packing density of the cementitious matrix around the fiber. All UHP-FRC specimens showed multiple cracking patterns, which could explain the superior energy absorption capacity and the strain hardening behavior of the material. Furthermore, the experimental results on rate sensitivity of UHP-FRC revealed that the increases in dynamic increase factor (DIF), for first cracking strength, post cracking strength, energy absorption capacity and strain capacity, are moderate and nearly linear in log-linear space at strain rates up to 0.1 /sec.

8.1.2 Development of New Impact Testing System for UHP-FRC

In Chapter 4, a compact impact testing system, M-SEFIM, was developed, based on the concept of suddenly released elastic strain energy, suggested by Kim et al. (2011), and the energy transmitting mechanism of the weighbar tube, suggested by Harding and Welsh (1983), to test strain hardening cementitious composites, such as UHP-FRC, under direct tension. Detailed finite element simulations using the commercial finite element program LS-DYNA were conducted to assess the validity of the new system and refine it to the point where it could produce meaningful and practical results.

A strain gage was attached to the transmitter bar to measure stress in the specimen, as with the split Hopkinson pressure bar (SHPB). The stress wave was amplified and conditioned using a signal amplifier (VISHAY 2310B) and then recorded using an oscilloscope. The digital image correlation (DIC) technique was used to measure strain in the specimen. A high speed camera (Photron SA5) was used to record images for the DIC application. Unlike ductile metal specimens, UHP-FRC specimens undergo multiple cracking, which caused speckles to flake off around cracks during testing, contaminating local strain data. Therefore, strain was computed from the displacements of the top and bottom points of the gage length of the specimen, just like with a linear variable differential transformer (LVDT).

Through a series of simulations using LS-DYNA, it was verified that a 0.95 m steel transmitter bar is long enough to properly capture stress signals of the specimen with a failure strain of 1% at strain rate of 35 /sec. However, a series of experiments revealed that UHP-FRC has substantial rate sensitivity under high strain rates and failed at more than 4 % strain. Brass was chosen as an alternative material for the transmitter bar due to its slower stress wave speed, which allows the transmitter bar to be shorter. The transmitter bar length was also increased to 1.55 m. The increased length and change in material were selected through computational simulation to ensure: 1) compactness of the impact system, and 2) its ability to accommodate strain hardening cementitious composites that fail at high strain levels.

The most important feature of M-SEFIM is its size. The length of the developed testing system is about one quarter of a conventional SHPB of similar capabilities. Another key feature of M-SEFIM is that it can test the same sized specimen used in low strain rate experiments, e.g.

using a hydraulic actuator. Therefore, the system allows direct comparison with low strain rate test results without concern about changes in specimen geometry. This is in contrast to the traditional SHPB, which requires a different specimen geometry than that used for low strain rate cases. Another important feature of M-SEFIM is that strain rates can be simply adjusted by changing the net area of the coupler. Three couplers with different net areas were considered in this study to adjust strain rates. In short, it was demonstrated through this research that the newly developed testing system, M-SEFIM, is an inexpensive, versatile, reliable and compact impact testing device.

8.1.3 Characterization of UHP-FRC under Direct Tension at High Strain Rates

In Chapter 5, the tensile mechanical properties of UHP-FRC were investigated at strain rates ranging from 90 to 146 /sec using M-SEFIM, developed in Chapter 4. Various types of steel fibers were investigated to evaluate their effectiveness in UHP-FRC under high strain rate loading. The evaluated mechanical properties of UHP-FRC were compared with those at low strain rates characterized in Chapter 3 to provide fundamental material properties of UHP-FRC over a wide range of loading conditions.

A series of experimental and simulation-based parametric studies on specimen geometry revealed that the effect of specimen length on stress-strain response is minor. Similarly, simulation results indicated no clear trend on specimen length in relation to DIF for post cracking strength, energy absorption capacity and strain capacity. However, there was clear evidence that strain rate is affected by specimen length. Accordingly, 55 mm was selected as a proper specimen length; long enough to have a sufficiently long gage length with respect to fiber length and yet short enough to avoid non-uniform loading during the experiments.

Multiple cracking in UHP-FRC specimens was also found in the high strain rate tests, which indicates the existence of strain hardening behavior under dynamic loading. This cracking was captured using the high speed camera. It was also observed that the energy absorption capacity of UHP-FRC specimens under impact loading is remarkable, about an order of magnitude higher than its quasi-static counterpart. This observation suggests that UHP-FRC is a highly promising cement-based material for applications requiring impact and blast resistance. Increasing fiber volume fraction led to an increase in post cracking strength, energy absorption

capacity and strain capacity for all fiber cases and volume fractions under impact loading. In addition, as seen in the lower strain rate tests reported in Chapter 3, the twisted fiber series showed generally better performance than the straight fiber series at high strain rates.

The increases in DIF of three parameters (post cracking strength, energy absorption capacity and strain capacity) follow a log-linear relationship at lower strain rates and increase dramatically at high strain rates. This follows general trends for regular concrete under tension, where the DIF for tensile strength increases mildly up to about 1 or 30 /sec, and then much more rapidly thereafter. The theoretical predictions (Equations (3.2) and (3.3)) used in Chapter 3 for lower strain rates are still valid in high strain cases to describe the relationships between the post-cracking strength and the reinforcing index, and energy absorption capacity and $V_f(l_f^2/d_f)$, respectively. The comparison with theoretical predictions also indicated that fiber twisting enhances the mechanical properties of UHP-FRC, especially at higher strain rates.

The results of this part of the work clearly show the potential UHP-FRC for use in impact- and blast resistant applications. The material has remarkable high strain rate mechanical properties, e.g. T-0.3-25-3% has a post cracking strength in excess of 60 MPa and dissipates more than 1000 KJ/m³ of energy under impact loading. The experimental results from this work combined with the work in Chapter 3 provide fundamental information for developing rate dependent constitutive models for UHP-FRC, which will be needed in the future to simulate the response of UHP-FRC structures subjected to extreme loading.

8.1.4 Characterization of Crack Propagation in UHPC

In Chapter 6, crack propagation in UHPC was investigated using notched specimens, in a three point bending test configuration, subjected to a wide range of loading rates. A hydraulic servo-controlled actuator was used to achieve low notch tip strain rates, in the range of 0.0255 to 1.04 /sec. M-SEFIM was modified to accommodate the bending testing to achieve high notch tip strain rates, ranging from 6.79 to 41.1 /sec. A high speed camera was used to record crack propagation in UHPC. Crack speed and strain rate in UHPC were evaluated using the Canny edge detector algorithm and DIC, respectively. Three fiber volume fraction cases (0%, 0.5% and

1.0%) were considered and their critical stress intensity factors were computed to evaluate the effectiveness of fiber reinforcement in improving fracture toughness.

It was found that the Canny algorithm worked well for detecting crack edge from images recorded using a high speed camera. Crack speed was calculated by averaging the slope of the crack length curves. The UHPC series with fiber reinforcement showed much lower crack speed than UHPC without fibers at the lower loading speeds, which indicates that steel fiber reinforcement play an important role in resisting crack opening at such speeds. In contrast, all UHPC series showed similar crack speeds at higher loading rates, suggesting that cracking is independent of fiber reinforcement at these higher loading rates. It should be noted, however, that UHPC without fibers failed right after crack propagation, while UHPC with fiber reinforcement continued to resist load after matrix cracking up to the point where fibers are pulled-out from the matrix. It was concluded from a series of experiments that crack speed increases asymptotically as strain rate increases and that the maximum asymptotic crack speed is below the theoretical maximum.

Careful examination of the crack surfaces of all UHPC specimens after the bending testing revealed that there were no noticeable changes in the features of the crack surfaces as a function of crack speed. It was found that single straight cracks developed predominantly in UHPC specimens without fibers. In contrast, cracks follow an irregular path in UHPC specimens with 1.0% fiber reinforcements. Furthermore, the stress intensity factor of UHPC increased substantially as fiber volume increases from 0.5% to 1.0%. It was clear from the test data that fiber reinforcement is more effective in improving fracture toughness than compressive strength.

8.1.5 Development of a Theoretical Modeling Scheme for Concrete under Dynamic Tension

In Chapter 7, a DIF modeling scheme based on crack velocity-dependent dynamic fracture mechanics was proposed to provide theoretical insight into the dynamic behavior of concrete under tension. Crack propagation simulations were carried out to offer additional interpretation of the experimentally observed asymptotic crack velocity reported in the literature. Three different mesh sizes were used in this study to simulate crack propagation in concrete. The three cases showed a similar trend: 1) crack velocity increases asymptotically as the strain rate

increases; 2) crack velocity slows as the mesh is refined; and 3) the maximum asymptotic crack velocities are below the theoretical maximum, the Rayleigh wave speed. Because more energy can be dissipated at the crack tip as strain rate increases, more distributed cracking and crack branching are developed as strain rate increases, which results in asymptotic increase in crack velocity as the strain rate increases. Furthermore, the observed crack branching is consistent with test data reported in the literature and observations made by other researchers. Therefore, the cohesive zone model employed in this research properly captured the increasing area of the fracture process zone as the strain rate increased.

Using the obtained relationship between crack velocity and strain rate, dynamic fracture models considering crack velocity-dependency were presented and used to predict the DIF of concrete under tension. Two approaches (Broberg (1960) and Freund (1972)) were considered to model the DIF in concrete under tensile loading. DIF can be expressed as a function of crack velocity of concrete, suggesting that strain rate sensitivity is strongly associated with the characteristics of dynamic crack growth, and specifically, inertial effects at the boundaries of the crack. It was shown that the proposed models capture well the observed trends and that the values that they predict are close to the experimental values. In particular, application of Freund's approach was shown to display better agreement with experimental results for this specific application and set of parameters. The proposed model was also used to predict DIF of UHPC experimentally obtained in Chapters 3 and 5. The relationship between crack speed and notch tip strain rate achieved in Chapter 6 was incorporated into the proposed model, which showed good comparison to the experimental data.

A constitutive modeling scheme was proposed to incorporate the proposed dynamic fracture models into a meso-mechanical model by Huang and Li (1989) to predict stress-strain behavior of concrete under dynamic tensile loading. The proposed constitutive modeling scheme properly captured concrete behavior under dynamic loading, including the higher proportional limit (i.e. elastic limit) and higher tensile strength as the strain rate increases. It was shown that Freund (1972)'s approach gives a slightly higher stress-strain response and higher tensile strength than Broberg (1960)'s approach for the same crack propagation velocity and strain rate. Moreover, a higher volume fraction of aggregate is shown to lead to a higher stress-strain response for both static and dynamic loading cases. Similar to predictions given by the DIF

model, the prediction with Freund (1972)'s approach to the stress-strain behavior of concrete showed better correlation with the experimental data than Broberg (1960)'s approach.

To achieve the above-described theoretical results, dynamic fracture toughness was assumed to be the same as static fracture toughness, following the work of Ravichandrana and Subhash (1995), Paliwal and Ramesh (2008) and Lu and Li (2011). Lambert and Ross (2000) presented conflicting data showing that dynamic fracture toughness does increase with strain rate in a nearly linear manner. Clearly such data may affect some specific findings of the research reported in Chapter 7. However, the proposed general formulations and methodologies can be easily adjusted to account for the new data when it becomes available.

8.2 FUTURE RESEARCH

Suggestions for future research that stems from this work include:

- **Nano-Sized Additives:** Nano-structured materials, such as nano silica Titanium dioxide nano particles (TiO_2), may be considered as an addition to UHPC to further improve its mechanical properties and durability by enhancing packing density of the material.
- **Further Modification of M-SEFIM:** Various strain rates can be conveniently achieved in M-SEFIM by changing the net area of the coupler. Yet, use of such couplers represents an added cost to each experiment because the coupler used in this research is not reusable. Each coupler costs about \$30 at present, but this cost can be alleviated by developing a reusable release mechanism, making the device truly customizable at low cost.
- **Mid-Range Strain Rates:** The direct tensile tests conducted in this work considered either low strain rates (generally less than 0.1 /sec) or high rates (generally more than 100 /sec). These limitations were imposed by the equipment used. Direct tension tests on UHPC under mid-range strain rates (1~100 /sec) are required to provide a full picture of the effect of strain rate on material properties of UHPC.
- **Numerical Prediction:** It will be beneficial to develop a new constitutive material model that can be implemented into commercial finite element programs to simulate the behavior

of structural members made with high performance construction materials under severe loading events.

- **Random Fiber Orientation:** All direct tension testing in this dissertation was carried out using specimens with 25 mm by 25 mm cross-section. Given the fact that fibers used in this research ranged in length from 18 mm to 25 mm, the fibers tended to be aligned along the major axis of the specimens. Therefore, it would be desirable to take into account the effects of fiber orientation when larger sized structure members need to be considered. However, the size of specimen was large enough for the purpose of the comparison of the effectiveness of different fibers under a wide range of loading rates.

REFERENCES

- [1] <http://quizlet.com/5058828/8th-grade-science-taks-review-flash-cards/>
- [2] AASHTO T 132-87 (2009). "Standard method of test for tensile strength of hydraulic cement mortars," American Association of State and Highway Transportation Officials, 8 pages.
- [3] Arakawa K, Mada T, Takahashi K (2000). "Correlations among dynamic stress intensity factor, crack velocity and acceleration in brittle fracture," *International Journal of Fracture*, 105, 311-320.
- [4] Arias I, Knap J, Chalivendra VB, Hong S, Ortiz M, Rosakis AJ (2007). "Numerical modelling and experimental validation of dynamic fracture events along weak planes," *Computer Methods in Applied Mechanics and Engineering*, 196, 3833-3840.
- [5] Barpi F (2004). "Impact behavior of concrete: a computational approach," *Engineering Fracture Mechanics*, 71, 2197-2213.
- [6] Belytschko T, Organ D, Gerlach C (2000). "Element-free Galerkin method for dynamic fracture in concrete," *Computer Methods in Applied Mechanics and Engineering*, 187, 385-399.
- [7] Bierwagen D and Abu-Hawash A (2005). "Ultra high performance concrete highway bridge," *Proceedings of the 2005 Mid-Continent Transportation Research Symposium*, Ames, Iowa, 1-14.
- [8] Bićanić N and Zienkiewicz OC (1983). "Constitutive model for concrete under dynamic loading," *Earthquake Engineering & Structural Dynamics*, 11, 689-710.
- [9] Bourne NK, Millett JCF, Field JE (1999). "On the strength of shocked glasses," *Proceedings of the Royal Society A*, 455, 1275-82.
- [10] Brandt AM (2008). "Fibre reinforced cement-based (FRC) composites after over 40 years of development in building and civil engineering," *Composite Structures*, 86, 3-9.

- [11] Brace WF and Jones AH (1971). "Comparison of uniaxial deformation in shock and static loading of three rocks," *Journal of Geophysical Research*, 76, 4913-4921.
- [12] Brara A, Camborde F, Klepaczko JR, Mariotti C (2001). "Experimental and numerical study of concrete at high strain rates in tension," *Mechanics of Materials*, 33, 33-45.
- [13] Broberg KB (1960). "The propagation of a brittle crack," *Arkiv Fysik*, 18, 159-192.
- [14] Camacho GT and Ortiz M (1996). "Computational modeling of impact damage in brittle materials," *International Journal of Solids and Structures*, 33, 2899-2938.
- [15] Canny J (1986). "A computational approach to edge detection," *IEEE Transactions on Pattern Analysis and Machine Intelligence*, 8, 679-698.
- [16] Cadoni E, Labibes K, Albertini C, Berra M, Giangrasso M (2001). "Strain-rate effect on the tensile behaviour of concrete at different relative humidity levels," *Materials and Structures*, 34, 21-26.
- [17] Cadoni E, Meda A, Plizzari GA (2009). "Tensile behavior of FRC under high strain-rate," *Materials and Structures*, 42, 1283-1294.
- [18] CEB. (1998). Concrete structures under impact and impulsive loading. In: CEB Bulletin d'information, vol. 187. Lausanne, France: Committee Euro-International du Beton.
- [19] Chaudhri MM (2009). "The role of residual stress in a Prince Rupert's drop of soda-lime glass undergoing a self-sustained and stable destruction/fracture wave," *Physica Status Solidi A*, 206, 1410-1413.
- [20] Chaudhri MM (2011). "Self-sustained fracture waves in a lead oxide-silica glass," *Journal of Applied Physics*, 110, 013523.
- [21] Chen R, Liu Y, Guo X, Xia K, Lu F (2011). "Dynamic tensile properties of steel fiber reinforced concrete," In *Dynamic Behavior of Materials*, 1, 37-42, Springer New York.
- [22] Chen W and Song B (2011). *Split Hopkinson (Kolsky) bar: design, testing and applications*, Springer New York.
- [23] Cotsovos DM and Pavlovic MN (2005). "Numerical investigation of RC structural walls subjected to cyclic loading," *Computers and Concrete*, 2, 215-238.
- [24] Cullis I, Hinon M, Gilbert S, Church P, Porter D, Andrews T, Proud W, Pullen A (2008). "Towards predictive modelling for concrete," *International Journal of Impact Engineering*, 35, 1478-83.

- [25] Curbach M and Eibl J (1990). "Crack velocity in concrete," *Engineering Fracture Mechanics*, 35, 321-326.
- [26] Cusatis G and Schaufert EA (2009). "Cohesive crack analysis of size effect," *Engineering Fracture Mechanics*, 76, 2163-2173.
- [27] Dally JW, Agarwal RK, Sanford RJ (1990). "A study of hysteresis in the K_{ID} - \dot{a} relation," *Experimental Mechanics*, 30, 177-183.
- [28] Dally JW, Fourny WL, Irwin GR (1985). "On the uniqueness of stress intensity factor-crack velocity relationship," *International Journal of Fracture*, 27, 159-168.
- [29] Donzé FV, Magnier S-A, Daudeville L, Mariotti C, Davenne L (1999). "Numerical study of compressive behavior of concrete at high strain rates," *Journal of Engineering Mechanics*, 125, 1154-1162.
- [30] Douglas KS and Billington SL (2011). "Strain rate dependence of HPFRCC cylinders in monotonic tension," *Materials and Structures*, 44, 391-404.
- [31] Duarte CA, Hamzeh ON, Liszka TJ, Tworzydło WW (2001). "A generalized finite element method for the simulation of three-dimensional dynamic crack," *Computer Methods in Applied Mechanics and Engineering*, 190, 2227-2262.
- [32] Dugat J, Roux N, Bernier G (1996). "Mechanical properties of reactive powder concretes," *Materials and Structures*, 29, 233-240.
- [33] Dyskin AV, Germanovich LN, Ustinov KB (1999). "A 3-D model of wing crack growth and interaction," *Engineering Fracture Mechanics*, 63, 81-110.
- [34] Eibl J and Curbach M (1989). "An attempt to explain strength increase due to high loading rates," *Nuclear Engineering and Design*, 112, 45-50.
- [35] Elmer VII W, Taciroglu E, McMichael L (2012). "Dynamic strength increase of plain concrete from high strain rate plasticity with shear dilation," *International Journal of Impact Engineering*, 45, 1-15.
- [36] Évora VMF, Jain N, Shukla A (2005). "Stress intensity factor and crack velocity relationship for polyester/TiO₂ nanocomposites," *Experimental Mechanics*, 45, 153-159.
- [37] Fineberg J, Gross SP, Marder M, Swinney HL (1991). "Instability in Dynamic Fracture," *Physical Review Letters*, 67, 457-460.

- [38] Fischer G, Fukuyama H, Li VC (2002). "Influence of matrix ductility on tension-stiffening behavior of steel reinforced engineered cementitious composites (ECC)," *ACI Structural Journal*, 99, 104-111.
- [39] Freund LB (1972). "Crack propagation in an elastic solid subjected to general loading—II. Non-uniform rate of extension," *Journal of the Mechanics and Physics of Solids*, 20, 141-152.
- [40] Freund LB (1990). *Dynamic fracture mechanics*. Cambridge, New York: Cambridge University Press.
- [41] Fujikake K, Senga T, Ueda N, Ohno T, Katagiri M (2006). "Effects of strain rate on tensile behavior of reactive powder concrete," *Journal of Advanced Concrete Technology*, 4, 79-84.
- [42] Gao H (1993). "Surface roughening and branching instabilities in dynamic fracture," *Journal of the Mechanics and Physics of Solids*, 41, 457-486.
- [43] Georgin JF and Reynouard JM (2003). "Modeling of structures subjected to impact: Concrete behaviour under high strain rate," *Cement and Concrete Composites*, 25, 131-143.
- [44] Gilat A, Goldberg RK, Roberts GD (2002). "Experimental study of strain-rate-dependent behavior of carbon/epoxy composite," *Composites Science and Technology*, 62, 1469-1476.
- [45] Gray GT (2000). "Classic split-hopkinson pressure bar testing," *American Society for Metals*, ASM Handbook Vol. 8 - Mechanical Testing and Evaluation, 462-476
- [46] Graybeal BA (2006). *Material Property Characterization of Ultra-High Performance Concrete*, Report No. FHWA-HRT-06-103, Federal Highway Administration, Washington, DC.
- [47] Graybeal BA (2009). "UHPC making strides," *Public Roads*, Federal Highway Administration, McLean, VA, 72, 17-21.
- [48] Graybeal BA (2011). *Ultra-High Performance Concrete*, Report No. FHWA-HRT-11-038, Federal Highway Administration, Washington, DC.
- [49] Graybeal BA (2013). *Development of non-proprietary ultra-high performance concrete for use in the highway bridge sector*, Report No. FHWA-HRT-13-100, Federal Highway Administration, McLean, VA.

- [50] Habel K and Gauvreau P (2008). "Response of ultra-high performance fiber reinforced concrete (UHPFRC) to impact and static loading," *Cement and Concrete Composites*, 30, 938–946.
- [51] Haralick R (1984). "Digital step edges from zero crossing of second directional derivatives," *IEEE Transactions on Pattern Analysis and Machine Intelligence*, 6, 58-68.
- [52] Harding J and Welsh LM (1983). "A tensile testing technique for fibre-reinforced composites at impact rates of strain," *Journal of Materials Science*, 18, 1810-1826.
- [53] Hauser FE, Simmons JA, Dorn JE (1961). "Strain rate effects in plastic wave propagation," In *Response of metals to high velocity deformation* (ed. P. G. Shewmon & V. F. Zackay), 93–109. New York: Interscience.
- [54] Hentz S, Donzé FV, Daudeville L (2004). "Discrete element modelling of concrete submitted to dynamic loading at high strain rates," *Computers and Structures*, 82, 2509-2524.
- [55] Huang J and Li VC (1989). "A meso-mechanical model of the tensile behavior of concrete. Part 1: modeling of the pre-peak stress-strain relation," *Composites*, 20, 361–369.
- [56] John R and Shah SP (1986). "Fracture of concrete subjected to impact loading," *Cement, Concrete and Aggregates*, 8, 24-32.
- [57] John R, Shah SP, Jenq YS (1987). "A fracture model to predict the rate sensitivity of mode I fracture of concrete," *Cement and Concrete Research*, 17, 249-262.
- [58] Johnson E (1992). "Process region changes for rapidly propagating cracks," *International Journal of Fracture*, 55, 47-63.
- [59] Keierleber B, Bierwagen D, Wipf T, Abu-Hawash A (2008). "Design of Buchanan County, Iowa bridge using ultra-high performance concrete and Pi-girder cross section," *Proceedings of the Precast/Prestressed Concrete Institute National Bridge Conference*, Orlando, FL.
- [60] Kim DJ, El-Tawil S, Naaman AE (2008). "Loading rate effect on pullout behavior of deformed steel fiber," *ACI Materials Journal*, 105, 576-584.
- [61] Kim DJ, El-Tawil S, Naaman AE (2009). "Rate-dependent tensile behavior of high performance fiber reinforced cementitious composites," *Materials and Structures*, 42, 399-414.

- [62] Kim DJ, El-Tawil S, Naaman AE (2012). Impact test apparatus by using energy frame, Patent filed in South Korea on 05/09/2011. Patent issued in 12/10/2012. Patent number 10-1212646.
- [63] Kim DJ, Sirijaroonchai K, El-Tawil S, Naaman, AE (2010). “Numerical simulation of the Split Hopkinson Pressure Bar test technique for concrete under compression,” *International Journal of Impact Engineering*, 37, 141–149.
- [64] Kim DJ, Wille K, El-Tawil S, Naaman AE (2011). “Testing of cementitious materials under high-strain-rate tensile loading using elastic strain energy,” *ASCE Journal of Engineering mechanics*, 137, 1-8.
- [65] Klepaczko JR (2003). “On a very high rate sensitivity of concrete failure at high loading rates and impact,” *Proceeding of international symposium on brittle matrix composites*, 7, ZTUREK RSI and Woodhead Publication, Warsaw, 1-28.
- [66] Kolsky H (1949). “An investigation of the mechanical properties of materials at very high rates of strain,” *Proceedings of the Physical Society. Section B.*, 62, 676-700.
- [67] Krafft JM and Irwin GR (1965). “Crack velocity considerations,” *Fracture Toughness Testing and Its Applications*, ASTM STP, 381, 114-129.
- [68] Lambert DE and Ross CA (2000). “Strain rate effects on dynamic fracture and strength,” *International Journal of Impact Engineering*, 24, 985-998.
- [69] Landis CM, Pardo T, Hutchinson JW (2000). “Crack velocity dependent toughness in rate dependent materials,” *Mechanics of Materials*, 32, 663-678.
- [70] Lee KH, Hawong JS, Choi SH (1996). “Dynamic stress intensity factors K_I , K_{II} and dynamic crack propagation characteristics of orthotropic material,” *Engineering Fracture Mechanics*, 53, 119-140.
- [71] Leppanen J (2006). “Concrete subjected to projectile and fragment impacts: Modelling of crack softening and strain rate dependency in tension,” *International Journal of Impact Engineering*, 32, 1828–1841.
- [72] Li M, Wang R, Han M-B (1993a). “A Kolsky bar: tension, tension-tension,” *Experimental Mechanics*, 33, 7-14.
- [73] Li QM and Meng H (2003). “About the dynamic strength enhancement of concrete-like materials in a split Hopkinson pressure bar test,” *International Journal of Solids and Structures*, 40, 343-360.

- [74] Li VC (2003). "On engineered cementitious composites (ECC)," *Journal of advanced concrete technology*, 1, 215-230.
- [75] Li VC, Wang S, Wu C (2001). "Tensile strain-hardening behavior of polyvinyl alcohol engineered cementitious composite (PVA-ECC)," *ACI Materials Journal*, 98, 483-492.
- [76] Li W and Xu J (2009). "Impact characterization of basalt fiber reinforced geopolymeric concrete using a 100-mm-diameter split Hopkinson pressure bar," *Materials Science and Engineering A*, 513-514, 145-153.
- [77] Li Z, Kulkarni M, Shah SP (1993b). "New test method for obtaining softening response of unnotched concrete specimen under uniaxial tension," *Experimental Mechanics*, 33, 181-188.
- [78] Lim CC, Gowripalan N, Sirivivatnanon V (2000), "Microcracking and chloride permeability of concrete under uniaxial compression," *Cement and Concrete Composites*, 22, 353-360.
- [79] Lindholm US and Yeakley LM (1968). "High strain-rate testing: Tension and compression," *Experimental Mechanics*, 8, 1-9.
- [80] Liu Y and Lapusta N (2008). "Transition of mode II cracks from sub-Rayleigh to intersonic speeds in the presence of favorable heterogeneity," *Journal of the Mechanics and Physics of Solids*, 56, 25-50.
- [81] Livermore Software Technology Corporation (2007). "LS-DYNA® Keyword User's Manual." May.
- [82] Lowke D, Stengel T, Schießl P, Gehlen C (2012). "Control of rheology, strength and fibre bond of UHPC with additions - effect of packing density and addition type," In *Ultra-High Performance Concrete and Nanotechnology in Construction. Proceedings of Hipermat 2012*, No. 19, 215-224.
- [83] Lu YB and Li QM (2011). "About the dynamic uniaxial tensile strength of concrete-like materials," *International Journal of Impact Engineering*, 38, 171-180.
- [84] Maalej M, Quek ST, Zhang J (2005). "Behavior of hybrid-fiber engineered cementitious composites subjected to dynamic tensile loading and projectile impact," *Journal of Materials in Civil Engineering*, 17, 143-152.
- [85] Maini R and Aggarwal H (2009). "Study and comparison of various image edge detection techniques," *International Journal of Image Processing*, 3, 1-11.

- [86] Malvar LJ and Crawford JE (1998). "Dynamic increase factors for concrete," *Twenty-eighth DDESB Seminar*, Orlando, August.
- [87] Markovic I (2006). "High-performance hybrid-fibre concrete: development and utilisation," PhD thesis, Delft University of Technology.
- [88] Marr D and Hildreth E (1980). "Theory of edge detection," *Proceedings of the Royal Society of London. Series B. Biological Sciences*, 207, 187-217.
- [89] Mechtcherine V, Millon O, Butler M, Thoma K (2011). "Mechanical behaviour of strain hardening cement-based composites under impact loading," *Cement and Concrete Composites*, 33, 1-11.
- [90] Millard SG, Molyneaus TCK, Barnett SJ, Gao X (2010). "Dynamic enhancement of blast-resistant ultra high performance fibre-reinforced concrete under flexural and shear loading," *International Journal of Impact Engineering*, 37, 405-413.
- [91] Mindess S, Banthia NP, Ritter A, Skalny JP (1986). "Crack development in cementitious materials under impact loading," *Materials Research Society Symposia Proceedings*, 64, 217-223.
- [92] Muria Vila D and Hamelin P (1987). "Comportement au choc des béton et mortiers a matrices hydrauliques," *1st International RILEM Congress 2, in Combining Materials: Design, Production and Properties* (Edited by J.C. Maso), Chapman and Hall, London, 725-732.
- [93] Naaman AE (2002). "Toughness, ductility, surface energy and deflection-hardening FRC composites," *Proceedings of the JCI international Workshop on Ductile Fiber Reinforced Cementitious Composites (DFRCC) - Application and Evaluation (DFRCC-02)*, Takayama, Japan, October, pp. 33-57.
- [94] Naaman AE (2003). "Engineered Steel Fibers with Optimal Properties for Reinforcement of Cement Composites," *Journal of Advanced Concrete Technology*, 1, 241-252
- [95] Naaman AE and Homrich JR (1989). "Tensile stress-strain properties of SIFCON," *ACI Material Journal*, 86, 244-251.
- [96] Naaman AE and Reinhardt HW (2003). "Setting the stage: Toward performance based classification of FRC composites," In *Proceedings of 4th International RILEM Workshop on High Performance Fiber Reinforced Cement Composites (HPFRCC 4)*, 1-4.

- [97] Naaman AE and Reinhardt HW (2006). "Proposed classification of HPFRC composites based on their tensile response," *Materials and Structures*, 39, 547-555.
- [98] Naaman AE and Wille K (2012). "The path to ultra-high performance fiber reinforced concrete (UHP-FRC): Five decades of progress," In *Proceedings of Hipermat 3rd International Symposium on UHPC and Nanotechnology for High Performance Construction Materials*, Kassel University Press, Kassel (pp. 3-16).
- [99] Nicholas T (1981). "Tensile testing of materials at high rates of strain," *Experimental Mechanics*, 21, 177-185.
- [100] Nöldgen M, Millon O, Thoma K, Fehling E (2009). "Hochdynamische Eigenschaften von Ultrahochleistungsbeton (UHPC)," *Beton- und Stahlbetonbau*, 104, 717-727, DOI: 10.1002/best.200900038 (in German).
- [101] Owens AT and Tippur HV (2009). "Tensile stress-strain response of glass-filled epoxy under elevated rates of loading using a split Hopkinson bar apparatus," *Experimental Mechanics*, 49, 799-811.
- [102] Ožbolt J, Sharma A, Reinhardt H (2011). "Dynamic Fracture of Concrete – 3D Numerical Study of Compact Tension Specimen," *Applied Mechanics and Materials*, 82, 39-44.
- [103] Paliwal B and Ramesh KT (2008). "An interacting micro-crack damage model for failure of brittle materials under compression," *Journal of the Mechanics and Physics of Solids*, 56, 896-923.
- [104] Pan B, Qian K, Xie H, Asundi A (2009). "Two-dimensional digital image correlation for in-plane displacement and strain measurement: a review," *Measurement science and technology*, 20, 062001.
- [105] Parant E (2003). "Mécanismes d'endommagement et comportements mécaniques d'un composite cimentaire fibré multi-échelles sous sollicitations sévères: fatigue, choc, corrosion," Doctoral thesis, Laboratoire Central des Ponts et Chaussées (LCPC), France, December, (in French).

- [106] Peters WH and Ranson WF (1982). "Digital imaging techniques in experimental stress analysis," *Optical Engineering*, 21, 427-431.
- [107] Pfeifer CG, Moeser B, Giebson C, Stark J (2009). "Durability of ultra-high-performance concrete," *Tenth ACI International Conference on Recent Advances in Concrete Technology and Sustainability Issues*. No. SP-261-1.
- [108] Pyo S and El-Tawil S (2013). "Crack velocity-dependent dynamic tensile behavior of concrete," *International Journal of Impact Engineering*, 55, 63-70.
- [109] Ravichandrana G and Subhash G (1994). "Critical appraisal of limiting strain rates for compression testing of ceramics in a split Hopkinson pressure bar," *Journal of the American Ceramic Society*, 77, 263-267.
- [110] Ravichandrana G and Subhash G (1995). "A micromechanical model for high strain rate behavior of ceramics," *International Journal of Solids and Structures*, 32, 2627-2646.
- [111] Rayleigh L (1885). "On waves propagated along the plane surface of an elastic solid," *Proceedings of the Royal Society A*, 17, 4-11.
- [112] Reinhardt HW, Körmeling HA, Zielinski AJ (1986). "The split Hopkinson bar, a versatile tool for the impact testing of concrete," *Materials and Structures*, 19, 55-63.
- [113] Remmers JJC, de Borst R, Needleman A (2008). "The simulation of dynamic crack propagation using the cohesive segments method," *Journal of the Mechanics and Physics of Solids*, 56, 70-92.
- [114] Repetto EA, Radovitzky R, Ortiz M (2000). "Finite element simulation of dynamic fracture and fragmentation of glass rods," *Computer Methods in Applied Mechanics and Engineering*, 183, 3-14.
- [115] Reu PL and Miller TJ (2008). "The application of high-speed digital image correlation," *The Journal of Strain Analysis for Engineering Design*, 43, 673-688.
- [116] Ross CA (1989). "Split Hopkinson pressure bar tests," Final Report, Air Force Engineering and Services Center, Tyndall AFB, FL, ESL-TR-88-82.
- [117] Ross CA, Jerome DM, Tedesco JW, Hughes ML (1996). "Moisture and strain rate effects on concrete strength," *ACI Materials Journal*, 93, 293-300.
- [118] Ross CA, Tedesco JW, Kuennen ST (1995). "Effects of strain rate on concrete strength," *ACI Materials Journal*, 92, 37-47.
- [119] Ross CA, Thomson PY, Tedesco JW (1989). "Split-Hopkinson pressure-bar test on

- concrete and mortar in tension and compression,” *ACI Materials Journal*, 86, 475-481.
- [120] Rossi P (1997). “High performance multimodal fiber reinforced cement composites (HPMFRCC): the LCPC Experience,” *ACI materials journal*, 94, 478–483.
- [121] Rossi P (2008). “Ultra High Performance Concretes,” *Concrete international*, 30, 31-34.
- [122] Rouse JM, Wipf TJ, Phares B, Fanous F, Berg O (2011). “Design, Construction, and Field Testing of an Ultra High Performance Concrete Pi-Girder Bridge,” *IHRB Project TR-754*, Iowa State University, Ames, Iowa.
- [123] Ruiz G, Ortiz M, Pandolfi A (2000). “Three-dimensional finite-element simulation of the dynamic Brazilian tests on concrete cylinders,” *International Journal for Numerical Methods in Engineering*, 48, 963-994.
- [124] Ruiz G, Pandolfi A, Ortiz M (2001). “Three-dimensional cohesive modeling of dynamic mixed-mode fracture,” *International Journal for Numerical Methods in Engineering*, 52, 97-120.
- [125] Schuler H, Mayrhofer C, Thoma K (2006). “Spall experiments for the measurement of the tensile strength and fracture energy of concrete at high strain rates,” *International Journal of Impact Engineering*, 32, 1635-1650.
- [126] Scott BD, Park R, Priestley MJN (1982), “Stress-strain behavior of concrete confined by overlapping hoops at low and high strain rates,” *ACI Journal Proceedings*, 79, 13-27.
- [127] Sercombe J, Ulm F-J, Toutlemonde F (1998). “Viscous hardening plasticity for concrete in high-rate dynamics,” *Journal of Engineering Mechanics*, 124, 1050-1057.
- [128] Shah SP (1990). “Determination of fracture parameters (K_{Ic}^S and $CTOD_c$) of plain concrete using three-point bend tests,” *Materials and Structures*, 23, 457-460.
- [129] Sharon E and Fineberg J (1999). “Confirming the continuum theory of dynamic brittle fracture for fast cracks,” *Nature*, 397, 333-335.
- [130] Shet C and Chandra N (2002). “Analysis of energy balance when using cohesive zone models to simulate fracture processes,” *Journal of engineering materials and technology*, 124, 440-450.
- [131] Shukla A and Nigam H (1986). “A note on the stress intensity factor and crack velocity relationship for Homalite 100,” *Engineering Fracture Mechanics*, 25, 91-102.
- [132] Sibiriakov BP (2002). “Supersonic and intersonic cracking in rock-like material under remote stresses,” *Theoretical and Applied Fracture Mechanics*, 38, 255-265.

- [133] Smerd R, Winkler S, Salisbury C, Worswick M, Lloyd D, Finn M (2005). "High strain rate tensile testing of automotive aluminum alloy sheet," *International Journal of Impact Engineering*, 32, 541-560.
- [134] Song B, Connelly K, Korellis J, Lu W-Y, Antoun BR (2009). "Improved Kolsky-bar design for mechanical characterization of materials at high strain rates," *Measurement Science and Technology*, 20, 115701-1-8.
- [135] Staab GH and Gilat A (1991). "A direct-tension split Hopkinson bar for high strain-rate testing," *Experimental Mechanics*, 31, 232-235.
- [136] Sun B, Liu F, Gu B (2005). "Influence of the strain rate on the uniaxial tensile behavior of 4-step 3D braided composites" *Composites Part A: Applied Science and Manufacturing*, 36, 1477-1485.
- [137] Sutton MA, Orteu JJ, Schreier H (2009). *Image correlation for shape, motion and deformation measurements: basic concepts, theory and applications*. Springer Publishing Company, Incorporated.
- [138] Sutton MA, Wolters WJ, Peters WH, Ranson WF, McNeill SR (1983). "Determination of displacements using an improved digital correlation method," *Image and Vision Computing*, 1, 133-139.
- [139] Takeda J, Tachikawa H, Fujimoto K (1982). "Concrete structures under impact and impulsive loading," in Proceedings, *RILEM-CEBIABSE-IASS Interassociation Symposium*, West Berlin, 83-91.
- [140] Tang T, Malvern LE, Jenkins DA (1992). "Rate effects in uniaxial dynamic compression of concrete," *Journal of engineering mechanics*, 118, 108-124.
- [141] Tedesco JW and Ross CA (1993). "Experimental and numerical analysis of high strain rate splitting-tensile tests," *ACI Materials Journal*, 90, 162-169.
- [142] Tran TK and Kim DJ (2012). "Strain energy impact test machine (SEFIM)," *Journal of Advanced Concrete Technology*, 10, 126-136.
- [143] Tran TK and Kim DJ (2013). "Investigating direct tensile behavior of high performance fiber reinforced cementitious composites at high strain," *Cement and Concrete Research*, 50, 62-73.

- [144] Verhulp E, van Rietbergen B, Huiskes R (2004). "A three-dimensional digital image correlation technique for strain measurements in microstructures," *Journal of Biomechanics*, 37, 1313-1320.
- [145] Vinh PC and Ogden RW (2004). "On formulas for the Rayleigh wave speed," *Wave Motion*, 39, 191-197.
- [146] Walley SM (2010). "Historical review of high strain rate and shock properties of ceramics relevant to their application in armour," *Advances in Applied Ceramics*, 109, 446-466.
- [147] Wang W, Huang Y, Rosakis AJ, Liu C (1998). "Effect of elastic mismatch in intersonic crack propagation along a bimaterial interface," *Engineering Fracture Mechanics*, 61, 471-485.
- [148] Wardeh G and Ghorbel E (2013). "Prediction of fracture parameters and strain-softening behavior of concrete: effect of frost action," *Materials and Structures*, in press.
- [149] Wille K, El-Tawil S, Naaman AE (2012). "Strain Rate Dependent Tensile Behavior of Ultra-High Performance Fiber Reinforced Concrete." In *High Performance Fiber Reinforced Cement Composites 6* (pp. 381-387). Springer, Netherlands.
- [150] Wille K, El-Tawil S, Naaman AE (2014). "Properties of strain hardening ultra high performance fiber reinforced concrete (UHP-FRC) under direct tensile loading," *Cement and Concrete Composites*, submitted.
- [151] Wille K, Kim DJ, Naaman AE (2011a). "Strain-hardening UHP-FRC with low fiber contents," *Materials and Structures*, 44, 583-598.
- [152] Wille K and Naaman AE (2010). "Bond stress-slip behavior of steel fibers embedded in ultra high performance concrete," *Proceedings of 18th European Conference on Fracture and Damage of Advanced Fiber-Reinforced Cement-Based Materials*, Contribution to ECF 18, V. Mechtcherine & M. Kaliske (eds.), Aedificatio Publishers, Dresden, 99 – 111.
- [153] Wille K and Naaman AE (2012). "Pullout behavior of high-strength steel fibers embedded in Ultra-high-Performance concrete," *ACI Materials Journal*, 109, 479-487.
- [154] Wille K, Naaman AE, Parra-Montesinos GJ (2011b). "Ultra-high performance concrete with compressive strength exceeding 150 MPa (22 ksi): A simpler way," *ACI Materials Journal*, 108, 46-54.

- [155] Wille K and Parra-Montesinos GJ (2012). "Effect of beam size, casting method, and support conditions on flexural behavior of ultra-high-performance fiber-reinforced concrete," *ACI Materials Journal*, 109, 379-388.
- [156] Wipf TJ, Phares BM, Sritharan S, Degen EB, Giesmann TM (2009). "Design and Evaluation of a Single-Span Bridge Using Ultra-High Performance Concrete," *IHRB Project TR-529*. Iowa State University, Ames, Iowa.
- [157] Xie H and Sanderson DJ (1995). "Fractal effects of crack propagation on dynamic stress intensity factors and crack velocities," *International Journal of Fracture*, 74, 29-42.
- [158] Xia K, Chalivendra VB, Rosakis AJ (2006). "Observing ideal "self-similar" crack growth in experiments," *Engineering Fracture Mechanics*, 73, 2748–2755.
- [159] Xu X-P and Needleman A (1994). "Numerical simulations of fast crack growth in brittle solids," *Journal of the Mechanics and Physics of Solids*, 42, 1397-1434.
- [160] Xu Z, Hao H, Li HN (2012). "Dynamic tensile behaviour of fibre reinforced concrete with spiral fibres," *Materials and Design*, 42, 72-88.
- [161] Yan D and Lin G (2006). "Dynamic properties of concrete in direct tension," *Cement and Concrete Research*, 36, 1371-1378.
- [162] Yang E and Li VC (2005). "Rate dependence in engineered cementitious composites," In *Proceedings, HPRCC-2005 international workshop*. Honolulu, Hawaii, USA.
- [163] Yoneyama S, Kitagawa A, Iwata S, Tani K, Kikuta H (2007). "Bridge deflection measurement using digital image correlation," *Experimental Techniques*, 31, 34-40.
- [164] Zaitsev YV (1985). "Inelastic properties of solids with random cracks," in *Mechanics of Geomaterials* (ed Z. Bazant), 89-128.
- [165] Zhai J, Tomar V, Zhou M (2004). "Micromechanical simulation of dynamic fracture using the cohesive finite element method," *Journal of Engineering Materials and Technology*, 126, 179-191.
- [166] Zhao H (1998). "A study on testing techniques for concrete-like materials under compressive impact loading," *Cement and Concrete Composites*, 20, 293-299.
- [167] Zhou F, Molinari J-F, Shioya T (2005). "A rate-dependent cohesive model for simulating dynamic crack propagation in brittle materials," *Engineering Fracture Mechanics*, 72, 1383-1410.

- [168] Zhu D, Peled A, Mobasher B (2011). "Dynamic tensile testing of fabric–cement composites," *Construction and Building Materials*, 25, 385-395.
- [169] Zielinski AJ, Reinhardt HW, Körmeling HA (1981). "Experiments on concrete under uniaxial impact tensile loading," *Matériaux et Constructions*, 14, 103-112.